Multiphase Dynamics of Colloidal Deposition and Resuspension at Membranes

Mehrphasendynamik kolloidaler Ablagerungen und Resuspendierungen an Membranen

Von der Fakultät für Maschinenwesen der Rheinisch-Westfälischen Technischen Hochschule Aachen zur Erlangung des akademischen Grades eines Doktors der Ingenieurwissenschaften genehmigte Dissertation

vorgelegt von

Johannes Lohaus

Berichter:
Univ.-Prof. Dr.-Ing. Matthias Wessling
Prof.Dr.Ir. Rob G.H. Lammertink

Tag der mündlichen Prüfung: 25.11.2021

Diese Dissertation ist auf den Internetseiten der Universitätsbibliothek online verfügbar.

Titel: Multiphase Dynamics of Colloidal Deposition and Resuspension at Membranes

Autor: Johannes Lohaus

Reihe: Aachener Verfahrenstechnik Series
AVT.CVT - Chemical Process Engineering
Volume: 22 (2021)

Herausgeber: Aachener Verfahrenstechnik
Forckenbeckstraße 51
52074 Aachen
Tel.: +49 (0)241 8097717
Fax.: +49 (0)241 8092326
E-Mail: secretary.cvt@avt.rwth-aachen.de
http://www.avt.rwth-aachen.de/AVT

Publications

Parts of this dissertation have been published. Reproduced with permission from:

J. Lohaus, Y.M. Perez, M. Wessling,
What are the microscopic events of colloidal membrane fouling?,
Journal of Membrane Science,
Volume 553,
2018,
Pages 90-98,
ISSN 0376-7388,
https://doi.org/10.1016/j.memsci.2018.02.023.

J. Lohaus, F. Stockmeier, P. Surray, J. Lölsberg, M. Wessling,
What are the microscopic events during membrane backwashing?,
Journal of Membrane Science,
Volume 602,
2020,
117886,
ISSN 0376-7388,
https://doi.org/10.1016/j.memsci.2020.117886

Johannes Lohaus, Deniz Rall, Maximilian Kruse, Viktoria Steinberger, Matthias Wessling,
On charge percolation in slurry electrodes used in vanadium redox flow batteries,
Electrochemistry Communications,
Volume 101,
2019,
Pages 104-108,
ISSN 1388-2481,
https://doi.org/10.1016/j.elecom.2019.02.013.

Acknowledgement

Die Zeit am Lehrstuhl für Chemische Verfahrenstechnik an der RWTH Aachen war ein aufregender und besonderer Abschnitt in meinem Leben. Ich habe in dieser Zeit viel gelernt und großartige Erfahrungen gemacht und sie wird mir immer in überaus positiver Erinnerung bleiben. Aber ganz besonders bleiben mir die vielen Menschen in Erinnerungen, mit denen ich lernen, lehren und forschen, aber vor allem viel Spaß haben durfte.

Mein besonderer Dank gilt meinem Doktorvater Prof. Dr.-Ing Matthias Wessling. Die Faszination am Forschen, die fortwährende Suche nach Erkenntnis und den Mut immer neue Wege einzuschlagen, hat mich zutiefst beeindruckt und geprägt. Matthias, ich bin stolz Teil deines Teams gewesen zu sein.

Many thanks to my second examiner Prof. Dr.ir. Rob G.H. Lammertink who gave me valuable advice for my research during the Winterschool. Prof. Dr.-Ing. Dr. h. c. Burkhard Corves danke ich für den Vorsitz und die sehr angenehme und faire Prüfungsführung.

Das Beste an der Zeit am Lehrstuhl sind die tollen Kollegen und Mitstreiter, mit denen ich das Glück hatte zusammenzuarbeiten. Ganz besonderer Dank an meine Kollegin und Cousine Theresa Rösener, die mich erst ermutigt hat, diesen Schritt zu gehen und die immer ein offenes Ohr für mich hat. Ich hatte das große Glück mit meinem sehr guten Freund Morten Logemann, meine Promotion zu starten und auch erfolgreich abzuschließen. Die gemeinsame Zeit, angefangen an der Wüllner Straße, war und ist weiterhin immer ein großer Gewinn für mich. Während der Zeit am Lehrstuhl hatte ich das Glück mit den ausgezeichneten Kollegen Monika Wiese, Alexandra Rommerskirchen, Morten Logemann, Maik Tepper, Jan Venneköter und Arne Lüken die Lehrveranstaltung Grundoperationen der Verfahrenstechnik zu betreuen. Anna Kalde, Theresa Rösener, Deniz Rall, Arne Lüken, Lucas Stüwe und Felix Stockmmeier danke ich für die großartigen Kooperationen. Hier auch ein besonderer Dank an John Linkhorst, der die Grundlage für meine Forschungen gelegt hat. Für die vielen fachlichen Diskussion und privaten Gespräche danke ich Michael Alders, Chris-

tian Linnartz, Maik Tepper, Daniel Felder, Korcan Percin, Jonas Lölsberg, Robert Femmer, Robert Keller, Georg Linz, Denis Wypsek und Benedikt Aumeier. Und natürlich auch ein Riesen Dank an meine Bürokollegen Laura Keller, Hanna Wolff, Berinike Göbel, Tao Luo, Daniel Menne, Hans Breisig und Patrick Bongartz. Neben den Doktoranden möchte ich noch den vielen festangestellten Mitarbeitern am Lehrstuhl danken, die das Rückgrat des Instituts sind. Vielen Dank Susanne Offermann für deinen ganzen Einsatz für uns Doktoranten, sowie dem Labor Team, der Werkstatt und dem IT-Team. Ein Riesendank geht auch an meine tollen Studenten, die ich betreuen durfte. Ohne euren Einsatz und guten Ideen hätte die Arbeit nicht so weit vorangetrieben werden können. Ferner möchte ich mich bei allen Kollegen bedanken, dass mein geliebter Grill nie ausgekühlt ist. Ich möchte die gemeinsame Zeit und die schönen Grillabende mit euch nicht missen.

Weiterhin bedanke ich mich bei meinen Freunden, meinem Kegelclub "KC Bierbuben" und Schalke für den wichtigen Ausgleich und die vielen großartigen Momente abseits der Arbeit. Abschließend möchte ich mich bei meiner großartigen Familie Lohaus und Hammeke bedanken. Meine drei Brüder Mathias, Andreas und Stefan Lohaus waren und sind meine wichtigsten Bezugspunkte. Auch an meine drei Schwägerinnen Katharina, Kathrin und Christine mit meiner Nichte Marie und meinem Neffe Noah ein ganz herzliches Dankeschön. Ein besonderer Dank an meine lieben Eltern, die mich seit dem ersten Tag an immer unterstützt haben. Auf die stetige Unterstützung und den Rückhalt meiner Familie konnte ich mich immer verlassen. Zuletzt bedanke ich mich bei meiner geliebten Frau Suzana Lohaus. Danke, dass du immer für mich da bist, mein Fels bist und mir mit unserer kleinen Tochter Sophia das schönste Geschenk gemacht hast.

Für meine Familie

Contents

Abstract

Colloidal fouling significantly limits the performance of membrane filtration processes. In particular, the complex interplay between surface potentials and hydrodynamic interactions on the pore-scale level pose a big challenge for science. Numerical simulations accompanied by microfluidic experiments enable to visualize the mechanisms occurring during fouling and thus helping to decode the fouling processes.

This thesis used coupled computational fluid dynamics - discrete element methods (CFD-DEM) simulations to examine pore-scale mechanisms during membrane fouling and membrane backwashing. The simulations were accompanied by microfluidic experiments.

The clogging behavior was analyzed inside varying pore structures with CFD-DEM simulations and compared to experimental findings from literature. The simulations revealed a dominant role of the inner pore structure, which is consistent with experimental observations from literature. The origin of clogging relied on a variety of parallel occurring processes: (1) adsorption on the constriction entrance; (2) interparticle interaction leading to adsorption; (3) gliding of adsorbed and loosely bond particles and, (4) particle resuspension.

In membrane backwashing, particle resuspension plays an important role and was therefore investigated in more detail. Simulations and experiments both revealed that the backwash is decisively controlled by particle clusters instead of single-particle effects. This clarifies that single-particle models are not representative of describing mechanisms occurring during backwash. Two dominant events of backwash were identified from the simulations and experiments: (1) partial resuspension of particle clusters and, (2) orientation of attached particle clusters in the region of lower drag.

Another important point in membrane fouling is temperature dependency which is only minorly addressed in literature. This thesis presents a systematic analysis of experimental and numerical study for particle-laden flow through a membrane mimicking pore-like channel under the influence of temperature. The effect of temperature on colloidal aggregation was incorporated by attractive and repulsive temperature-dependent potentials between particles and membrane. This study showed that are still gaps between theory and experimental observation, which have to be resolved in future studies.

Another property which is of decisive interest in understanding colloidal fouling is the softness of the particle. The role of softness during filtration was studied with the help of CFD-DEM simulations. The simulations demonstrated that soft particles arrange in highly-ordered and compact filter cake structures due to hydrodynamic stress. Therefore, the soft filter cake caused significantly higher resistance in comparison to hard filter cakes. Furthermore, the simulations revealed that cake relaxation of soft filter cakes is fully reversible, whereas a short-term flux increase can lead to irreversible changes in cake structure.

In summary, this thesis highlights and illustrates microscopic events of particle depo-

sition and resuspension, which will ultimately help to understand colloidal fouling and make membrane backwashing more efficient.

Zusammenfassung

Kolloidales Fouling ist bei vielen Membranfiltrationsprozessen die entscheidende Limitierung. Insbesondere das komplexe Wechselwirkungen zwischen Oberflächenpotentialen und hydrodynamischen Interaktionen auf der Porenebene stellt eine große Herausforderung für das Verständnis des Foulingprozesses dar. Numerische Simulationen in Kombination mitmikrofluidischen Experimenten, ermöglichen es ide auftretenden Foulingmechanismen zu visualisieren und damit die Foulingprozesse zu entschlüsseln.

In dieser Arbeit werden gekoppelte CFD-DEM-Simulationen (Computational Fluid Dynamics - Discrete Element Method) verwendet, um die Porenskalenmechanismen während des Membranfoulings und der Membranrückspülung zu untersuchen. Die Simulationen werden von eigenen oder auf Literatur basierenden mikrofluidischen Experimenten begleitet.

Das Clogging innerhalb verschiedener Porenstrukturen wird mit CFD-DEM Simulationen analysiert und mit experimentellen Ergebnissen aus der Literatur verglichen. Die Simulationen zeigen eine dominante Rolle der inneren Porenstruktur, was mit experimentellen Beobachtungen aus der Literatur übereinstimmt. Der Ursprung des Cloggings beruht auf einer Vielzahl von parallel ablaufenden Prozessen: (1) Adsorption am Eingang der Verengung; (2) Interpartikel-Wechselwirkung, die zur Adsorption führt; (3) Gleiten der adsorbierten und locker gebundenen Partikel und (4) Partikel-Resuspendierung.

Die Partikelresuspendierung wird bei der Membranrückspülung durch kombinierte Mikrofluidik- und CFD-DEM-Simulationen genauer untersucht. Sowohl die Simulationen als auch die Experimente zeigen, dass die Rückspülung entscheidend durch Partikelcluster anstelle von Einzelpartikel-Effekten kontrolliert wird. Dies verdeutlicht, dass Einzelpartikelmodelle nicht aussreichend für die Beschreibung der auftretenden Prozesse während des Rückspülens sind. Aus den Simulationen und den Experimenten wurden zwei dominante Ereignisse der Rückspülung identifiziert: (1) partielle Resuspension von Partikel-Clustern und (2) Orientierung der anhaftenden Partikel-Cluster in den Bereich geringere Scherkräfte. Die Studie zeigte, dass reduzierte Membran-Partikel-Wechselwirkungen ein wirksames Mittel zur Verbesserung der Rückspülleistung sind.

Ein Prozessparameter, der in der Literatur nur wenig untersucht wird, ist die Temperaturabhängigkeit des Foulings. In dieser Arbeit wird eine systematische Analyse mithilfe numerischer Simulationen für die partikelbeladene Strömung durch einen membranähnlichen, porenähnlichen Kanal beschrieben. Der Einfluss der Temperatur auf die kolloidale Aggregation wird durch attraktive und abstoßende temperaturabhängige Potentiale zwischen Partikeln und Wand des Kanals für verschiedene Materialien berücksichtigt. Diese Studie zeigt eine Lücke zwischen Theorie und Experiment im Bezug auf die Temperaturabhängigkeit vom kolloidalen Fouling auf.

Eine Partikeleigenschaft, die für das Verständnis des kolloidalen Foulings von entscheidendem Interesse ist, ist die Weichheit. Die Rolle der Weichheit bei der Filtration wird mit Hilfe von CFD-DEM-Simulationen untersucht. Die Simulationen zeigen, dass

sich weiche Partikel in sehr strukturierte Filterkuchenmorphologien anordnen und durch hydrodynamischen Druck kompaktieren. Daher verursachen die weichen Filterkuchen einen deutlich höheren hydrodynamischen Widerstand als harte Filterkuchen. Darüber hinaus zeigen die Simulationen, dass die Kuchenrelaxation weicher Filterkuchen vollständig reversibel ist, während eine kurzfristige Verdichtung des Kuchens zu irreversiblen Veränderungen der Kuchenmorphologie führen kann.

Zusammenfassend beschreibt diese Arbeit mikroskopische Ereignisse der Ablagerung und Resuspension, die letztlich dazu beitragen werden, das kolloidale Fouling zu kontrollieren und die Membranrückspülung effizienter zu gestalten.

1 Scope and outline

1.1 Introduction and motivation

Particle deposition, jamming, and clogging are encountered in a large variety of industrial processes such as membrane filtration, packed beds and chromatography. In membrane filtration, these accumulation phenomena are classified as fouling. Fouling seriously limits the filtration performance and is often recognized as the key challenge in membrane application. Understanding the complex interplay of surface interactions and mechanical properties of the filtered particles as well as the hydrodynamic conditions inside and near the porous structure is crucial to develop new and efficient strategies to prevent or delay fouling [Wyss2006]. Despite the importance, the complex mechanisms leading to the fouling still lacks in understanding.

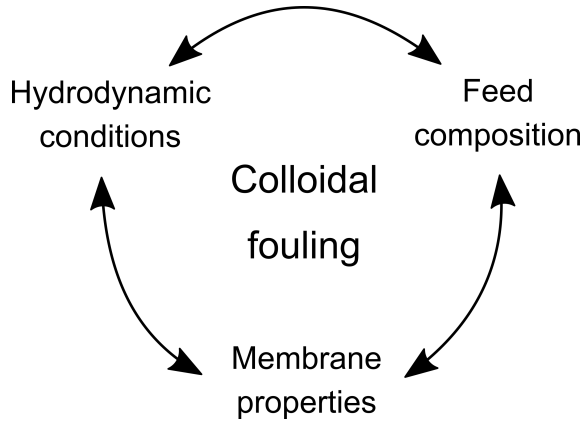

Figure 1.1: Colloidal membrane fouling is governed by the complex interplay between the feed composition, membrane properties and hydrodynamic conditions [Tang2011].

The complex interplay between the feed composition, membrane properties and hydrodynamic conditions governs membrane fouling as illustrated in Figure 1.1 [Tang2011]. These three categories conceal a large number of properties such as the nature of the foulant, the ionic strength and

the pressure level [Nobl1995]. These properties span a multidimensional matrix determining the fouling. Since these properties are often interdependent, the matrix is strongly interwoven, whereby the complexity of the fouling leaps up dramatically.

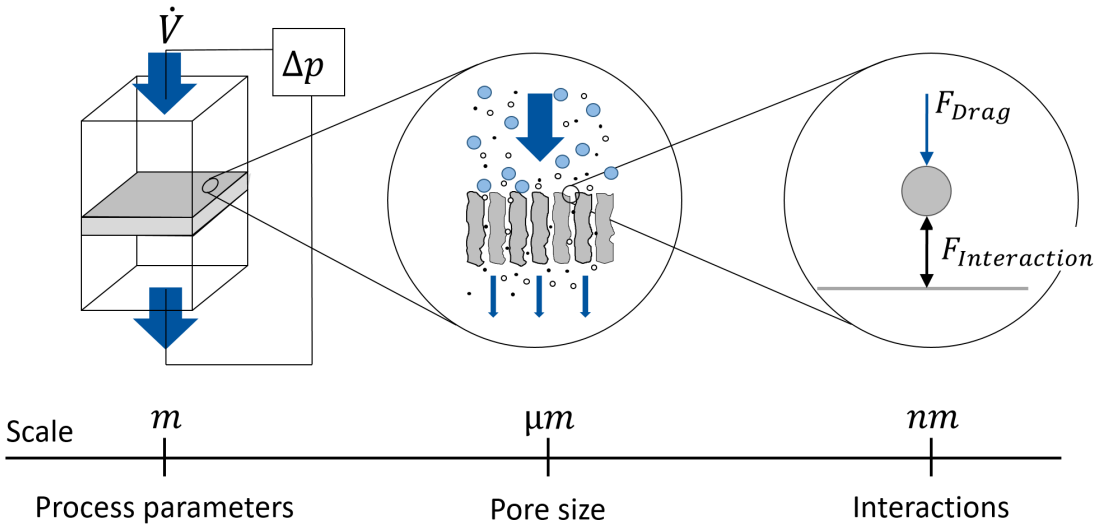

Figure 1.2: The different length scales of fouling.

A major difficulty in investigating the fouling process relies in the different length scales of fouling illustrated in Figure 1.2. During an industrial filtration process only the macroscopic measurable process parameters such as the transmembrane pressure (TMP) can be monitored. However, the exact causes and nature of the fouling can hardly be deducted by the measurement of macroscopic process parameters. Pore scale analysis is necessary to visualize and characterize the phenomena responsible for the fouling [Wyss2006]. For pore scale analysis, microfluidic experiments were designed to non-invasively visualize the fouling process in recent years [Wyss2006; Ngen2010; Ngen2011; Bacc2011; Bacc2014b; Link2016; Link2019]. One limitation remains that the driving forces causing deposition act on a nanometer range and particle deposition can only take some microseconds. Processes acting on these time and length scale can hardly be experimentally visualized during filtration. Numerical simulations overcome the limitations of small time and length scales to improve understanding of the fundamental procedures during fouling [Wess2001;

Ando2010; Ando2012a; Bacc2014b; Mino2018]. Besides the detecting processes on small time and length scales, the simulations allow to decompose hydrodynamic and colloidal physics helping to decrypt the multidimensional matrix determining the fouling. Therefore, combing microfluidic experiments with numerical simulations offer a natural synergy to study the physical processes of fouling.

1.2 Objectives and structure of this thesis

This thesis describes pore scale phenomena during colloidal fouling and backwash with multiphase simulations supplemented by microfluidic experiments.

Fouling results from the complex interplay of the colloidal interactions, hydrodynamic interactions and the membrane characteristics. How this interplay controls the fouling on the microscopic level is the central point of this thesis. Thereby, the following research questions are addressed:

- What are the microscopic events of colloidal clogging?
- What are the microscopic events of backwashing?
- How does temperature control pore scale deposition?
- How does the softness of particles change cake formation?

Structure of this thesis

Chapter 2 provides an overview of the current state of the art in clogging research with specific focus on microscopic observations and numerical analysis. Thereby, the role of important process parameters and conditions affecting colloidal clogging are discussed. Since colloidal and hydrodynamic interactions play a predominant role in clogging, the physical origin and their mathematical description are presented.

Chapter 3 introduces the basic principles of the modeling approach CFD-DEM used in this thesis. The particle calculation, the fluid simulation and

the coupling between fluid and particle side is discussed. Further, microfluidic experiments are briefly presented.

Chapter 4 describes the microscopic events during colloidal clogging. CFD-DEM simulations were performed to examine mechanisms of colloidal fouling in a microfluidic architecture mimicking a porous microfiltration membrane. These simulations were compared with microfluidic experiments from literature. The findings allow a basic understanding of microscopic fouling events during colloidal filtration.

Chapter 5 investigates the microscopic events during backwashing. CFD-DEM simulations combined with microfluidic experiments were performed to describe how particles re-suspend during membrane backwash. Both simulations and experiments reveal the predominant role of particle cluster behavior during backwash. This clarifies that single-particle models are not representative of describing processes occurring during backwash.

Chapter 6 describes the temperature dependency of hydrodynamic and colloidal interactions on deposition with CFD-DEM simulations. The model comprises temperature dependent XDLVO potentials and hydrodynamic interactions. The chapter discusses the temperature dependency of each potential individually. The resulting temperature dependence of colloidal clogging are investigated in a single pore constriction.

Building on the numerical results, Chapter 7 investigates the temperature dependency of colloidal clogging by microfluidic experiments. A temperature control setup for microfluidic device was developed, which enables to temper the suspension during filtration and backwash. The experiments show significant deviations from the theoretical considerations of the previous chapter highlighting the need for future research.

Chapter 8 discusses the cake filtration of soft colloids compared with hard colloids. Contrary to hard colloids, soft colloids can deform and interpenetrate, which enables a filter cake consisting of soft colloids to compact. Through compaction of the soft filter cake, the transmembrane pressure does not linearly scale with the flux as it is the case for hard colloids. This study shows how the cake morphology and the pressure drop change depending on flow conditions and particle's softness.

2 Background and fundamentals

2.1 Colloidal clogging

The removal of colloidal particles is a common and important industrial process; e.g. in membrane filtration, deep bed filtration or liquid chromatography. In these processes, colloidal clogging seriously limits the performance and can even lead to a complete failure of the operation. Despite the importance of clogging, the understanding of the microscopic processes governing the clogging remains limited due to the complex interplay of hydrodynamic and colloidal interactions [Wyss2006; Dres2017].

Microfluidic analysis of colloidal clogging

When investigating colloidal clogging, research faces the major challenge of different length scales between experimental measurements and physical phenomena. The fundamental mechanisms of colloidal clogging occur on a single-pore level. However, macroscopic measurements are commonly performed in packed bed columns or in porous membranes. Although, these studies deliver important information of the clogging dynamic, the microscopic and nanoscopic mechanisms on a single pore level can hardly be deducted [Wyss2006]. The pioneering work of Wyss et al. [Wyss2006] demonstrated the possibility to observe the physical microscopic events of clogging on a pore scale level with the aid of microfluidic experiments as illustrated in Figure 2.1. The application of microfluidics allows to close the gap between the pore-scale events and the macroscopic measurements.

The usage of microfluidic clogging experiments enables fundamental insight into the clogging dynamic on a pore scale level. Thereby, research distinguishes between three types of clogging depending on the level of confinement and the colloidal interactions which are displayed in Figure 2.2 [Dres2017]:

1. Sieving
2. Bridging
3. Aggregation

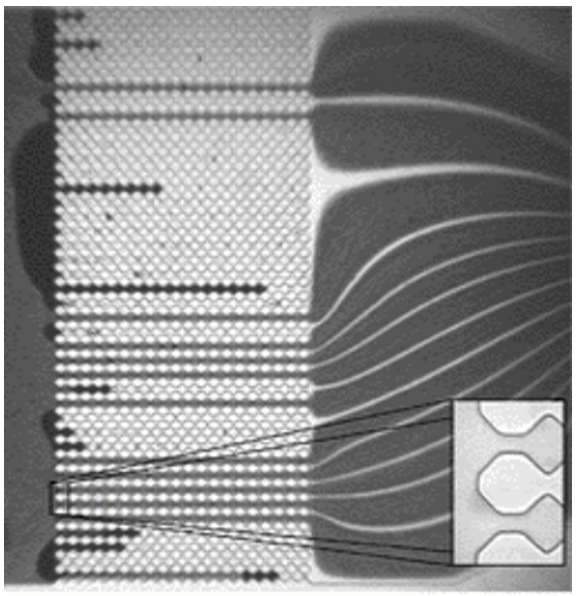

Figure 2.1: Microfluidic observation of pore clogging in a membrane mimicking pore structure performed by Wyss et al. [Wyss2006], reprinted with permission of American Physical Society

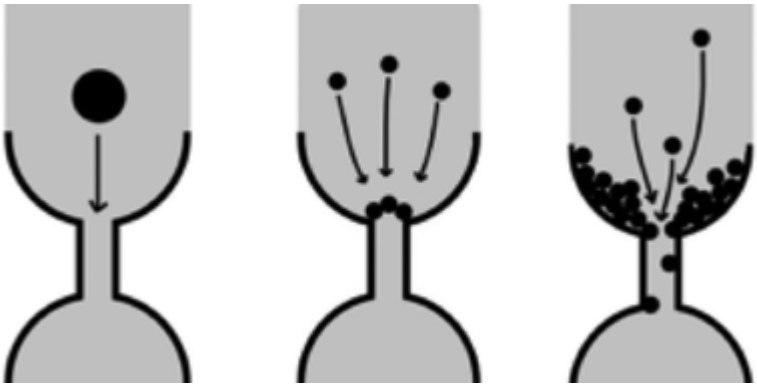

Figure 2.2: Mechanism of clogging: Sieving, Bridging, Agglomeration, reprinted with permission from [Dres2017]

Sieving describes the process in which the constriction size is smaller than the particle diameter. It is widely used in microfluidics to selective separate poly-disperse particle systems. Recent research in sieving discusses the question of entrapment or permeation of deformable particles through narrow microchannels depending on the mechanical properties. This serves for example to understand the flow of red blood cells through micro-vascular systems [Dres2017].

When the diameter of the particle is smaller than the size of the constriction, two dominant phenomena are distinguished: bridging and aggregation. Both phenomena occur depending the

- the colloidal interactions
- the particulate concentration
- the particles stiffness
- the hydrodynamic conditions
- the geometrical aspects [Dres2017]

An overview of how the clogging depends on these parameters is presented in the following.

Impact of colloidal interactions on colloidal filtration:

The colloidal surface interaction decisively control colloidal deposition and are thus fundamental in understanding clogging behavior. Therefore, section provides a detailed description of the colloidal interactions 2.3. The colloidal interactions control the kinetic of the clogging, the clogging formation/ morphology as well as the fragility of the clogs.

A variety of studies discuss how colloidal interactions impact the clogging kinetic. These studies usually tuned colloidal interactions by the addition of ions, which allows to shift the colloidal interactions from repulsive to attractive. The shift in potential increases the clogging kinetic as demonstrated by [Wyss2006; Agba2012; Sain2016]. The dependence between ion concentration and characteristic clogging time characterizing the clogging kinetic is plotted in Figure 2.3 based on the results of [Wyss2006].

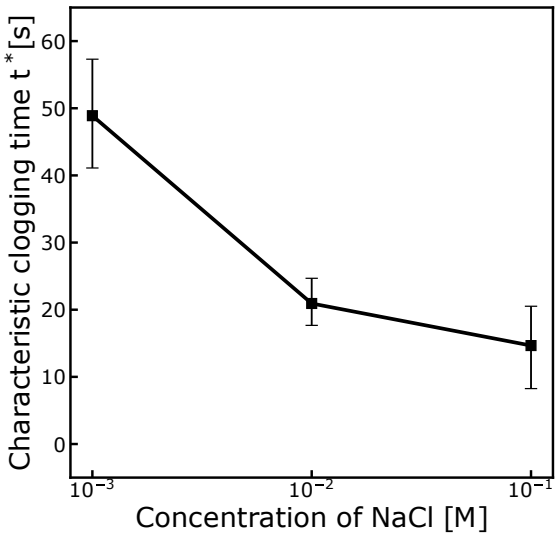

Figure 2.3: Characteristic clogging time scale t^* of single pores versus the concentration of NaCl. The error bars represent the standard deviation of t*, redrawn from results of [Wyss2006]

Besides the clogging kinetic, the stability of deposition layer changes with the colloidal potential as demonstrated by Sendekie et al. [Send2016a]. They described three different clogging scenarios based on the repulsive or attractive nature of the colloidal potential. At low ionic strength ($0.01mM$), the repulsive nature of the colloidal interactions induces pushing effect between the particles resulting in robust arches. At medium ionic strength ($10mM$), secondary minimum effects enhanced the transport through the pore. Lastly at high ionic strength ($100mM$), the deposition was fast and the capture efficiency was high. However, the formed aggregates were fragile and partly broke during filtration. The role of an energy barrier during clogging and backwash is discussed in the chapters 4 and 5. Besides ionic strength, other suspension parameters such as temperature or pH can change the colloidal interactions. The impact of temperature on the colloidal potentials and thus on the clogging is further discussed in chapter 6.

Impact of particle concentration on colloidal filtration

The clogging kinetic increased with the solid fraction of a suspension Φ. At $\Phi < 0.5\%$, Wyss et al. [Wyss2006] and Mustin et al. [Must2010] found that the mean blockage time scales t as $1/\Phi$. This revealed that the clog-

ging kinetic was proportional with the particles passing the pore structure independent of the initial solid concentration. This arguably indicates a minor role of particle-particle interactions in the clogging dynamic. At particle content higher than $\Phi > 1.\%$ particle-particle interactions had a noticeable effect on the clogging. How the particle-particle interactions can impact the clogging dynamic is further discussed in chapter 4 of this thesis.

Impact of hydrodynamic conditions on colloidal filtration

Besides the colloidal side, the hydrodynamics of a filtration process co-controls the clogging. Several studies show that low-pressure microfiltration with consequently low flux is beneficial over high-pressure microfiltration due to the slower development of colloidal fouling [Fiel1995]. Field et al. [Fiel1995] explained this behavior by the concept of a critical flux. The critical flux characterizes the flux under which no irreversible fouling occurs. The theory of the critical flux was supported by measurements on a pore scale level by Agbangla et al. and Bacchin et al. [Agba2012; Bacc2014a]. The particle clustering and pore clogging only occurred at higher flow rates. At low flow rates barely any particle deposition was observed. Besides the deposition the hydrodynamic conditions play a key role in particle resuspension, which is further discussed in chapters 4, 5 and 6

Impact of geometry on colloidal filtration

The clogging dynamic is controlled by a variety of geometrical features. To name but a few: the level of confinement, the inner pore structure and the pore shape. The level of confinement between pore and particle decisively controls the mechanism occurring during the clogging process. At a high degree of confinement, in which the particle size D is on slightly smaller than the pore size W, clogging relies chiefly on the particle interaction with the pore wall [Ders2017]. Contrary, at mild confinements, clogging occurs due to the aggregation of particles. Therefore, particle particle interactions decisively control the clogging rather than particle wall interactions. Obviously, the clogging accelerates with a higher degree of confinement. Thereby, the number of passing particles N^* scale with a power law with the degree of confinement [Wyss2006; Ders2015]: $N^* \propto (W/D)^n$. For the index n values of 4-7 can be found in literature. Interestingly, the actual

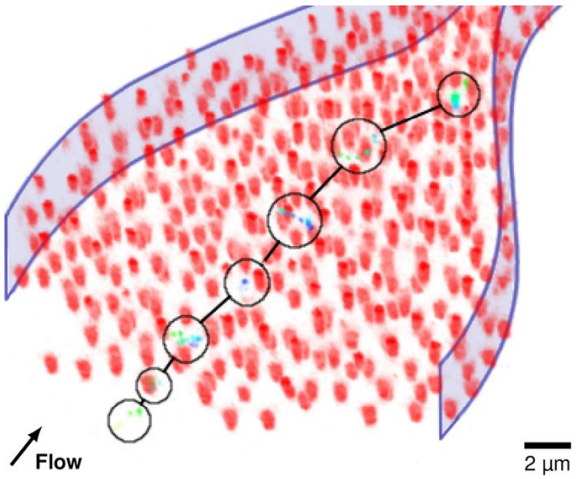

Figure 2.4: Permeation of tracer particle through a soft filter cake presented by Linkhorst et al. [Link2016]. The red points represent the core of a core-shell microgel forming the filter cake. The circles and lines mark the positions and jumps of the tracer particle, respectively.

size of the particles only minor effects the clogging kinetic as long as the level of confinement stays constant. Besides the level of confinement, the inner pore structure has far-reaching effects on clogging. As Bacchin et al. [Bacc2014b], the increased tortuosity of the pore structure significantly enhanced clogging. How the inner pore structure affects the clogging is investigated in chapter 4 of this thesis.

Impact of particle softness on colloidal filtration

In technical filtration applications the filtered particles are often soft in nature or possess a soft shell such as bacteria or viruses. These particles can deform, interpenetrate and shrink due to external stress. The particles softness can decisively control the permeation of particles and cake resistance during filtration.

On single particle level, the particle's softness can drastically change its ability to permeate through porous media. Due to particle deformation, soft particles are able to permeate through constrictions much smaller than their size, which is clearly impossible for hard particles [Hend2010; She2012; Li2013]. Hendrickson et al. [Hend2010] showed that ultra-soft microgels were able to permeate through pores only one tenth of their original size. Linkhorst et al. [Link2016; Link2019] showed that filter cakes composed of soft microgels form amorphous and crystalline regions. Linkhorst et al.

[Link2016] revealed that amorphous and crystalline regions have different permeation behavior. By confocal imagining of microfluidic channels, they showed how tracer particles permeate through the filter cake as illustrated in Figure 2.4. They measured that the permeation velocity of small tracer particles increased in region of higher crystallinity [Link2016].

Besides the cake morphology, the hydrodynamic resistance depends on the particles softness. Through deformation, the solid volume concentration of soft spheres can exceed the hard sphere limited of 0.74, whereby the filter cake resistance increases significantly [Hwan2003]. Chapter 8 discusses how particle softness, hydrodynamic pressure and filter cake morphology are related.

2.2 Numerical analysis of colloidal filtration

Hydrodynamic conditions and colloidal interactions determine if, how and how fast colloidal clogging occurs. But how and in which magnitude each part contributes to the clogging is hard to decode out of experimental studies. Clogging experiments often show overlaying effects of the hydrodynamic side and of the colloidal side whereby an allocation, which side is responsible for the observed phenomena is difficult to decode. Numerical simulations help to distinguish effects of the hydrodynamic and colloidal side to gain a comprehensive understanding of the underlying physics. Various numerical approaches are used to investigate the clogging process. These range from Eulerian-Eulerian, Eulerian-Lagrangian, fully Lagrangian as well as statistical modeling approaches [Ho2000; Wess2001; Ando2010; Henr2012; Ando2012a; Mars2015; Agba2014b; Mino2018; Nish2019].

Eulerian-Lagrangian have been proven to be a useful tool in examining clogging phenomena on a pore scale level. The Eulerian-Lagrangian approach allows to combine multi-particle dynamics with hydrodynamic effects with reasonable computational effort. Similar to microfluidic experiments, the application of Eulerian-Lagrangian simulations allow to investigate how process and geometrical parameters impact the clogging on a pore scale level. In contrast to the microfluidic experiments, the Eulerian-

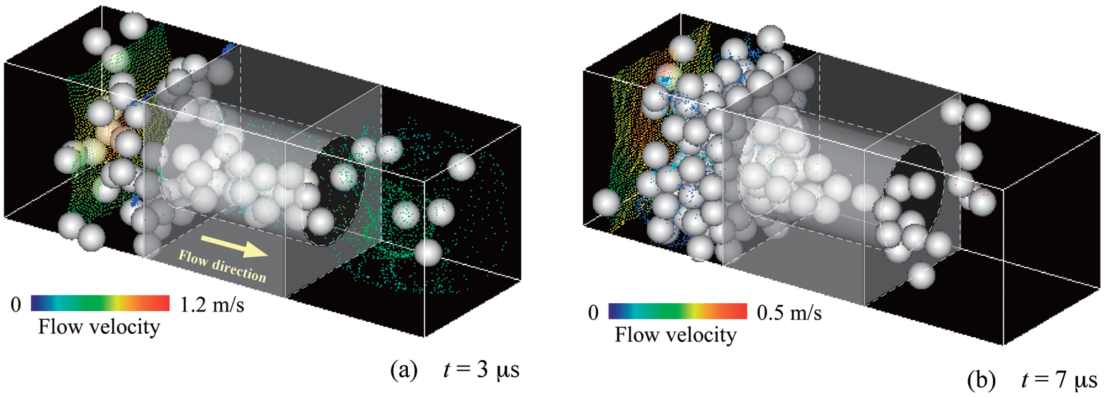

Figure 2.5: Euler-Lagrangian simulation of pore clogging performed by Ando et al. [Ando2012a] (with permission from the Society of Chemical Engineers, Japan)

Lagrangian simulations allow the resolution of nanometer-scale processes and to enable to decode the impact of individual physical properties. Therefore, Eulerian-Lagrangian simulations combined with microfluidic experiments offer powerful synergies to comprehend clogging phenomena.

One of the first Euler-Lagrangian approaches investigating pore clogging were published by the working groups of Nakao and Fujita [Ando2010; Ando2012a]. They examined pore clogging in a single pore constriction as illustrated in Figure 2.5 [Ando2010]. They demonstrated that the location of particle deposition depend on feed particle concentration. At high particle concentration particle predominantly deposited on the feed side whereas at smaller concentration ($< 5\%$) enabled downstream deposition of particles. Additionally, Mino et al. showed that downstream deposition can be caused by low rolling friction as well [Mino2018].

Continuing, the working group of Bacchin performed simulations on the clogging concentrating on the effect of the colloidal interaction forces and solid feed concentration [Agba2014b]. Without repulsive forces, cluster-dendrites at the pore entrance formed, which lead to a complete blockage of the pore. Contrary, when repulsive forces are introduced, a minimal flow rate had to be exceeded before clogging occurs. The need of a minimal flow rate agreed with the theory of a critical flux presented by Fields et al. [Fiel1995]. Further, they observed that at solid feed fractions of 5%, clogging results through successive deposition, while for volumetric fractions of 20 % sudden bridging form on the constriction [Agba2014b].

Besides the solid feed fraction and particle interactions, the geometry of the pore structure crucially impacts the clogging. Ando et al. investigated the impact of the pore to particle ratio on the clogging [Ando2012a]. Their simulations demonstrated that at smaller pore-to-particle ratios particles formed a cake layer directly on the membrane surface. Contrary, for smaller particle-to-pore ratios the particle first deposited inside the pore leading to a formation of a cake layer on the surface [Ando2012a].

In a combined experimental and numerical study, Bacchin et al. [Bacc2014b] demonstrated the effect of an inner structure on pore clogging. Their numerical results showed that purely attractive particles majorly deposited on the upstream side of the pore structure. Contrary, the experiments emphasized the role of inner pore deposition. To close the gap between experimental observation and numerical results, this thesis showed that a repulsive energy barrier and the movement of attached particles can explain inner structure deposition, which is further explained in chapter 4.

2.3 Colloidal potentials

Colloidal particles experience interfacial interactions when approaching each other. These potential decisively determine the stability of the colloidal suspension and play a key role in colloidal deposition and stability. A first universal approach to quantitatively describe these interactions is the DLVO theory named after Derjaguin, Landau, Verwey and Overbeek [Isra2011]. The DLVO theory comprises the electrodynamic Lifschitz-van der Waals interactions and the electrostatic interactions [Elim2013]. However, the DLVO theory often fails to describe the colloidal potentials in polar solutions such as in water [Van 2006]. This is attributed to hydrophilic or hydrophobic interactions potentials, which are often described by Lewis acid base interactions. The combination of DLVO theory and the acid base potentials is often referred to as extend DLVO (xDLVO) [Van 2006]. Further, many biological colloids such as viruses and bacteria and selected synthetic colloids such as microgels contain macromolecules or polymer

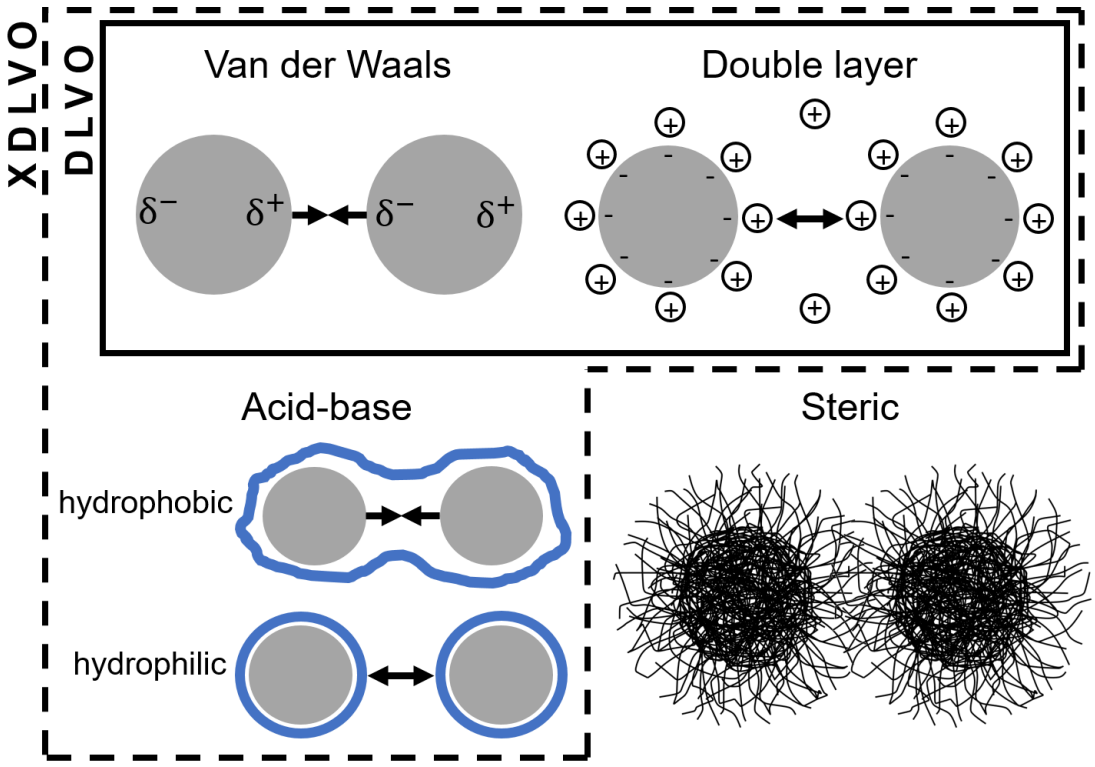

Figure 2.6: Schematic illustration of the colloidal potentials discussed in this section.

chains located on the surface of the colloid. These chains strongly impact the colloidal stability and can lead to a steric stabilization of the suspension, which is referred to as steric interactions.

Summarized the colloidal potentials can be classified as follows [Van 2006]:

1. Electrodynamic, or Lifshitz-van der Waals, interactions,
2. Electrostatic interactions,
3. Polar, electron-donor-electron-acceptor, or Lewis acid-base interactions,
4. Steric interactions

The potentials are graphically illustrated in Figure 2.6. The following subchapters give an overview over the physical origin and the mathematical description of these potentials. Further potentials such as Brownian forces,

solvation oscillatory forces or depletion interactions caused by excluded volume of small solutes are not discussed in this chapter.

2.3.1 Van der Waals forces

Van der Waals forces are non covalent intermolecular interactions named after it's discoverer J.D. van der Waals [Van 1873]. The movement of the electron probability density cause a permanent change in the charge distribution of molecules. The changing charge distribution cause fluctuating dipole moments resulting in a netforce between molecules. These van der Waals force comprise three types of interactions:

- Keesom interactions between two permanent dipoles of polar molecules
- Debye interactions between a permanent dipole of a polar molecule and an induced dipole of a non-polar molecule
- London dispersion interactions between two induced dipoles of non-polar molecules

These three van der Waals interaction energies W are inversely proportional to the sixth power of distance D between the molecules [Isra2011]:

$$V_{molecules} = -\frac{C}{D^6} \tag{2.1}$$

C is the coefficient in the atom-atom pair potential. By summing up these pairwise intermolecular interactions [Hama1937], Hamaker developed an expression for the dispersion intermolecular interaction energy (van der Waals-London) of macroscopic bodies:

$$V_{London} = -\frac{A}{12\pi D^2} \tag{2.2}$$

The interaction energy is proportional to the Hamaker constant A, which

depends on material properties and geometrical aspects as well as inversely proportional to the second power of distance D. Hamakers theory bases on the assumption of the additivity of the pairwise interactions which is usually valid in the gas phase [Isra2011]. However, this assumption does not held in condensed media because it ignores the influence of the media and neighbors on the molecular interactions whereby the Hamaker constant is not accurately determined. Lifschitz developed a theory for the van der Waals interaction energy which is derived from continuum properties as the dielectric constants and refractive indices [Lifs1992; Isra2011].

At separation distance above $D > 30\,\text{nm}$, the van der Waals energy between molecules decays faster than $1/D^6$ approaching a $1/D^7$ dependence by $D > 100\,\text{nm}$ which is called retardation [Isra2011]. This retardation effect is attributed to the time taken for the electric field of the first molecule to approach the second and return can become comparable with the period of the fluctuating dipole itself leading to a reduction in potential. The retardation effect is not considered in the following parts because at separation distance above some nanometers double layer interactions and hydrophilic/ hydrophobic interactions become more dominant than the van der Waals interactions in aqueous media, whereby the effect of retardation is of minor importance.

By neglecting retardation effects, the Lifshitz theory for two surfaces of two materials 1 and 2 across a media 3, the Hamaker constant is calculated by the following equation:

$$A_{132} \approx \frac{3}{4} kT \left(\frac{\varepsilon_1 - \varepsilon_3}{\varepsilon_1 + \varepsilon_3}\right)\left(\frac{\varepsilon_2 - \varepsilon_3}{\varepsilon_2 + \varepsilon_3}\right) + \frac{3h\nu_e}{8\sqrt{2}} \frac{(n_1^2 - n_3^2)(n_2^2 - n_3^2)}{(n_1^2 + n_3^2)^{1/2}(n_2^2 + n_3^2)^{1/2}\{(n_1^2 + n_3^2)^{1/2} + (n_2^2 + n_3^2)^{1/2}\}}, \quad (2.3)$$

where k is the Boltzmann constant, T the absolute temperature, h the Planck constant and ν_e the main electronic absorption frequency in the ultraviolet light.

The van der Waals interaction energy can be determined between two

macroscopic spheres (S) with radiis $R1$ and $R2$ whose surfaces are separated by the distance D with $R1, R2 >> D$ is given by [Isra2011]

$$W_{\mathrm{VDW}}^{132}(D) = -\frac{A_{132}}{6D}\left(\frac{R_1 R_2}{R_1 + R_2}\right) \tag{2.4}$$

and for a sphere and an infinite flat plate (P) by

$$W_{\mathrm{VDW}}^{\mathrm{SP}}(D) = -\frac{A_{132} R}{6D} \tag{2.5}$$

The force F acting on a sphere in such a potential field is computed by the relation

$$\boldsymbol{F}(D) = -\nabla W(D). \tag{2.6}$$

As two surfaces approach each other, the separation distance moves towards zero and the van der Waals force would increase to infinite according to the equations 2.4, 2.5. This nonphysical behavior is avoided by the consideration of a cutoff distance D_0, which has a value of around $0.16-1\,\mathrm{nm}$. The cutoff distance originates from the overlap of electron clouds of the two surfaces, giving rise to a repulsive force termed the Born or hard core repulsion [Isra2011].

2.3.2 Electric double layer forces

Colloidal particles usually possess a surface charge when immersed in an electrolyte solution due to the dissociation of surface groups as well as the adsorption of ions onto the surface [Ohsh2006]. The surface charge leads to an attraction of counterions from the surrounding electrolyte solution. The charged surface combined with the counterions built the so called electrostatic double layer.

Helmholtz formulated a first simplified theory on the double layer [Helm1853]. Therein, the charge of a surface is compensated by a monolayer of counterions which are directly located on the surface. Helmholtz

theory neglects the thermal energy of the ions. Gouy and Chapman independently developed an extension of the Helmholtz theory accounting the thermal energy. According to Gouy and Chapman the ions distribute in a spatial dimension close to the surface called the diffusive boundary layer contrary to the monolayer assumption of Helmholtz [Gouy1910; Chap1913]. With the Gouy-Chapman model, the potential distribution $\Psi(\vec{r})$ can be derived by the Poisson-Boltzmann equation:

$$\vec{\nabla} \cdot \left[\epsilon(\vec{r})\vec{\nabla}\Psi(\vec{r})\right] = \rho^f(\vec{r}) - \sum_i c_i^{\infty} z_i \lambda(\vec{r}) q \exp\left(\frac{-z_i q \Psi(\vec{r})}{kT}\right) \tag{2.7}$$

where $\epsilon(\vec{r})$, $\rho^f(\vec{r})$, c_i^{∞}, z_i, q, k and T are the permittivity, the charge density, the bulk concentration, the valency of the ions, the charge of a proton, the Boltzmann constant and the temperature, respectively. However, the Poisson-Boltzmann treats the ions as point charge which neglects the finite size of the ions [Hunt2013]. Thereby, the model incorporates short comings in the immediate neighborhood of the some surface ($<1\,\mathrm{nm}$) [Hunt2013]. Therefore, Stern developed an approach which combines the concepts of the monolayer and the diffusive layer schematically drawn in Figure 2.7 [Ster1924]. With Sterns' model, the electrical potential in the diffusive layer is well described by the Poisson Boltzmann equation. On the other hand, the monolayer also called Stern or Helmholtz layer can be modeled as a molecular capacitor [Hunt2013; Elim2013]. Further refinements to Stern's model were provided by Grahame. Grahame's model distinguishes between a hydrated and non hydrated ions inside the Stern layer allowing the specific adsorption of ion species.

In colloidal systems, the electrostatic double layer becomes of decisive importance when two surfaces approach each other. While two similarly charged surfaces approach, dissociated counterions in the diffusive layer are pushed to the surface. Thereby, their configurational entropy decreases which induces a repulsive force between the surfaces. Therefore, the repulsive force of the double layer interaction is entropic/ osmotic in nature

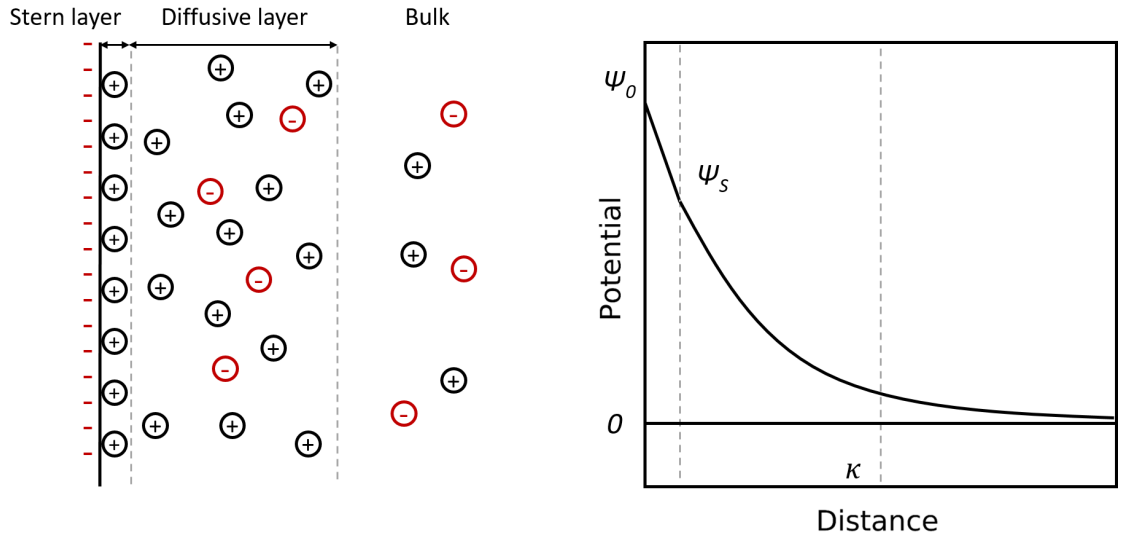

Figure 2.7: The left figure schematically illustrates the electrostatic double layer. The surface is negatively charged. The surface charge is balanced by positive counterions forming a layer directly on the surface called Stern layer and a diffusive layer. A potential is formed beyond the surface into the electrolyte phase, since the charge is not completely compensated in the Stern layer. The distribution of the potential over distance is schematically illustrated in the right graph.

[Isra2011].

Mathematically, the double layer interaction potential of approaching colloids can be derived from the Poisson-Boltzmann equation. However, the Poisson-Boltzmann equation does usually not give a simple analytical solution [Will1998]. Therefore, one of the following three approximate models is usually applied: the constant charge approximation (CCA) by Wiese and Healy [Wies1970], the constant potential approximation (CPA) by Hogg et al. [Hogg1966] or the linear superposition approximation (LSA) by Gregory [Greg1975]. Warszynski and Adanczyk [Wars1997] showed that the LSA model is the better estimate for the numerical solution of the Poisson-Boltzmann equation and is therefore used in the following.

The linear superposition approximation assumes that two surfaces are fairly far apart from each other such that the potentials of each surface do not disturb each other and can be superposed. This approximation becomes inaccurate for very small separation distances. However, when the surfaces are close to each other, van der Waals and hydrophobic/ hydrophilic interactions are usually more dominant and this uncertainty is tol-

erable [Wars1997]. The double layer potential between two equal spheres is given by [Greg1975]

$$W_{\mathrm{DL}}^{\mathrm{SS}}(D) = 2\pi\varepsilon_0\varepsilon a \left(\frac{kT}{e}\right)^2 \Upsilon_{\mathrm{S}}^2 \exp(-\kappa D) \tag{2.8}$$

and between a sphere and a plate by

$$W_{\mathrm{DL}}^{\mathrm{SP}}(D) = 4\pi\varepsilon_0\varepsilon a \left(\frac{kT}{e}\right)^2 \Upsilon_{\mathrm{S}}\Upsilon_{\mathrm{P}} \exp(-\kappa D), \tag{2.9}$$

where ε_0 denotes the vacuum permittivity, e the elementary charge, κ the inverse Debye length and ε refers to the dielectric constant of the electrolyte solution. Υ_{S} and Υ_{P} are the effective surface potentials of the sphere and the plate, respectively. One obtains the corresponding force by using Equation (2.6). The Debye length is a measure of the range of the diffusive layer and can be expressed for a 1:1 electrolyte such as a sodium chloride solution as [Isra2011]

$$\kappa^{-1} = \left(\frac{\varepsilon_0\varepsilon kT}{2e^2 N_{\mathrm{A}} c}\right)^{1/2}, \tag{2.10}$$

where N_A is the Avogadro constant. The Debye length decreases with increase the molar concentration c of the electrolyte in the bulk phase. As a comparison, the Debye Length is $0.96\,\mathrm{nm}$ in a $100mM$ electrolyte solution, where else it is $9.6\,\mathrm{nm}$ in a $1mM$ electrolyte solution.

The effective surface potential of a sphere Υ_S is expressed as [Ohsh1982]:

$$\Upsilon_{\mathrm{S}} = \frac{8\tanh\left(\frac{\Psi_S e}{4kT}\right)}{1+\sqrt{1-\frac{2\kappa a+1}{(\kappa a+1)^2}\tanh^2\left(\frac{\Psi_S e}{4kT}\right)}}. \tag{2.11}$$

This expression reduces for the limit radius $a \to \infty$ to the effective surface

potential of a plate

$$\gamma_{\mathrm{P}} = 4 \tanh\left(\frac{\Psi_S e}{4kT}\right). \tag{2.12}$$

The surface potential at the Stern plane Ψ_S is generally not known with sufficient certainty. It is usually assumed to be equal to the zeta potential [Will1998; Elim2013]

$$\Psi_S \approx \zeta. \tag{2.13}$$

The zeta potential defines the Coulomb potential on the slipping plane of the double layer. A schematic representation of the electrostatic double layer and its course of the potential is presented in Figure 2.7.

2.3.3 Acid-base forces

In polar solutions such as water, the DLVO theory often fails to predict the interactions between surfaces and particles [Isra2011]. For example, silica dispersions sometimes remain stable at high ionic strength which is unexpected when applying DLVO theory. Further, the low solubility and strong attraction between hydrocarbon molecules in water is not accurately predicted by the DLVO theory [Isra2011]. These phenomena are attributed to hydrophobic and hydration interactions. Theories which physically explain and quantify describe these interactions are diverse and still under wide debate. One prominent theory was developed by Good, Chaudhary and van Oss [Van 1988] and is discussed in the following.

Good, Chaudhary and van Oss attribute hydrophobic and hydration interactions to the polar electron-donor-electron-acceptor (Lewis acid-base) potentials of the solute and the solvent [Van 2006]. The electron-donor potential of a material defines the affinity of a species to share electrons with another compound. This behavior classifies a Lewis base. Whereas, the electron-acceptor potential of a species defines the affinity to attract electrons from another compound which classifies a Lewis acid. The electron-

donor-electron-acceptor potential can be derived from the electron donicity γ^- and electron-accepticity γ^+. These parameter determine the surface tension component of the Lewis acid base interaction γ^{AB} of a species 1 as follows [Van 2006; Van 2008]:

$$\gamma_1^{AB} = 2\sqrt{\gamma_1^- \gamma_1^+} \tag{2.14}$$

The addition of γ^{AB} with the surface tension parameter of the apolar Lifshitz van der Waals interactions γ^{LW} results in the total surface tension γ of a polar condensed-phase material:

$$\gamma_1 = \gamma_1^{AB} + \gamma_1^{LW} \tag{2.15}$$

From the total surface tension γ the free energy of cohesion Delta G_1^{coh} can be derived:

$$\Delta G_1^{coh} = -2\gamma_1 \tag{2.16}$$

In addition to the total surface tension, the interfacial tension γ_{12} between two different condensed-phase materials 1 and 2 can be derived:

$$\begin{aligned} \gamma_{12} &= \gamma_{12}^{LW} + \gamma_{12}^{AB} \\ &= (\sqrt{\gamma_1^{LW}} - \sqrt{\gamma_2^{LW}})^2 + 2(\sqrt{\gamma_1^+ - \gamma_2^-})(\sqrt{\gamma_2^+ - \gamma_1^-}) \end{aligned} \tag{2.17}$$

Out of the surface and interfacial tension, the free energy of interaction ΔG_{ij} between two components i and j can be determined by applying the Dupre equation:

$$\Delta G_{12} = \gamma_{12} - (\gamma_1 + \gamma_1) \tag{2.18}$$

The Dupre equation can be expended to the free energy of interaction ΔG_{132} between two different condensed-phase materials, 1 and 2, immersed in a liquid, 3, as follows:

$$\Delta G_{132} = \gamma_{12} - (\gamma_{13} + \gamma_{23}) \tag{2.19}$$

Hydrophobic/ Hydrophilic interactions decay exponentially with distance [Isra1982; Van 2006]. Therefore, the acid base free energy over distance $\Delta G_{\mathsf{AB}}(D)$ can be described as follows:

$$\Delta G_{\mathsf{AB}}(D) = \Delta G_{\mathsf{AB}}^{\mathsf{132}} \exp\left(\frac{D_0 - D}{\lambda}\right). \tag{2.20}$$

The minimum equilibrium distance D_0 is almost constant for a variety of material system with a value of $\approx 0.16\,\mathrm{nm}$ [Van 2006]. How far these interactions reach is characterized by the decay length λ. Usually, values for the decay length λ of $0.6 - 1.1\ \mathrm{nm}$ can be found in literature [Isra1982; Van 2006]. Hence, the effective particle-particle interaction potential [Van 2006] can be derived by applying Derjaguin's technique [Derj1934]

$$W_{\mathsf{AB}}^{\mathsf{SS}}(D) = \pi a \lambda \Delta G_{\mathsf{AB}}^{\mathsf{132}} \exp\left(\frac{D_0 - D}{\lambda}\right) \tag{2.21}$$

and analogously the particle-wall interaction potential

$$W_{\mathsf{AB}}^{\mathsf{SP}}(D) = 2\pi a \lambda \Delta G_{\mathsf{AB}}^{\mathsf{132}} \exp\left(\frac{D_0 - D}{\lambda}\right). \tag{2.22}$$

The derivative of the interaction potentials W_{AB} gives the interaction forces F according to Equation 2.6.

2.3.4 Steric interactions

Many biological and synthetic colloids such as microgel possess flexible polymer-like hydrophilic groups, which expose into the aqueous phase [Leck2001; Napp1977]. The spatial extension of these chains is usually comparable or greater than the range of the DLVO interactions [Napp1983]. Thereby, the potential of the DLVO potential of the smooth colloid surface diminishes, whereby the flexible chains dominate the interaction forces [Napp1983].

These chains critically effect the colloidal interactions and stability of a suspension. The interactions between the chains include the DLVO potentials namely van der Waals and double layer interactions. Especially, the

double layer interactions often play a critical role in biological systems since the chains of biological colloids commonly contain charged surface groups, which have manifold effects on the system [Leck2001; Ohsh2006].

In addition to the DLVO potentials, the further interactions between chains include elastic and osmotic potentials [Vinc1986]. First, the elastic potential results from the elastic compression of the chains when two colloids are in contact. This compression corresponds to a net loss of configurational entropy resulting in a repulsive force between colloids [Fern2001]. Second, the osmotic potential results from chain-solvent and chain-chain interactions when two colloids are in contact. The polymer chain densities increases in the region of interpenetration between contacting colloids. Depending on the polymer-solvent interaction parameter χ (Flory Huggins parameter) the overlap of the chains is either energetically favorable ($\chi >$ 0.5) or vise versa ($\chi <$ 0.5). This leads either to an osmotic attraction (χ $>$ 0.5) or a repulsion ($\chi <$ 0.5). Among others Napper and Vincent developed theories to describe the elastic and the osmotic contributions of soft particles such as microgels [Napp1977; Vinc1986].

For simplicity, effective pair potential of microgels can be used to describe the interactions, which follows a power law expression [Senf1999; Heye2009; Rovi2019]:

$$V(r) = \epsilon \left(\frac{\sigma}{r}\right)^n \tag{2.23}$$

where r is the distance between the center of the colloids, σ is the colloidal diameter, and ϵ is the energy scale. The exponent n controls the stiffness of the particle [Heye2009]. In chapter 8 such a power law expression based on Hertzian theory is used to describe the pair interactions of microgel particles.

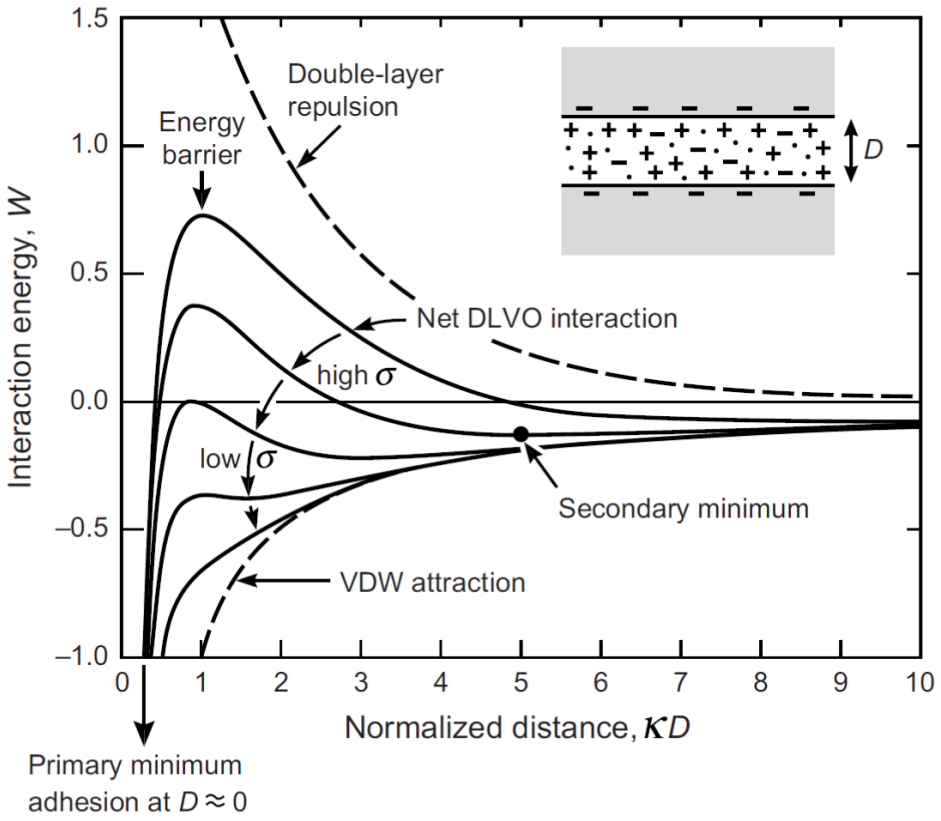

Figure 2.8: Schematic representation of the interaction energy W versus normalized distance profiles of the DLVO interaction. The distance is normalized with the Debye length κ; reprinted with permission from [Isra2011]. Copyright ©2011, Elsevier Inc.

2.3.5 Total intermolecular pair potentials

The sum of the individual potential energies $W_i(D)$ results in the total interaction energy $W(D)$:

$$W(D) = \sum W_i(D) \tag{2.24}$$

The total potential energy is commonly plotted over the separation distance D between two surfaces. Thereby, a positive slope of the potential energy curve implies attraction whereas a negative slope implies repulsion. The Figure 2.8 displays a DLVO interaction between two surface in a $1:1$ electrolyte solution [Isra2011]. The DLVO potential comprises van der Waals and double layer interactions. Considering further potentials such as acid

base interactions can shift the calculated potential to be more attractive or repulsive. However, due to simplification these potentials are not considered in the following explanations. The van der Waals interactions scale with a power law formulation ($W_{vdw} \propto 1/D^n$), whereas the double layer interactions decay exponentially ($W_{dl} \propto exp(-D)$). Due to the exponential decay, the double layer interactions raise slower when $D \rightarrow 0$ compared to the power law formulation of the van der Waals interactions. Hence, the van der Waals interactions usually exceed the double layer interactions at a minimum separation distance denoted as a primary attractive minimum. However, the double layer interactions can exceed the van der Waals interactions at larger separation. Three cases are distinguished: kinetically stable, meta stable and unstable. First, if double interactions exceed van der Waals interactions significantly at a separation distance, a high energy barrier exists. The energy barrier prevents from aggregation during any reasonable time period referred to as kinetically stable. Second, at lower surface charge density or potential, the double layer interactions only slightly surpass the van der Waals interactions, which magnifies itself in a low energy barrier. This results in slow aggregation known as coagulation or flocculation and is referred to as meta stable. Third, the potential curve is purely attractive leading to fast aggregation referred to as unstable. The potential course can sometimes contain three parts: at small separation an attractive part, at medium separation a repulsive part and at larger separation an attractive part again. Then the latter part possess a further attractive minimum called secondary minimum. Besides the DLVO potentials. Steric interactions as well as hydrophilic or hydrophobic interactions can exceed the DLVO potential as explained in the previous sections. These potentials can shift the total potential curve to be more repulsive or attractive depending on the suspension composition.

2.4 Hydrodynamic interactions / Lubrication

Viscous fluids transmit mechanical stress of immersed particles effecting the motion of the other suspended particles [Lisi2016]. These fluid-

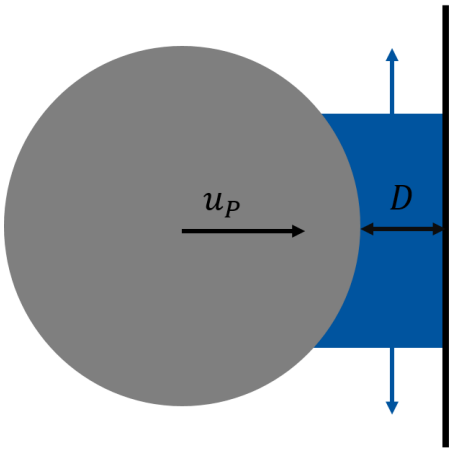

Figure 2.9: Schematic drawing of viscous lubrication.

mediated particle interactions are referred to as hydrodynamic interactions. Hydrodynamic interactions control diffusion and rheological properties of a colloidal suspension [Dhon1996]. Therefore, they are important for a variety of biological processes and colloidal applications.

Hydrodynamic interactions are characterized by three distinguishing features [Lisi2016]. Hydrodynamic interactions 1) are long range interactions, 2) are of many body character, and 3) they do not affect the equilibrium structure without being exposed to an external field. These three features cause hydrodynamic interactions to be difficult to describe and deal with. To describe the resulting long-range and multi-body characteristics of hydrodynamic interactions is out of the scope of this thesis. Detailed information are presented in [Dhon1996; Lisi2016]. However, one effect of hydrodynamic interaction namely viscous lubrication is of specific importance in particle deposition and is further explained in the following.

If two spheres in a viscous fluid approach each other, the fluid between the spheres has to be squeezed out illustrated in Figure 2.9. When the distance between the surfaces decreases, the pressure gradient necessary to squeeze out the fluid increases. The viscous friction raises through the increased pressure leading to slower relative velocities of the approaching spheres. Contrary to approaching spheres, if two spheres move apart from each other, the fluid experience a receding motion to fill the gap between the spheres. Again the receding motion of the fluid results in viscous friction

leading to slower relative velocities. The resulting hydrodynamic drag force / lubrication force acting between the two surfaces can be approximated by the following equation [Lisi2016]:

$$F = \frac{6\pi\eta v_{rel}}{D}\left(\frac{a_1 a_2}{a_1 + a_2}\right)^2 \tag{2.25}$$

where η is the fluid viscosity, v_{rel} is the relative velocity between the two surfaces, D is the distance between the two surfaces, a_1 and a_2 are the radii of the two spheres. The lubrication interaction raises to infinity if the separation distance D goes to zero. A cut-off distance D_0 can be applied at which the separation distance is assumed to be constant. The lubrication force scales with $1/D$ and decays slower compared to van der Waals interaction $(1/D^2)$ or the double layer interactions $exp(-D)$. Therefore, lubrication forces are of longer range than DLVO or xDLVO potentials.

In high-resolution coupled fluid-particle simulations, lubrication interactions do not need to be specify separately, since they are reassembled via the fluid-particle coupling. However, since lubrication forces increase significantly with decreasing separation distance. the fluid resolution must highly be resolved to capture the strong nature of these interactions at small separation distance. This is impractical for micrometer-sized particles, because the high resolution would increase the computing time drastically. To reduce the computational effort, lubrication interaction can be included separately as pair potential on the particle side [Ando2012b].

3 Methods

This thesis combines numerical CFD-DEM simulations with microscopic observations in microfluidic devises to analyse colloidal clogging and resuspension. Both methods are presented in the following.

3.1 CFD-DEM modeling

In this thesis, the open source software CFDEM © is applied to simulate the microscopic process of colloidal deposition and resuspension. CFDEM © combines computational fluid dynamics (OpenFOAM ©) with a discrete element method (LIGGGHTS ©) to simulate particle motion inside a fluid flow [Goni2010; Klos2012]. Thereby, a four way coupling algorithm determines interactions between particle-particle, fluid-particle, wall-particle and wall-fluid.

3.1.1 Discrete Element Method

Discrete element method (DEM) is a Lagrangian simulation method developed by Cundall and Strack [Cund1979]. It allows to compute the motion and interactions of particles by solving Newton's law of motion. Each particle trajectory is explicitly solved by the following force balance [Klos2012]:

$$m\ddot{x}_i = F_n + F_t + F_b + F_f \tag{3.1}$$

where m and $\ddot{x}_i$ are the mass and the acceleration of the particle, respectively. The motion of each particle depends on contact forces (F_n, F_t), body forces (F_b) and forces arising due to the surrounding fluid phase (F_f). F_f summarizes the fluid forces acting on each particle [Zhu2007].

A Hertz contact modeling approach as represented in Figure 3.1 is used

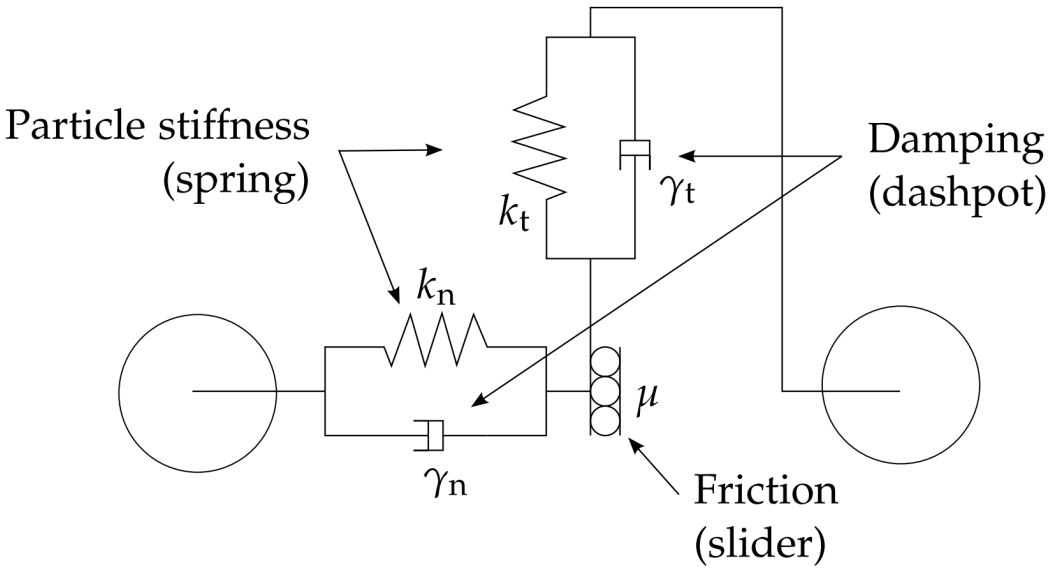

Figure 3.1: Schematic representation of the Hertzian spring dashpot model, redrawn from [Hærv2017]

to determine the tangential and the normal contact forces F_n and F_t:

$$\begin{aligned} F_n &= k_n \delta_n - \gamma_n v_n \\ F_t &= k_t \delta_t - \gamma_t v_t \end{aligned} \tag{3.2}$$

δn and δt denote the normal and tangential overlap of two surfaces. The constants k_n and k_t are the elastic constants and γ_n and γ_t the viscoelastic damping constants. The constants k and γ are material properties depending on the Young modulus E, the Poisson ratio ξ and the coefficient of restitution e [Di M2005]. The normal and tangential relative velocity is termed v_n and v_t. The relative tangential velocity includes both the tangential velocity between the spheres and the relative motion due to rotation characterized by the angular velocity.

In addition to the force balance, a torque balance is applied in the DEM framework:

$$I \frac{d\omega}{dt} = \sum M \tag{3.3}$$

where I is moment of inertia, ω is the angular velocity and M are the con-

tact torques. The torque acting between contacting particles comprises two contributions: a rotational torque caused by the interparticle contact force and a rolling friction torque. The former causes particles to rotate while the latter resists against the rotations [Noro2016]. The rotational torque $\vec{M}^t$ is calculated as follows:

$$\vec{M}^t = r\vec{n} \times \vec{F}^c \tag{3.4}$$

where r is the radius of the particle, $\vec{n}$ is the normal vector and $\vec{F}^c$ is contact force. Contrary, the rolling friction force is often controled by plastic deformation and viscous hysteresis. There exist several models proposed in literature to describe the rolling friction torque [Ai2011]. This thesis applies the simplified constant direct torque model, which is determined as follows:

$$M_{rf} = C_{rf} k_n \delta n r \frac{\omega_{rel,shear}}{|\omega_{rel,shear}|} \tag{3.5}$$

C_{rf} defines the coefficient of rolling friction and $\omega_{rel,shear}$ is the projection of the relative angular velocity into the shear plane.

In DEM, a linear spring dashpot model is usually applied to calculate the contact mechanics between spheres [Zhu2007; Klos2012]. It neglects possible contact deformations but in return allows for the overlap of the particles. The normal contact force is calculated based on Hertzian theory as follows:

$$F_n = -k_n \delta_n + c_n \delta u_n \tag{3.6}$$

where δ_n is the normal overlap and δu_n the relative velocity of the intersecting bodies. k_n is the normal spring coefficient and c_n the damper coefficient. They are derived from the mechanical properties of the intersecting particles [Di R2004; Klos2012]:

$$k_n = \frac{4}{3} Y^* \sqrt{R^* \delta_n} \tag{3.7}$$

$$c_n = -2\sqrt{\frac{5}{6}} \beta \sqrt{S_n m^*} \tag{3.8}$$

with:

$$S_n = 2Y^* \sqrt{R * \delta_n} \tag{3.9}$$

$$\beta = \frac{ln(e_r)}{ln^2(e_r) + \pi^2} \tag{3.10}$$

$$\frac{1}{Y^*} = \frac{1 - \nu_1^2}{Y_1} + \frac{1 - \nu_2^2}{Y_2} \tag{3.11}$$

$$\frac{1}{R^*} = \frac{1}{a_1} + \frac{1}{a_2}, \quad \frac{1}{m^*} = \frac{1}{m_1} + \frac{1}{m_2} \tag{3.12}$$

Here a is the particles' radius, m their mass, Y the Young's modulus, ν the Poisson ratio and e_r the coefficient of restitution.

The tangential contact force F_t is calculated in a similar fashion:

$$F_t = min\left\{ \left[k_t \int_{t_{c,0}}^{t} \Delta u_t dt + c_t \Delta u_t \right], \mu F_n \right\} \tag{3.13}$$

where k_t is the elastic constant for tangential contact, Δu_t the relative tangential velocity, c_t viscoelastic damping constant for tangential contact and μ the friction coefficient. The tangential force is restricted to the Coulomb friction limit. Further, it should be noted that the tangential spring deflection is calculated from the temporal integral of the intersecting bodies' tangential velocity difference. Again, the spring and damper coefficients are

calculated from mechanical properties [Di R2004; Klos2012]:

$$k_t = 8G_S^* \sqrt{R^* \delta_n} \tag{3.14}$$

$$c_t = -2\sqrt{\frac{5}{6}}\beta\sqrt{S_t m^*} \tag{3.15}$$

with:

$$S_t = 8G_S^* \sqrt{R * \delta_n} \tag{3.16}$$

$$\frac{1}{G_S^*} = \frac{2(2-\nu_1)(1+\nu_1)}{Y_1} + \frac{2(2-\nu_2)(1+\nu_2)}{Y_2} \tag{3.17}$$

where G_S is the shear modulus.

3.1.2 CFD-DEM approach

Computational fluid dynamics (CFD) is used to solve mass, momentum, energy, and species conservation equations of fluid flow. Industry and research widely apply CFD to simulate, design and optimize process systems in chemical and mechanical engineering. Even fluid and solid particulate phases can be modeled by treating the particles as continuum phase ("Eulerian-Eulerian approach"). However, this Eulerian-Eulerian approach is less accurate in describing the solid phase compared to fluid flow. To get a more detailed description of the particular phase, CFD simulation were coupled with Discrete Element Method (DEM) which is called CFD-DEM modeling. CFD-DEM incorporates the benefits of the accurate description of fluid phase of CFD with the individual particle tracking method of DEM [Noro2016].

Two types of CFD-DEM methods exist, namely, the "unresolved" and "resolved" [Goni2010; Klos2012]. Unresolved CFD-DEM is applied when the particle sizes are smaller than the CFD grid. It is used when the global behavior of a large number of particles is of interest. Contrary, resolved CFD-DEM is applicable for large particles compared to the CFD mesh size. It is applied for detailed analysis of few, large particles [Hage2012]. Due to the high computational effort of the resolved CFD-DEM, the unresolved method is applied in this thesis.

In unresolved CFD-DEM, the equation of continuity and the volume-averaged Navier-Stokes equation determine the motion of an incompressible fluid phase in the presence of a particulate phase [Klos2012].

$$\begin{aligned} \frac{\partial \epsilon}{\partial t} + \nabla \cdot (\epsilon u_f) &= 0 \\ \frac{\partial \epsilon u_f}{\partial t} + \nabla \cdot (\epsilon u_f u_f) &= -\epsilon \nabla \frac{p}{\rho_f} + \nabla \cdot \tau - R_{pf} \end{aligned} \tag{3.18}$$

ϵ and u_f are the void fraction and the velocity of the fluid, respectively. τ, p and ρ_f represent the stress tensor, the pressure and the density of the fluid. R_{pf} determines the momentum exchange between the fluid and particulate phase and is calculated by the following expression [Klos2012]:

$$R_{pf} = K_{pf} \cdot (u_f - \langle u_p \rangle) \tag{3.19}$$

where the momentum exchange coefficient K_{pf} is

$$K_{pf} = \frac{\sum_i F_d}{V_{cell} \cdot |u_f - \langle u_p \rangle|} \tag{3.20}$$

u_p, F_d and V_{cell} represent the cell-based ensemble averaged particle velocity, the drag force and the volume of the mesh cell.

Drag correlation:

A variety of drag correlations can be applied to determine the momentum exchange coefficient K_{pf} [Zhu2007; Noro2016]. For an individual particle moving through a fluid the drag resistance force F_D is well established:

$$F_d = C_d / 2\pi \rho_f r^2 (u_f - u_p) |u_f - u_p| \tag{3.21}$$

with the drag coefficient C_d being:

$$C_d = 24(1 + Re_p^{0.687}) / Re_p \tag{3.22}$$

The drag resistance force scales with the particle's Reynolds number Re_p,

which is equal to:

$$Re_p = \frac{\rho_f d_p |u_f - u_p|}{\nu_f} \tag{3.23}$$

Three regimes with increasing Reynolds number can be distinguished: the Stoke's Law region, the transition region, and Newton's law region. Since, the colloidal particle and the flow velocities during filtration are rather small, the particle's Reynolds number is correspondingly low. Therefore, the drag force F_d simplifies to Stokes drag force:

$$F_d = 6\pi\eta r(u_f - u_p) \tag{3.24}$$

However, Stokes drag becomes insufficient by the presence of other particles. The presence of other particles reduces the space of the fluid which generates a sharp fluid velocity gradient resulting in an increased shear stress on the particles' surfaces [Zhu2007]. A variety of drag correlations exist describing the increased drag coefficient with increased solid concentration, which are more detailed discussed in [Zhu2007]. One commonly applied drag correlation bases on the work of Gidaspow [Gida1991]:

$$F_d = \beta_{pf}/\rho_f(u_f - u_p) \tag{3.25}$$

The drag pre-factor β_{pf} decreases with the void-fraction ϵ of the fluid phase with the following expressions:

$$\beta_{pf} = \begin{cases} \frac{3}{4} C_d \frac{\rho_f(1-\epsilon)|u_f - u_p|}{d_p} \epsilon^{-2.65}, & \epsilon > 0.8 \\ 150 \frac{(1-\epsilon)^2 \nu_f}{\epsilon d_p^2} + 1.75 \frac{(1-\epsilon)|u_f - u_p|\rho_f}{d_p}, & \epsilon \leq 0.8 \end{cases} \tag{3.26}$$

Since the fluid-particle interaction scale with the void fraction, the void fraction in the CFD mesh elements is crucial. Different ways exist to calculate the void fraction, where two are presented in the following. The easiest way is to calculate the void fraction with the center approach. Thereby, the particle is considered to be in the mesh element where the particle's

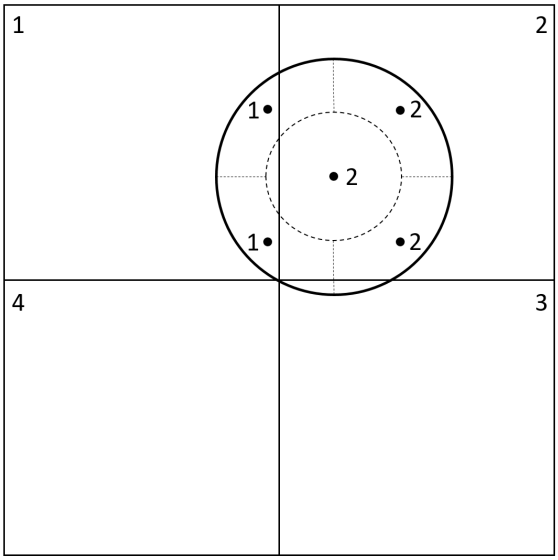

Figure 3.2: Illustration of the void fraction approximation in CFD mesh by the divided approach. The particle is split in five elements. Two elements locate in the first element and three elements are located in the second mesh element.

center is located. Thereby, the overlap of the particle with other mesh elements is neglected. This approach is only suitable if the particle is much smaller than the mesh size ($2r << D_{mesh}$). If the particles are only slightly smaller than the mesh size, this method is not applicable because it inaccurately describes the void fraction. To get a more accurate description of the void fraction, the divided approach can be used which is schematically illustrated in Figure 3.2. The divided approach splits the particle volume in a finite number of equally sized elements. The center point of each element is calculated and the solid fraction is spread over the mesh elements. The divided approach is distinguished by being mass conservative while smoothing the void fraction and the momentum exchange term.

Additional smoothing of the void fraction can be applied to improve accuracy and stability of the particle-liquid coupling [Blai2016]. The smoothing of the void fraction is advisable, if the particle diameter reaches the size of the mesh cell. Without smoothing there can be dependencies between drag force and the particle's mesh position. The isotropic diffusive smoothing can efficiently be applied to smooth the void fraction field and the momentum exchange term. The following equation is solved for both variables

which are represented ξ:

$$\frac{d\xi}{dt} = \nabla^2 \left(\frac{\lambda^2}{\Delta t_{CFD} \xi} \right) \tag{3.27}$$

The isotropic smoothing method is conservative, easy to implement and is simply controlled with the smoothing length λ, which is chosen to be the particle's diameter.

Coupling routines:

Summarized, Figure 3.3 presents the coupling routine between CFD and DEM. The coupling routine consists of multiple steps:

- DEM calculates the positions and velocities of the particles
- the occupied volume of the solid phase and the average velocities in the CFD mesh elements is calculated based on the particles position
- the particle-fluid exchange forces are calculated
- the CFD solver calculates the fluid velocity and pressure
- the particle's Reynolds number and the difference velocity between particle and fluid phase are determined
- the force the fluid exerts on the individual particles is calculated
- the routine is repeated

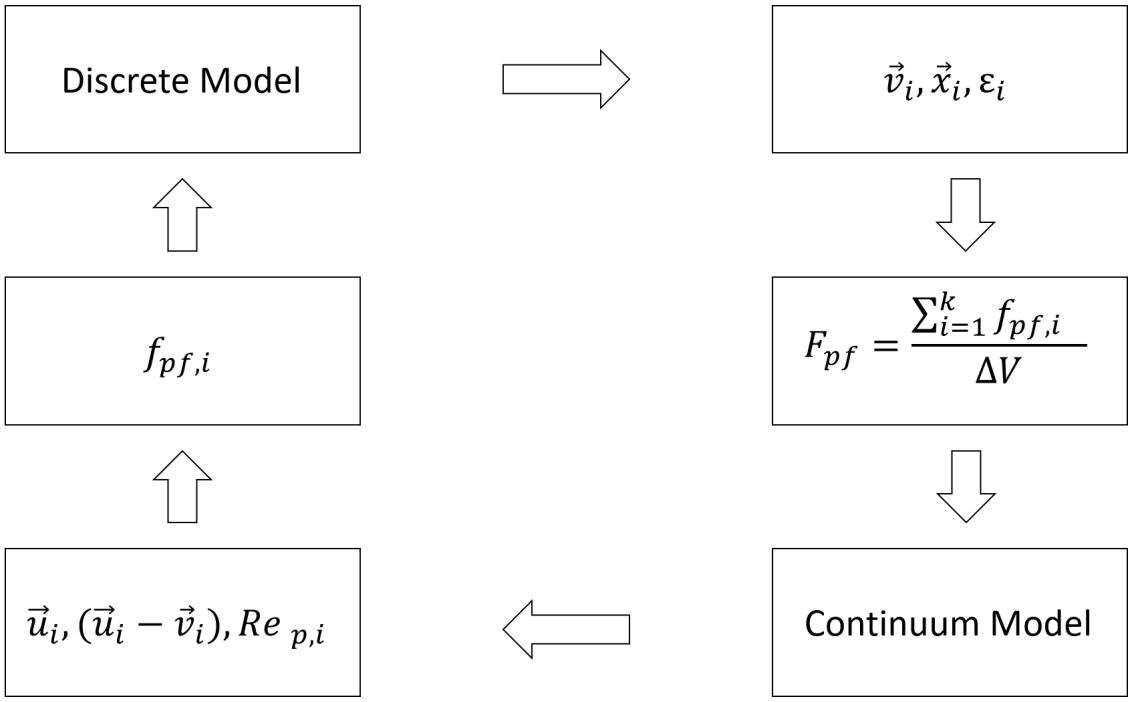

Figure 3.3: Coupling and data exchange between continuum (CFD) and discrete (DEM) models, redrawn from [Zhu2007]

3.2 Microfluidics

Microfluidics refers to the behavior, control, and manipulation of fluids in micrometer sized flow channels. Microfluidics technologies are characterized by a number of useful features: the capability of using small quantities of samples and reagents, and to carry out separation and detection with high resolution and sensitivity; low cost; short times for analysis; and small footprints for the analytical devices [Whit2006]. Therefore, microfluidic devises are applied for inkjet printheads, DNA chips, lab-on-a-chip technology, micro-propulsion, and micro-thermal technologies.

Many material systems such as glass, silicon or various elastomers have been used in microfluidics. The most popular material is polydimethylsiloxane (PDMS). It is easy to handle, since these devises can be produced at low temperatures (40 °C - 70 °C) and on a nanometer resolution. Additionally, it is optically transparent enabling the observation with optical microscopes.

Since microfluidic enables the observation of micrometer sized flow channels with tailor made geometries, it is well suited to non-invasive mon-

itor clogging and resuspension events of colloidal particles.

4 What are the microscopic events of membrane fouling?

Parts of this chapter have been published as:
Johannes Lohaus, Yannic Martin-Perez, Matthias Wessling
What are the microscopic events of membrane fouling?, Journal of membrane science, 2018
DOI: https://doi.org/10.1016/j.memsci.2018.02.023

Parts of the study was developed and presented in the bachelor thesis of Yannic Martin-Perez:

Y. Martin-Perez. “CFD-DEM based examination of the influence of DLVO forces and turtuosity on fouling in microfluidic systems [Bachelor thesis]”. RWTH university(2016).

4.1 Introduction

Colloidal fouling is challenging in a broad range of processes such as membrane filtration, microfluidics, 3-D printing and liquid chromatography [Wyss2006; Mass2016]. In these applications fouling profoundly limit the performance and can even cause a complete failure of the process. In membrane filtration, colloidal fouling occurs inside and in front of the membrane. Colloids may be of different nature such as viruses [Wick2010], solid nanoparticles [Trza2016], and soft gel-like colloids [Nir2016]. The observation of physical microscopic events have only become recently available through the application of sophisticated methods combining microfabrication [Ngen2010], microfluidics [Ngen2011; Agba2012] and confocal laser optical analysis [Link2016].

Despite it's importance, physical understanding of fouling is limited due to complex surface and hydrodynamic interactions on nanometer and micrometer scales. The balance between these interactions determines the fouling probability and it would be highly desirable to have a simulation methodology at hand which could resolve colloid/membrane/hydrodynamics interaction at the different scales to answer the question to what extent the geometry of porosity affects clogging under a concomitant change in flow field.

This study uses coupled computational fluid dynamics - discrete element methods (CFD-DEM) simulations to examine mechanisms of colloidal fouling in a microfluidic architecture mimicking a porous microfiltration membrane.

4.1.1 Simulations and Experiments

Three different geometries were realized in this study, which are shown in Figure 4.1. Such structures mimic the complex geometry of membranes with three defined regular geometries referred to as the straight parallel microchannel, connected square pillars and staggered square pillars. In these microfluidic architectures, fouling experiments with $5\,\mu m$ polystyrene sulfate

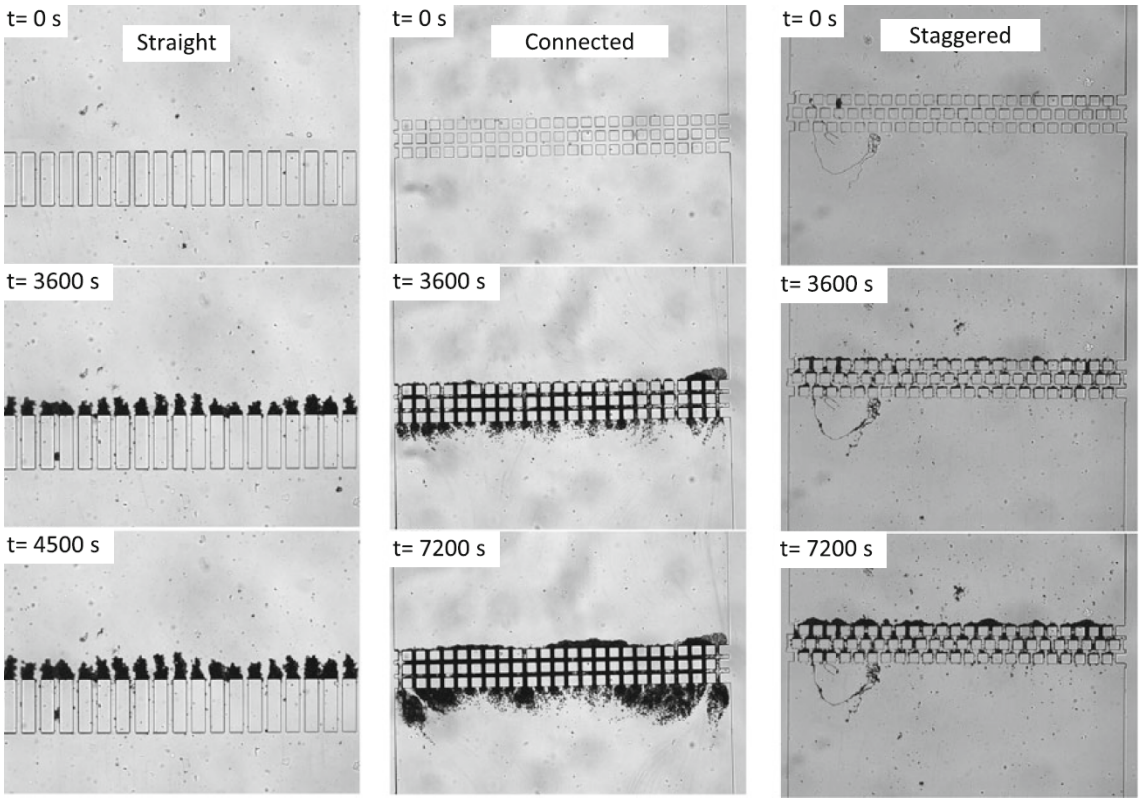

Figure 4.1: Experimental results showing the influence of the geometry of the micro-channel on the clogging process of 5 µm sized polystyrene particles, reprinted with permission from Bacchin et al. [Bacc2014b]. Copyright 2014 Springer Verlag.

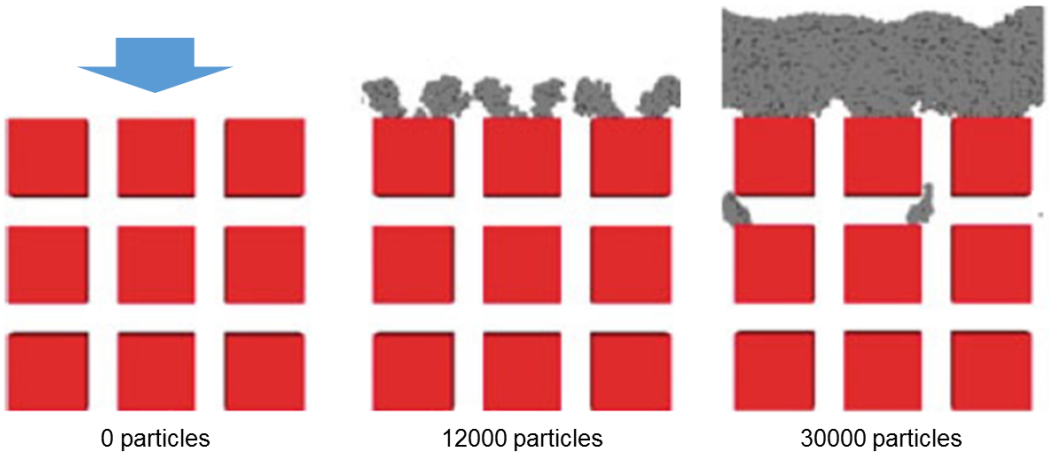

Figure 4.2: Simulation results of the clogging of the connected channel performed by Bacchin et al . [Bacc2014b], adopted and redrawn with permission from Bacchin et al. [Bacc2014b]. Copyright 2014 Springer Verlag.

particles were performed by Bacchin et al. [Bacc2014a]. They performed the experiments with a 100 mM KCl solution which is less than the critical coagulation concentration (200-300 mM) of the particles. Therefore, there is a significant impact of repulsive electrostatic interactions. The fouling varied significantly: while the straight channel geometry developed almost no internal fouling, the aligned square pillars are almost filled entirely with polystyrene sulfate particles, at the end of the experiment. Also the surface fouling exhibits great differences for the different geometries. In addition to the experiments, Bacchin et al. [Bacc2014b] compared their experimental results with simulations. Figure 4.2 shows Bacchin's simulation results of the clogging of the connected geometry.

Some discrepancies between the simulation and experiments exist, especially with regard to the fouling formation and the accumulation kinetics. Some important assumptions in the simulation study applied by Bacchin et al. [Bacc2014b] may be responsible for these differences between experiments and simulation. The used model neglects (a) particle-particle short range interactions, (b) re-suspension of adhered particles, as well as (c) the repulsive part of the DLVO forces. Another rigorous assumption dictates the walls parallel to the flow direction to be non-adherent. Due to these simplifications, the particle attachment mainly occurred artificially on

the upstream side of the pillars and resembles to a certain extend the findings in [Wess2001]. This rejection in front of the membrane contradicts their experimental findings, where clogging mainly occurs on the inner structure or even at the backside.

4.2 Numerical method

This study presents a simulation model, which overcomes some of the mentioned limitations such as the re-suspension of particles and consideration repulsive double layer interaction, whereby effects of the secondary minimum can be demonstrated. The aim is to identify the events occurring during the filtration of colloidal particles which are significantly smaller than the pore size. Special attention is given on how particles overcome repulsive barriers to adsorb onto the surface and which role particle clusters can play in the adsorption and re-suspension dynamic.

Besides contact forces, electrostatic forces strongly influence the clogging process, which are considered by the widely known DLVO theory. The DLVO theory comprises the attractive van der Waals and the repulsive electrostatic double layer potential. For particle-particle (p-p) and particle-wall (p-w) interactions both potentials are calculated as follows [Isra2011]:

Van der Waals potential:

$$E_{VDW,p-p} = -\frac{A}{6}\left(\frac{2r^2}{D\,(D+4r)} + \frac{2r^2}{D\,(D+4r)+4r^2} + \ln\frac{D\,(D+4r)}{D\,(D+4r)+4r^2}\right) \tag{4.1}$$

$$E_{VDW,p-w} = -\frac{A}{6}\left(\frac{2r\,(D+r)}{D\,(D+2r)} + \frac{D\,(D+2r)\,(\ln D - \ln D + 2r)}{D\,(D+2r)}\right) \tag{4.2}$$

Electrostatic double layer potential:

$$E_{EDL,p-p} = \left(\frac{r_i r_j}{r_i + r_j} \right) Z e^{-\kappa D}$$
$$E_{EDL,p-w} = r Z e^{-\kappa D} \tag{4.3}$$

D and r term the distance between particle and the wall and the particles radius, respectively. A signs the Hamaker constant. The interaction constant Z depends on the surface potential of particle and wall and κ is the Debye length. The surface charge density is calculated based on the charge titration data provided by the manufacturer of the particle suspensions Thermo Fisher scientific Inc to determine interaction constant Z. The equivalence point of the titration E_t is according to the manufacture $0.4 \mu Eqg^{-1}$. The surface charge density σ is determined according to the following relation:

$$\sigma = \frac{1}{3} F \rho_p r \tag{4.4}$$

where F is the Faraday constant. The surface potential of the particle is calculated according to the Graham equation [Isra2011]:

$$\sigma = \sqrt{8 \epsilon_0 \epsilon k T} \sinh \frac{e \Psi_0}{2kT} \sqrt{c_{\mathrm{KCl}}} \tag{4.5}$$

The interaction constant Z for the particle-particle interaction is then derived from the equations 2.11 f.. The particle-wall interaction are approximated based on the zeta potential measured by Mustin et al. [Must2016] (referring to Equation 2.12 f.).

Since the reciprocal function of the van der Waals potential approaches infinity at direct contact a constant force is chosen below a separation distance of $0.4\,\mathrm{nm}$ [Dahn1972; Viss1995].

Figure 4.3 shows the DLVO interaction potentials over distance for $5\,\mu\mathrm{m}$ polystyrene sulfate particles used in the simulation among themselves and with the PDMS wall in a 100 mM KCl solution. Based on the potentials

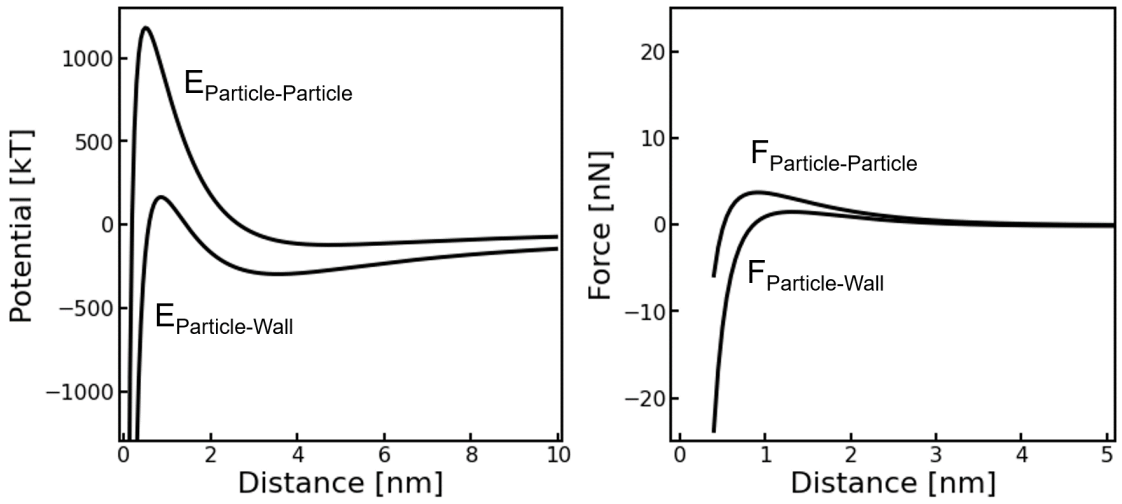

Figure 4.3: Computed DLVO energy profiles and force of particle/ particle (polystyrene sulfate) and particle/ wall (polystyrene sulfate/ PDMS) interaction in a 100 mM KCl solution

particles can accumulate at two stable positions. The first position lies at direct contact with the surface called primary minimum, the second position is located $3 - 4$ nm away from the surface termed secondary minimum. Since the attractive potential in the primary minimum are significantly higher compared to the one in the secondary minimum, particles attach stronger in the primary minimum. The characteristic of the primary and secondary minimum influences the adsorption process decisively as shown by Kuznar [Kuzn2007].

4.2.1 Simulation method and conditions

In the following the simulation conditions, such as geometry, mesh, process conditions and simulation settings are presented. We intend to resemble the conditions of the experiments and the simulations performed by Bacchin et al. [Bacc2014b]. Similar to the work of Bacchin et al. [Bacc2014b] three types of geometries are chosen. These are referred to as the straight, the connected and the staggered geometry (see Figure 4.4). $5\,\mu$m sized polystyrene particles are filtered from top to bottom through the devices. The properties chosen for the PDMS walls and the particles are listed in Table 5.1. We neglect the DLVO forces of the top and button

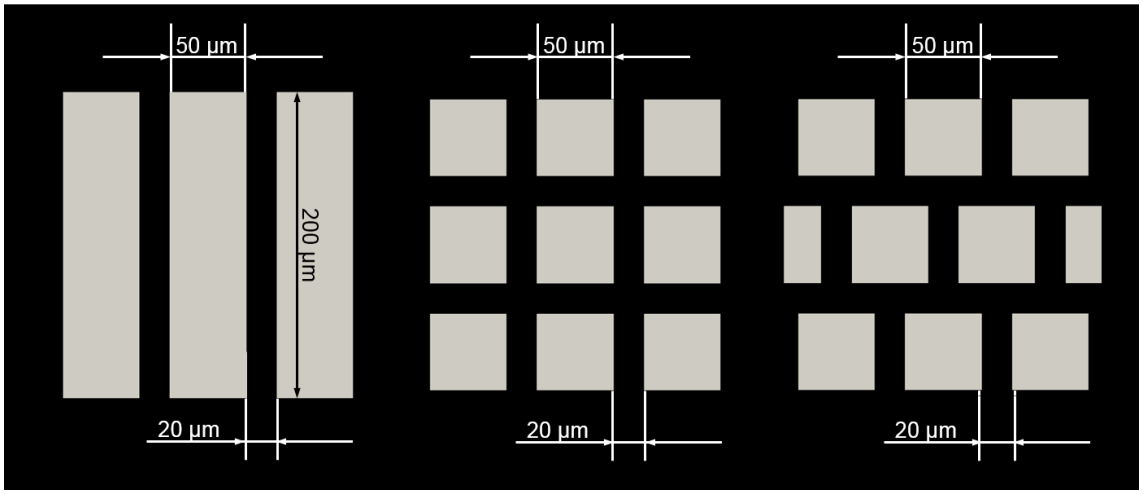

Figure 4.4: The straight parallel microchannels, the connected microchannels and the staggered square pillars from left to right

side of the microfluidic device to keep the focus on the adsorption of the pillars. As in the experiments performed by Bacchin et al. [Bacc2014b], a constant mean inlet velocity was chosen to be $4.5\,\mathrm{mm\,s^{-1}}$. For further information we refer to Bacchin et al. [Bacc2014b].

The computational effort strongly depends on the DEM - simulation. Therefore, the choice of the DEM - time step is crucial to gain simulation results in a reasonable time frame. The DEM - time step complies with the Rayleigh time, expressed by the following equation [Gu2016]:

$$t_{Coll} = 2.943 \left(\frac{5\sqrt{2}\pi\rho_P \left(1 - \nu_{Poisson}^2\right)}{4E} \right)^{\frac{2}{5}} \frac{r}{u_{Feed}} \tag{4.6}$$

It is good practice to set the DEM-time step to 10-30 % of the Rayleigh time and set the coupling interval with CFD to 100 DEM-time steps. To reduce the computational time the Young's modulus of the particle was chosen 3 orders of magnitude smaller than the literature value to reduce the DEM-time step. Test simulation indicate negligible differences result due to changing the Young's modulus. To further reduce the computational time, the simulations were performed with a particle concentration of 5 vol % which is 10 to 50 times higher compared to experimental work of Bacchin

Parameter	Symbol	Value	Literature
Filtration velocity	v_0	$4.5\ \mathrm{mm\,s^{-1}}$	-
Particle radius	a	$5\ \mu\mathrm{m}$	-
Young modulus wall	E	$8.7 \times 10^6\ \mathrm{Pa}$	[Arma1999]
Young modulus particle	E	$3.6 \times 10^6\ \mathrm{Pa}$	-
Poisson ratio	$\tilde{\nu}$	0.45	assumed
Coefficient of restitution	e	0.95	assumed
Friction coefficient	μ_f	0.5	assumed
Rolling friction coefficient	μ_r	0.5	assumed
Distance of closest approach	D_{int}	$0.4\ \mathrm{nm}$	[Dahn1972; Viss1995]
Particle density	ρ_{P}	$1000\ \mathrm{kg\,m^{-3}}$	-
Salt concentration	c_{KCl}	$0.1\ \mathrm{mol\,L^{-1}}$	-
Surface potential particle	Ψ_0	$-43\ \mathrm{mV}$	-
Zeta potential particle	ζ	$-37\ \mathrm{mV}$	[Must2016]
Zeta potential wall	ζ	$-23\ \mathrm{mV}$	[Must2016]
Hamaker constant particle	A	$1.4 \times 10^{-20}\ \mathrm{J}$	[Isra2011]
Hamaker constant wall	A	$1.4 \times 10^{-20}\ \mathrm{J}$	-
DEM-time step	Δt_{DEM}	$1 \times 10^{-8}\ \mathrm{s}$	-
CFD-time step	Δt_{CFD}	$1 \times 10^{-6}\ \mathrm{s}$	-

Table 4.1: Parameters applied in the simulation

et al. [Bacc2014b]. Similar to the work of Bacchin et al. [Bacc2014b], simulations have been performed for 30.000 particles over a filtration time of $0.9\,\mathrm{s}$. In contrast to Bacchin et al. [Bacc2014b], where particles are inserted batch wise, particles constantly enter the simulation domain in our model.

The DEM and the CFD are coupled with an unresolved divided volume fraction method. The particle volume is split into distributed marker points, which apportion the particle's volume to the covered mesh elements [Klos2012]. Due to this coupling of CFD and DEM, the mesh size fineness depends on the particle diameter leading to a relative coarse mesh ($5\,\mu\mathrm{m}$ mesh elements). Agbangla et al. present a model in which the resolution of the hydrodynamics is higher leading to a more accurate description of the fluid profile [Agba2014b]. Therefore, future studies could merge the high resolution of the fluid model of Agbangla with the more detailed description of the colloidal interactions of this work. A possible way in the CFDEM

framework to improve the accuracy of the CFD and DEM coupling is to apply an immersed boundary approach [Klos2012]. However, the simulation were not performed with this method because of the computational effort.

4.3 Results & Discussion

4.3.1 Macroscopic fouling and clogging

Simulation results are performed which show the formation of colloidal fouling in three microfluidic topologies. To compare and validate the results, the geometries are based on the experimental and numerical work of Bacchin et al. [Bacc2014b]. Figure 4.5 shows the results of the fouling formation over time in the three topologies. In this Figure, particles with a velocity lower than $800\,\mu m\,s^{-1}$ are displayed which keeps the focus on attached particles.

In the straight geometry, particles adsorbed on the inner surface building up a monolayer as time progresses. Also, some particle agglomerates can be observed. Interestingly, particle accumulated at the downstream zone of the pillars as well. But no complete blockage of a channel developed during the filtration. Figure 4.1 shows that during the experiments of the straight geometry most internal channel do not get blocked with progressing time. Instead, dendrites are formed on the inlet side of the channels. That differs from our simulation results in which most particles form dendrites on the downstream side which is discussed in Section 4.3.4. Furthermore, the kinetics of the fouling process between experiments and simulation are not comparable. In our simulation the fouling progresses much faster compared to the experimental results. One explanation is the high particle concentration, which 1) increases particle-particle interaction and 2) increase the viscous drag force due to an decrease in void fraction of the fluid. Further, increased fouling in the simulation can be explained by the assumption of smooth surfaces and the neglection of lubrication effects. Lubrication forces reduce the relative velocity of approaching surfaces and therefore, reduce particle adsorption kinetic [Isra2011]. The model treats the particles

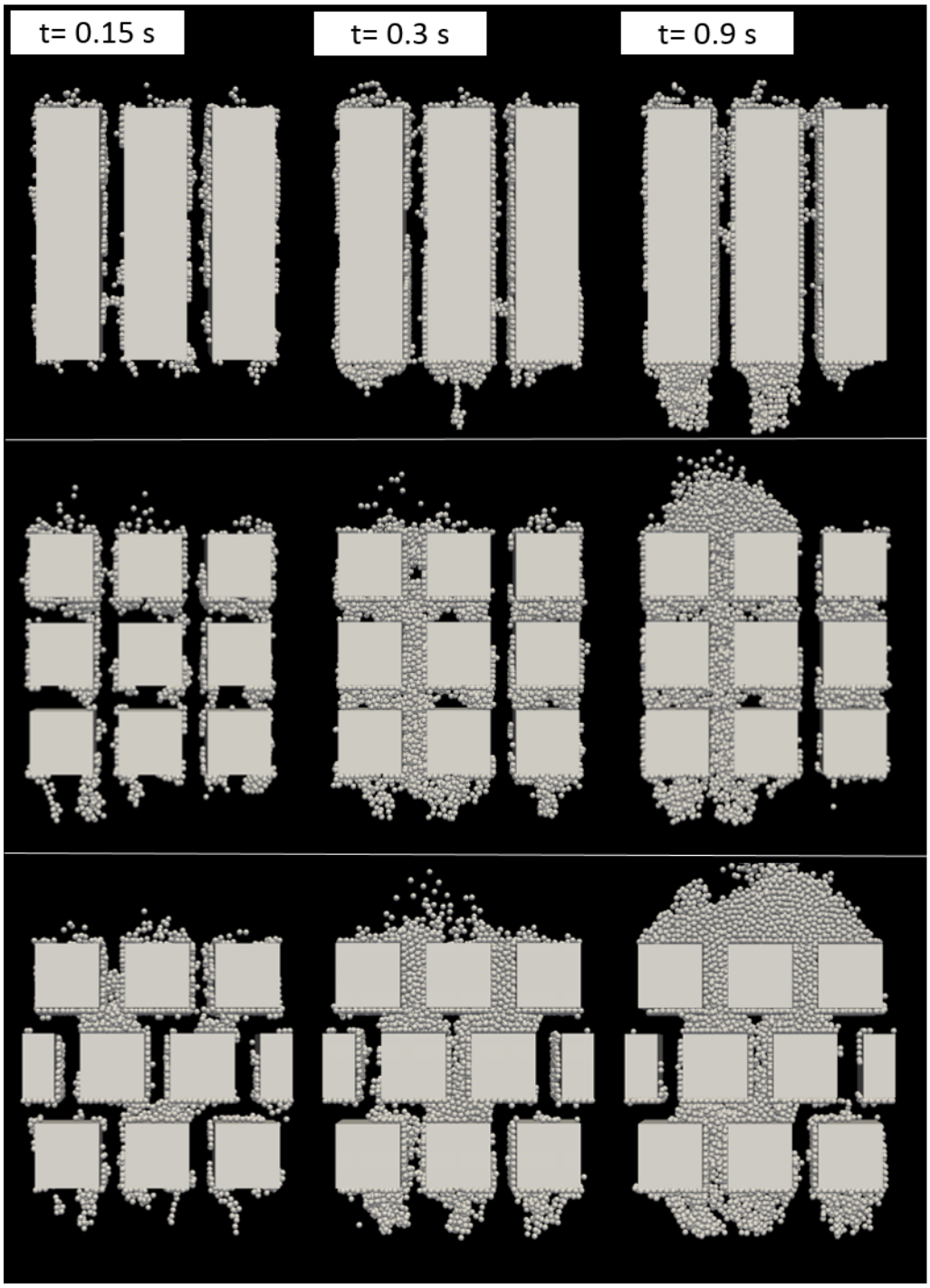

Figure 4.5: Simulation of the clogging development in the staggered, connected and straight geometries.

as well as the pore surface as completely homogeneous which neglects influences of surface roughness and charge heterogeneities. Both non idealities influence the colloidal interactions significantly [Song1994; Tan2005; Hoek2006]. Moreover, the model neglects Lewis acid-base interactions which are mainly responsible for hydrophilic and hydrophobic interactions [Van 2006].

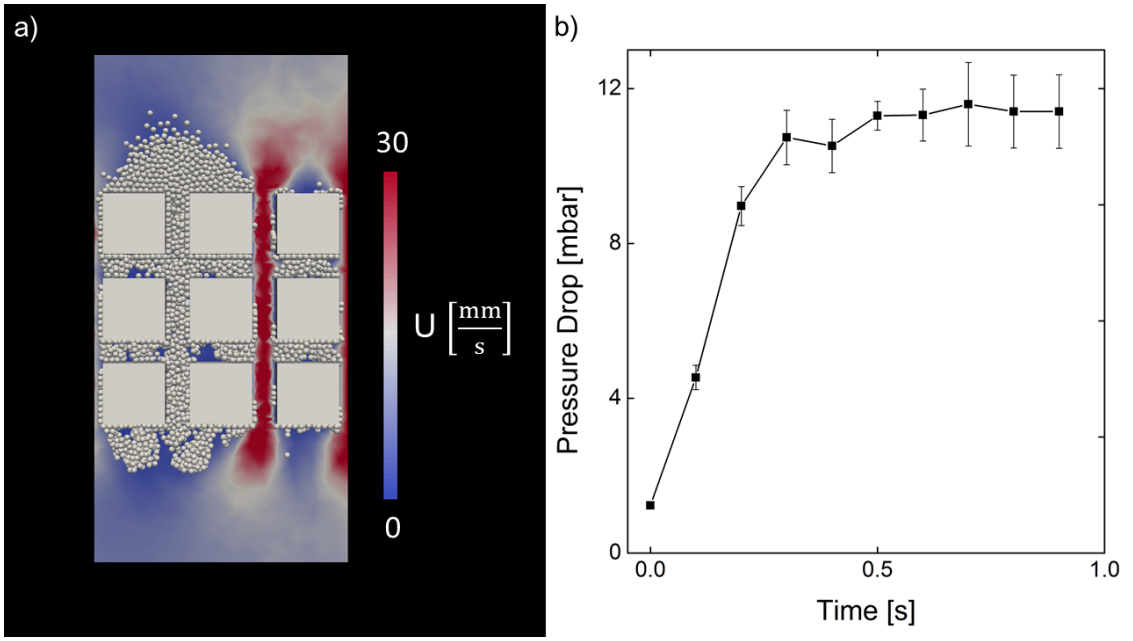

Figure 4.6: a) Demonstration of the flow profile through the connected channel at 0.9s. b) Development of the pressure drop as a function of time in the connected channel.

In the connected square pillars, the particle accumulate inside the inner structure which leads to a complete blockage of the left channel in course of the simulations (see Figure 4.5). As time proceeds, a filter cake builds up. This behavior particularly highlights the growth of a clog from the inner structure to a cake layer. Due constant volume flow condition the flow velocity in the remaining channels increases, which prevents from complete clogging (see Figure 4.6a). Due to the clogging, the pressure drop increases over time until it follows an asymptotic course (see Figure 4.6b). The pressure drop reaches asymptotic behavior when the center-left channel is completely blocked and the majority of the flow goes to the right channel. Pressure fluctuations are observed due to adsorption and des-

orption phenomena as well due to particles enter and leave the simulation domain. The pressure drop in Figure 4.6b displays an averaged pressure drop over 1 ms. In the clogged pore, the particles occupy a volume concentration of 0.45 to 0.55 and the distribution of the coordination number of the attached particles on the pillars is as follows:(0: 12.0 % , 1: 29.1 %, 2: 37.8 % 3: 18.3 %, 4: 2.5 % 5: 0.3 % (at 0.6 s)). The calculated volume concentration and the coordinate number distribution are comparable with the results of Agbangla et al. [Agba2014b]. Similar behavior is observed in the staggered structure, in which particle adhesion starts mainly in the inner structure. Due to the cluster formations in the channels, the middle segment clogged with time and a filter cake develops. The side channels remain unclogged due to an increased flow velocity. The results of the fouling formation in the geometries with an inner structure the experiments and our simulation show good agreement. As in the simulation, particle adhered in the inner structure of the device during the experiments (see Figure 4.1). These adhered particles enhance further particle deposition and lead to the blockage of flow channels and a cake formation. In addition, particle deposit in the downstream zone in our simulation as well as in the aligned channel in the experiments. Bacchin et al. [Bacc2014a] interpreted this downstream deposition with particle clusters which detach from the surface and settle in time. Because of the short simulation times and the little density difference between colloid and solvent, settling of particles cannot only be responsible for the deposition on the downstream side. Our model includes particle detachment as well as particle gliding which we will show later to be important microscopic events governing observations such as downstream aggregation. 4.3.4.

4.3.2 Transition from secondary to primary minimum

The simulations give access to all particle trajectories in time and space and enable us to investigate different microscopic events which are responsible for the clogging of the channel. One adsorption mechanism during our simulation is demonstrated in Figure 4.7. It exemplary demonstrates

the adhesion process of a single particle (marked in blue) due to the interaction with another particle (marked in red).

At the beginning of the adsorption process of the blue marked particle, both particles are located in the bulk phase and their trajectory of movement point towards the surface of a pillar. The blue particle adsorbs into the secondary minimum with the pillar, but is not able to overcome the repulsive barrier to get into the primary minimum. The trajectories of the red particle is directed towards the blue particle leading to interaction between both particles. Due to the collision of both particles, the blue particle is pushed towards the surface of the pillar. The blue particle overcomes the repulsive barrier of the particle-wall potential and reaches the primary minimum. Due to the higher repulsive barrier of the particle-particle potential both particle do not agglomerate and the red colored particle remains in the solution.

This adsorption process is even more pronounced at the side walls of the pillars (4.8). Due to higher drag forces which particles experience in the channels, the particle collision leads to a transition from secondary to primary minimum on the wall as well as an agglomeration of both particles.

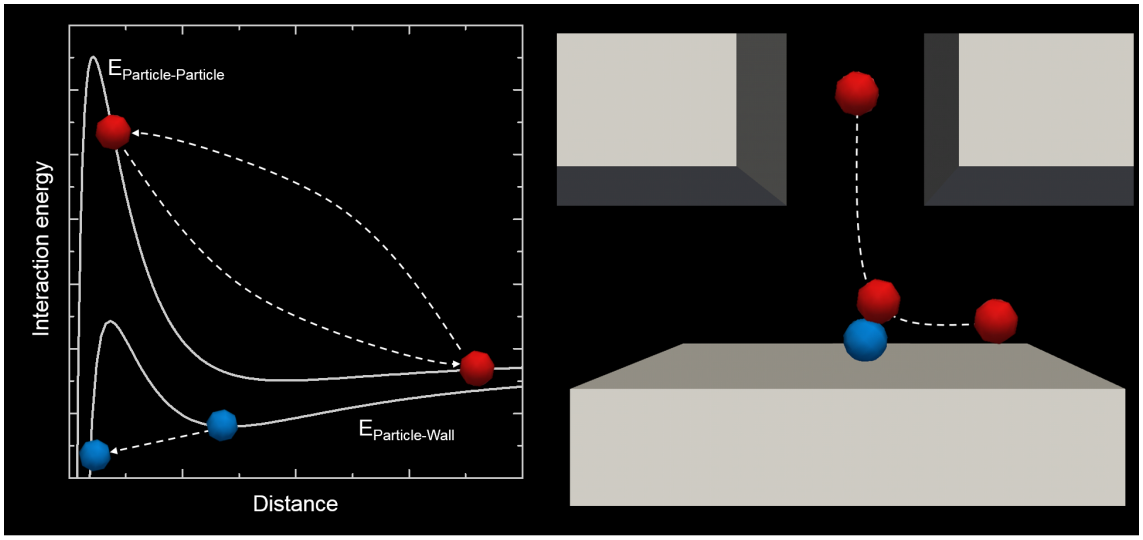

Figure 4.7: Particle-particle interaction leading to overcome of the repulsive barrier of the wall-particle potentials (blue colored particle). Due to the higher repulsive barrier of the particle/ particle potential both particles do not agglomerate. Therefore, the fluid flow entrains the red colored particle.

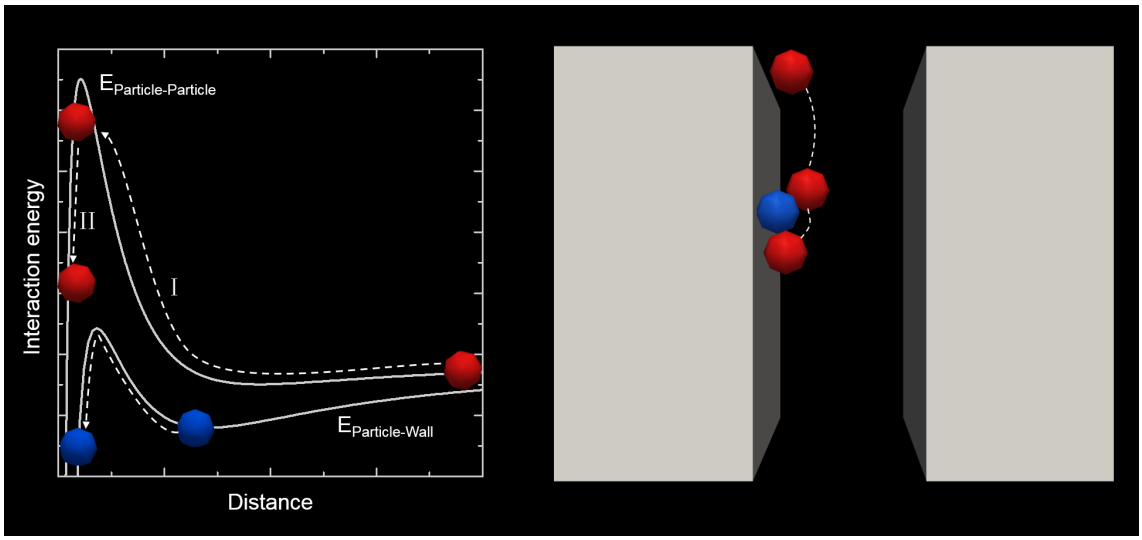

Figure 4.8: Particle-particle interaction leading to overcome of the repulsive barrier of the wall-particle potentials as well as of the particle-particle potentials, whereby an agglomerate is formed on the surface of the pillar.

This clustering deposition is experimentally observed during a filtration experiment by Zamani et al. [Zama2016]. They showed that a glass particle sticking to a membrane surfaces caught a particle from the bulk, which leads to a deposition on the membrane surface.

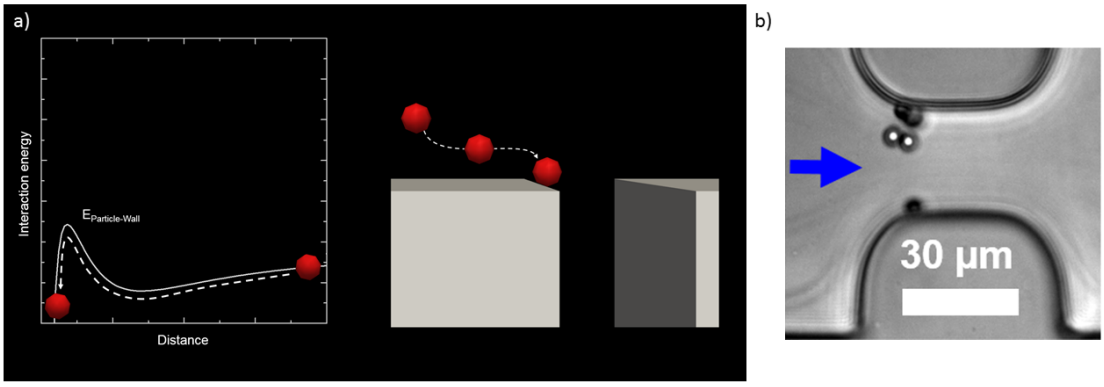

Figure 4.9: a) Schematic drawing of a particle adsorption on the edges of the pillars in the simulations. b) Experimental observation of polystyrene particle deposition on the edges, reprinted with permission from Desoir et al. [Ders2015]. Copyright 2015 Springer Nature

In summary, particles can overcome the repulsive barrier due to particle-particle interactions and the attached particles transits into the primary minimum.

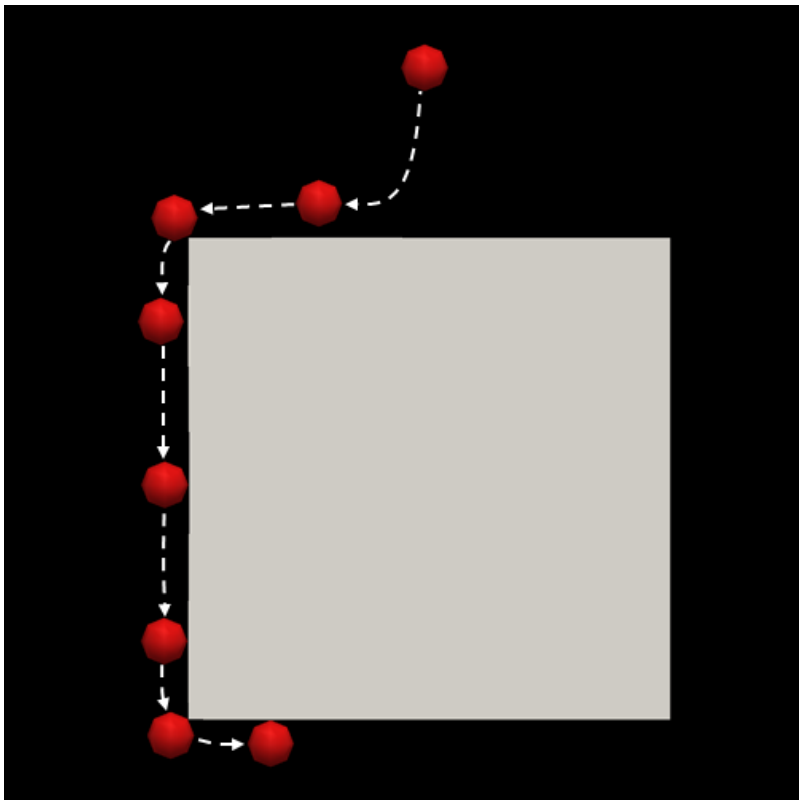

Figure 4.10: Particle glides over the surface leading to attachment on the downstream zone of the pillars during simulation.

4.3.3 Particle adsorption on the edges

In contrast to the previous section which deals with the adsorption of particles due to particle-particle interactions, this section shows the adsorption of single particles into the primary minimum. To reach the primary minimum the drag force needs to be sufficient to overcome the repulsive barrier. Particularly at the entrance of the pillars the drag is sufficient to reach the necessary potential. Therefore, particle deposit on the edge of the pillars as shown in Figure 4.9.

The adsorption of particles at the entrance of the constriction was also observed in several experimental systems of high or mild confinement [Must2010; Ders2015; Send2016a; Kim2017]. This mechanism of adsorption is relevant to comprehend the bridge formation of particles leading to blockage of the channel [Agba2012].

Both phenomena, particle adsorption on the edges as well as adsorption due to collision, play a decisive role in the clogging dynamic. During

our simulation the adsorption due to collision was the dominant mechanism because of the high collision frequency at high particle concentration. Further parameters such as the pore size to particle diameter and the velocity influence the behavior of the clogging dynamic.

4.3.4 Dynamics of the clogging process

A variety of numerical studies treat particles in contact with the surface as fixed and do not solve the equations of motion for these particles [Bacc2014b; Agba2014b; Agba2014a]. In contrast to these studies, we are able to show their dynamic behavior even though they might have been adsorbed initially. Now, one observes that particles glide over the surface as demonstrated in Figure 4.10 during the clogging process. Due to gliding, particles can deposit in the downstream zone of the pillars, which was also observed by [Mino2018]. The downstream deposition is visually very similar to the long streamers observed in bacteria filtration [Mart2012]. Particle gliding is also observed experimentally by Sendikie et al. [Send2016a] at high confinement. In their study, polystyrene particles deposit downstream the pillars at 10 mM salt concentration leading to clogging in the downstream corner. Some deposition on the downstream side of the corner is also shown by Desoir et al. [Ders2015] at a degree of confinement of 7.5. But the deposition was less compared to our simulations. Our model formulation overestimates the evolution and the velocity of gliding particles. The reason lies in the assumption of a perfectly smooth surface and the neglection of non-DLVO potentials used in the modeling approach. Particles located in the secondary minimum do not experience friction forces leading to an unhindered movement tangential to the PDMS surface. These particles tend to move over the corners to the center of the downstream surface, which results in increased particle deposition on the downstream surface. Additionally, the adhesive strength resulting due to DLVO interactions is relatively low. Therefore, particles located in regions of high drag can overcome the Coulomb friction criterion and move downstream. Further, the model did not incorporate a stabilizing van der Waals torque when the par-

ticle rolls over the pore edge as proposed by Duru et al. [Duru2015]. This additional torque hinders particles to move over pore edges and reduces the downstream deposition. Nonetheless, the particles movement downstream on the interface can be decisive in the clogging dynamic, especially in systems with an inner structure such as membranes. Due to gliding of the particles, we observe a relatively homogeneous distribution of particles on the pillars surface, which shows similarities with the experimental results of [Sain2016].

4.3.5 Re-entrainment and re-attachment

During the clogging process, resuspension phenomena are frequently observed. Particles in the first monolayer on the surface show strong attachment and nearly do not re-entrain. In contrast, interparticle bonds in a particle multilayer frequently break. The increasing velocity to the middle of the channel and the smaller energy necessary for desorption of interparticle interaction compared to particle/ wall interaction explain the breakage of particle bonds. The breakage of particle agglomerates is far more often observed than the re-entrainment of single particles. The resuspension of a particle agglomerate is demonstrated in Figure 4.11 a). In so far unpublished microfluidic experiments, we confirmed the cluster breakage of $4\,\mu m$-sized polystyrene sulfate particles during filtration as shown in Figure 4.11 b). The experiments were performed similar to the work of Bacchin in the straight geometry. The filtration velocity was $4.5\,\mu m\,s^{-1}$ and the ionic strength was 100mM KCl. Similarly, Saint Vincent et al. [Sain2016] showed experimentally that polystyrene particles were swept out from a PDMS surface at high flow velocities. Sendekie et al. [Send2016a] reported at high ionic strength (100 mM salt) that clogging of some channels occurred, which are labile and frequently break away. Contrary, Dersoir et al. [Ders2015] observed in their experiments that the stability of the clogs are independent of the ionic strength of the solution. The differences may be originated in the different degree of confinement of the channels between both works (pore to diameter ratio: Sendekie et al. [Send2016a] equal

2, Dersoir et al. [Ders2015] up to 10), which strongly influences the hydrodynamic conditions. After resuspension, the agglomerates are pushed into the inner structure of the device. Due to their large volume, the agglomerates tend to re-attach again as demonstrated in Figure 4.11. These agglomerates serve as initiator for the complete blocking of a channel. Due to flow deflections in the inner structure the attachment of agglomerates is significantly amplified. Among other things, this explains why the straight channel does not show a complete blockage of a channel during the simulation in contrast to both other devices (see Figure 4.5). This mechanism demonstrates the importance of an inner structure on the clogging process.

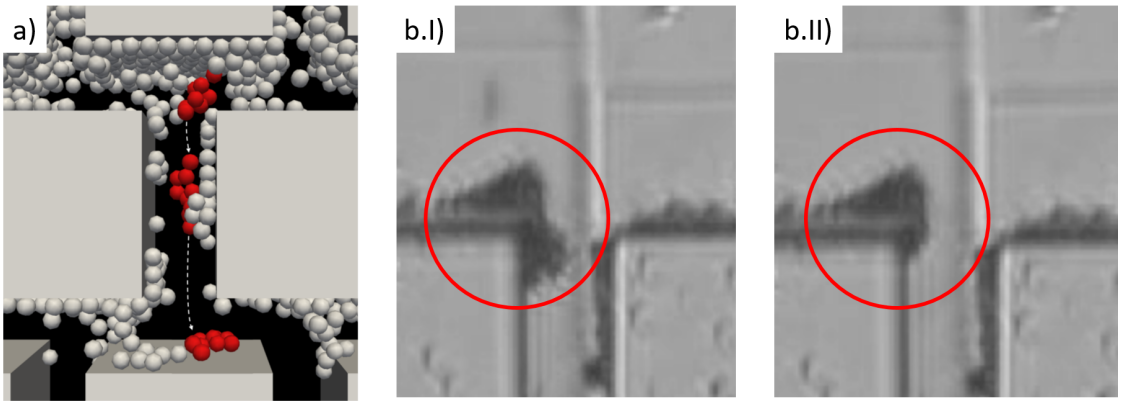

Figure 4.11: Resuspension of a particle cluster. a) Particle cluster resuspension and re-attachment during the simulations. b) Experimental observations of particle resuspension during filtration (for more information see chapter 6). b.I) Particle cluster attached to the geometry. b.II) Particle cluster has broken off

4.4 Role of attractive strength

The presented simulations reveal particle cluster resuspension during the filtration. The resuspension of particle cluster mainly results due to low cohesion strength. The cohesion strength significantly depends on the chosen distance of closest approach. In the presented simulations, a value of $0.4\,\mathrm{nm}$ was chosen, which is a typical value found in literature [Dahn1972; Viss1995]. Israeliachvilli and van Oss suggest values of around $0.16\,\mathrm{nm}$ for macroscopic bodies in aqueous media [Van 2006; Isra2011]. A smaller value for the distance of closest approach decisively strengthen the attrac-

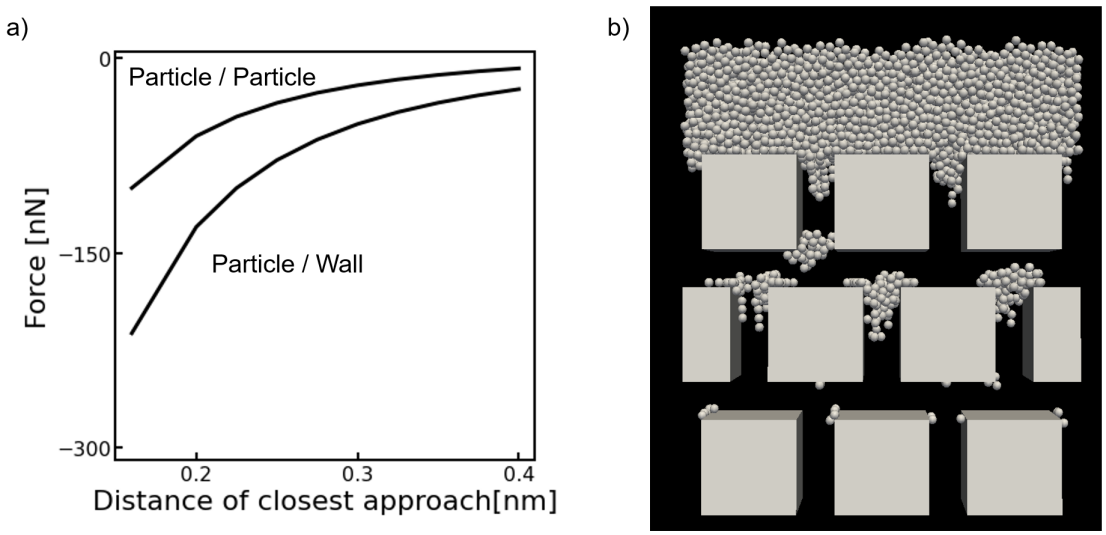

Figure 4.12: a) Dependency between the distance of closest approach and the cohesion and adhesion strength. b) Simulations of the staggered geometry at $0.1s$ when choosing the distance of closest approach to be $0.16\,\mathrm{nm}$. The particles form a stable filter cake due to the high attractive cohesion and adhesion strength.

tive DLVO interactions in the primary minimum as shown in Figure 4.12 a). If the distance of closest approach is chosen to be $0.16\,\mathrm{nm}$, the attractive force is by a magnitude higher than at $0.4\,\mathrm{nm}$.

A simulation in the staggered geometry was performed, in which the distance of closest approach is chosen to be $0.16\,\mathrm{nm}$. The simulation result is displayed in Figure 4.12 b). The simulation revealed that particles built a deposition layer on the upstream part of the pore structure. Particle resuspension did not occur due to the strong attractive interactions. In contrast to the results with lower attractive interaction shown in Figure 4.6, the particles build up a stable deposition layer over the whole geometry. The significant differences between the simulations highlight the strong dependency regarding the distance of closest approach. In addition to the distance of closest approach, the surface topology and surface charge heterogeneity play a crucial role in the attractive interactions making quantitative statements about the actual adhesion and cohesion strength difficult.

4.5 Impact of lubrication and acid-base interactions

This study uses the DLVO potential to describe the interactions between particle and membrane. However, the DLVO potential inadequately describes hydrophilic and hydrophobic interactions [Van 2006; Isra2011]. Non DLVO interactions such as the Lewis acid-base potential provide a more accurate determination of the interaction potential. Furthermore, lubrication interactions can significantly impact the adsorption kinetics [Isra2011]. This section discusses the role of lubrication and acid-base interactions.

Role of lubrication interactions

When two bodies are immersed in a liquid approach, the liquid between the surfaces is squeezed out, referred to as lubrication interaction. The following equation approximates the resulting lubrication force acting between the two surfaces [Lisi2016]:

$$F = \frac{6\pi\eta v_{rel}}{D}\left(\frac{a_1 a_2}{a_1 + a_2}\right)^2 \tag{4.7}$$

as explained in Section 2.4. Lubrication increases with decreasing separation distance similar to surface potentials such as Van der Waals interactions. Contrary to the surface potentials, which only depend on the separation distance, the lubrication interaction scale with the relative velocity. Lubrication decelerates the relative movement between the surfaces. In case two surfaces have sufficient time for the adsorption process, the lubrication force does not prevent the adsorption. However, if the surfaces have only a limited time to adsorb, lubrication can prevent the adsorption process. During filtration, the adsorption time is crucial since particles passing the pore structure in a finite time range.

Figure 4.13 illustrates the lubrication force per velocity over the distance. At relative velocities above approximately $0.1\,\mathrm{mm\,s^{-1}}$, the lubrication force

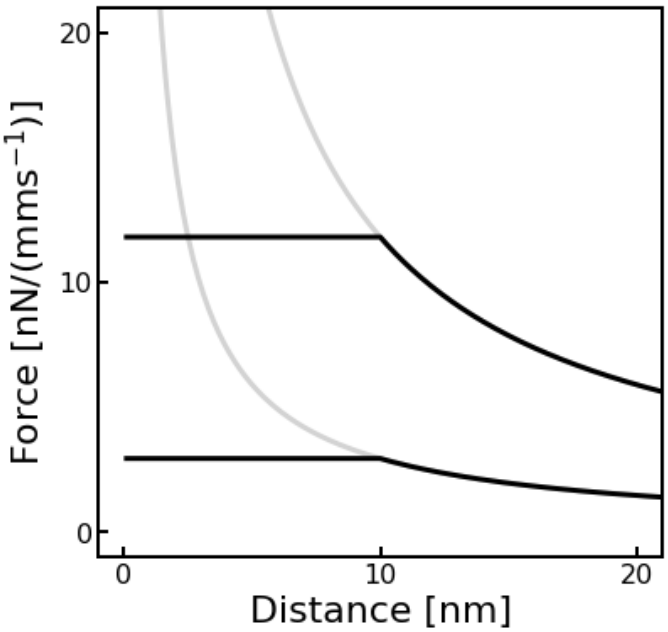

Figure 4.13: Velocity-normalized lubrication force over separation distance in water at $20\,°C$. The cut-off distance of the lubrication force is chosen to be $10nm$, which is indicated by the black line.

drastically exceeds the DLVO forces. In the simulations, velocities reach values above $30\,mm\,s^{-1}$. Therefore, the lubrication force can exceed the DLVO forces and the drag force by over 3 magnitudes. As a result, the particles drastically decelerate when approaching. It is important to note that when the particles decelerate to a velocity lower than $0.01\,mm\,s^{-1}$, the DLVO forces can dominate over the lubrication interactions. The drastic deceleration due to lubrication requires to reduce of the DEM - time step of the simulation. Otherwise, the simulation will not converge due to self-amplifying oscillations. Since the simulations already lasted more than a week, it is not yet possible to resolve lubrication forces smaller than $10\,nm$ in an acceptable simulation time in these relatively large geometries. Therefore, the lubrication force is chosen to be constant at separation distances below $10\,nm$ and a DEM time step of $1\,ns$.

Simulations in the staggered geometry were performed, including lubrication interactions and the presented DLVO potential. Figure 4.14 illustrates the filtration after $0.2\,s$. Clogging does not occur. Particles only accumulate on the flow averted side. The accumulation of particles can be

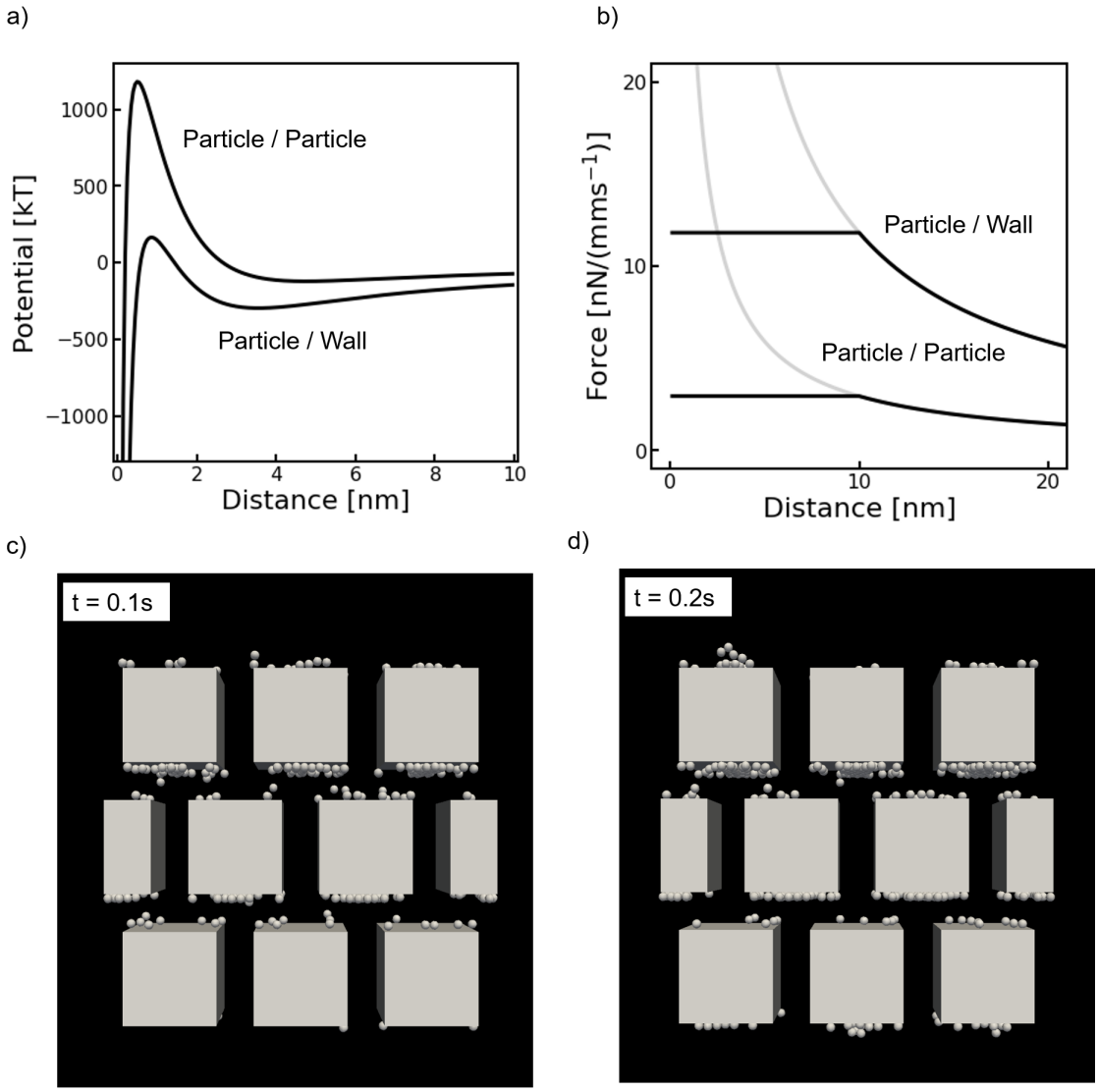

Figure 4.14: a) Calculated DLVO potential and force of PS-PDMS system at $100mM$ ionic strength and b) the lubrication interactions. c),d) Simulations of the staggered geometry at $0.1s$ and $0.2s$, when considering lubrication and DLVO interactions. The simulations reveal no particle adsorption to the surface. Deposition is only observed on the downstream part of the geometry due to particle gliding in the secondary minimum.

explained by gliding effects in the secondary minimum, as highlighted before in 4.10. These particles were unable to overcome the energy barrier but rather remain in the secondary minimum. Therefore, lubrication prevents particles from passing the repulsive energy barrier.

However, the interaction energies are calculated based on smooth surfaces. The interaction energy of rough surfaces can be a significant smaller based on calculations of Hoek and Elimelech [Hoek2003; Hoek2006]. For simplicity, the interaction energy and force are reduced by a magnitude resulting in a reduced energy barrier as well as lower cohesive and adhesive forces. Figure 4.15 shows the resulting DLVO interaction energy.

A simulation in the staggered geometry was performed containing lubrication forces and the reduced DLVO interactions. The simulation results are displayed in Figure 4.15. The particles overcame the reduced energy barrier of the particle-wall and the particle-particle interactions. First, particles deposited on and inside the geometry. The reduced cohesive interactions result in continuous breakage of particle agglomerates as previously highlighted in Figure 4.11. The agglomerates partly re-attached in the inner structure of the geometry causing the clogging of individual channels. Subsequently, parts of the geometry are completely clogged. In contrast to the simulations with high cohesive strength shown in Figure 4.12, an individual channel remains open due to continuous particle resuspension.

The results highlight that it is essential to include lubrication interactions in the simulations since lubrication can either prevent or reduce the probability of particles passing the energy barrier.

Role of acid-base interactions

Besides lubrication, the previously presented simulations do not consider non-DLVO forces. Since both the particles and the PDMS surface are hydrophobic, an attractive hydrophobic force acts between the two. The hydrophobic interaction can be quantified based on the theory of Good, Chaudhary, and van Oss with Lewis acid-base interactions, as explained in Section 2.3.3. The theory determines the acid-base interactions by sur-

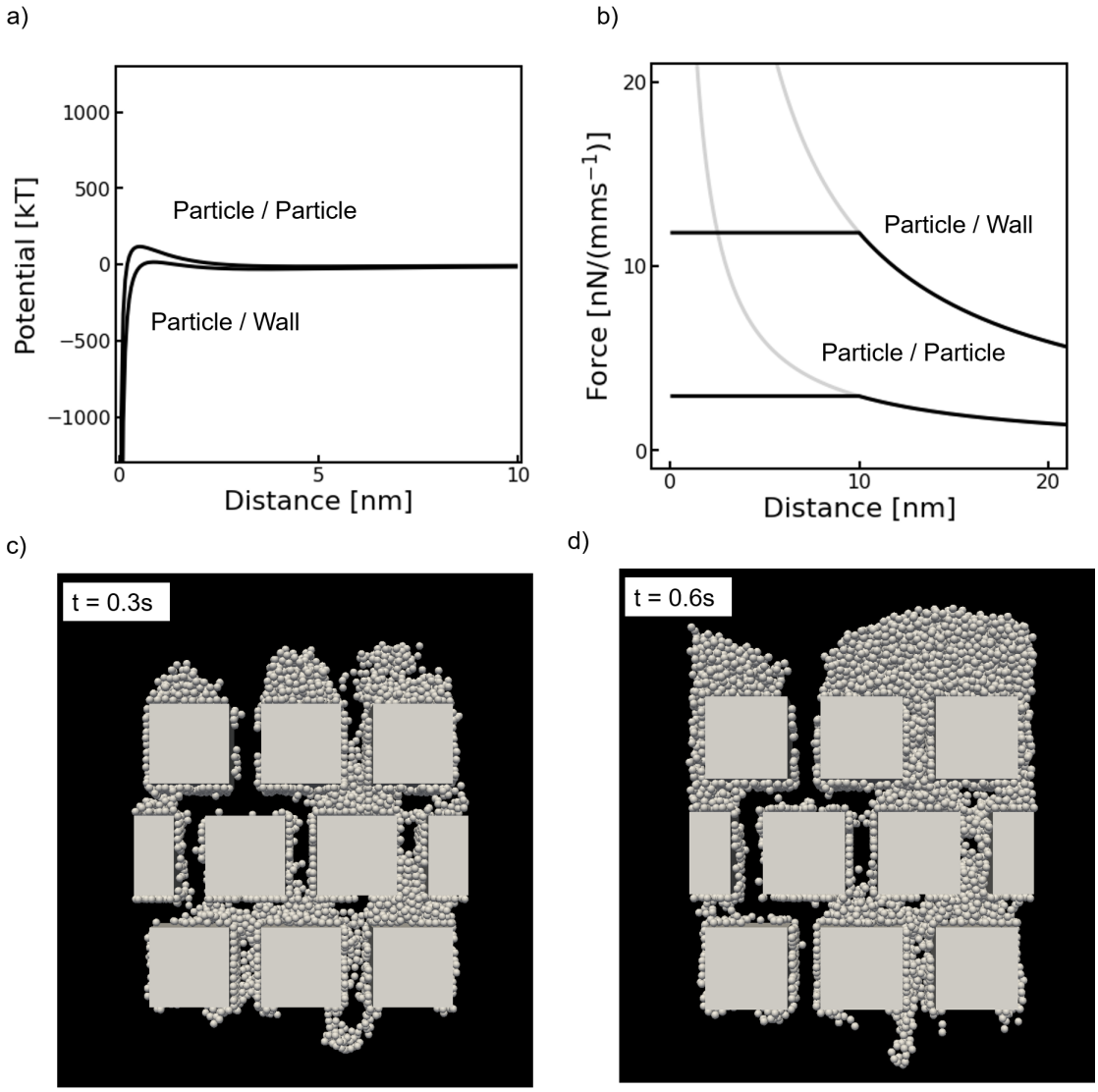

Figure 4.15: a) Calculated DLVO potential and force of PS-PDMS system at $100mM$ ionic strength reduced by a magnitude and b) the lubrication interactions. c),d) Simulations of the staggered geometry at $0.1s$ and $0.2s$, when considering lubrication and DLVO interactions. The simulations reveal no particle adsorption to the surface. Deposition is only observed on the downstream part of the geometry due to particle gliding in the secondary minimum.

face tension properties of the material system. The values of the surface tension of PDMS can be taken from the literature (e.g., [Must2016]). The surface tension of charge-stabilized polystyrene particles strongly depends on the surface stabilizing group's nature and the amount of the surface stabilizing group. Therefore the surface tension properties can vary for each particle. Due to a lack of data, the surface tension properties for the sulfate latex particles are approximated. The surface tension component γ^- of the particles (see Equation 2.14) was chosen that the particle-particle energy barrier vanishes at a salt concentration $200mM$, which is the critical coagulation concentration of the particles [Bacc2014a]. Therefore, γ^- is chosen to be $25\,\mathrm{mJ\,m^{-2}}$. The additional parameters are chosen to be the same as presented in Table 5.1 of the following chapter 5. The resulting force and potential profiles are shown in Figure 4.16 a),b). In the case of the particle-wall interactions, the energy barrier completely vanishes due to the PDMS's strong hydrophobic nature. Furthermore, the primary minimum of the interactions is deeper, resulting in higher cohesive and adhesive strength.

The cut-off distance for the lubrication interaction is again assumed to be $10\ nm$ to reduce the computational time. Figure 4.16 shows the clogging in the staggered geometry after 0.1 and $0.2\,\mathrm{s}$, when accounting acid-base and lubrication interactions. Particles accumulate first on the surface due to the attractive interactions with the PDMS. First, particles deposit at the pore entrance due to the hydrodynamic transport, which is in agreement with experimental observations (see e.g., Figure 4.9) [Must2010; Ders2015; Send2016a; Kim2017]. Due to the narrowing of the adhered particles' flow channel, particles accumulate above the pore entrances. These particles can overcome the energy barrier of the particle-particle interactions leading to strong cohesive clog formation. The clog formation is stable, and particle resuspension does not occur, which leads to filter cake formation. Furthermore, the clogging is focused on the upstream part of the geometry. However, as e.g. shown later in Figure 4.11, it is demonstrated that particle resuspension can play a vital role during the filtration of sulfate latex particles, which are not resembled with the presented xDLVO potential. The overestimation of the xDLVO interaction could again be a result

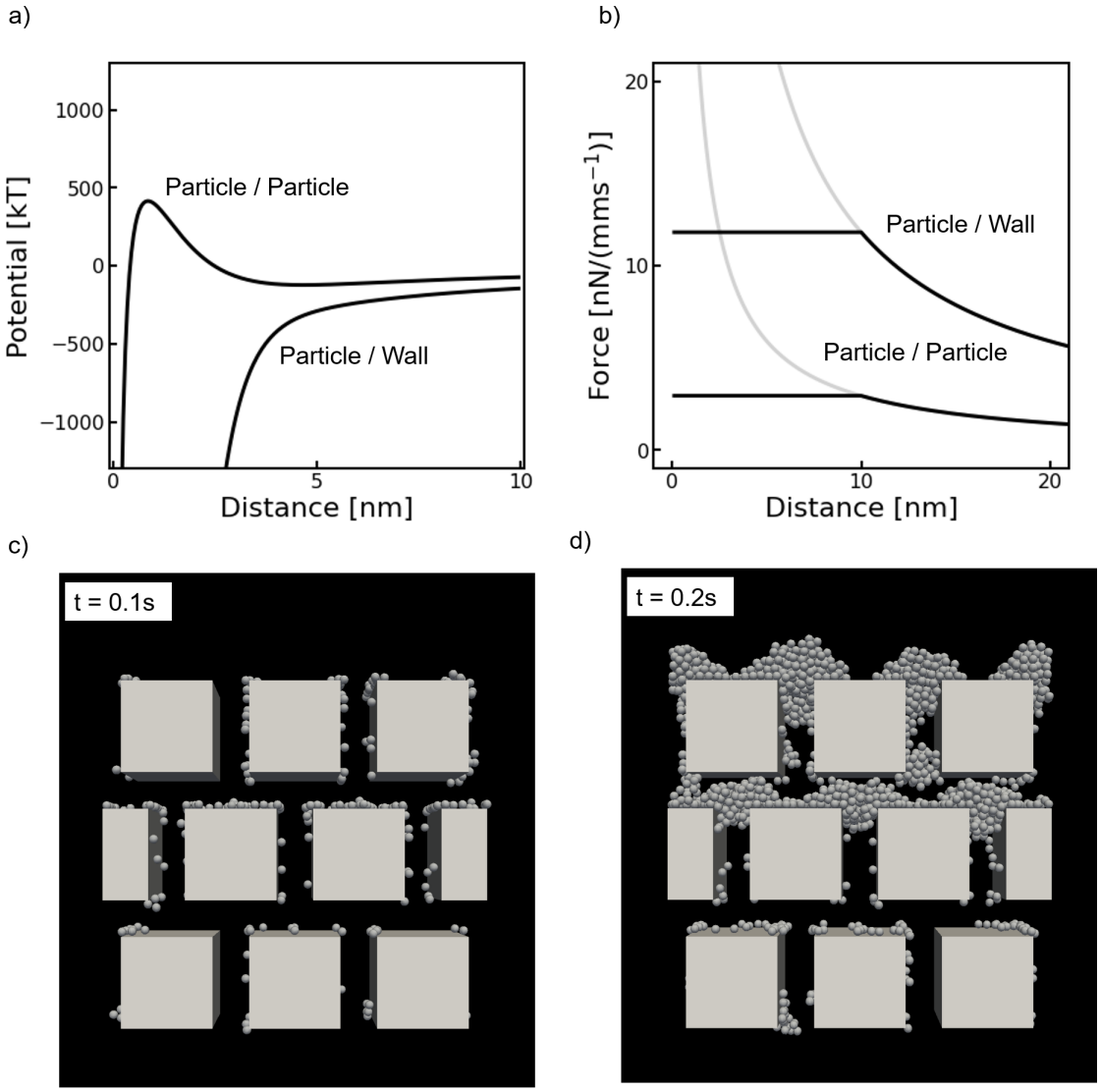

Figure 4.16: a) Calculated xDLVO potential and force of PS-PDMS system at $100mM$ ionic strength and b) the lubrication interactions. c),d) Simulations inside the staggered geometry at $0.1s$ and $0.2s$, when considering lubrication and xDLVO interactions. The simulations reveal particle adsorption on the pore entrance followed by cake formation.

due to the assumption of a smooth surface. Similarly, viscous lubrication should reduce in quantity for short distances due to roughness. Contrary, the viscous drag force resulting from the fluid flow on micrometer-sized colloids is only minorly affected by surface topology. Thus, the role of colloidal interactions and viscous lubrication is overestimated compared to viscous drag. Therefore, future work should address the influence of surface charge distribution and surface roughness on the deposition and resuspension of colloids. While a more detailed description of the interaction potential can be patiently answered with simulations, the experimental support needs to be developed as well. Hence, the reported finding can only be considered another contribution to colloidal membrane fouling puzzles and requires further experimental proof.

4.6 Conclusion

We carried out numerical simulations of a fouling process in a microfluidic membrane mimic using an CFD-DEM approach. The simulation results show good agreement with the experimental work of Bacchin et al. [Bacc2014b] and we discuss the improvements compared to their simulation. The presented method identifies important microscopic events of the clogging process and compares them to experimental findings. Interparticle interactions can have a strong effect on the clogging dynamics. Adsorbed particles can resuspend from the inner membrane surface or they can glide downstream. The inner structure of the porous membrane can significantly affect the clogging process. In particular the resuspension of particle clusters and their reattaching to the inner surface can lead to a complete blockage of the flow channel. Besides the clogging process, cluster resuspension is the main driver of membrane cleaning during backwash as discussed in detail in the next chapter.

The methodology presented allows to quantify the transition process of particles from the secondary to primary minimum adsorption during filtration. The latter is almost undetectable in an experimental study as it would require of a nanometer spatial resolution and a very high temporal resolu-

tion.

The methodology now enables to perform systematic studies comparing experiments and simulations leading to a more comprehensive understanding of the deposition phenomena in micron and sub-micron sized porous filtration media. It encourages and directs experimentalist and simulation scientist to further join forces and unravel the intricacies of colloidal deposition in porous media such as synthetic porous membranes.

5 What are the microscopic events during membrane backwashing?

Parts of this chapter have been published as:
Johannes Lohaus, Felix Stockmeier, Philipp Surray, Jonas Lölsberg, Matthias Wessling
What are the microscopic events during membrane backwashing?, Journal, 2020
https://doi.org/10.1016/j.memsci.2020.117886
The experiments were conducted and presented in the master thesis of Philipp Surray:
P. Surray “Determine colloidal detachment by combining microfluidic experiments with CFD-DEM modeling [Master thesis]”. RWTH university(2018).

5.1 Introduction

Resuspension of colloidal particles is a widely spread and relevant phenomenon in various engineering processes such as particle filtration, enzyme fixation, and migration of surface contaminants. For membrane filtration research, resuspension events encompass all microscopic detachment events of colloidal particles during the backwash process from the filter deposit as well as from the membrane surface. The backwash is usually investigated on a macroscopic level. Contemporary engineering research activities address (a) to increase the efficiency of particle removal, (b) to optimize process parameters, or (c) to develop new concepts of backwash processes for decentralized water treatment [Xu1995; Ma2000; Ven2008; Mart2018; Aume2018]. However, the underlying microscopic mechanism controlling the removal of deposited particles can only be insufficiently deducted from the macroscopic analysis.

In literature, three microscopic key mechanisms for spherical particle resuspension were so far identified: lifting, sliding, or rolling. The dominant mechanism of single-particle detachment is rolling rather than sliding or lifting [Tsai1991; Shar1992; Berg1999b]. Based on this knowledge, theories to describe resuspension of single colloidal particles were developed [Berg1999b; Berg1999a; Berg2003]. However, theories of single-particle resuspension insufficiently describe the flushing of a clogged pore because these neglect particle-particle interactions and cluster effects.

Below, microfluidic experiments are applied to understand the dominant mechanism of the flushing of a clogged pore. Microfluidic experiments are particularly suited to visualize local clogging phenomena on a pore-scale level. Extensive insights into clogging dynamics and cake filtration were gained by microfluidic experiments over the past years [Wyss2006; Ngen2010; Bacc2011; Bacc2014b; Ders2015; Link2016; Ders2019]. Several of these authors mention the breakage of clusters during their filtration experiments. However, they do not rigorously investigate this resuspension phenomenon.

Detachment events during backwash happen rapidly [Zisk2006], and

even though they were recorded, statistically relevant conclusions can hardly be drawn. This missing fundamental understanding can be closed by putting face-to-face microfluidic experiments and multiphase simulations, which allow access to short time scales and a high spatial resolution. Several numerical studies deal with the clogging and jamming dynamics of colloidal particles [Wess2001; Ando2012a; Agba2014b; Bacc2014b; Mars2015; Mond2016; Must2016; Mino2018]. Some of these studies treat adhered particles as fixed whereby resuspension is suppressed [Bacc2014b; Agba2014b]. The previous chapter showed that particle resuspension can play a crucial role in the clogging process. Ando et al. [Ando2012a] performed simulations incorporating particle resuspension, which investigate the flushing of a pore structure during a backwash cycle. During their simulations, some particles remain on the pore structure after the backwash cycle, which served as clogging initiators in the subsequent filtration cycle. However, the work of Ando et al. [Ando2012a] does not provide experimental data of the flushing on a pore-scale level.

This work investigates microscopic events of the membrane backwash of a clogged pore. The study is unique as microfluidic experiments are combined with numerical simulations to visualize and describe the collective particle dynamics during backwash.

5.2 Materials & Experimental Methods

Microfluidic chips for fouling experiments are prepared in a two-step process [Löls2018; Löls2019]. First, a negative structure of the channel is 3D printed with a Photonic Professional GT system (Nanoscribe GmbH) on microscopy slides by two-photon lithography [Maru1997]. This master cures for about six hours in an oven at $60\,^{\circ}\mathrm{C}$. Then, the slide with the master is glued on a Petri dish using two-component glue. A 10:1 (w/w) PDMS-Hardener mixture (Sylgard 184 Silicone Elastomer Kit, Dow Corning GmbH) is poured over the master. The result is evacuated and later cured at $70\,^{\circ}\mathrm{C}$ for 4 hours. After curing, the PDMS structure is cut out, and holes for tubing are punched. The cast is cleaned by sonication in Iso-

propanol for five minutes and dried for twelve hours. The clean structure is then plasma bonded to a microscope slide (TePla 100 Plasma System, PVA Metrology & Plasma Solutions GmbH). Afterward, tubing is connected and sealed with glue (Max Repair Extreme, UHU GmbH & Co KG).

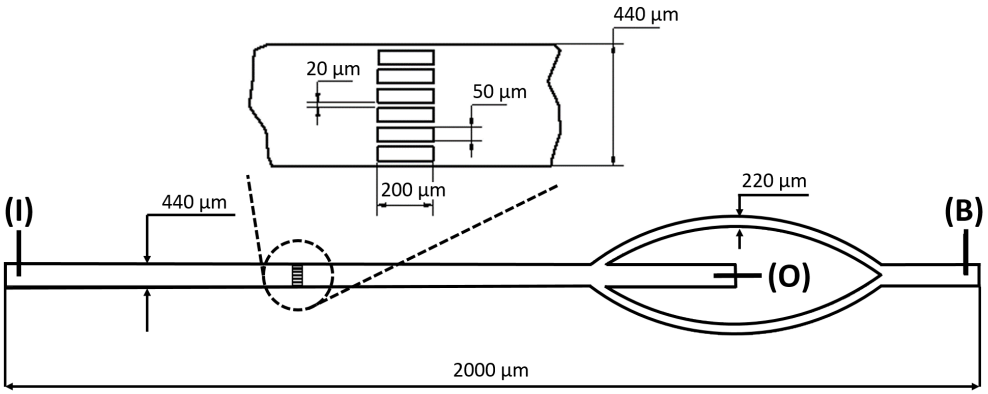

Figure 5.1: Experimental set-up

Filtration experiments are conducted in a chip containing a pore structure, see Figure 5.1. This pore structure consisting of seven pores is the essential element of the chip. Each pore has a width of 20 $\bar{}\mathrm{m}$, a length of 200 $\bar{}\mathrm{m}$, and a depth of 50 $\bar{}\mathrm{m}$. The pores are 50 $\bar{}\mathrm{m}$ apart from each other. The pore geometry of the chip is similar to the one used by Bacchin et al. [Bacc2014b].

Filtration suspensions are prepared by diluting a suspension of monodisperse polystyrene particles (4.2 $\bar{}\mathrm{m}$, solid content 5 %(w/v), BS Partikel GmbH) with the respective KCl solution to a solid content of 0.1 w%.

For the experiments, syringes are connected to the outlet (O) and backwash (B) ports. The inlet (I) ends in a beaker. The chip is submerged in water to prevent the diffusion of air into the chip.

The first step of each experiment is deaerating the channel. Therefore, the system is flushed with the KCl solution. Afterward, the particle suspension is filtered through the channels. The filtration velocity of $4.5\,\mathrm{mm\,s^{-1}}$ is adopted from the experiments of Bacchin et al. [Bacc2014a], which is close to the ones used in a microfiltration process [Bacc2014a; Send2016a] The

Reynolds number is 0.4. Time measurement for the filtration experiment starts when the first particles reach the pores. During filtration, particles deposit on the microstructure leading to clogging of the pores. Due to the limitation of 2D observation, the deposited layer needs to be rather small to be able to still optically visualize phenomena occurring inside on the pore structure during backwash. Otherwise, if there is a fully developed filter cake, the observation of pore scale phenomena can be overshadowed by particles attached to the bottom or top side of the channel. Therefore, after the pore structure shows some clogging, the pump at the outlet port (O) is turned off, and the pump at the backwash port (B) is set to infuse mode with $0.1\,\mu L\,s^{-1}$. During backwash, the volume flow is increased step-wise from $0.1\,\mu L\,s^{-1}$ up to a maximum of $10\,\mu L\,s^{-1}$, which corresponds to an empty channel velocity of $4.5\,mm\,s^{-1}$ up to $450\,mm\,s^{-1}$ ($Re = 0.41 - 41$). Each step is held for a maximum of five minutes. The range of flow rates was selected, starting from the filtration flow rate to a flow rate at which the chip is still operational. Thus, the effect of a wide range of applied drag forces is monitored. Each backwash step is timed separately. Here, timing begins when the volume flow is increased.

5.3 Simulation methodology

5.3.1 Extended DLVO potential & lubrication

The deposition of colloids on a surface results from the interplay of hydrodynamic and colloidal interactions. While hydrodynamic forces transport colloids to the surface, colloidal interactions can lead to adsorption of particles and particle cluster formation. These interactions are classically described by the Derjaguin-Landau-Verwey-Overbeek (DLVO) theory [Isra2011]. The DLVO theory considers two types of interactions: the Van der Waals interactions and the electrostatic double-layer interactions. However, the DLVO theory often fails to describe the colloidal potentials in polar solutions such as in water [Oss2006]. This is often attributed to non-DLVO Lewis acid-base interactions. The combination of DLVO theory and the acid-base interaction

potentials is often referred to as extend DLVO (xDLVO) [Oss2006]. Besides the colloidal potentials, lubrication effects can have a major impact on the deposition rate. The simulations consider the xDLVO theory and lubrication effects. Effects of Brownian motion are neglected since the Peclet number is $1e5$ up to $1e7$ depending on the backwash velocity.

This section gives a brief overview of the potentials used in the simulation and its mathematical description. Detailed information can be found in Section 2.3 and in literature [Isra2011; Oss2006; Elim2013]

Van der Waals interactions: The van der Waals interaction energy $W_{\mathrm{VDW}}(D)$ determined between two macroscopic spheres (S) with radii a is approximated by the following equation [Isra2011]:

$$W_{\mathrm{VDW}}(D) = -\frac{Aa}{12D} \tag{5.1}$$

where A and D define the Hamaker constant and the separation distance, respectively.

Double layer interactions: The double layer potential between two equal spheres is determined by the linear superposition approximation [Elim2013]

$$W_{\mathrm{DL}}(D) = 4\pi\varepsilon_0\varepsilon a \left(\frac{kT}{e}\right)^2 Y_{\mathrm{S}}^2 \exp(-\kappa D) \tag{5.2}$$

where ε_0 denotes the vacuum permittivity, e the elementary charge, κ the inverse Debye length, and ε refers to the dielectric constant of the electrolyte solution. Y_{S} is the effective surface potentials of the sphere.

The Debye length κ^{-1} is a measure of the range of the diffusive layer and can be expressed for a 1:1 electrolyte such as a sodium chloride solution as [Isra2011]

$$\kappa^{-1} = \left(\frac{\varepsilon_0\varepsilon kT}{2e^2 N_{\mathrm{A}} c}\right)^{1/2}, \tag{5.3}$$

where N_A is the Avogadro constant.

Acid-base interactions:

The solvation potential is described by Lewis acid-base theory based on the work of van Oss [Oss2006]:

$$W_{\mathsf{AB}}(D) = \pi a \lambda \Delta G_{\mathsf{AB}}^{131} \exp\left(\frac{D_0 - D}{\lambda}\right) \tag{5.4}$$

D_0 is the distance of closest approach. $\Delta G_{\mathsf{AB}}^{131}$ represents the Gibbs energy of interaction of the acid-base interaction. It is characteristic of the strength of the interactions and its repulsive or attractive nature. $\Delta G_{\mathsf{AB}}^{131}$ is determined with the surface tension parameters of the solid as well as the solution according to [Oss2006]. The decay length λ characterizes the reach of the acid-base interactions. Usually, values for the decay length λ of $0.6 - 1.1\ \mathrm{nm}$ can be found in literature [Oss2006].

The applied particle-particle and the particle-wall potential in the simulation is shown in Figure 5.2. Both potentials are purely attractive. The attractive nature arises due to the high ionic strength $(100\ mM)$ and the hydrophobic nature of the materials PDMS and charge-stabalized polystyrene, which are used in the experiments. The forces that have to be overcome to break a particle-particle and a particle-wall contact are $4.0\mathrm{e}-7\,\mathrm{N}$ and $8.2\mathrm{e}-7\,\mathrm{N}$, respectively. When applying stokes law, this corresponds to a necessary drag velocity to break the contact of 10 or $20\,\mathrm{m\,s^{-1}}$.

Lubrication effect: When two particles approach each other, the solvent between the particles is displaced. A part of the particle's potential energy dissipates to displace the solvent. This lubrication effect can be approximated for macroscopic bodies by the following equation [Cox1967; Ladd2001]:

$$F_{\mathsf{Lub}}^{\mathsf{SS}}(v, D) = 3/2\pi a^2 \eta \frac{\Delta u}{D} \tag{5.5}$$

where η and Δu are the fluid viscosity and the relative velocity, respectively.

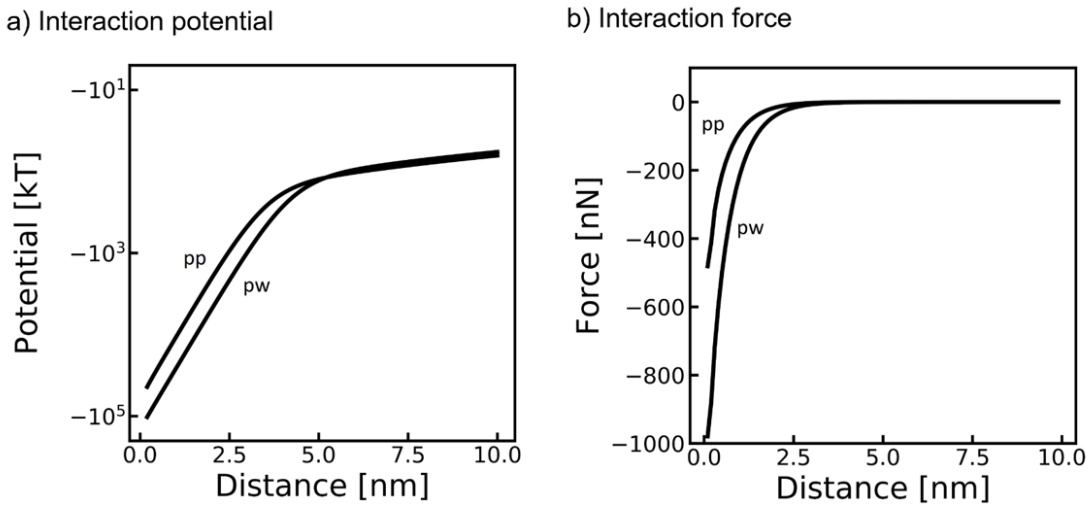

Figure 5.2: The computed xDLVO potential energy profiles and force profiles of particle-particle (pp) and particle-wall (pw) interaction in a 100 mM KCl solution (b).

5.3.2 Simulation conditions

The simulations were performed in a single pore constriction, which is shown in Figure 5.3. In a first step, particles were filtered through the pore until a filter cake developed. Afterward, the flow direction is changed to perform a backwash. During backwash, the velocity is increased in a stepwise manner. Table 5.2 provides the applied velocities at the specific time intervals, and Table 5.1 gives an overview of the simulation parameters used.

The DEM and the CFD simulations are coupled with an unresolved divided volume fraction method [Blai2016]. The particle volume is split into distributed marker points, which apportion the particle's volume to the covered mesh elements [Klos2012]. The divided volume fraction method restricts the mesh size fineness to the particle diameter leading to a coarse structured mesh (5x5x5 µm mesh elements). Therefore, the treatment of hydrodynamics and the fluid-particle interactions is rather qualitative than quantitative. For future research, it is interesting to improve the resolution of the fluid interactions with the more advanced DNS-DEM simulations [Ando2012a; Ishi2013; Agba2014b; Akam2016; Mino2018]. Contrary to

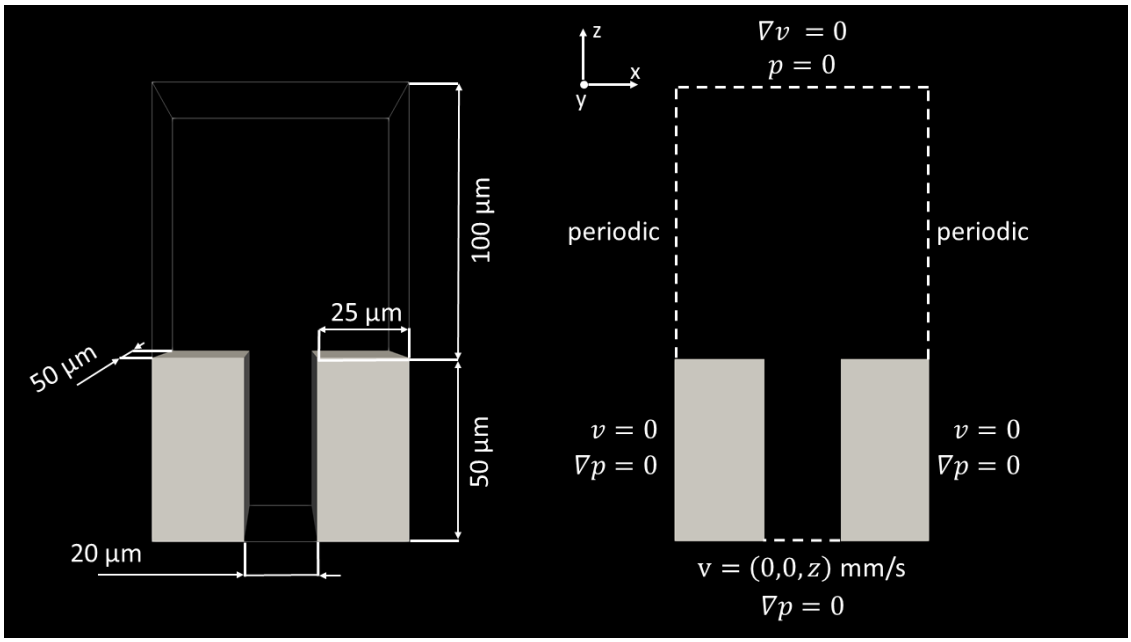

Figure 5.3: Dimension of the pore geometry and the applied boundary conditions in the simulation

the unresolved volume fraction method, these methods resolve the boundary of the fluid-particle interface. They provide a very accurate description of the fluid-particle interaction. However, due to the high computational effort of these methods, the simulations here were performed with the unresolved approach.

In the unresolved CFD-DEM approach, the computational demanding is the particle simulation. Therefore, the choice of the DEM - time-step is crucial to achieve results in a reasonable time. In DEM simulations, $30 - 10\%$ of the Rayleigh time is usually a reasonable estimate of the DEM-time-step [Gu2016]. However, lubrication forces and acid base interactions are considered. These forces become very strong at small separation distance (e.g. more than a magnitude bigger than the van der Waals interactions). To ensure stability and prevent strong oscillations the DEM-timestep has to be chosen relatively small. Lubrication forces depend on the separation distance and on the normal relative velocity between two approaching surfaces, as presented in Equation 5.5. These interactions act as a damper and reduce the relative velocity v between two surfaces. For stable simulations, it has to be assured that the lubrication force only reduces the relative

Parameter	Symbol	Value	Literature
Filtration velocity	v_0	$4.5\ \mathrm{mm\,s^{-1}}$	-
Backwash velocity	v_0	$4.5 - 450\ \mathrm{mm\,s^{-1}}$	-
Particle radius	a	$4.2\ \mu\mathrm{m}$	-
Young modulus particle	E	$3.6 \times 10^9\ \mathrm{Pa}$	[Bhus2008]
Young modulus wall	E	$8.7 \times 10^6\ \mathrm{Pa}$	[Arma1999]
Poisson ratio	$\tilde{\nu}$	0.45	assumed
Coefficient of restitution	e	0.6	assumed
Friction coefficient	μ_f	0.5	assumed
Rolling friction coefficient	μ_r	0.01	assumed
Distance of closed approach	D_{int}	$0.158\ \mathrm{nm}$	[Van 2006]
Particle density	ρ_{P}	$1000\ \mathrm{kg\,m^{-3}}$	-
Salt concentration	c_{KCl}	$0.1\ \mathrm{mol\,L^{-1}}$	-
Zeta potential particle	ζ	$-37\ \mathrm{mV}$	[Must2016]
Zeta potential wall	ζ	$-23\ \mathrm{mV}$	[Must2016]
Hamaker constant particle	A	$1.4 \times 10^{-20}\ \mathrm{J}$	[Isra2011], Eq. 2.3
Hamaker constant wall	A	$0.6 \times 10^{-20}\ \mathrm{J}$	[Isra2011], Eq. 2.3
Surface energy particle	γ^+	$0.57\ \mathrm{mJ\,m^{-2}}$	[Must2016]
Surface energy particle	γ^-	$5.27\ \mathrm{mJ\,m^{-2}}$	[Must2016]
Surface energy wall	γ^+	$0\ \mathrm{mJ\,m^{-2}}$	[Must2016]
Surface energy wall	γ^-	$3.04\ \mathrm{mJ\,m^{-2}}$	[Must2016]
Surface energy water	γ^+	$25.5\ \mathrm{mJ\,m^{-2}}$	[Oss2006]
Surface energy water	γ^-	$25.5\ \mathrm{mJ\,m^{-2}}$	[Oss2006]
Decay length	λ	$0.6\ \mathrm{nm}$	[Oss2006]
DEM-time step	Δt_{DEM}	$1 \times 10^{-10}\ \mathrm{s}$	-
CFD-time step	Δt_{CFD}	$1 \times 10^{-8}\ \mathrm{s}$	-

Table 5.1: Parameters applied in the simulation

velocity rather than changing its sign. If the relative velocity changes its sign due to lubrication, the particles start to oscillate. From this consideration, the DEM time step can be derived based on a Newtonian balance:

$$t_{DEM} < \frac{vm}{F_{Lub}(v, D0)} \tag{5.6}$$

This condition is fulfilled in our simulations for $t_{DEM} < 1.5\mathrm{e}-10\,\mathrm{s}$ when taking the minimal separation distance for lubrication to be $D_0 = 1\,\mathrm{nm}$.

The DEM time-step is chosen to be $1\mathrm{e}-10\,\mathrm{s}$ and the CFD time-step to be 100 times the DEM time-step, which is common practice in CFD-DEM simu-

#	Time ms	Velocity $mm\,s^{-1}$
1	0 - 0.5	0 - 4.5
2	0.5 - 2.5	4.5
3	2.5 - 3	4.5 - 22.5
4	3 - 5	22.5
5	5 - 5.5	22.5 - 45
6	5.5 - 7.5	45
7	7.5 - 8	45 - 90
8	8 - 10	90
9	10 - 10.5	90 - 225
10	10.5 - 12.5	225
11	12.5 - 13	225 - 450
12	13 - 15	450

Table 5.2: The velocity stepping during backwash simulations

lations. The Courant-Friedrichs-Lewy condition is always fulfilled ($C << 1$), ensuring CFD convergence. The simulation times were up to two weeks on four cores on an Intel Xeon E5-2630 v3 processor.

5.4 Results & Discussion

Microfluidic experiments were conducted to record the detachment of particles and agglomerates during backwash.These detachment events occur during a few microseconds. Numerical simulations were performed to gain insight into these detachment events. Following, we compare the results of the experiments and the simulations and discuss the mechanisms occurring during colloidal detachment.

5.4.1 Microfluidic filtration

A filtration and a backwash step were conducted in each microfluidic experiment. First, polystyrene particles were filtered through the micro-channels with a constant filtration velocity of $4.5\,mm\,s^{-1}$, which corresponds to a flow rate of $0.1\,\mu L\,s^{-1}$. The particles deposit on the membrane mimicking a structure, as shown in Figure 5.4. Initially, particles mainly deposit on the

upstream edges of the constrictions (Image A). Further, a small amount of particles deposit in the inner structure of the pore. Afterward, particle clusters form on the sides, spanning bridges over the channels (Image B). Subsequently, newly arriving particles build up a filter cake (Image C). The filtration is stopped before a large filter cake is formed, which makes observation of resuspension events more difficult. The backwash process is then initiated.

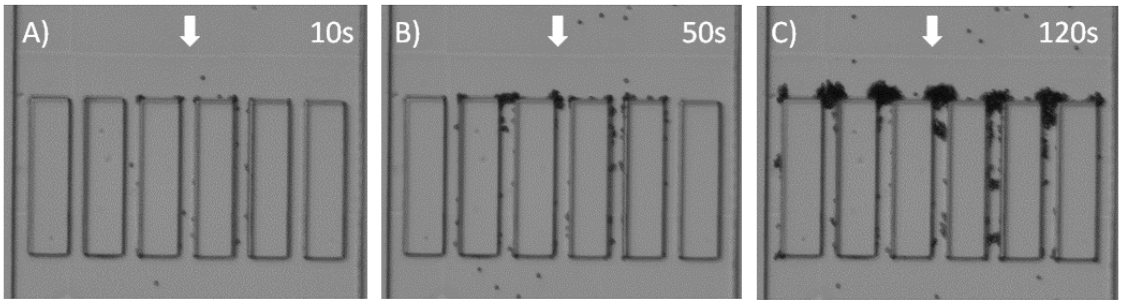

Figure 5.4: Microfluidic clogging of polystyrene particles during filtration in a 100mM KCl solution

Similar microfluidic filtration experiments were performed by the research groups of Bacchin and Tabuteau [Agba2012; Bacc2014b; Ders2015]. The microfluidic design presented here is based on the experiments of Bacchin [Bacc2014b]. However, differences between both experiments are observed. Under similar conditions, the particles here deposit faster compared to Bacchin's study. Further, the particles in Bacchin's study form dendritic structures at the upstream side. Contrary, the particles here build particle bridges leading to a faster complete clogging of the structure. The

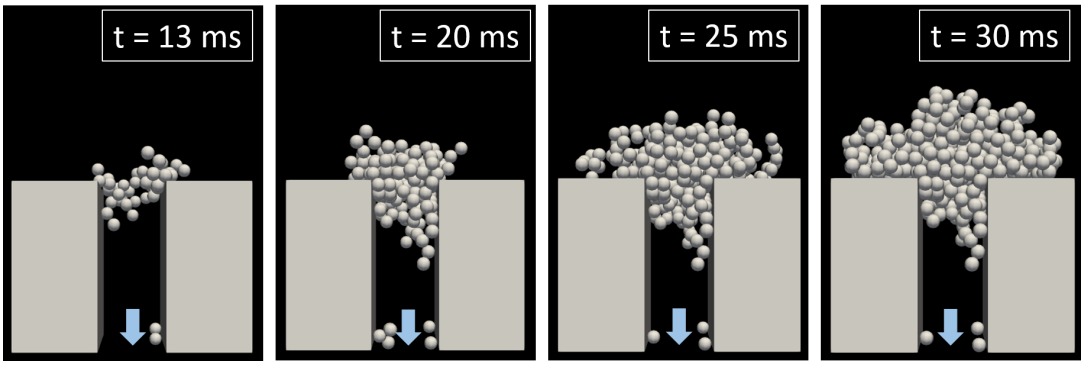

Figure 5.5: Numerical results of pore clogging over time

faster deposition and the bridge formation indicated that the interaction potential of the particles used here is more attractive as compared to the system of Bacchin. This can be explained by the surface active group used. Bacchin uses polystyrene sulface, which have a critical coagulation concentration of 200 - 300 mM, whereas the particles used here show a lower stability, which fits to the range of the calculated xDLVO potential. One have to keep in mind that the critical coagulation concentration can naturally vary depending on the production process. Strictly speaking, the critical coagulation concentration has to be determined for the respective particles used. However, in this study the critical coagulation concentration fits with the experimental observation.

5.4.2 Filtration simulation

Numerical simulations of the filtration were performed to detect microscopic events of the particle resuspension and identify the conditions under which these occur. The numerical filtration simulation was performed in a single pore with $4.2\,\mu m$-sized polystyrene particles. A number of particles periodically enter the simulation domain to sustain a solid feed concentration of 5%. The chosen concentration is 50 times higher than in the experiments, which significantly reduces the computational effort. Figure 5.5 shows the clogging process over time in the simulations. Initially, particles deposit on the edges of the constriction. Subsequently, the particles form a bridge, which leads to a complete blockage of the pore. Finally, a filter cake grows.

5.4.3 Comparison between simulation and experiments - Filtration

Some constraints have to be taken into account to compare the experimental and numerical results. The microfluidic device includes a pore structure with seven pores, whereas in the simulation, only one pore is considered due to the computational effort. Since the clogging formation is unevenly distributed in the pore structure of the experimental system, the

flow velocity will be unequal in each pore. This affects clogging as well as backwash and prevents an exact quantitative comparison between experiment and simulation. Further, the simulations assume that the particles and the pore surface are entirely homogeneous. However, charge modified polystyrene particles can possess an uneven distribution of surface charge groups [Tan2005]. An uneven charge distribution may affect the strength of the colloidal interactions. The effect of an uneven charge distribution may stochastically be accounted for in a future study [Must2016]. Besides the charge distribution, the surface topology of the particles and the PDMS structure can be rough instead of being perfectly smooth, as assumed in the simulations. However, charge modified polystyrene particles can possess surface heterogeneities such as surface roughness and an uneven distribution of surface charge groups [Tan2005]. These heterogeneities are considered to influence particle deposition and detachment decisively [Hoek2003; Hoek2006]. Furthermore, parameters of the colloidal interactions adopted from the literature, although been qualitatively identical, can sometimes differ quantitatively between sources, which is discussed in more detail by [Must2016]. On the one hand, the inconsistency between sources may result from different measuring methods or measuring accuracy, but on the other hand it may also be due to differences in the surface composition. For example, the polystyrene particles used here may differ in surface charge density and surface active groups between literature data, which can lead to deviations in the double layer potential and in the acid-base potential. Besides the mentioned constraints, semi-quantitative and qualitative observations can still be compared.

In the simulations and in the experiments, particles form bridges during the filtration step. The majority of particles deposit at the entrance of the constriction leading to a fast clogging. The clogging is three orders of magnitudes slower in the experiments compared to the simulations. Since the feed concentration in the simulation is 50 times higher compared to the experiments (experiment 0.1%; simulation 5%), the clogging time can be normalized to the number of filtered particles for a more meaningful comparison [Wyss2006]. There remains a difference between simulation and

experiment in the order of 1-2 magnitudes when regarding the number of filtered particles. The difference between experiment and simulation can originate from the higher particle concentration used in the simulations. In the experiments, the particles mainly enter the pore one by one. Whereas, due to the higher volume concentration in the simulations, particles aggregate near the constriction increasing the deposition probability. The increase in clogging probability with the volume fraction of particles was experimentally demonstrated by [Agba2012]. Further, pore clogging leads to an uneven flow distribution between the seven pores, which results in particles increasingly passing through pores with no or minor deposition. A single pore setup as used in the simulations can not reflect this effect.

In general, the resulting clog formation shows qualitative similarities between experiment and simulation. This is promising to compare the results of the following backwash cycle.

5.4.4 Microfluidic backwash

The backwash step was conducted after pore-clogging occurred. The backwash solutions contained no particles and had the same KCl concentration as the corresponding suspensions during filtration. The volume flow during backwash was increased step-wise from $0.1\,\mu L\,s^{-1}$ up to $10\,\mu L\,s^{-1}$.

Figure 5.6 displays the particle deposition before and after the backwash. The bridges broke during the backwash. Furthermore, particles in the inner structure are entirely removed. However, there are still particle agglomerates deposited on the pore structure. These are almost entirely located in regions of the lowest shear at the upstream side of the filtration.

A more detailed interpretation of the backwash process is achieved by a grey-scale analysis of the microscopic images taken during the backwash process. In the grey-scale analysis, the images taken during the backwash experiments were converted into monochrome images and then inverted. The resulting images mainly highlight the deposited particles, as shown in Figure 5.6. The number of pixels containing deposited particles before and after backwash is compared, resulting in the relative reduction of the partic-

ulate phase. Thereby, the accumulated reduction of the deposited particles can be calculated and plotted over the volume flow rate, as demonstrated in Figure 5.6. It should be noted that the evaluated backwash efficiency results from 2D images. Therefore, experimentally evaluated backwash efficiency only represents an estimate of the actual backwash efficiency. At a backwash flow rate of $0.1\,\mu L\,s^{-1}$, weakly bound or unbound particles were flushed out. Afterward, at volume flow rates of 1 to $2\,\mu L\,s^{-1}$, the particle resuspension increases sharply. These jump-like sharp increases in particulate removal can also be detected at higher flow rates and originate from the breakage of particle cluster. Figure 5.6 shows that these jump-like sharp increases in particulate removal most dominant control the backwash-efficiency. This suggests that the breakage of clusters is the decisive mechanism of fouling removal during backwash. suggests that the breakage of clusters is the decisive mechanism of fouling removal during backwash. In contrast to the complete resuspension of a cluster, some particle bridges only partially break. The bridge unfolds and the cluster fixed on one edge moves into the region of lower drag. The cluster located in the region of low drag remains stable on the pore structure during the backwash process.

Summarizing, three types of backwash events are identified:

1. flushing of weakly or unbonded individual particles
2. cluster breakage and unfolding of particle bridges
3. fragmentation and resuspension of a cluster

The physical origin of the dominant phenomena cluster breakage and particle bridge unfolding will be evaluated by the help of numerical simulation in the following section.

5.4.5 Backwash simulation

Backwash is performed on clogging states at three points in time of the filtration simulation: at $20, 25$, and $30\,ms$. The three states are depicted in Figure 5.5. To reduce the computational effort, only attached particles are

a) Grayscale analysis

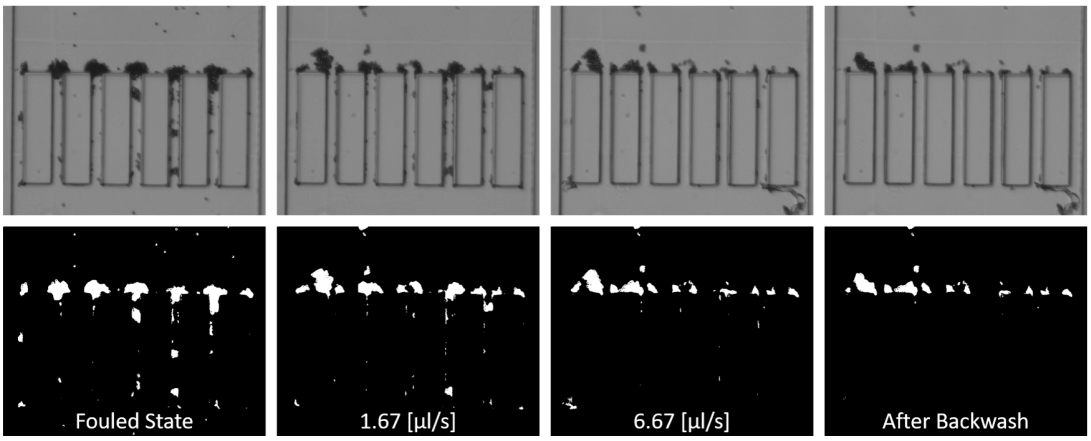

b) Backwash efficiency

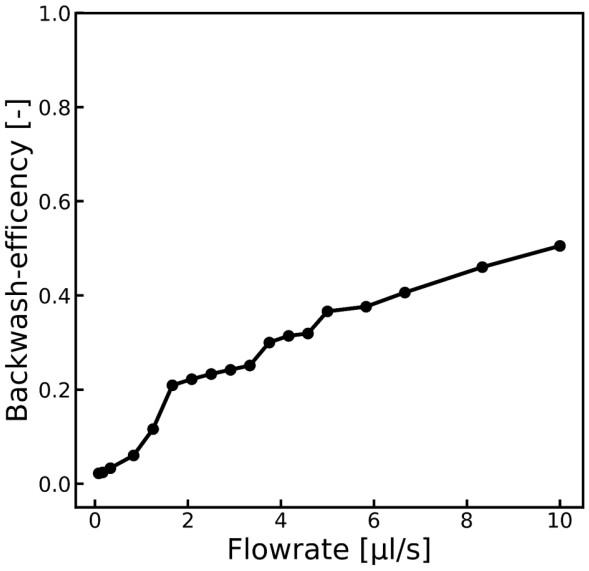

Figure 5.6: Figure a) displays the particle deposition before and after the backwash step. The microscopy pictures were converted into black white pictures to determine the backwash efficiency. The resulting backwash efficiency is shown in Figure b).

included in the backwash simulations. During the backwash process, the flow rate step-wise increases comparable to the experiments. At velocities v <45 mm s^{-1}, the particles only slightly move in all three simulations. At velocities v < 45 mm s^{-1}, particles located in the constriction start to move leading to a compaction of the agglomerate. A further increase in velocity to 225 mm s^{-1} induces the breakage of particle-particle contacts causing particle agglomerates to be resuspended by the flow. However, a significant amount of particles remain attached to the pore structure. These remaining particles restructure and tend to orientate in regions of lower drag. This restructuring is observed predominantly during backwash of the smallest clogging structure (see 20 ms in Fig. 5.7). There, the behavior of the remaining particles is reminiscent of opening a bascule bridge. By opening the particle bridge, the fluid flows unhindered through the pore. Hence, the drag force on the remaining particles reduces significantly. Therefore, the restructuring and the movement into the region of lower drag significantly reduce the backwash-efficiency.

The backwash-efficiency in these three cases is plotted over the backwash velocity in Figure 5.8. Here, the backwash-efficiency defines the ratio between particles connected to the pore (particles located in a cluster or directly bond to the surface) to the initial amount of particles. The backwash efficiency rises in the transition zone from 225 - 450 mm s^{-1} in all three simulations due to the breakage of particle clusters. The backwash efficiency is significantly lower in the smallest clogging structure (20 ms) compared to the others. This is explained by the reorientation of a particle cluster in the region of lower drag.

5.4.6 Comparison between simulations and experiments - Backwash

Backwash was experimentally and numerically performed under similar conditions. The experimental and simulation results are compared in the following.

In the experiments and in the simulations, the backwash process is char-

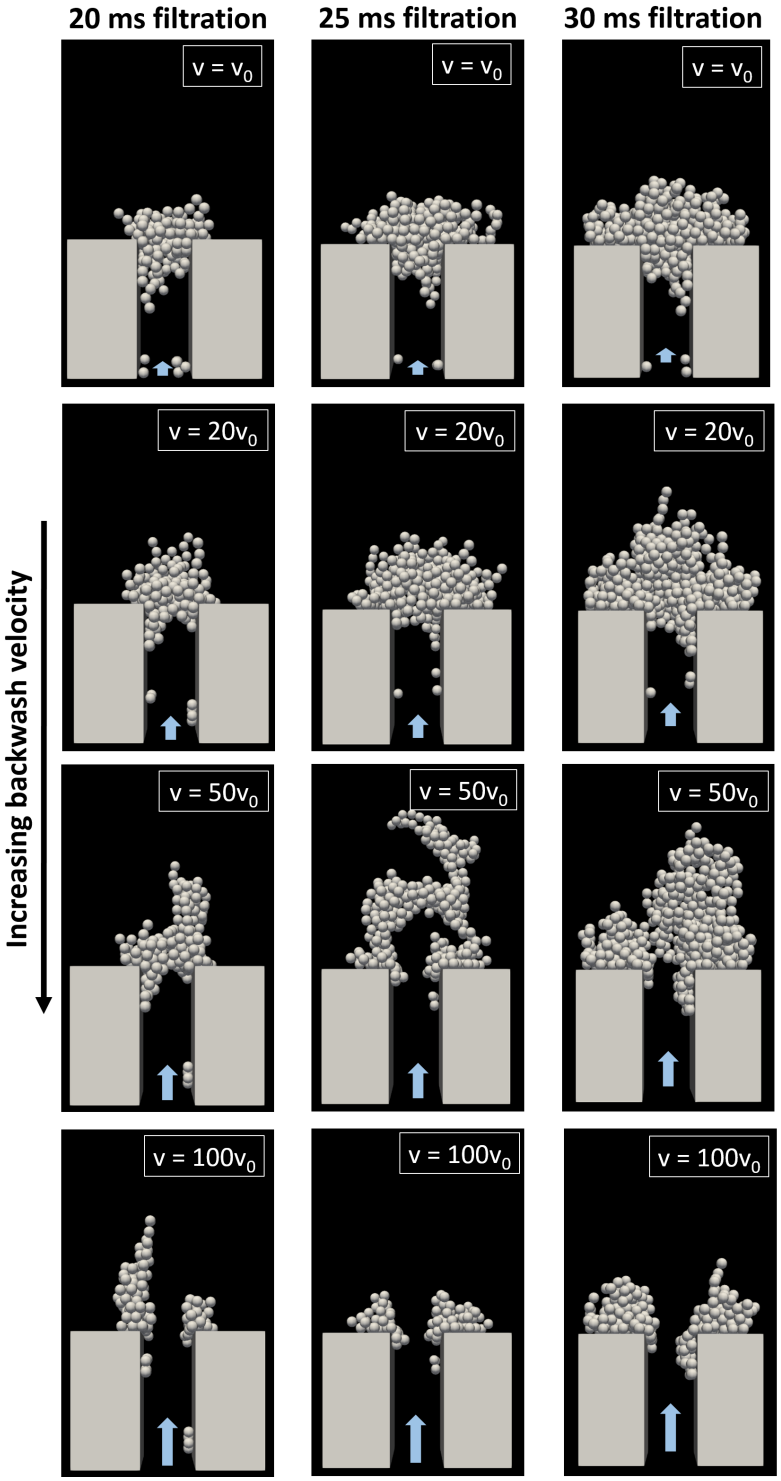

Figure 5.7: Numerical results of the backwash step at different velocities (v_0 =4.5 mm s^{-1}). Simulations were performed with three different states of the clogging: after 20, 25 and 30 ms filtration.

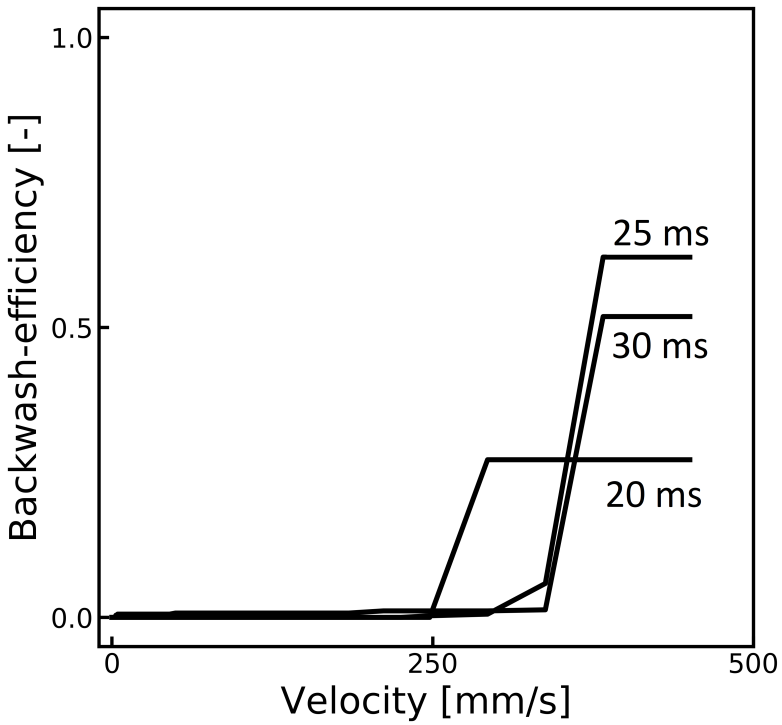

Figure 5.8: Calculated backwash efficiency with increasing backwash velocity of these three simulations.

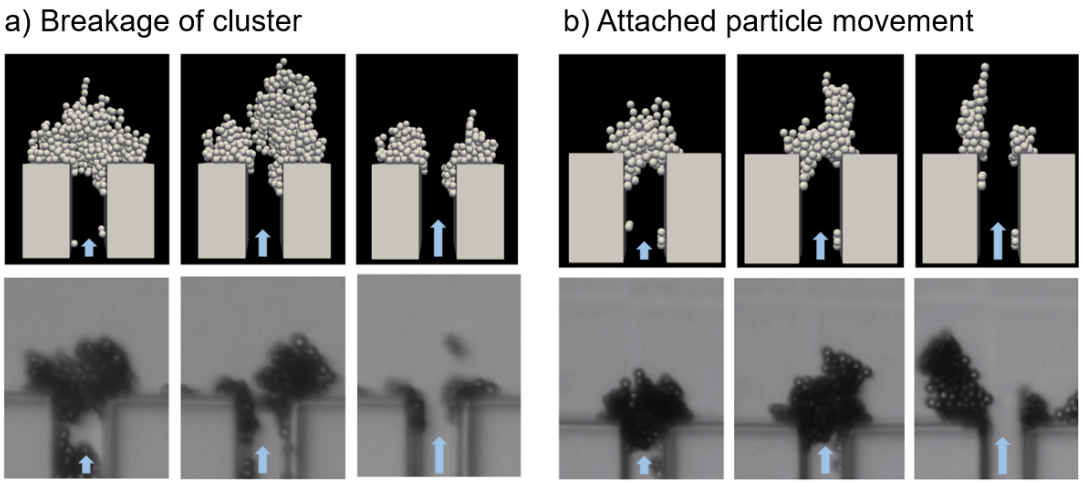

Figure 5.9: The microscopic backwash events occurring in the experiment and in the simulation. a) The breakage of a particle cluster from the pore structure. b) Attached particles move into the region of lower drag. The behavior of the cluster is reminiscent of opening a bascule bridge.

acterized by multi-particle interactions rather than single-particle dynamics. The detachment of particles during membrane backwash is mainly accomplished by the breakage of whole particle agglomerates instead of single-

particle detachment. Thus models describing the detachment of single particles are not able to describe backwash process accurately. Two dominant multi-particle events during backwash are observed in experiments and simulations: the partial breakage of agglomerates and the movement of attached particle clusters into regions of lower drag (see Figure 5.9). Up to 50% of the deposited particles remain attached to the pore structure both in the simulations and in the experiments. It has to be noted that the calculation methods of the backwash efficiency differ in the experiment and simulation (see Figures 5.6 and 5.8). Due to the 2D monitoring in the experiments, the backwash-efficiency is only estimated since shadowing effects occur. These shadowing effects probably lead to underestimation of the calculated backwash-efficiency. Contrary, the 3D information of the simulation results allow an exact calculation of the backwash-efficiency. Therefore, the Figures 5.6 and 5.8 can only be compared qualitatively. For a future study, it would be of interest to use microfluidic experiments combined with confocal imaging as performed by [Link2016; Ders2019; Link2019] to get 3D information of the backwash. Despite the inaccuracy of the experimental calculation, it can be ascertained that a large proportion of the particles remain on the pore structure after the backwash both in the experiment and in the simulation. Mainly particle clusters in a region of low drag are not removed during backwash. These would enhance particle deposition in a following up filtration. It can be noticed that especially inter-particle bonds break instead of particle-wall bonds. This behavior is explained by the stronger attraction of the particle-wall interactions compared to the particle-particle interactions (see Figure 5.2). Further, the stability of a bond varies with aggregate properties (e.g. coordination number, location inside the flow channel). The coordination of the filter cake is here rather small. More than 90% of the particles have a coordination number which is 4 or smaller. Therefore the particle-particle bonds are relatively weak in the filter cake. In a more compact filter cake (e.g. in the extreme case of a crystalline filter cake), the higher coordination may lead to preferred breakage particle-wall bonds instead of particle-particle bonds, although the adhesion strength is higher than the cohesion strength. Therefore, an

investigation of the dependency between cake properties and backwash efficiency is of high interest for a future study.

However, there are also some differences between experiments and simulations. The first cluster detachments occur at lower mean velocities in the experiments compared to the simulations. This indicates that the cohesive and the adhesive energy in the simulations is overestimated. The parameters for the interaction energy are taken from the literature as referenced in Table 5.1. However, there might be some differences in charge and surface chemistry between the particles used to measure the characteristic values and the particles applied here. The potentials are particularly sensitive to the surface tension properties.

Further, the simulation model does not account for the size distribution of the particles, surface roughness, and heterogeneities in surface charge. Of particular importance could be the assumption of a smooth surface. In this context, Hoek et al. approximate the dependence between surface roughness and surface interaction potential by applying the surface element integration [Hoek2006]. They showed that the attractive minimum of a smooth surface is more pronounced than the one of a rough surface. This results in enhanced particle resuspension due to surface roughness. Therefore, the assumption of a smooth surface used in this study overestimates the interaction energy.

Since the interaction energies seem to be overestimated, simulations were performed at lower adhesion and cohesion strength to investigate the influence of the particle wall and particle interactions. The results are explained in the following.

5.4.7 The impact of colloid interactions on the backwash efficiency

Colloidal interactions control the deposition and detachment on a single particle level [Berg1999b]. Yet, it is difficult to study such events experimentally. How these interactions control the collective behavior of the backwash process can be investigated with numerical simulations as elaborated be-

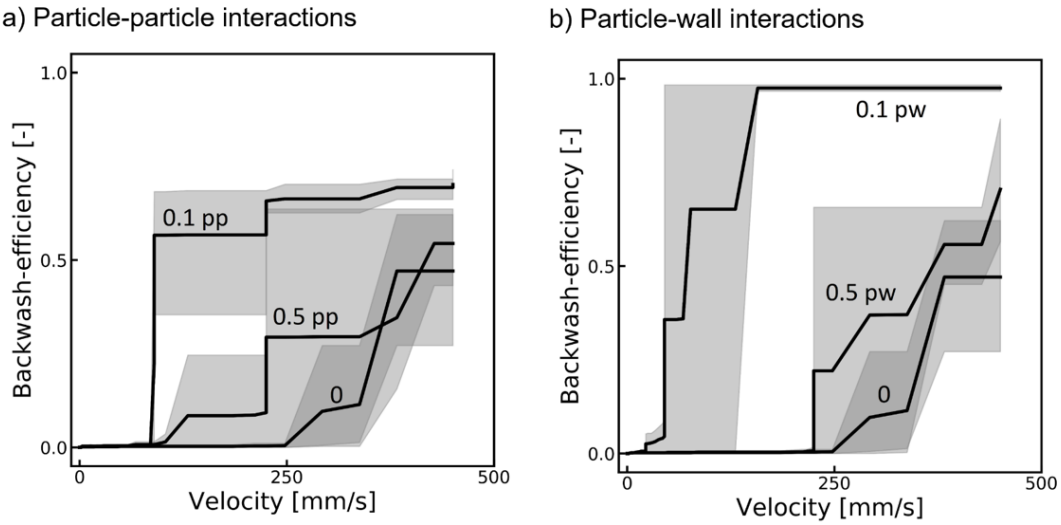

Figure 5.10: The graphs show simulation results of the backwash efficiency in which the particle-particle (a) or the particle-wall interactions (b) are reduced by a factor of 0.5 and 0.1. Simulations were performed at three stages of the clogging, which are highlighted in Figure 5.7. The black lines show the course of the mean value of three simulations at a specific interaction strength (0.5, 0.1, and the original interaction strength 0). The gray areas enclose the regions of the maximum and the minimum backwash efficiency of the respective three simulations.

low. For this purpose, backwash simulations are conducted in which the interaction force of the particle-particle and the particle-wall interactions are reduced by factors of 0.5 and 0.1. The clogging structure is adopted from the filtration simulations displayed in Figure 5.5 and besides the potentials, the simulation conditions are kept the same. This allows a direct comparison of the numerical results.

Figure 5.10 plots the backwash efficiency when changing the particle-particle interactions by a factor of 0.5 and 0.1 at the three different clogging states mentioned before. The resuspension of particles starts at lower backwash velocities by the reduction of the attractive force of the particle-particle interactions. Further, the backwash efficiency increases from a mean value of approximately 50 $\%$ to a maximum of 70 $\%$. However, there is still a significant amount of particles remaining on the pore structure. The backwash efficiency remains in the same order of magnitude as in the experimental results shown in Figure 5.6. The resuspension at lower backwash velocities is more comparable to the experimental results. Figure

5.6 highlights that the first cluster resuspension, which manifest in jumps in the backwash efficiency, experimentally occur at backwash flow rates of $1-2\,\mu L\,s^{-1}$ (superficial velocity: $45-90\,mm\,s^{-1}$). These superficial velocities are in a similar order of magnitude as the cluster resuspension occurring in the simulation with lower attractive strength (see Figure 5.10). This indicates that the initially used xDLVO potential overestimates the cohesive force between the particles. As explained in Section 5.4.6, an overestimation of the cohesive force can be caused by the approximation of a smooth homogeneous surface.

By the reduction of the adhesive force of the particle-wall interaction by a factor of 0.5, it reaches the same order as the cohesive force of the particle-particle interaction. As shown in Figure 5.10, the reduction of the adhesive force results in the resuspension of particles at lower flow velocities. Further, the mean backwash efficiency increase to 70% compared to 50% at the original adhesive force. The particles are almost entirely removed from the pore structure by a further decrease in the adhesive force to 10% of the original force. The results demonstrate that the particle-wall interactions stronger impact the backwash efficiency than the particle-particle interactions.

5.5 Conclusion

The study targets to visualize and analyze particle resuspension during backwash on a pore-scale level. For this purpose, microfluidic experiments and numerical CFD-DEM simulations were conducted. The experiments and the simulations comprise two steps: a filtration and a backwash step. During filtration, polystyrene particles were filtered through a pore structure. These particles build bridges between the pores leading to clogging both in the simulations and in the experiments. Following up, backwash was conducted with gradually increased velocities. During backwash, three phenomena were detected: Detachment of individual particles; Breakage of clusters and orientation of attached particle clusters/bridges in the region of lower drag; fragmentation of a cluster and partial removal of par-

ticle agglomerates from the pore structure. The detachment of individual particles was predominantly observed at the beginning of the backwash process, which indicates that these particles were not or only weakly bond to fouling cake or the pore structure. This effect contributed only little to the overall backwash efficiency. Therefore, individual particles are of minor importance during the backwash. Particle clusters dominate the backwash process instead of individual particles. Especially, the movement of attached clusters into the region of lower drag reduces backwash efficiency since they are protected from the removal by the hydrodynamic flow. These clusters can enhance clogging in a following up filtration step. Deeper insight into the interplay between hydrodynamic and colloidal interactions is gained by analyzing the numerical multi-body simulations data.

The numerical results show that clog-size and colloidal interactions influence these backwash events and backwash efficiency. The results reveal that particle-membrane interactions dominantly control backwash efficiency and that the influence of particle-particle interactions is comparatively small. Fewer particle clusters remain on the structure if particle-wall interactions are weaker than particle-particle interactions. This leads to the conclusion that tuning particle-membrane interactions can significantly increase backwash efficiency. Besides surface potential, filter cake properties (e.g. degree of coordination, packing density) significantly influence the cluster resuspension. How these properties affect the backwash is still to the best of our knowledge an unanswered question. Further studies are necessary to analyze the resuspension events in the inner pore structure of a membrane. Further, the role of sterical interactions of soft particles is of interest because these play a predominant role in biological deposition and resuspension.

6 How does temperature effect colloidal clogging ? - Theoretical study

This study is developed in cooperation with Theresa B.M. Rösener. Parts of this chapter are published in her dissertation:
Rösener, T.B.M. "Temperature modulated membrane transport phenomena". Dissertation RWTH Aachen (2019).

Parts of the theory presented in this chapter were developed and presented in the master thesis of Tony Rosemann:

T. Rosemann “Investigation of the temperature dependence of colloidal fouling using coupled CFD-DEM simulations [Master thesis]”. RWTH university(2017).

6.1 Introduction

Colloidal aggregation and jamming, sometimes also called fouling, is a challenging problem that occurs for a broad range of applications [Henr2012]. Due to the complex interplay of hydrodynamic and surface interactions, the clogging still lacks understanding. The application of sophisticated methods combining microfabrication [Ngen2010], microfluidics [Agba2012], and confocal laser optical analysis [Link2016] provides the opportunity to visualize the clogging on a microscopic level. A variety of studies have been performed to analyze the formation of colloidal clogging on a pore-scale level [Wyss2006; Ngen2011; Agba2012; Sain2016; Link2016]. However, little is known about how the temperature can affect the clogging process. Answering the question is difficult as temperature influences the hydrodynamics, the physical properties of the materials as well as colloidal interactions. However, knowledge on how temperature influences the colloidal deposition process is relevant for various applications such as membrane distillation, membrane filtration, or microfluidic operations.

The impact of temperature has rarely been considered in experimental and numerical studies. The few studies available have shown that temperature can affect the particle deposition and flux decline [Mo2008; Jin2009; Yan2015; Loha2018b; Loha2020]. Attempts to explain these observations are closely connected to the nanoscopic particle-particle and particle-membrane interactions. Colloidal interaction models often invoke the Derjaguin-Landau-Verwey-Overbeek (DLVO) theory, which originated in the 1940s and comprised van der Waals forces and electrostatic double-layer forces [Derj1941; Verw1948]. Though being very appealing due to its simplistic description, the DLVO theory has been proven inaccurately to predict interactions in aqueous solution [Isra2011]. The inaccuracy led to the recent advent of new models that extend the DLVO theory by additional phenomena such as Lewis acid-base interactions [Gras2002; Ninh1999]. However, there is still no comprehensive understanding, which nanoscopic phenomena dominate the clogging process, let alone how temperature affects them.

This study aims to systematically analyze how temperature influences colloidal interactions as well as the hydrodynamic properties and how this influence affects the clogging behavior of colloidal particles at a pore-like micron-sized flow channel constriction. We incorporate the variable temperature in the available force models and evaluate its impact on the individual forces and particle-particle and particle-wall interactions. The interplay of the individual forces acting on a set of suspended particles in a fluid flow is hard to predict and especially for nano-particles not easily accessible by experiments. Most studies use fouling models such as the colloidal filtration theory to predict membrane fouling [Tufe2004; Tufe2005] rather than to investigate single-particle behavior [Wess2001; Bacc1995; Loha2018a]. We perform simulations using the CFD-DEM framework, as explained in chapter 3.1. This chapter systematically investigates the phenomena through flow simulations with different material combinations of particle and surfaces using the CFDEM®coupling software [Goni2012] and analyze the temperature dependence of van der Waals forces, electrostatic double layer and Lewis acid-base forces.

6.2 Simulation domain and conditions

The pore geometry used is depicted in Figure 6.1 to simulate the clogging of a porous medium. The geometry is identical to the pore constriction presented in chapter 5.It consists of an upstream flow domain where the fluid enters with constant velocity u_0 and a rigid pore such as in porous membranes. The pore serves as a constriction for the flow and allows us to observe pore-clogging and particle deposition.

The fluid enters the upstream domain through the inlet with constant velocity v_0. The particles are inserted regularly at random positions to maintain a constant solid feed fraction of $1\%vol$. The lateral surfaces of the upstream domain are periodic for the fluid as well as for particles. The no-slip condition holds on the surface of the rigid pore. The pore surfaces are walls that interact with the particles by contact, van der Waals, double layer, and acid-base forces. The pressure is kept constant at the outlet. Particles

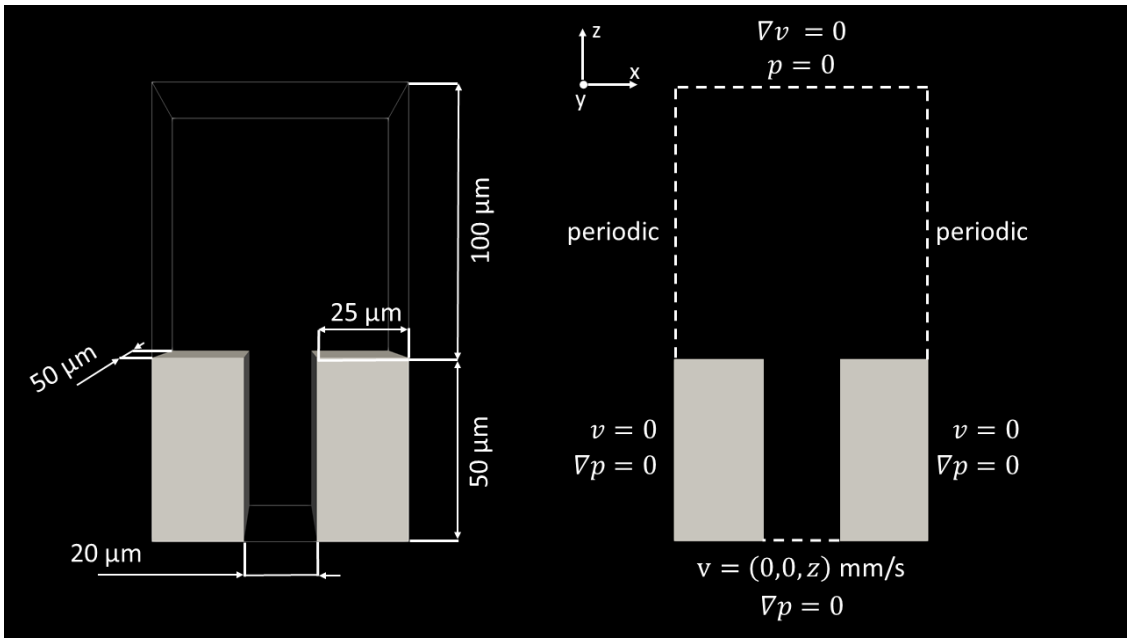

Figure 6.1: Dimension of the pore geometry and the applied boundary conditions in the simulation

leaving the simulation domain through the outlet at the bottom of the pore are deleted. The chosen simulation parameters are presented in Table 6.1

Parameter	Symbol	Value	Literature
Filtration velocity	v_0	$5\ \mathrm{mm\,s^{-1}}$	-
Particle radius	a	$4.2\ \mu\mathrm{m}$	-
Young modulus particle	E	$3.6 \times 10^9\ \mathrm{Pa}$	[Bhus2008]
Young modulus wall	E	$8.7 \times 10^6\ \mathrm{Pa}$	[Arma1999]
Poisson ratio	$\tilde{\nu}$	0.45	assumed
Coefficient of restitution	e	0.6	assumed
Friction coefficient	μ_f	0.5	assumed
Rolling friction coefficient	μ_r	0.01	assumed
Distance of closed approach	D_{int}	$0.158\ \mathrm{nm}$	[Isra2011]
Particle density	ρ_{P}	$1000\ \mathrm{kg\,m^{-3}}$	-
Particle concentration	c_{P}	$5\ \%vol$	-
Salt concentration	c_{KCl}	$0.01 - 0.05\ \mathrm{mol\,L^{-1}}$	-
DEM-time step	Δt_{DEM}	$1 \times 10^{-10}\ \mathrm{s}$	-
CFD-time step	Δt_{CFD}	$1 \times 10^{-8}\ \mathrm{s}$	-

Table 6.1: Parameters applied in the simulation

6.3 Temperature dependence of colloidal deposition

The present work aims to analyze the temperature dependence of colloidal clogging. Yan et al. [Yan2015] analyzed the temperature dependence of polystyrene particle deposition on polymethyl methacrylate surfaces. The experiments suggested that particle deposition is facilitated by increasing temperature. Yan et al. used the DLVO potential to explain their results.

Since acid-base forces have a significant impact on particle adhesion, it is worthwhile to reassess the temperature dependence of particle deposition using the XDLVO theory. Moreover, the important question is, if particle deposition is always facilitated by increasing the temperature or if this behavior depends on the considered materials. While Yan et al. [Yan2015] considered a resting fluid, it is worth investigating the effect of temperature for colloidal deposition with the applied fluid flow as the flow is relevant in many applications such as microfluidics and membranes.

Here, XDLVO potentials and the corresponding CFD-DEM simulation results at two different temperatures ($20\,^{\circ}\mathrm{C}$/ $80\,^{\circ}\mathrm{C}$) for two material systems are

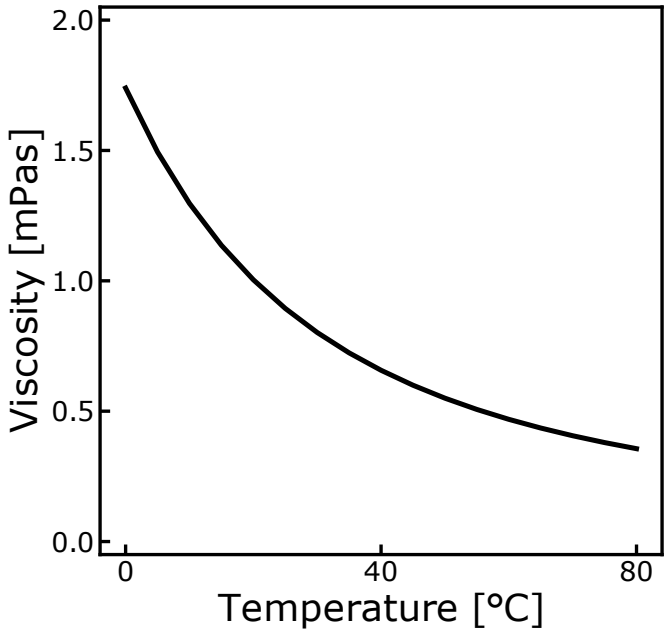

Figure 6.2: The change in viscosity of water with temperature.

presented. The model uses a particle diameter of $4.2\,\mu m$ and a pore width of $20\,\mu m$. The model does not consider the Brownian force on the particles.

6.3.1 Temperature dependence of hydrodynamic

The hydrodynamics strongly depends on the temperature mainly due to changes in viscosity with increasing temperature. Contrary to gases where viscosity rises with temperature, the viscosity of liquids decreases with rising temperature. The empirical Vogel equation determines the change in viscosity η (mPa s) over the temperature T [Visw2007]:

$$\eta = exp(A + \frac{B}{C - T}) \tag{6.1}$$

whereby the coefficients are $A = -4.5318$, $B = -220.57$ and $C = 149.39$ for liquid water. The change in viscosity with temperature is shown in Figure 6.2. Thereby, the change in viscosity with temperature has counteractive effects on particle deposition.

On the one hand, the viscous drag force exerted on the colloids reduces with an increase in temperature. Thereby, the potential of the hydrodynamic

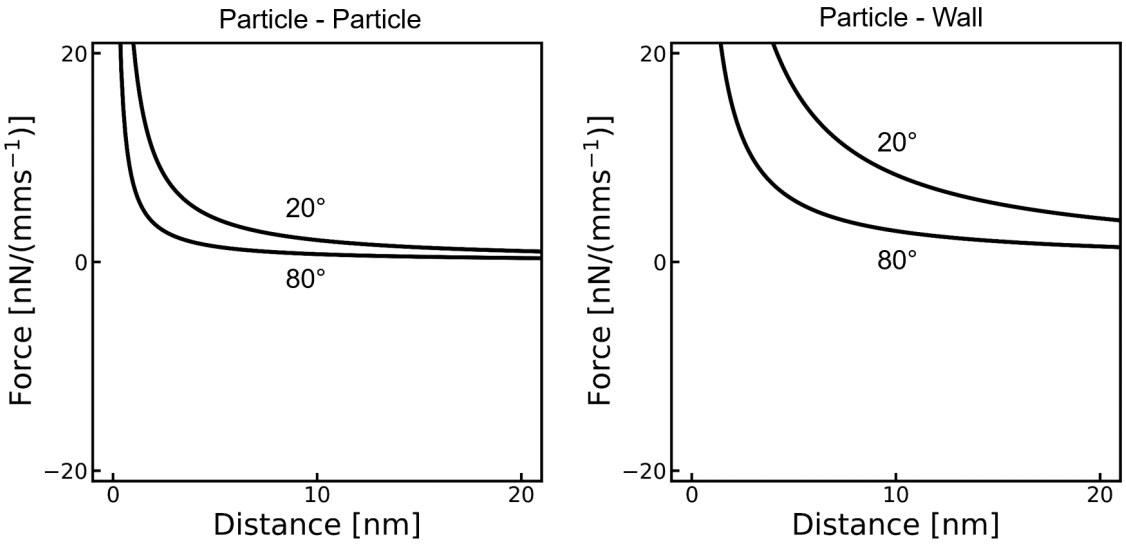

Figure 6.3: The lubrication force per relative velocity arising at 20 °C and 80 °C

flow to push the particle over an energy barrier decreases. Stokes drag correlation (valid at low Reynolds numbers $Re < 0.1$) expresses the link between viscous drag force F_D and the viscosity η as follows:

$$F_D = 6\pi\eta a\Delta v \tag{6.2}$$

where Δv and a denote the difference in velocity between the fluid and the particle as well as the particle radius, respectively. Thus, the drag force linearly changes with viscosity. On the other hand, viscous lubrication scales linear with the viscosity, to [Lisi2016]:

$$F = \frac{6\pi\eta v_{rel}}{D}a^2 \tag{6.3}$$

where v_{rel} is the relative velocity between a sphere approaching a wall. Contrary to the drag force originate from hydrodynamic flow, lubrication reduces the probability of particle deposition. The change in the lubrication force with temperature is demonstrated in Figure 6.3. Due to the opposing effects of hydrodynamic drag caused by fluid flow and viscous lubrication, there is no general rule if temperature enhances or reduces deposition due to hydrodynamic changes.

6.3.2 Temperature dependence of colloidal potentials

Three interaction potentials play a major role in colloidal systems: Van der Waals forces, electrostatic double-layer forces, and Lewis acid-base forces [Oss2006]. To assess their influence on temperature-dependent particle deposition, first, their temperature dependency will be evaluated individually. The following material combinations are considered for the colloid and channel/membrane system as they are representative for the two applications: anionic polystyrene particles (as used in Chapter 5) with a polydimethylsiloxane (PDMS) channel as used in a microfluidic device, and cationic polystyrene particles with a polyamide material as used for filtration membranes.

Van der Waals forces

Colloidal systems consider macroscopic bodies surrounded by a medium such as water. By summing up all pairwise intermolecular interactions between two macroscopic bodies, Hamaker [Hama1937] derived an expression for the van der Waals forces acting on them. This expression is composed of the Hamaker constant A that depends on material properties and a geometrical part that depends on the bodies' size as well as their separation distance. The van der Waals potential determined between two spheres (S) with radii a whose surfaces are separated by the distance D is given by [Hama1937]

$$W_{\mathrm{VDW}}^{132}(D) = -\frac{A_{132}a}{12D} \tag{6.4}$$

and for a sphere and an infinite flat plate (P) by

$$W_{\mathrm{VDW}}^{\mathrm{SP}}(D) = -\frac{A_{132}a}{6D}. \tag{6.5}$$

The force acting on a sphere in such a potential field is computed by the relation

$$\boldsymbol{F}(D) = -\nabla W(D). \tag{6.6}$$

The Hamaker constant A is calculated by a simplified approach based on Lifshitz theory [Lifs1956]:

$$A_{132} \approx \frac{3}{4}kT\left(\frac{\varepsilon_1-\varepsilon_3}{\varepsilon_1+\varepsilon_3}\right)\left(\frac{\varepsilon_2-\varepsilon_3}{\varepsilon_2+\varepsilon_3}\right) + \frac{3h\nu_e}{8\sqrt{2}}\frac{(n_1^2-n_3^2)(n_2^2-n_3^2)}{(n_1^2+n_3^2)^{1/2}(n_2^2+n_3^2)^{1/2}\{(n_1^2+n_3^2)^{1/2}+(n_2^2+n_3^2)^{1/2}\}}, \tag{6.7}$$

where k is the Boltzmann constant, T the absolute temperature, h the Planck constant and ν_e the main electronic absorption frequency in the ultraviolet light. The Hamaker constant describes the interaction of two macroscopic bodies of material 1 and 2 interacting across a medium 3. It depends especially on the optical properties refractive index n and dielectric constant ε of the three bulk phases.

Absorption frequencies are typically around $3 \cdot 10^{15}$ Hz [Isra2011] and the specific values for the selected membrane and colloid materials are listed in Table 6.2. The simulations use the average ν_e of the considered three phases.

Table 6.2: Absorption frequencies ν_e and dielectric constants ε based on literature.

Material	ν_e [10^{15} Hz]	Ref.	ε [-]	Ref.
Anionic Polystyrene	2.3	[Isra2011]	2.55	[Isra2011]
Cationic Polystyrene	2.3	[Isra2011]	2.55	[Isra2011]
Polyamid	3.0	[Isra2011]	3.6	[Mark1999]
Polydimethylsiloxan	2.8	[Sun2004]	2.75	[Drum1997]
Water	3.0	[Isra2011]		

The temperature dependence of van der Waals forces arises from the temperature-dependent behavior of the Hamaker constant. This dependence is explicitly given in the first term of Equation (2.3), but implicitly by

the temperature-dependent variables ε and n. Malmberg et al. [Malm1956] found the following interpolation function for the dielectric constant of water

$$\varepsilon(t) = 87.74 - 0.4008t/^{\circ}C + 0.0009398t^2/(^{\circ}C)^2 - 0.00000141t^3/(^{\circ}C)^3, \quad (6.8)$$

where t denotes the temperature in degrees Celsius. The value of ε decreases from 87.7 at $0\,^{\circ}\mathrm{C}$ to 55.7 at $100\,^{\circ}\mathrm{C}$. The dielectric constant of water also decreases with increasing salt concentration, but this influence is negligible for salt concentrations chosen in this work ($c_{\mathrm{NaCl}} \ll 1\mathrm{M}$) [Gavi2016]. According to Table 6.2, the dielectric constants of the considered solid materials are one order lower than the dielectric constant of water. Therefore, the temperature variations of ε of the solid materials are assumed to be negligible.

Under the assumption of a constant temperature gradient, the refractive index n changes with temperature according to

$$n(T) = n(T_0) + \left(\frac{dn}{dT}\right)(T - T_0), \quad (6.9)$$

where $(\mathrm{d}n/\mathrm{d}T)$ denotes the thermo-optic coefficient and T_0 the reference temperature. Table 6.3 lists the coefficients for this equation. These coefficients were measured at room temperature $T_0 = 293.15$ K in all cases and for wavelengths around the average wavelength of visible light ($589\,\mathrm{nm}$).

Table 6.3: Refractive indices n and thermo-optic coefficients $(\mathrm{d}n/\mathrm{d}T)$ at room temperature based on literature.

Material	n [-]	Ref.	$(\mathrm{d}n/\mathrm{d}T)$ $[10^{-4}/\mathrm{K}]$	Ref.
Anionic Polystyrene	1.557	[Isra2011]	-1.42	[Mark1999]
Cationic Polystyrene	1.557	[Isra2011]	-1.42	[Mark1999]
Polyamid	1.565	[Wied2011]	$-1.$	[Parq2013]
Polydimethylsiloxan	1.41	[Mark2010]	-4.5	[Mark2010]

For the solid materials given in Table 6.3 this work assume that the thermo-optic coefficient is constant over the temperature ranges consid-

ered and Equation (6.9) holds. The refractive index of water as a function of temperature, wavelength λ and density ρ can be calculated with [Inte1997]:

$$\frac{n^2-1}{\bar{\rho}(n^2+2)} = k_0 + k_1\bar{\rho} + k_2\bar{T} + k_3\bar{\lambda}^2\bar{T} + \frac{k_4}{\bar{\lambda}^2} + \frac{k_5}{\bar{\lambda}^2 - \bar{\lambda}_{\mathrm{UV}}^2} + \frac{k_6}{\bar{\lambda}^2 - \bar{\lambda}_{\mathrm{IR}}^2} + k_7\bar{\rho}. \tag{6.10}$$

Here, $\bar{\rho} = \rho/(1000\,\mathrm{kg\ m^{-3}})$, $\bar{T} = T/(273.15K)$ and $\bar{\lambda} = \lambda/(589nm)$ are non-dimensional variables and $k_0 - k_7, \bar{\lambda}_{\mathrm{IR}}$ as well as $\bar{\lambda}_{\mathrm{UV}}$ are constants. The model uses the average wavelength of visible light (λ=589 nm). The temperature-dependent density ρ of water can be calculated with the interpolation formula provided by Kell [Kell1975]:

$$\rho = \frac{\sum_{i=0}^{5} q_i T^i/(^\circ C)^i}{1 + q_6 T/(^\circ C)} \quad [\mathrm{kg/m^3}] \tag{6.11}$$

where $q_0 - q_6$ are constant parameters. Compared with the model of Yan et al. [Yan2015], our model also takes into account the thermo-optic coefficients of the solid materials. The inclusion of this coefficient can lead to a significant difference when predicting the temperature-dependent behavior of the Hamaker constant. For example, for the interaction between an anionic polystyrene particle (phase 1) with PDMS (phase 2) in water (phase 3) our model yields the Hamaker constants $A_{132}(20\,^\circ\mathrm{C}) = 0.67 \times 10^{-20} J$ and $A_{132}(80\,^\circ\mathrm{C}) = 0.63 \times 10^{-20} J$. The decreasing value for higher temperatures means the van der Waals attraction between the particle and the membrane decreases with temperature. In contrast, when neglecting the thermo-optic coefficients of polystyrene and PDMS, the Hamaker constant yields $A_{132}(80\,^\circ\mathrm{C}) = 0.76 \times 10^{-20} J$. In this case, the attraction increases with temperature. As a result, thermo-optic coefficients should generally be included when analyzing the temperature dependence of van der Waals forces.

Figure 6.4 displays the Hamaker constants for varying material system over temperature. The Hamaker constant nearly stays constant with temperature. Therefore, the van der Waals interactions are temperature inde-

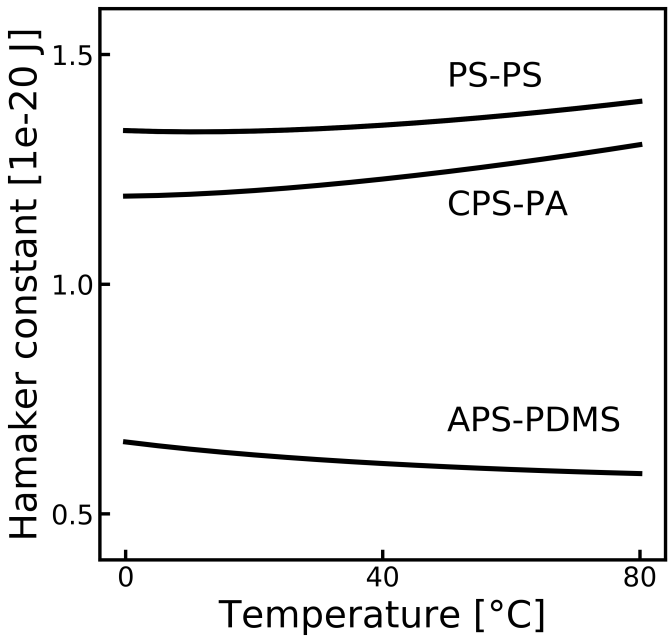

Figure 6.4: The Hamaker constant for the particle-particle and particle-wall interactions of anionic polystyrene (APS), cationic polystyrene (CPS), polyamid (PA) and polydimethylsiloxan (PDMS) with temperature.

pendent, which corresponds with literature [Seth2010]. It has to be noted that in biological systems, slight changes of the van der Waals interaction with temperature can occur resulting from permanent dipole interaction (Keesom interaction) [Pars1970], however, Keesom interactions are of minor importance in this study.

Electric double layer forces

The charge of surfaces in colloidal systems leads to an attraction of counterions from the surrounding electrolyte solution, which are arranged in two layers: in direct contact to the surface (Stern layer) and a diffusive boundary layer. When two surfaces with solvated ions approach each other, an electrostatic double-layer force will act on them. For equally charged surfaces, the electrostatic double layer is repulsive while it is attractive for differently charged surfaces. The strength of this force depends on the strength of the electric potential Ψ. Three particular potential values can be found at the boundaries between the layers: the surface potential Ψ_0, the Stern potential Ψ_S at the Stern plane, and the zeta potential ζ at the slipping

plane. The Poisson-Boltzmann equation describes the double layer interactions accurately but does not usually give a simple analytical solution [Will1998]. Therefore, one of the following three approximate models is usually applied: the constant charge approximation (CCA) by Wiese and Healy [Wies1970], the constant potential approximation (CPA) by Hogg et al. [Hogg1966] or the linear superposition approximation (LSA) by Gregory [Greg1975]. Warszynski and Adamczyk [Wars1997] showed that the LSA model is the better estimate for the numerical solution of the Poisson-Boltzmann equation and is therefore used in this work.

The linear superposition approximation assumes that the two surfaces are fairly far apart from each other such that the potentials of each surface do not disturb each other and can be superposed. This approximation becomes inaccurate for very small separation distances. However, when the surfaces are close to each other, van der Waals interactions are usually more dominant and this uncertainty is tolerable [Wars1997]. The double layer potential between two equal spheres is given by [Greg1975]

$$W_{\mathrm{DL}}^{\mathrm{SS}}(D) = 2\pi\varepsilon_0\varepsilon a \left(\frac{kT}{e}\right)^2 \Upsilon_{\mathrm{S}}^2 \exp(-\kappa D) \tag{6.12}$$

and between a sphere and a plate by

$$W_{\mathrm{DL}}^{\mathrm{SP}}(D) = 4\pi\varepsilon_0\varepsilon a \left(\frac{kT}{e}\right)^2 \Upsilon_{\mathrm{S}}\Upsilon_{\mathrm{P}} \exp(-\kappa D), \tag{6.13}$$

where ε_0 denotes the vaccum permittivity, e the elementary charge, κ the inverse Debye length and ε refers to the dielectric constant of the electrolyte solution. Υ_{S} and Υ_{P} are the effective surface potentials of the sphere and the plate, respectively. One obtains the corresponding force by using Equation (6.6). The Debye length is a measure for the thickness of the diffusive layer and can be expressed for a 1:1 electrolyte such as a sodium chloride solution as [Isra2011]

$$\kappa^{-1} = \left(\frac{\varepsilon_0\varepsilon kT}{2e^2 N_{\mathrm{A}} c}\right)^{1/2}, \tag{6.14}$$

where N_A is the Avogadro constant and c the molar concentration of the electrolyte in mol/L. The following expression for the effective surface potential of a sphere was derived by Ohshima et al. [Ohsh1982]:

$$\gamma_S = \frac{8 \tanh\left(\frac{\Psi_0 e}{4kT}\right)}{1 + \sqrt{1 - \frac{2\kappa a + 1}{(\kappa a + 1)^2} \tanh^2\left(\frac{\Psi_0 e}{4kT}\right)}}. \tag{6.15}$$

This expression reduces for the limit radius $a \to \infty$ to the effective surface potential of a plate

$$\gamma_P = 4 \tanh\left(\frac{\Psi_0 e}{4kT}\right). \tag{6.16}$$

Since the surface potential is generally not known with sufficient certainty, it is usually assumed to be the zeta potential which can be measured in experiments [Will1998] and is used in this work as well

$$\Psi_0 \approx \zeta. \tag{6.17}$$

Table 6.4: Coefficients α_1 and α_2 from Equation (6.19) as well as coefficients β and T_0 from Equation (6.20) derived from literature. The

Material	α_1 [mV]	α_2 [mV]	Ref.	β [10^{-2}/K]	T_0 [°C]	Ref.
Anionic PS	5.8	44.96	[Must2016]	0.39	25	[Yan2015]
Cationic PS	-11.3	27.1	[Sado2014][a]	1.5	20	[Garc2006]
Polydimethylsiloxan	6.8	29.8	[Kirb2004b]	0.25	20	[Vend2006]
Polyamid	-7.61	-14.55	[Kirb2004a][b]	0	20	assumed

[a] the values base on data at $pH > 6$
[b] the values base on data at $pH = 3 - 4$

The zeta potential is a function of ion concentration, buffer and ion type, pH, ion valency and temperature [Kirb2004a]. Reppert and Morgan [Repp2003] collected studies on temperature-dependent zeta potentials and showed that most of the few studies available found an increase in magnitude with temperature. This work only considers a sodium chlo-

ride solution at different concentrations and temperatures. Temperature-dependent zeta potentials are usually only reported for specific electrolyte concentrations and concentration-dependent zeta potentials only for specific temperatures. Because of this lack of sufficient data, it is assumed that the zeta potentials follow the equation

$$\zeta(c,T) = g(c)h(T), \tag{6.18}$$

where g and h are independent interpolation functions derived from available experimental data. The following interpolation functions is used

$$g(c) = \alpha_1 + \alpha_2 \log c \tag{6.19}$$

and

$$h(T) = 1 + \beta(T - T_0). \tag{6.20}$$

Equation (6.19) works well for a wide range of concentrations but its usage is limited to high zeta potentials [Kirb2004b]. Equation (6.20) assumes that the zeta potential changes linearly with temperature. The derived coefficients $\alpha_1, \alpha_2, \beta$ and T_0 are listed in Table 6.4 for anionic polystyrene, cationic polystyrene, polyamid and polydimethylsiloxan. It should be noted that finding consistent data for Equation (6.18) is cumbersome, since the experimental conditions such as pH, electrolyte type and buffer type vary depending on literature.

Figure 6.5 shows the temperature dependency of the zeta potential. The magnitude of zeta potentials of polydimethylsiloxane and anionic polystyrene increase slightly with temperature. Contrary, the zeta potential of cationic polystyrene sharply decreases with temperature. The decreasing zeta potential is attributed to the deprotonation of the amidine head groups ($NH2$ $(NH2)^+$) at higher temperatures [Garc2006]. The sharp decrease of the zeta potential of cationic polystyrene with temperature is consistent with the decreased colloidal stability of cationic polystyrene with temperature [Good1979]. It has to be noted that the linear decrease with

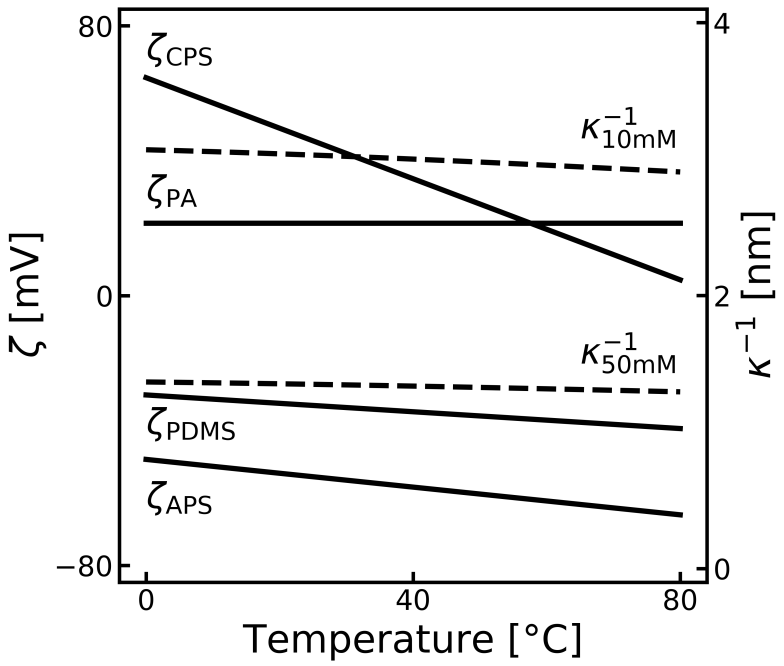

Figure 6.5: Zeta potentials as a function of temperature for anionic polystyrene (APS) and polydimethylsiloxan (PDMS) at an ionic concentration of 50mM as well as for cationic polystyrene and polyamid (PA) at an ionic concentration of 10Mm. Zeta potentials derived based on Equation 6.18 with data from literature according to Table 6.4. Further, the Debye length at 10mM and 50mM depending on temperature is shown.

the temperature of the zeta potential of cationic polystyrene has to be taken with caution since it results from measurements at only two temperatures (20 and 80 °C) [Garc2006]. For this study, the cause of the zeta potential of cationic polystyrene between 20 and 80 °C is not relevant, since, in the following, the simulations are only performed at both temperatures. Figure 6.5 further shows that the Debye length nearly stays constant with the temperature at 10 and $50mM$ ionic concentration. The minor changes of the Debye length with temperature result from the counteracting increase in ion mobility and decrease in permittivity.

Acid-base forces

Table 6.5: Surface tension parameters γ^{LW}, γ^+ and γ^- at room temperature based on literature.

Material	γ^{LW} [mJ/m^2]	γ^+ [mJ/m^2]	γ^- [mJ/m^2]	Ref.
Anionic Polystyrene	42	0.57	5.27	[Must2016]
Cationic Polystyrene	42	0.4	1.0	[Boua1998]
Polydimethylsiloxan	22.9	0	3.05	[Wang2014]
Polyamid	36.4	0.02	21.6	[Oss2006]
Water	21.8	25.5	25.5	[Oss1993]

Lewis acid-base interactions occur in polar media such as water and comprise attractive hydrophobic interactions as well as repulsive hydrophilic interactions. These interactions were characterized in detail by van Oss [Oss1993]. The hydrophobic effect describes the tendency of apolar chains, solutes or particles to aggregate in water and exclude water molecules. As a result, the hydrogen bonding between the polar water molecules is maximized, while the contact area between water molecules and apolar molecules is minimized. In contrast, the hydrophilic effect describes the resistance of hydrated monopolar surfaces to dehydrate and aggregate. This effect is caused by the strong hydrogen bonding of water molecules to the monopolar surface and the structured orientation of water molecules near the surface.

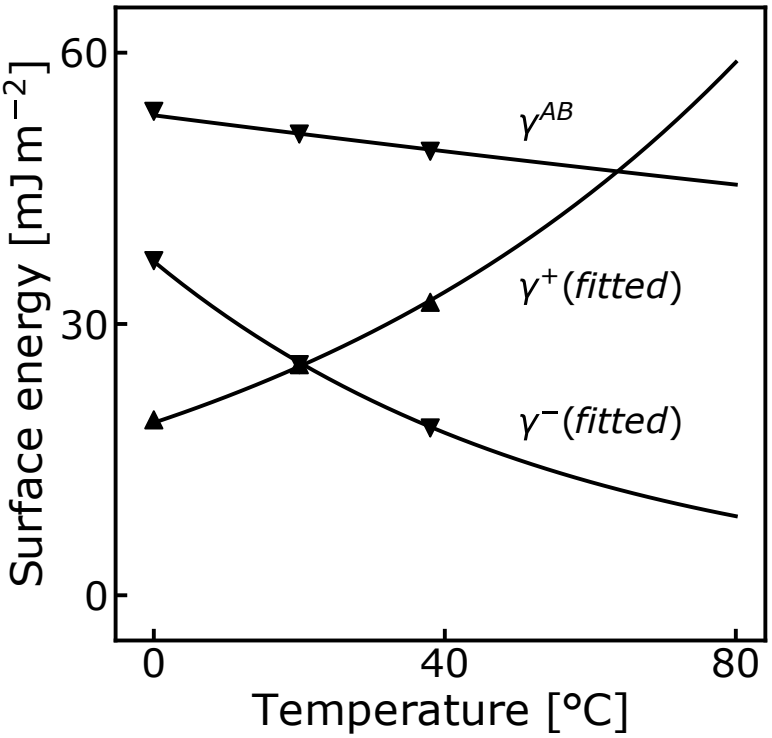

Figure 6.6: Surface tension data points of water from van Oss [Oss2006]. Electron acceptor γ^+ and electron donator γ^- functions fitted to data. Acid-base surface tension γ^{AB} calculated from fitted functions.

The calculation of acid-base interactions is based on surface tension parameters. The surface tension γ consists of two components [Oss1993]:

$$\gamma = \gamma^{LW} + \gamma^{AB}, \tag{6.21}$$

where γ^{LW} denotes the apolar Lifshitz-van der Waals component and γ^{AB} the polar acid-base component. The acid-base component can be expressed as [Oss1988]

$$\gamma^{AB} = 2\sqrt{\gamma^+\gamma^-}, \tag{6.22}$$

where γ^+ denotes the electron-acceptor and γ^- the electron-donor parameter. Therefore, acid-base interactions are also called electron-acceptor-electron-donor interactions. The free energy of adhesion per unit area ΔG_{AB}^{132} of two parallel plates 1 and 2 immersed in a medium 3 is given

by [Oss1993]

$$\Delta G_{\mathrm{AB}}^{132} = 2\sqrt{\gamma_3^+}\left(\sqrt{\gamma_1^-}+\sqrt{\gamma_2^-}-\sqrt{\gamma_3^-}\right) + 2\sqrt{\gamma_3^-}\left(\sqrt{\gamma_1^+}+\sqrt{\gamma_2^+}-\sqrt{\gamma_3^+}\right) - 2\sqrt{\gamma_1^+\gamma_2^-}-2\sqrt{\gamma_1^-\gamma_2^+} \quad (6.23)$$

and decays exponentially according to [Oss2006]

$$\Delta G_{\mathrm{AB}}(D) = \Delta G_{\mathrm{AB}}^{132}\exp\left(\frac{D_0-D}{\lambda}\right). \quad (6.24)$$

The minimum equilibrium distance $D_0 \approx 0.158$ nm [Oss1993] is constant. The decay length is $\lambda \approx 0.6-1$ nm at ambient temperatures [Oss2006]. By applying Derjaguin's technique [Derj1934], one obtains the particle-particle potential [Oss2006]

$$W_{\mathrm{AB}}^{\mathrm{SS}}(D) = \pi a\lambda\Delta G_{\mathrm{AB}}^{132}\exp\left(\frac{D_0-D}{\lambda}\right) \quad (6.25)$$

and analogously the particle-wall potential

$$W_{\mathrm{AB}}^{\mathrm{SP}}(D) = 2\pi a\lambda\Delta G_{\mathrm{AB}}^{132}\exp\left(\frac{D_0-D}{\lambda}\right). \quad (6.26)$$

The corresponding forces to these potentials follow again from Equation (2.6).

The surface tension parameters for the considered solid materials and water are listed in Table 6.5. The free energy of adhesion $\Delta G_{\mathrm{AB}}^{\mathrm{SWS}}$ between two surfaces (S) of the same material immersed in water (W) indicates whether the material is hydrophobic or hydrophilic. Cationic polystyrene, anionic polystyrene, PDMS and polyamide are hydrophobic ($\Delta G_{\mathrm{AB}}^{\mathrm{SWS}} < 0$).

The temperature dependence of acid-base forces arises from the temperature dependence of the surface tension parameters. This work only considers the dependence for water and assumes that is negligible for solid materials. Van Oss [Oss2006] provided data for the parameters γ^{AB}, γ^+

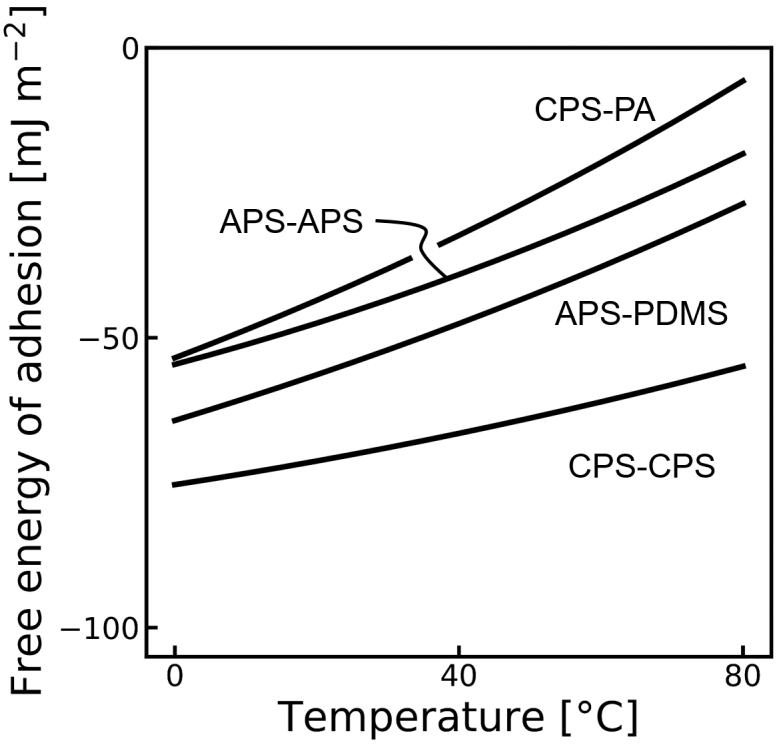

Figure 6.7: Free energy of adhesion of the acid-base interaction between two surfaces immersed in water depending on the temperature for different material combinations.

and γ^- at $0\,^\circ\mathrm{C}$, $20\,^\circ\mathrm{C}$ and $38\,^\circ\mathrm{C}$, respectively, shown in Figure 6.6. This data is extrapolated for higher temperatures using the following fitting functions:

$$\gamma^-(T) = 36.913 \exp\left(-0.018 T/^\circ\mathrm{C}\right) \quad (\mathrm{mJ/m^2}) \tag{6.27}$$

and

$$\gamma^+(T) = 19.08 \exp\left(0.0141 T/^\circ\mathrm{C}\right) \quad (\mathrm{mJ/m^2}) \tag{6.28}$$

Based on these data, the ratio between the acceptor and the donor surface tension parameter γ^+/γ^- increases with temperature. Van Oss explained the change of the ratio by a decrease in the cluster size of water at elevated temperatures [Van 2006]. The smaller the water clusters become, the more H atoms, as compared to O atoms, are exposed per water cluster, whereby the acceptor potential of water increases. As a result, polar or partially polar

compounds are more hydrated increasing their solubility in water. That is the cause e.g. for an increased ease of detachment of “dirt” from soiled surfaces when washed with warm rather than with cold water [Van 2008].

By applying the functions 6.27 and 6.28 to calculate the polar acid-base surface energy γ^{AB} according to Equation (6.22), the resulting graph follows the linear trend of the data. Derived from Jasper [Jasp1972], γ^{AB} decreases at the rate of about $1.08\,\mathrm{mJ\,m^{-2}}$ per $10\,^{\circ}\mathrm{C}$. As shown by van Oss [Oss2008], a temperature increase reduces the hydrophobizing capacity of water slightly and enhances the hydrophilic repulsion. The decrease in attractive interaction is consistent with atom force microscopy measurements, which determined that the strength of adhesive force reduces by 23% between 20 and $60\,^{\circ}\mathrm{C}$ between two hydrophobic surfaces [Stoc2015].

Besides the free energy of adhesion, the decay length of the acid-base interaction λ varies with temperature. The decay length is linked to the radius of gyration of clustered water, which is approximately between $0.6-1\,\mathrm{nm}$ at $20\,^{\circ}\mathrm{C}$ and an average cluster size of approximately 4.5 water molecules. At elevated temperatures, the cluster size of water decreases [Oss2006]. It is plausible to assume that the cluster size will completely tend toward the monomolecular form at the boiling point, which would lead to a radius of gyration of approximately $0.2\,\mathrm{nm}$ [Van 2008]. As the decay length correlates with the radius of gyration, the decay length of the acid-base interaction decreases with temperature. The more rapid decay of hydrophobic interactions with temperature confirms with experimental measurements of Israelachvili [Isra1984].

To the authors knowledge, there exists no correlation between the temperature and decay length yet. Therefore it is assumed that the decay length linearly decreases with the temperature T:

$$\lambda = \lambda_{20} + (\lambda_{100} - \lambda_{20}) \frac{T/^{\circ}\mathrm{C} - 20\,^{\circ}\mathrm{C}}{80\,^{\circ}\mathrm{C}} \tag{6.29}$$

Thereby, it is assume that the decay length λ_{100} at $100\,^{\circ}\mathrm{C}$ is $0.2\,\mathrm{nm}$ as explain before.

Remarks on the acid-base forces

Acid-base interactions play a critical role in the temperature dependency of colloidal interactions. This study shows that to the state of knowledge, the acid-base interaction can decisively change colloidal interactions with temperature. However, the theory relies on some assumptions, which have to be reviewed in future work.

One critical assumption is that temperature predominantly affects the acceptor and the donor surface tension parameter of water, whereas the surface tension parameters of the polymers are assumed to be constant. This assumption was adopted from van Oss [Van 2006]. However, van Oss used this assumption in the range $0-38\,^{\circ}\mathrm{C}$, whereas, in this study, the assumption is used over the temperature range of $20-80\,^{\circ}\mathrm{C}$.

A second related assumption is that the surface tension parameters change exponentially with temperature extrapolated from the measured results of van Oss [Van 2006]. To validate the exponential course, experimental measurements at temperatures above $38\,^{\circ}\mathrm{C}$ are of interest. A third assumption is the temperature dependence of the decay length of the acid-base interactions. This study assumes that the decay length declines with temperature based on experimental observations of Israelachvilli [Isra1984] and the theoretical considerations of van Oss [Van 2006]. However, how the decay length declines with temperature is to the best of the author's knowledge not resolved. Further, it remains questionable if the decline in decay length only depends on the aqueous phase or if the solid surface also plays a role.

It is of decisive importance for future research to evaluate these assumptions to get a more profound knowledge of the temperature dependency of acid-base interactions.

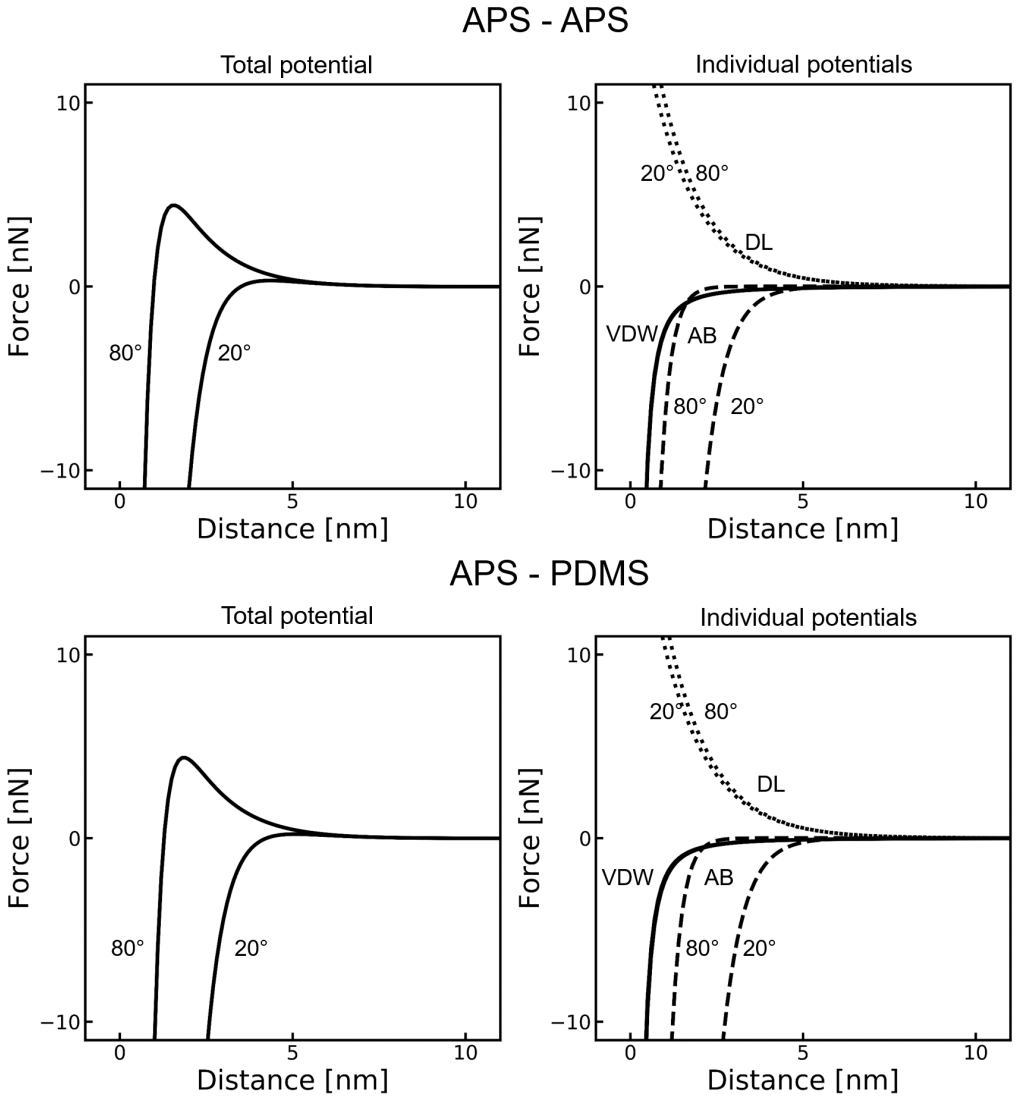

Figure 6.8: Temperature dependent forces for the anionic polystyrene/ PDMS system at 20 °C and 80 °C. The left side displays the total XDLVO force and right side the individual force of acid base (AB), double layer (DL) and van der Waals interactions in an aqueous 50mM salt solution

6.4 Results and discussion

Decreased particle deposition at elevated temperatures

Anionic polystyrene particles (APS) and a PDMS pore in a 50mM salt solution are investigated. Figure 6.8 shows the temperature-dependent potentials for the particle-wall interaction. On the left graphs, the total potential is displayed, whereas the right side shows the contributions of the individual force. At $20\,^{\circ}C$, the particle-particle (APS-APS) and the particle-wall (APS-PDMS) interactions are attractive, as shown in the total potential curve. The temperature dependence of the van der Waals contribution is negligible, which is observed in all considered systems in the present work. An increase in temperature increase minorly impacts the double layer contribution. However, the acid-base contribution becomes less repulsive when increasing the temperature, which is depicted in Figure 6.9. The reduction of the attractive acid-base potential results in a repulsive energy barrier at $80\,^{\circ}C$ temperature, which has to be overcome to get to the adhered state.

CFD-DEM simulations were performed at both temperatures. The CFD-DEM simulation snapshots in Figure 6.9 show that particle deposition occurs at $20\,^{\circ}C$ due to the purely attractive particle-wall potential. Since the particle-particle interactions are also purely attractive, the pore structure is clogged over the course of the simulation. Contrary, the simulations at $80\,^{\circ}C$ show that the particles are unable to overcome the repulsive energy barrier. For this system, a temperature increase diminishes the clogging of the pore. In this case, the acid-base contribution is the main cause of the temperature dependency of the clogging.

Enhanced particle deposition at elevated temperatures

Cationic polystyrene particles and a polyamide pore are considered in a $10mM$ salt solution. Figure 6.10 illustrates the particle-wall and particle-particle forces for this material combination, where on the left side are the total force, whereas the right side shows the contributions of the individual forces. The graphs show that the double layer force strongly re-

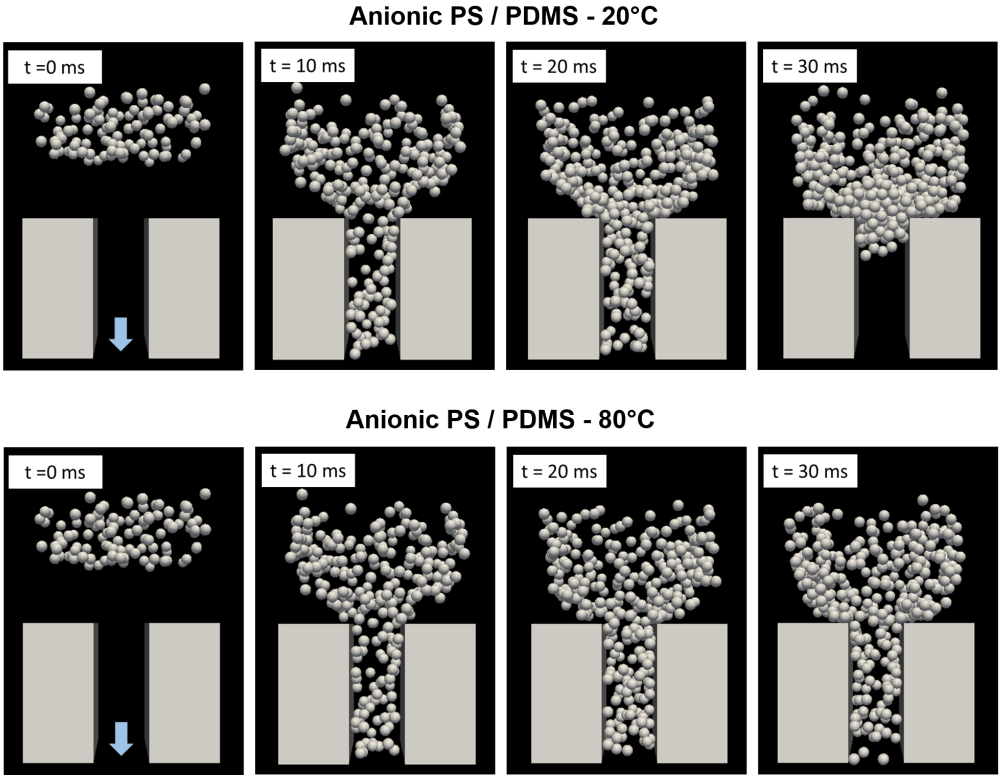

Figure 6.9: Deposition of anionic polystyrene particles on a PDMS pore at 20 °C and 80 °C at 0, 10, 20 and 30 ms.

duces with temperature. This results from the deprotonation of the amidine head groups of cationic polystyrene [Garc2006]. The hydrophobic acid-base contribution weakens at higher temperatures. Therefore, in this case, the double layer and acid-base interactions have counteracting effects with temperature. The total force profile shows that the energy barrier at 20 °C vanishes at elevated temperatures, which results from the strong weakening of the double-layer forces.

Figure 6.11 depicts snapshots of the CFD-DEM simulations with the applied potentials. At 20 °C, neither particle deposition nor aggregation occurs due to the energy barriers. In contrast, at 80 °C particles deposit and block the pore because of the attractive interaction potential. As a result, a temperature increase enhances particulate fouling in this system, which is mainly caused by the weakened double-layer contribution. The temperature effect is thus opposite to the previous system. Moreover, the double-layer contribution is the dominant cause for the temperature dependency

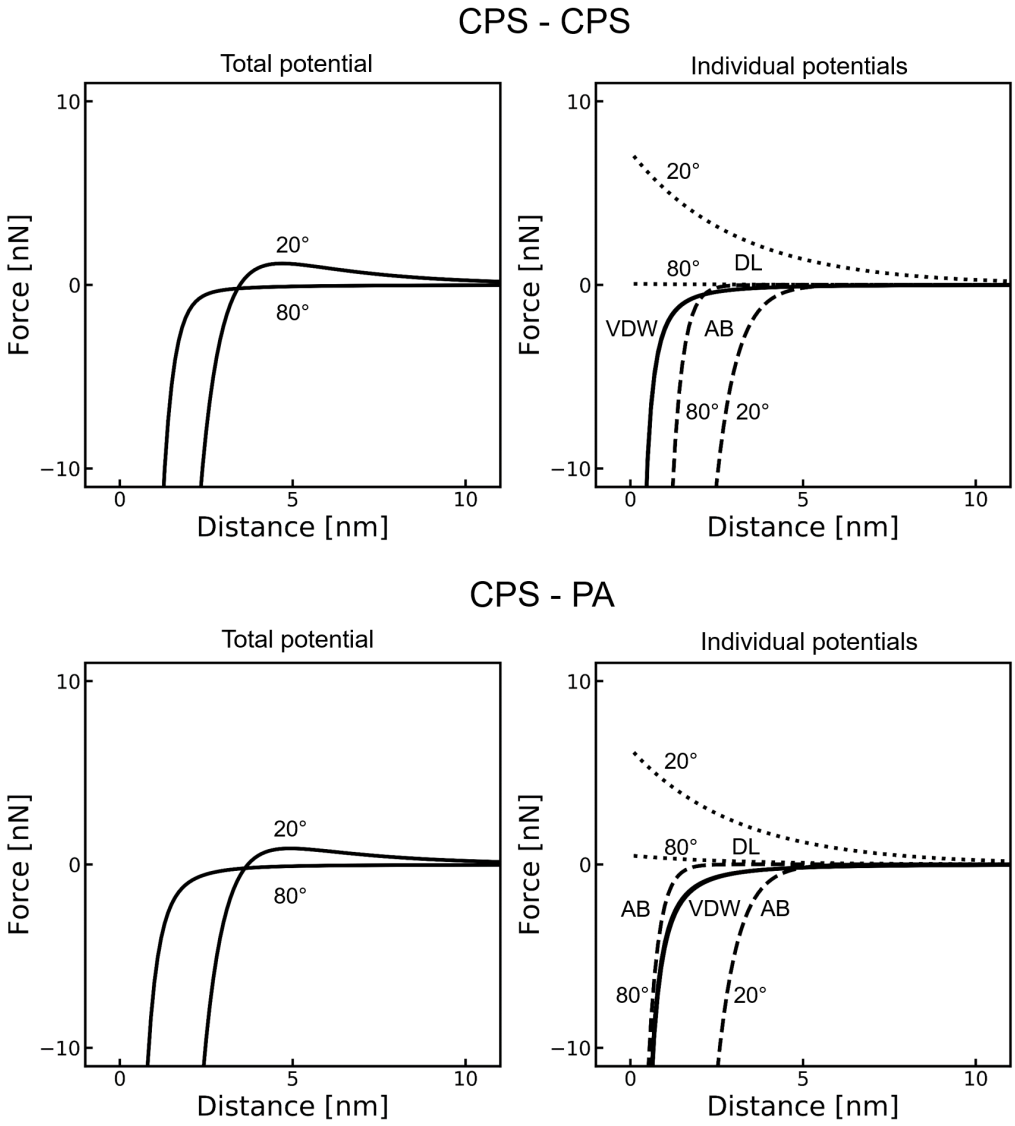

Figure 6.10: Temperature dependent forces for the cationic polystyrene/ polyamid system at 20 °C and 80 °C. The left side displays the total XDLVO force and right side the individual force of acid base (AB), double layer (DL) and van der Waals interactions in an aqueous 10mM salt solution

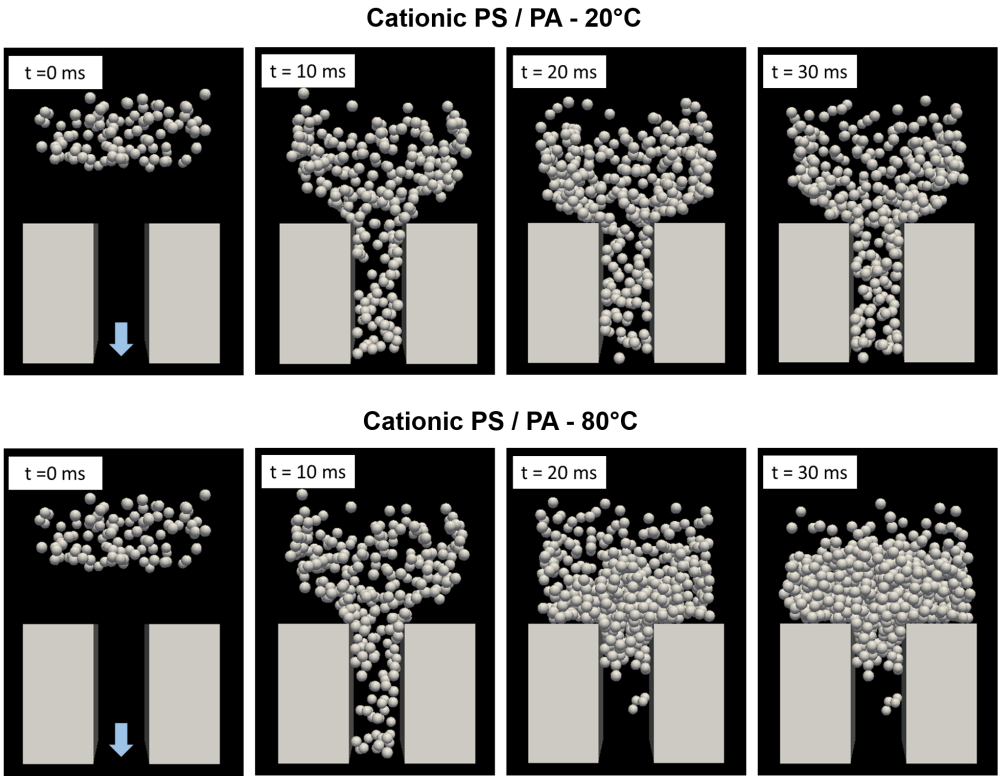

Figure 6.11: Deposition of cationic polystyrene particles on a polyamide pore at 20 °C and 80 °C at 0, 10, 20 and 30 ms.

and not the acid-base contribution.

6.4.1 Sensitivity analysis of temperature dependent properties

The presented theory relies on a variety of assumptions and parameters, which crucially impact the calculated colloidal potentials. A sensitivity analysis is performed to investigate how individual parameters can impact the temperature dependence of colloidal potentials. As example. the APS-PDMS system is chosen. To test the sensitivity, single parameters or single parameter pairs were changed while remaining the other properties constant.

Figure 6.12 summarizes the effects of the sensitivity of individual parameters on the colloidal interactions of particle-particle and particle-wall interactions. The individual sensitivities are explained in the following.

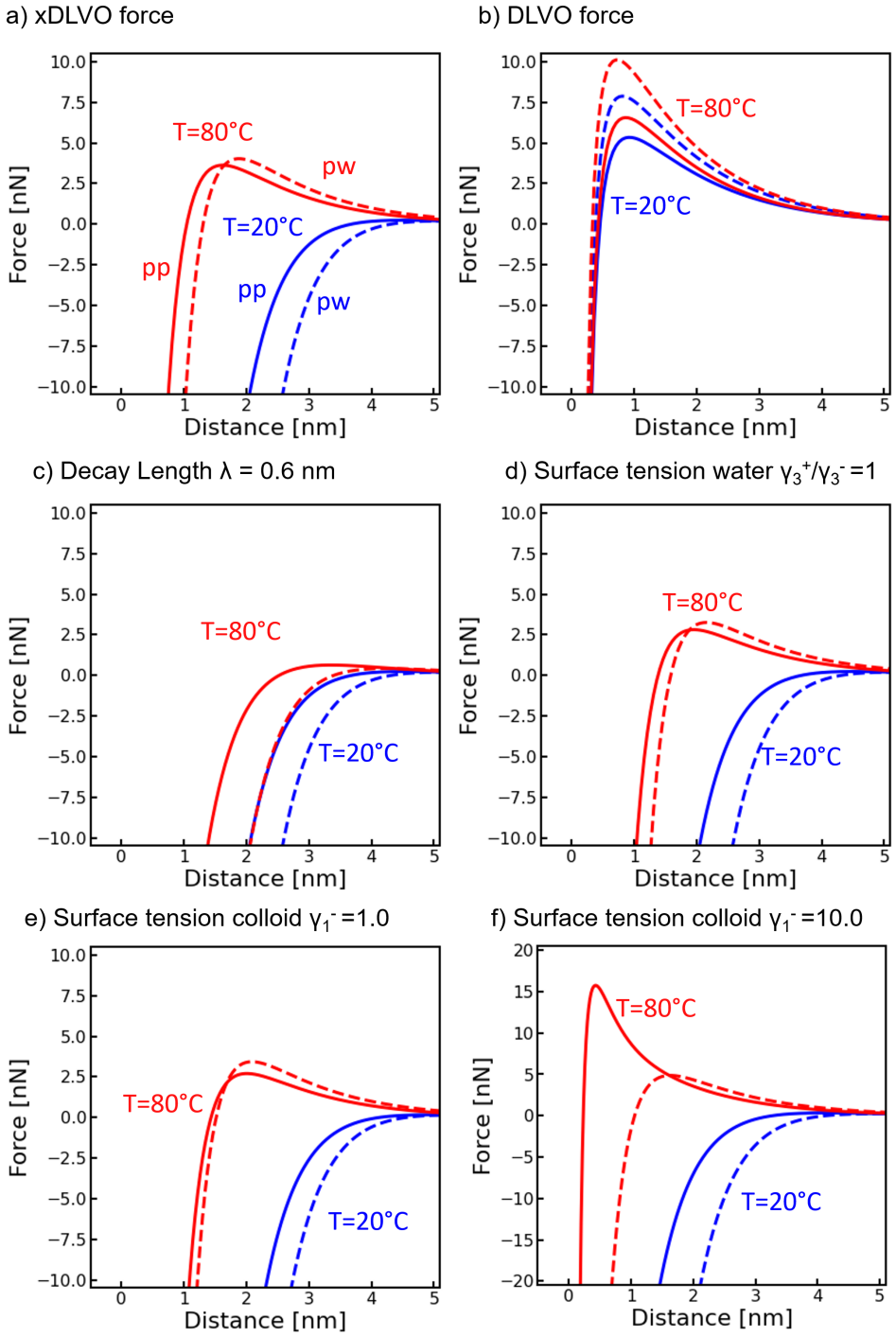

Figure 6.12: The sensitivity of the interaction forces of the APS-PDMS system towards specific properties at 20 and $80\,^{\circ}\mathrm{C}$. Figure a) presents the xDLVO used for simulations and serves as reference; Figure b) shows pure DLVO interactions; Figure c) assumes a constant decay length $\lambda = 0.6nm$ over the whole temperature range; Figure d) assumes constant surface tension properties of water at elevated temperatures; In Figure e,f), the electron donor component of surface tension property $\gamma_1^- = 1; 10$ of the APS is varied

Figure 6.12 a) serves as reference and represents the force plot used in the simulations. First, Figure 6.12 b) shows the interaction forces when only DLVO potentials (van der Waals and Double layer potentials) are considered and the acid-base interactions are neglected. Especially the neglect of the acid-base interactions for the PDMS-APS interactions is critical, because in experiments a high affinity between the particles and the PDMS is observed, which is well explained by attractive hydrophobic acid-base interactions (see Experiments in Chapter 5 or in literature e.g. [Must2016]). Nevertheless, the figure illustrates that pure DLVO potential result in repulsive interactions between the particles among themselves as well as with the PDMS wall. Additionally, the repulsive barrier raise with temperature caused by increasing surface potentials as explained in Section 6.3.2. In summary, considering only pure DLVO lead to increased repulsive interactions at elevated temperatures.

The temperature dependence connected to the acid-base potential are reviewed in the following. The temperature induced changes in the acid base interactions are connected to the surface tension properties of water, the decay length and the material constants for the APS and the PDMS.

First, the temperature dependence of the decay length is evaluated. There are no reliable data providing an exact cause of this relationship to the best of the author's knowledge. It is assumed that the decay length decreases with temperature according to equation 6.29 based on the considerations of Israeliachvili and van Oss [Isra1984; Van 2008]. To investigate the sensitivity towards the decay length, the decay length is assumed to be constant over the whole temperature range. Figure 6.12 c) illustrates the changes in interaction force resulting when keeping the decay length constant with temperature. The repulsive barrier at elevated significantly reduces under the assumption of a constant decay length. This demonstrates that the interaction force is very sensitive towards the changes in the decay length, which highlight the need for further investigation.

Second, the effect of the change in surface tension properties of water is considered. Van Oss stated that the ratio of the water's electron donator $\gamma-$ and the water's electron acceptor $\gamma+$ parameter change with temper-

ature [Van 2006; Van 2008]. The provided data for $0{,}20$ and $38\ ^{\circ}\mathrm{C}$ are extrapolated to $80\ ^{\circ}\mathrm{C}$ in this thesis, which contains a great uncertainty. To investigate the sensitivity of the colloidal potentials on this extrapolation, the $\gamma-$ and $\gamma+$ were assumed to be the same as at $20\ ^{\circ}\mathrm{C}$. Figure 6.12 shows the resulting interaction forces for the particle-wall as well as the particle-particle interactions. The repulsive barrier reduces due to the change in the surface tension properties. The reduced repulsive barrier is mainly caused by the multiplication of the components $\sqrt{\gamma_3^+} \cdot \sqrt{\gamma_{1/2}^-}$ (see equation 6.23). However, the tendency of increased repulsive strength at elevated temperature remains unchanged.

Third, values for the material properties of the APS particles can significantly differ depending on the used particles. For APS polystyrene a series of surface tension properties can be found in literature, which is expected since surface tension properties scales with e.g. the manufacturing conditions, surface groups and the surface group density. Thereby, the particle's surface tension acceptor parameter γ_1^+ only slightly varies between $0-2$ [Boua1998; Van 2006; Must2016]. Contrary, values for the particle's surface tension donor parameter γ_1^- range from $1-13$ [Boua1998; Van 2006; Must2016] and even become higher depending on the density and nature of the polar group on the surface. Two parameters of the particle's surface donor property $\gamma_1^- = 1; 10$ are considered. Figure 6.12 e,f highlights strong sensitivity towards the particle's surface tension parameter γ_1^-. Especially at $\gamma_1^- = 10$, the repulsive barrier of the particles increases significantly. The increased repulsive barrier is caused by the multiplication of the components $\sqrt{\gamma_3^+} \cdot \sqrt{\gamma_1^-}$, which is a scale for the hydrophilicity of the material (see equation 6.23). This signifies that if the used particles posses more hydrophilic properties, according to theory, increased repulsive interactions are expected at elevated temperatures.

The sensitivity analysis demonstrates that the temperature dependent colloidal interaction forces significantly scale with the chosen material properties. This emphasizes that the calculated potentials are to be regarded with caution and the presented theory only represents trends towards the temperature dependency.

6.5 Conclusion

The present study investigates how temperature influences colloidal clogging phenomena at a single-channel constriction. Temperature-dependent models for the XDLVO forces are integrated into a CFD-DEM framework. The clogging behavior at the constriction varies to a great extent depending on the applied material combination and respective interaction potentials. The potential energy barriers between the colloids and the membrane walls are essential to prevent particle deposition, and energy barriers between colloids can prevent particle coagulation. In the considered colloid-wall systems, the height of energy barriers both increased or decreased when increasing temperature depending on the material. A temperature change can enhance or diminish the clogging.

The effect of temperature on the energy barrier depends on how the individual XDLVO forces react to temperature changes and how they interact in the total interaction potential. The temperature dependency of van der Waals forces is negligible: their influence is small compared to double layer and acid-base forces. The influence of temperature on double-layer forces depends on the behavior of the zeta potential. Unfortunately, data on temperature-dependent zeta potentials are only rarely available in the literature. Acid-base forces become less attractive and more repulsive at elevated temperatures. However, the calculated potentials should be considered with caution, as they are sensitive to the chosen parameters. The calculation of the potentials primarily describe trends.

In both discussed material combinations, the temperature dependence of the surface potentials controls the clogging probability. The counteracting hydrodynamic effects of lubrication and viscous drag with temperature minorly affect the clogging. However, the filtration velocity is not varied, and only two specific temperatures were regarded, which does not allow a final conclusion on the temperature dependency of the clogging of the hydrodynamic side.

In summary, the work discloses the influence of temperature on colloidal clogging. The interplay between temperature-dependent interaction poten-

tials makes it tenuous to draw simplistic generalizations about the temperature effect because the effect varies for every colloid-channel system.

While the simulations help to predict the temperature-dependent jamming and may serve to select the appropriate material systems, it also shows the need for more temperature-dependent property data and experimental transport studies for verification of the observations obtained through the simulations, which are presented in the following chapter.

7 How does temperature effect colloidal clogging ? - Experimental study

The experiments presented in this chapter were developed in cooperation with M.Sc. Anna Kalde and our master student Stephan Mushold and were presented in the master thesis:
S. Mushold “Temperature and charge dependent deposition and resuspension of colloids in microfluidic experiments and in CFD-DEM simulations [Master thesis]”. RWTH university(2020).

7.1 Introduction

The temperature can play a crucial role in colloidal interactions and deposition. The previous chapter evaluates the impact of temperature on colloidal interactions and hydrodynamic properties. By applying numerical simulation, the role of temperature on colloidal clogging is evaluated for two material combinations.

This chapter targets to evaluate the role of temperature with the help of microfluidic experiments. A tempered microfluidic setup is developed to investigate the clogging and backwash at elevated temperatures. 4 µm sized polystyrene sulfate particles were filtered on a PDMS pore structure at varying temperatures. Subsequently, backwashing of the pore structure is performed providing information about the stability of the cake layer and the interparticle interactions. This chapter will show that the simulation results from the previous chapter can not be verified with the experiments. Contrary, the experiments show contradicting effects on the presented theory.

7.2 Material and methods

This section describes the microfluidic device's setup to perform microfluidic filtration at elevated temperatures and used materials.

7.2.1 Chip design

A microfluidic device was designed and manufactured to investigate pore clogging at elevated temperatures. The microfluidic chip is manufactured similarly, as described in Chapter 5. The microfluidic channel's negative was printed with a Photonic Professional GT system (Nanoscribe GmbH) on microscopy slides by two-photon lithography. By casting PDMS onto the negative, an open channel was created and subsequently closed by bonding the PDMS body onto a glass slide. The centerpiece of the microfluidic device was a membrane-mimicking structure consisting of 11 pores with a

pore size of 20x50x200 µm. The chip contained three ports to the outside for filtration and backwash, as explained in Chapter 5. The fluid flows in a meander structure towards the pore structure to allowing heating of the fluid from outside. Figure 7.1 illustrates the rendered microfluidic flow channel containing three ports, two meander structures, and the membrane-mimicking pore structure magnified on the right side of the Figure. The fabricated microfluidic chip (left) and the pore structure magnified with a microscope (right) are shown in Figure 7.2.

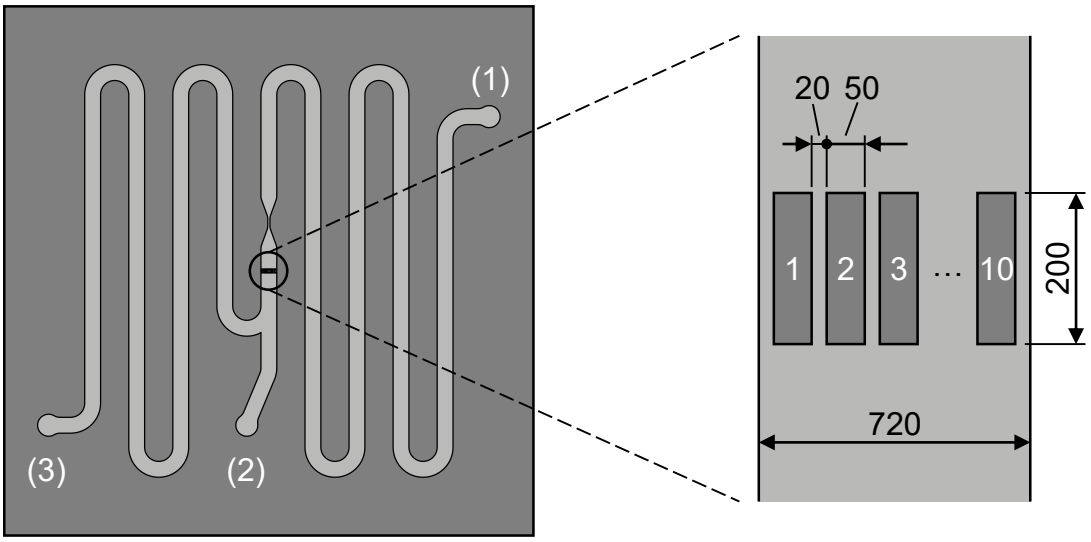

Figure 7.1: Left: Internal structure of the microfluidic chip. Numbers (1), (2), and (3) indicate inlet and outlet ports. Right: Detail of the filtration section. Numbers 1 to 10 indicate pillars which define the adjacent pores. Dimensions are in micrometers. The height of the channel is 50 µm.

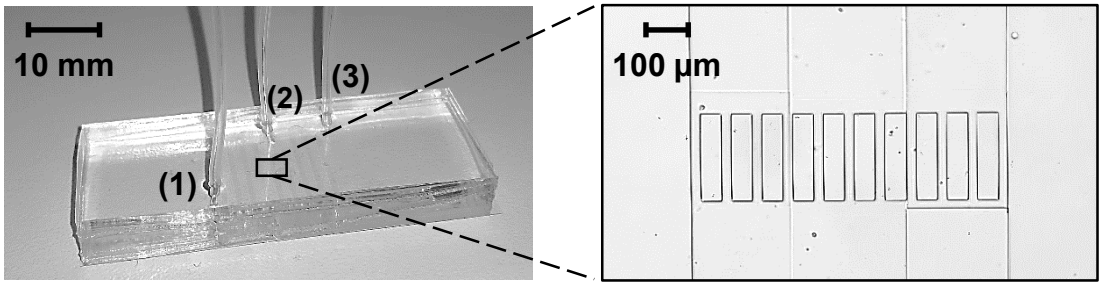

Figure 7.2: Left: Image of the microfluidic chip. Numbers (1), (2), and (3) indicate inlets and outlets. Right: The filtration section taken with a microscope with 10 fold magnification.

7.3 Experimental Setup and Procedure

An overview of the experimental setup is given in Figure 7.3 and explained in the following paragraphs.

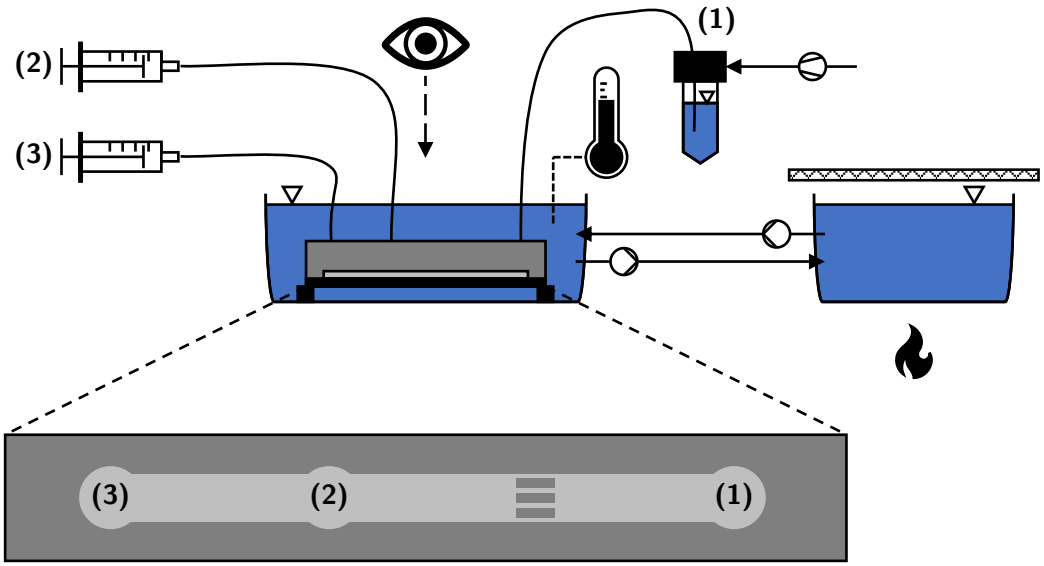

Figure 7.3: Top: Schematic of the experimental setup in side view. Bottom: Simplified depiction of the channel within the microfluidic chip in top view. (1), (2), and (3) indicate inlet and outlet ports.

Heating and Temperature Control The filtration suspension inside the microfluidic channel is heated and kept at the desired temperature to investigate the fouling at elevated temperatures. The microfluidic device is submerged into a tempered water bath to heat the suspension, as shown in Figure 7.3. Thereby, the suspension inside the microfluidic channel is heated while passing through the channel. The length of the meander structures ensures that the suspension reaches the temperature of the heated water bath. A tempered circulating water flow controls the temperature of the water bath. Therefore, a glass petri dish (diameter 180 mm, height 30 mm) was filled with de-ionized water, covered with aluminum foil, and heated to the desired temperature on an IKA® C-MAG HS 7 hotplate stirrer (heating temperature 240 °C) with a magnetic stir bar (diameter 6 mm,

length 20 mm). The temperature was measured with an IKA® ETS-D5 temperature sensor. Upon reaching the set temperature, de-ionized water was continuously pumped between the petri dish and the water bath using an Ismatec® ecoline VC-MS/CA8-6 peristaltic hose pump (Cole-Parmer GmbH, Germany).

Deaeration A key challenge to perform microfluidic experiments at elevated temperatures is gas evolution inside the flow channel. Dissolved gas can evolve at elevated temperatures due to the lower solubility of gases in the fluid phase and the PDMS. Therefore, the solution and the device were deaerated to prevent gas evolution.

Before the experiments, the 25 ml KCl solution and approximately 3 ml of the relevant suspension were filled into 50 ml and 15 ml Falcon (conical centrifuge) tubes, respectively. The Falcon tubes were kept in an upright position, and their lids were loosely put on top.

Both, the solutions and the microfluidic chip were deaerated in a desiccator for 1 h. Both solutions were weighed before and after deaeration to rule out concentration changes due to water evaporation. The weight of the solution remained nearly constant proving that the solution concentration remained constant.

Then, two 10 ml syringes (Omnifix ® Solo, B. Braun) were filled with 2 ml and 8 ml deaerated KCl solution, respectively, and sealed with combistopper closing cones (B. Braun). The microfluidic chip was fixated in a 3D printed support, and both were submerged in a water bath (crystallization beaker; DURAN® glass, DWK Life Sciences) with approximately 150 ml de-ionized water. The beaker was then placed under an Oxion Inverso microscope (10 fold magnification, Euromex Microscope BV).

Filling and suppression of gas bubble formation Syringe pumps generate the flow of solutions inside the microfluidic channel. A Harvard Apparatus PHD Ultra™and Harvard Apparatus Pump 11 Elite syringe pump were equipped with the two aforementioned 10 ml syringes filled with 2 ml, and 8 ml KCl solution via cannulas connected to ports (2) and (3), respec-

tively. Then, the microfluidic chip was flushed with KCl solution operating both syringe pumps at $+100\,\mu l\,min^{-1}$ where the plus sign indicates infuse operation. After approximately $4\,min$, both syringe pumps were stopped, and the tubing connected to port (1) was connected to the aforementioned $15\,ml$ Falcon tube filled with deaerated suspension. Besides deaeration, gas formation is suppressed by applying counter pressure. The system was loaded with $+500\,mbar$ overpressure using a self-made constant pressure unit connected to the $15\,ml$ Falcon tube and fed from an external compressed air line to suppress the degassing of dissolved gases inside the chip. An airtight connection between tubing from port (1), $15\,ml$ Falcon tube, and constant pressure system was established using an Elveflow microfluidic adapter and matching fittings.

Filtration. The filtration procedure was initiated by setting the Harvard Apparatus PHD Ultra™to $-9.72\,\mu l\,min^{-1}$ corresponding to an empty channel velocity of $4.5\,mm\,s^{-1}$). As soon as the first particles reached the filtration section, image recording and time measurement were started simultaneously ($t = 0$). Single images were recorded every $30\,s$. The recording was stopped as soon as the pores were completely blocked or the latest after $2\,h$. The Harvard Apparatus PHD Ultra™syringe pump was yet not stopped to avoid flow reversal which could cause cake detachment. In case experiments were run at elevated temperatures, the crystallization beaker's temperature was kept constant by manually adjusting the speed of the hose pump.

Backwash Backwashing was initialized by setting the syringe pump connected to port (3) to a volumetric flow rate of $+9.72\,\mu l\,min^{-1}$. After approximately $5\,s$, the syringe pump connected to port (2) was stopped. The time measurement was started ($t = 0$) when the flow direction of the particle stream reversed (approximately after $30\,s$ to $90\,s$). The volume flow rate was then gradually doubled every $2\,min$ for a total of $16\,min$ in eight consecutive steps.

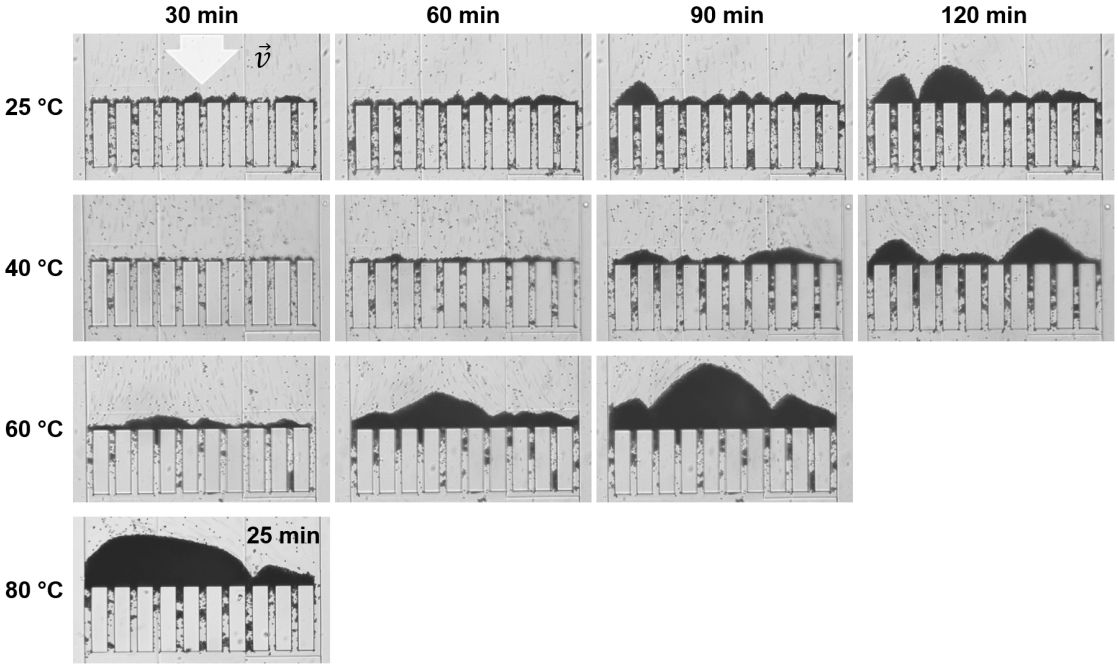

Figure 7.4: Fouling of 4 µm sized polystyrene sulfate particles on PDMS pore structure at 20, 40, 60 and $80\,°C$ over time in a 50 mM KCl solution.

7.3.1 Particle solution

For the filtration, a $0.1\ w\%$ suspension of 4 µm sized anionic polystyrene sulfate (aPSS) particles in $50 mM$ KCl solution was applied. A surfactant-free concentrated suspension of $39\,g\,L^{-1}$ sulfate latex beads in de-ionized water (Invitrogen, Eugene, OR USA, purchased through ThermoFisher Scientific; lot number: 1876103) was diluted to $0.1\ w\%$ with $50\ mM$ KCl solution on a gravimetric basis. The salt concentration was diluted by the de-ionized water from the purchased concentrated suspension, which results in the final KCl concentration of $48.7\ mM$ of the suspension.

7.3.2 Microfluidic filtration

First, microfluidic filtration experiments were conducted at varying temperatures. 4 µm - polystyrene sulfate particles were filtered on a PDMS surface with a filtration velocity of $4.5\,mm\,s^{-1}$ at 25, 40, 60 and $80\,°C$.

Figure 7.4 shows the cake development at the specific temperatures over time. The filter cake developed for $30 - 120$ minutes, which is in a similar

range than in the experiments of Bacchin et al. [Bacc2014a]. However, the long filtration time is very different from the filtration experiments presented in Chapter 5, in which clogging propagates in only $1-2$ minutes. The difference in filtration time can be explained by the more repulsive nature of the polystyrene sulfate particles, which have, according to the manufacturer Thermo Fisher Scientific, a critical coagulation concentration (CCC) of $200-300mM$. Contrary, the polystyrene particles used in Chapter 5 coagulate at ionic concentrations below $100mM$.

More importantly, the experiments revealed that elevated temperatures enhance the fouling kinetic. At $25\,^{\circ}\mathrm{C}$, a pronounced pore-blocking developed over a period of $90-120$ minutes, whereas it only took 30 minutes at $80\,^{\circ}\mathrm{C}$. The elevated deposition contradicts the simulation findings of the APS-PDMS material system explained in Chapter 6. It has to be noted that the interaction potential characteristic of the APS particles used in the simulation does not match with the polystyrene sulfate particles since the critical coagulation concentration of the APS is below $100mM$ as explained before. However, the trend of reduced or diminished deposition at elevated temperatures for the APS-PDMS system should be transferable to the polystyrene sulfate particles, which is not the case. Therefore, there is a mismatch between theory and experimental results. One simple explanation could be that particles resuspend more frequently at lower temperatures due to the higher fluid viscosity resulting in higher drag forces at lower temperatures. Frequent particle resuspension would delay the fouling kinetic and could explain lower fouling kinetics at lower temperatures. Indeed, particle cluster resuspension was frequently observed at $25\,^{\circ}\mathrm{C}$, which is shown in Figure 4.11 in Chapter 4. Contrary at $80\,^{\circ}\mathrm{C}$, particle or cluster resuspension was not observed. However, the backwash experiments at elevated temperatures presented in the next section reveal that particle resuspension can not be the only explanation for the mismatch between theory and experiment.

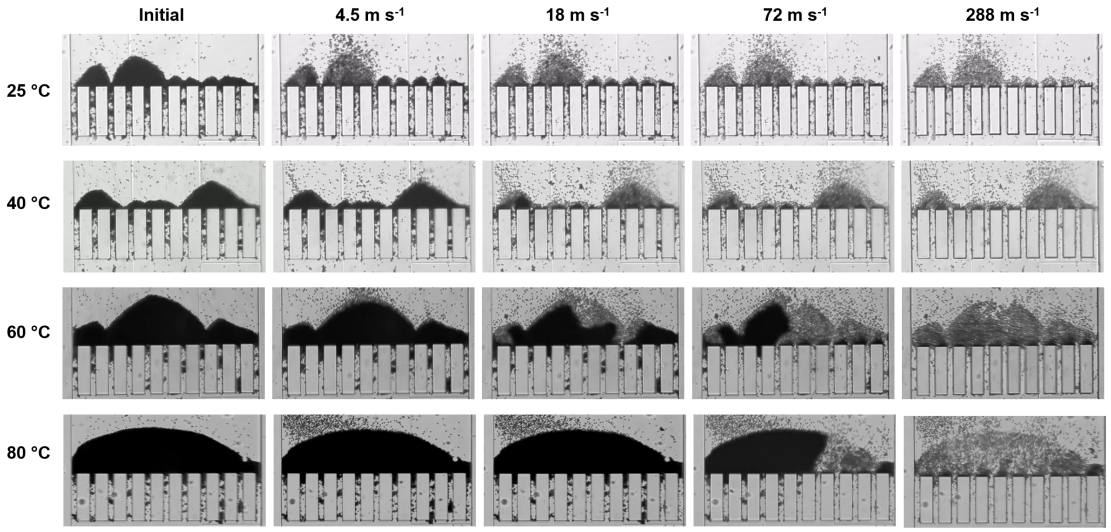

Figure 7.5: Backwash of $4\,\mu m$ sized polystyrene sulfate particles on PDMS pore structure at 20, 40, 60 and $80\,°C$ with raising backwash velocities in a 50 mM KCl solution.

7.3.3 Backwash at elevated temperatures

Backwash at elevated temperatures is performed to obtain more information about the temperature dependence of the polystyrene sulfate - PDMS system. Therefore, the flow rate is inverted and gradually doubled every two minutes.

Figure 7.5 shows the filter cake at raising backwash velocities and temperatures. At $25\,°C$, the filter cake nearly completely decomposed at low backwash velocities. Particle assemblies were completely washed out. Only particles on the opposite side of the flow direction remained attached to the pore structure due to shadowing effects. Further, some particles stuck to the bottom of the flow channel. Similar backwash characteristics were observed at $40\,°C$. Similarly, even at low backwash flow rates, almost all particles were washed out. Contrary, at $60\,°C$ and $80\,°C$ the filter cake remained intact at low backwash velocities ($4.5 - 9\ mm\,s^{-1}$). Only a top layer of particles detached from the fouling layer. These particles were only loosely bound or unbounded to the filter cake. Only a significant increase in backwash velocity caused the filter cake to break away at elevated temperatures. Large agglomerates broke from the filter cake at elevated temperatures, which contrasts with the loose particle resuspension observed

at lower temperatures.

One explanation for the higher backwash rates necessary at elevated temperatures could be decreased viscosity and, consequently, lower drag forces at higher temperatures. However, reduced drag forces provide an insufficient explanation for the results. Since on the one hand, the viscosity only reduces by a factor of approximately 3 between 25 and $80\,^{\circ}\mathrm{C}$, while the required backwash velocity for particle resuspension is at least ten times different. On the other hand, a distinctive difference between the backwash mechanisms at low and high temperatures was observed.

Figure 7.6 displays the dominant backwash mechanism observed at 25 and $40\,^{\circ}\mathrm{C}$. At low backwash velocities ($4.5 - 9\ \mathrm{mm\,s^{-1}}$), a single pore clogging broke open. The single pore clogging breakage induces washing out of a swarm of individual particles and small agglomerates. This swarm-like behavior of individual particles during backwash is a strong indication that the interactions between particles were majorly repulsive. Only individual particles exhibit weakly, attractive interactions. These weakly attractive interactions between the particles are presumably to be responsible for pore blockage during filtration. After the pore blockage, repulsive particles deposited causing a pile formation. The pile is only stabilized by the hydrodynamic flow and not by inter-particular bonds. Therefore, this pile is decomposed into small agglomerates and individual particles by reversing the flow. Pile formation of primarily repulsive particles explains the relatively long filtration time and the low backwash velocities necessary for resuspension at low temperatures.

Contrary at 60 and $80\,^{\circ}\mathrm{C}$, the backwash mechanism differ fundamentally. At 60 and $80\,^{\circ}\mathrm{C}$, only a layer of unbounded individual particles resuspend at low backwash velocities. Afterward, the filter cake remained intact for low and medium backwash rates. At higher backwash rates, big particle agglomerates broke from the filter cake highlighted in Figure 7.7. The breakage of large particle agglomerates proves strong, attractive interactions between the particles.

The increased attractive particle-particle interactions at elevated temperatures contradict the APS-PDMS system's calculations in Chapter 6.

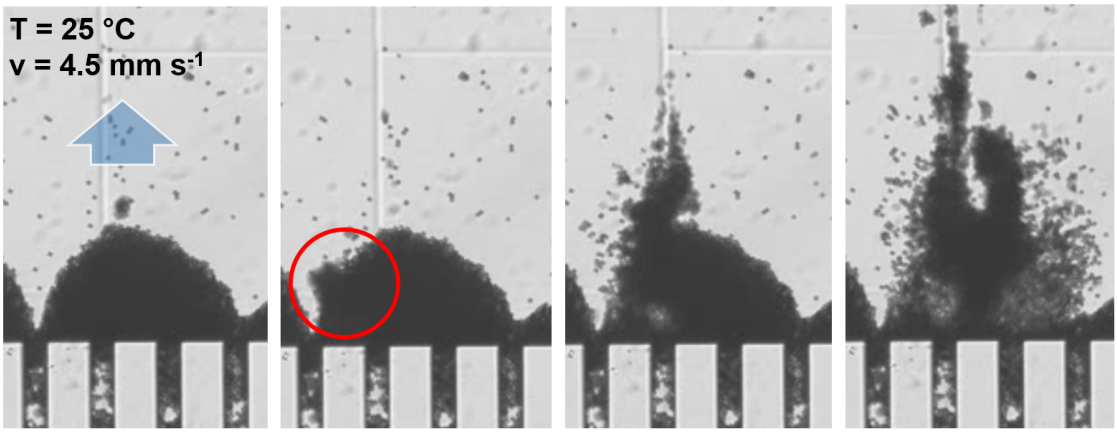

Figure 7.6: Backwash mechanism at $20\,^{\circ}\mathrm{C}$ at a backwash velocity smaller than 4.5 $\mathrm{mm\,s^{-1}}$. Breakage of a clogged pore induces resuspension of a particle swarm .

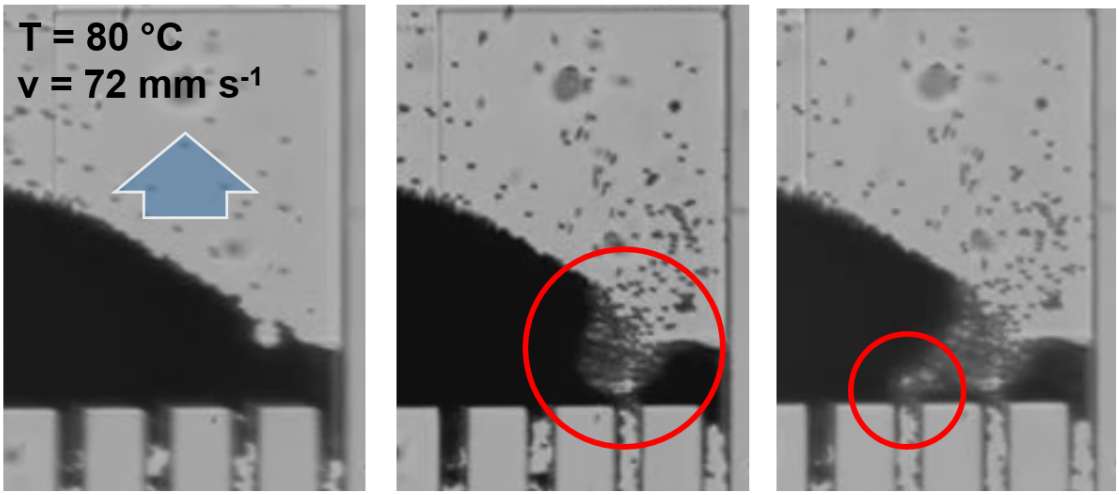

Figure 7.7: Backwash mechanism at $80\,^{\circ}\mathrm{C}$ at a backwash velocity of 72 $\mathrm{mm\,s^{-1}}$. Breakage of particle agglomerate.

Based on the theory, the attractive acid-base interactions decrease through increasing temperature, which would lead to a reduced attractive forces. Thus, the theory of temperature-dependent fouling described in Chapter 6 is incomplete and partly incorrect. The next section will discuss possible reasons for the mismatch between theory and the experiments.

7.3.4 Possible explanation for the mismatch between theory and experiments

This chapter demonstrates a mismatch between the experimental results and the theoretical developments. Whereas the numerical results calculate a reduced fouling probability for the APS-PDMS system, the experimental results indicate a reverse trend. This mismatch between theory and experiment can be based on various reasons, which are presented in the following.

First, the particles are electrostatically stabilized by sulfate groups. Sulfate groups are known to hydrolyze to uncharged hydroxyl groups at high temperatures [Seeb1995]. Seebergh et al. [Seeb1995] treated among others polystyrene sulfate particles with $120\,^{\circ}\mathrm{C}$ for $4 - 12$ h. The heat-treated particles possessed a critical coagulation concentration in a potassium nitrate solution of $15\ mM$. Contrary, they measured a critical coagulation concentration of $300\ mM$ for the untreated particles. Besides the hydrolysis of the sulfate groups, Seebergh et al. [Seeb1995] attribute the changes due to heat treatment with a hairy layer on the polystyrene surface. The hairy layer is assumed to be a result of protruding polymer chains on the polystyrene surface [Van 1987]. The concept of a hairy structure is one possible explanation that measured zeta potential of latex particles often pass through a maximum as ionic strength is increased [Elim1995]. The hairy layer would give rise to an additional electrosteric stabilization of the polystyrene particles. The authors state that heat treatment removes the hairy layer on the surface, reducing the stability of the suspension [Seeb1995]. The hairy layer's removal could be an explanation for the enhanced aggregation during filtration at elevated temperatures. Against the theory of fuzzy layers

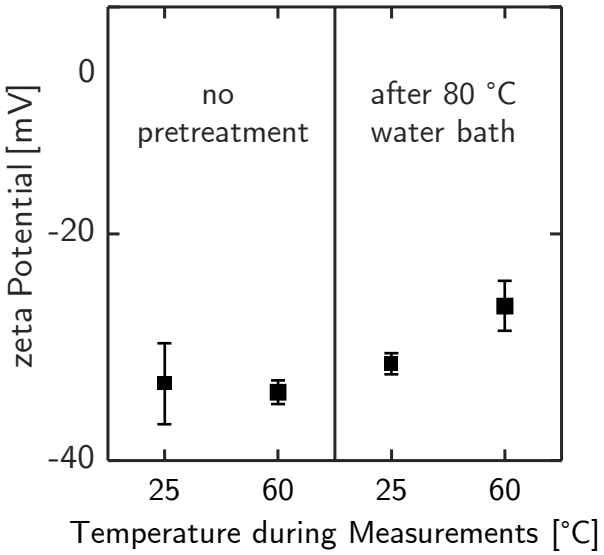

Figure 7.8: Zeta potentials of used polystyrene sulfate particles measured at 25 °C and at 60 °C. Left: Without pretreatment. Right: After 30 min heat treatment in 80 °C water bath. Each probe measured in triplets.

and hydrolyzing, the particles are stable at elevated temperatures according to the particle's manufacturer (Invitrogen). Furthermore, the manufacturer recommends in case of contamination to sterilize the polystyrene particles before proceeding with pasteurization for 24 hours at $78 - 80$ °C. If the surface groups hydrolyze or an electrosterically-stabilizing layer is removed, the particle would aggregate due to the proceeding, making them unusable in the following.

To analyze the particles' stability, zeta potential measurements of a diluted suspension of the sulfate stabilized particles in tap water were conducted at 25 °C. Besides, the same measurements were conducted with a diluted suspension of sulfate stabilized particles after heat treatment in a 80 °C water bath for 30 min and subsequent cooling down to room temperature. Each probe was measured in triplets. The measured average zeta potential values and their respective standard deviations are illustrated in Figure 7.8.

Measurements reveal that the zeta potentials of the used particles are almost constant after 80 °C heat treatment referring Figure 7.8. Only small changes in the zeta potential are measured at 60 °C after heat treatment at 80 °C. The deviation might result from electrode corrosion of the sam-

ple container, which was not replaced between measurements at 25 °C and 60 °C. Apart from that, the standard deviation between the measurements lies within experimental error. Thermal degradation of electrostatically-stabilizing surface groups would significantly reduce the magnitude of the zeta potential. Hence, the constant zeta potentials indicate the thermal stability of the used particles within the applied temperature range.

Second, the current theory neglects the influence of dissolved gases. In literature, the existence and the role of nanobubbles forming on hydrophobic surfaces are critically discussed [Atta2003]. Some scientists attribute long-range hydrophobic interactions to nanobubbles. The main concern in the nanobubbles theory is to account for the stability of the nanobubbles due to the high Laplace pressure inside the nanobubble [Atta2003]. If existent, nanobubbles would enhance coagulation and adhesion of hydrophobic surfaces since attached nanobubbles would coalesce to form a stable vapor bridge between the two hydrophobic surfaces and result in an attractive capillary force. Concerning the performed experiments, dissolved gases in the polymers and the fluid may form nanobubbles on the surface during the suspension's heating due to the reduced solubility of gases at elevated temperatures. The formation of the nanobubbles on the hydrophobic surfaces could explain increased deposition's experimental observation at elevated temperatures.

Third, the theory is based on various assumptions concerning the acid-base potential, such as the temperature independence of the material constants and change in decay length (for more detail, see Section 6.3.2). If the polymer surface changes significantly with temperature, this could explain the difference between theory and experiment.

As none of these hypotheses could be proven so far, the exact reason for the mismatch between theory and experimental results remains unsolved.

7.3.5 Interpretation of the experiments concerning the interactions

The applied theory of the xDLVO potentials cannot be reconciled with the experimental results. The previous section offers the first explanations of the reasons for the discrepancy between experiment and theory. However, these approaches lack a mathematical description. Although it is difficult to make quantitative statements about the actual potential, qualitative statements can be extracted from the results. These statements will be discussed in this section.

The experiments provide insights into the temperature dependency of interparticle interactions of the polystyrene sulfate particles summarized in Table 7.1. The filtration reveals that the fouling cake grew over hours. The slow growth indicates a repulsive barrier between the particles. Moreover, small agglomerates and single particles break up during the filtration and the backwash. The particle agglomerates break mainly at interparticle bonds, which indicates weak cohesion. Weak cohesion indicates either adsorption in a secondary minimum or a weak primary minimum. Contrary at $80\,^{\circ}\mathrm{C}$, the filter cake grew much faster than at $25\,^{\circ}\mathrm{C}$. During the backwash, a loose layer of individual particles resuspended at $80\,^{\circ}\mathrm{C}$, indicating a small energy barrier between the particles. Particularly noticeable is that only a small amount of particles are washed away at low backwash rates. The breaking up of whole agglomerates occurs at high velocities, which is a strong sign that the particles are located in a deep attractive minimum. That the particles at high temperature are captured in a deep attractive minimum is the crucial difference to the low temperatures, where the particles are only weakly or unbounded.

Besides the particle-particle interaction, the particle interactions with the PDMS pore structure can be reviewed. The particle-pore interactions do not change significantly with temperature in contrast to the interparticle interactions. Fast and robust adhesion to the PDMS was observed in all temperature ranges. When attached, most of the particles remained on the PDMS structure and mainly did not resuspend during filtration. The

Table 7.1: Qualitative statements about interactions between anionic polystyrene particles.

T [°C]	Observation	Interpretation	Force plot
25	Slow fouling layer growth	High energy barrier	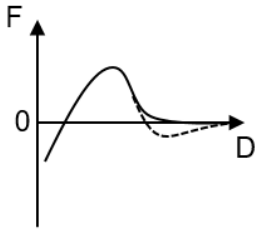
	Particle resuspension during filtration	Secondary minimum or weak attraction	
	Detachment of particles at low flow velocities during backwashing	Weak attractive minimum	
80	Fast fouling layer growth	Small or no energy barrier	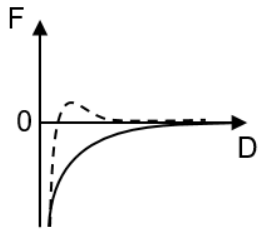
	Loose particle layer detaches upon reversal of flow	Secondary minimum or weak attraction	
	Detachment of clusters from fouling layer at high flow velocities during backwashing	Strong attractive minimum	

strong adhesion to the PDMS surface is evidence for a deep attractive minimum attributed to the hydrophobic interaction between the particles and the PDMS. This statement is confirmed by the fact that particles remained attached to the PDMS structure after the backwash.

In summary, the temperature-related changes in fouling and backwash behavior are mainly caused by particle interactions. There are clear indications that the particle-particle interactions become more attractive at elevated temperatures causing enhanced deposition and agglomeration. The theory used so far does not describe increased attractive interactions with temperature. Hence, sophisticated measuring techniques accompanied by an extension or a new development of a theory describing the physical/chemical processes are crucial in future studies to understand the temperature-dependency of colloidal fouling.

Table 7.2: Qualitative statements about interactions between anionic polystyrene particles and PDMS.

T [°C]	Observation	Interpretation	Force plot
25	Fast deposition on PDMS	Small or no energy barrier	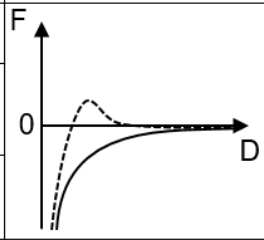
	Minor/ no resuspension from PDMS during filtration	Strong attractive minima	
	Some Particles remain after backwash	Strong attractive minima	
80	Fast fouling layer growth	Small or no energy barrier	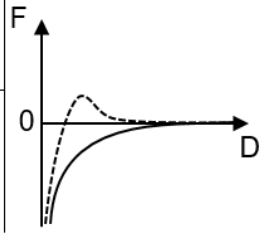
	Particles not completely removed after backwash	Strong attractive minima	

7.4 Conclusion

This chapter presents microfluidic experiments investigating the role of temperature on colloidal clogging. The experiments were performed with $4\,\mu m$ sized polystyrene sulfate particles. A setup to control the microfluidic chip's temperature was developed to characterize the fouling at 25, 40, 60 and $80\,^{\circ}C$. The experiments reveal that the colloidal deposition of the polystyrene sulfate particles was enhanced at elevated temperatures. This behavior contradicts the numerical results presented in the chapter before. Backwash was performed to gain more information about the temperature dependency of the colloidal deposition and resuspension. The backwash revealed that the filter cake was constructed like a pile of weakly bound and repulsive particles at ambient temperatures. Thus, the filter cake was removed even at low backwash rates, at which individual particles and small aggregates were flushed. Contrary to elevated temperatures, the backwash revealed that the particles form an attractive network. The attractive network is stable at low backwash rates. Only a significant increase in the backwash velocity causes the filter cake to break up in the form of large agglomerates.

The difference in clogging and backwash cannot only be attributed to changes in viscosity with temperature. The colloidal interactions shift to more attractive interactions at higher temperatures, which contradicts the theory explained in the chapter before. Several possibilities could explain the discrepancy to a theory, such as shortcomings in the used assumptions, steric interactions, sulfate hydrolysis, and neglecting the role of dissolved gases. In any case, the study shows that there is still much work necessary to understand the role of temperature in colloidal interactions and deposition.

8 Compression of a soft filter cake

Parts of the theory presented in this chapter were developed and presented in the bachelor thesis:
H. Oberlack “How do soft particles compact in the filter cake? - A CFD-DEM study [Bachelor thesis]”. RWTH university(2020).

In pressure-driven membrane filtration, colloidal particles (colloids) tend to deposit on the membrane surface. A filter cake develops during filtration. This cake layer controls the transport and rejection of the species and effectively takes over the membrane's role in many filtration processes [Guo2012]. Particles forming the filter cake are often soft, enabling them to deform and compress when exposed to external stress.

The softness of the particles can significantly affect the filtration properties. Nakanishi et al. [Naka1987], and Tanaka et al. [Tana1994] measured that the filtration resistance of a cake formed by microorganisms depends upon filtration pressure. In contrast, the filtration resistance is almost constant for hard particles. Models such as the conventional cake filtration theory often inaccurately describe the filtration process when applied to soft filter cakes [Lu2001; Hwan2003]. Hwang et al. [Hwan2003], and others developed models based on empirical correlations to account for the softness of filter cakes. However, these empirical models do not account for how the mechanical properties of particles control the cake compression and the cake resistance. Further, particle scale mechanism controlling cake morphology and compaction can only hardly be predicted by empirical models.

A modeling approach is of high interest, which is able to resolve phenomena occurring inside the filter cake during soft particle filtration. Particle scale modeling coupled with fluid mechanics enables to track phenomena inside a filter cake and can provide insides into cake formation and compaction. Within this chapter, coupled CFD-DEM simulations were presented, which connect the mechanical properties of soft microgel particles with filter cake compaction. A Multi-Hertz approach based on the theory of Bergman et al. [Berg2018] is used to calculate the mechanics of individual microgels. The model enables investigating soft particle filtration depending on the particle's properties and filtration conditions.

8.1 Microgels

Microgels are intramolecularly cross-linked polymer networks, which are swollen by a solvent [Heye2009]. Their size commonly ranges from $10-$

10000 nm. Microgels combine typical features of 1) macromolecules, 2) colloids, and 3) surfactants: 1) As macromolecules, microgels are soft, they swell in a solvent, and their local configuration responds fast to changes in the solvent's quality; 2) As a colloid, they crystallize at high volume fractions; 3) As a surfactant, they adsorb to interfaces and impact the interfacial tension [Karg2019]. Microgels are of particular interest because depending on the chosen material system their degree of swelling responds to external stimuli such as pH, temperature, and magnetic fields [Fern2011]. Due to their controlled responsiveness to external stimuli, microgels are often referred to as "intelligent" materials. The controlled responsiveness gives rise to many possible biomedical area applications, such as controlled drug delivery, tissue engineering, and spinal column implants [Heye2009]. The softness of the microgel is of particular interest in this work since it resembles important features of technically relevant biological materials.

8.2 Filtration of microgels

In recent years, microgels were filtered to investigate the behavior of soft particle filtration [Nir2016; Link2016; Hing2017; Link2018; Link2019]. Therefore, microgel filtration was analyzed in macroscopic [Nir2016; Hing2017; Lüke2020] and microscopic studies [Link2016; Link2018; Link2019]

On the macroscopic side, Nir et al. [Nir2016] filtered slightly positive charged VCl/AAEM microgels on a microfiltration membrane. They measured the hydrodynamic resistance depending on the applied transmembrane pressure (TMP). The results indicate that classical blocking laws inaccurately describe the filtration of soft colloidal microgels. Further, they detected microgels penetrating the inner structure of the membrane and permeating through the membrane. They performed electric impedance spectroscopy (EIS) to gain insights into the contribution of inner pore narrowing. The characterization of hydrodynamic filtration and EIS measurements enables the distinction between pore narrowing and cake formation.

Hinge and Christensen [Hing2017] measured the hydraulic resistance fil-

tered core-shell poly(ST-co-NIPAM) latexes (PSN) particles and developed a semi-theoretical filtration model for deformable microgels. The experiments, combined with the fitted model, reveal that the gels partly filled the remaining void of the fluid at a low amount of microgel, which increases the specific cake resistance. At high amount of microgels, the microgels filled out nearly the entire void leading to a drastic increase in cake resistance. A critical limitation of the model is that the filter cake is considered isentropically compressed. Since the pressure on the particles increases towards the membrane, increasing the soft particles' compression inflow direction is more probable.

Microscopic analysis is necessary to understand phenomena occurring inside the filter cake. Microfluidic filtration experiments combined with confocal microscopy have been promising to visualize cake behavior non-invasively [Link2016; Link2018; Link2019]. Linkhorst et al. [Link2016] visualized how small colloids permeate though a soft microgel filter cake with confocal microscopy. Interestingly, colloids' permeation velocity accelerated in highly ordered filter cake regions, whereas it slowed down in amorphous regions. Thereby, Linkhorst et al. [Link2016] were able to link particle permeation with filter cake properties.

Proceeding, Linkhorst et al. [Link2019] visualized the deformation of core-shell microgels in a filter cake depending on the degree of crystallinity of the cake. They found in amorphous domains of the filter cake that individual microgels deform strongly anisometric. Contrary, in crystalline regions, the particles deform into ordered hexagonal arrangements [Link2019].

The compression and relaxation of a microgel filter cake depending on the distance to the membrane are presented in Linkhorst's thesis [Link2018]. Figure 8.1 a-c) illustrates 3D Confocal Laser Scanning Microscope pictures of the cake's compression and relaxation at varying pressure levels. Figure d) shows the measured transmembrane pressure in the experiment. Figure e). illustrates the compression is measured by the distances between the center of the particles. The graph highlights that the filter cake compression anisotropically increases closer to the membrane and reveals that the compression promotes an irreversible compaction.

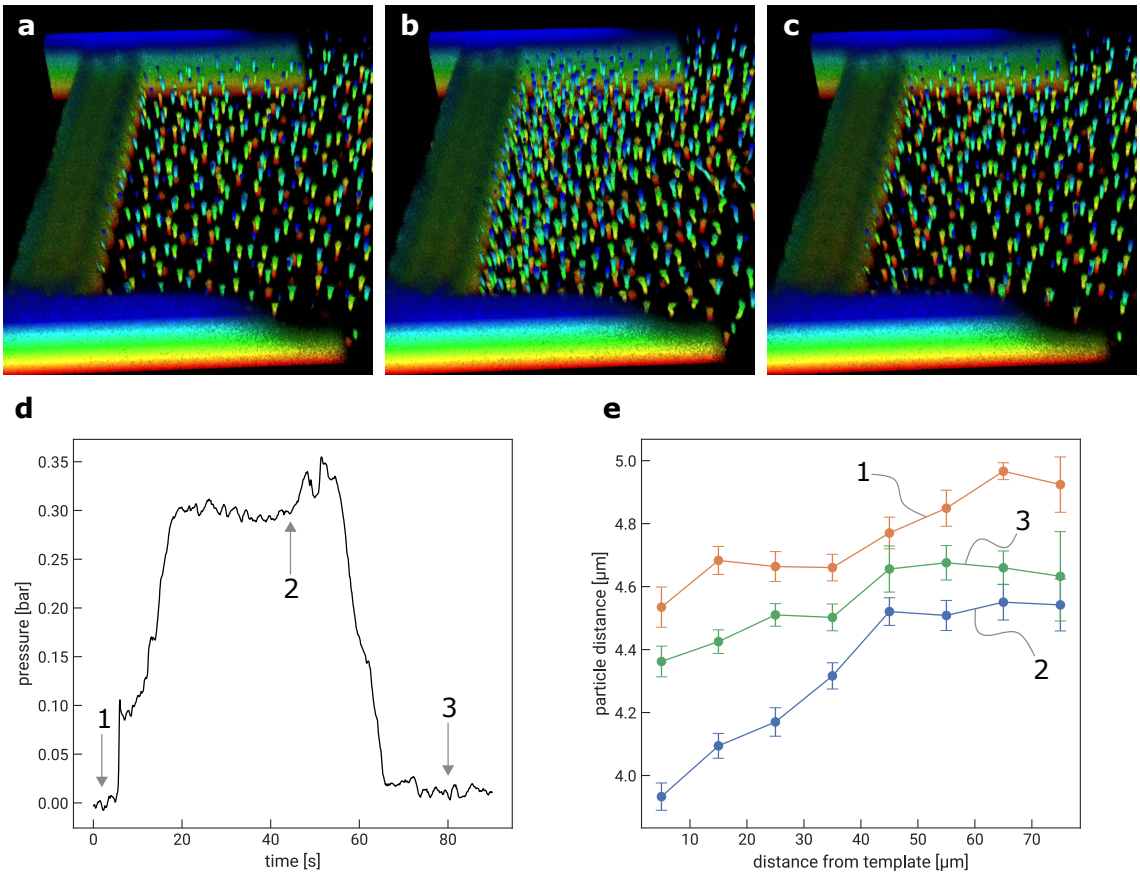

Figure 8.1: 3D Confocal Laser Scanning Microscope time series of the consecutive compression and relaxation of the microgel filter cake: a) uncompressed reference state; b) compressed state at $0.3\ bar$ (TMP); c) relaxed state at 0 bar to analyze reversibility; d) measured pressure during the experiment; e) average next-neighbor particle distance of the states 1, 2, and 3 as a function of the distance from the template surface (error bars show normalized standard deviation). ; adopted with permission from [Link2018]

8.3 Modeling approach

8.3.1 Multi-Hertz contact model

Typically, the elastic properties of materials can be described based on the Hertzian theory [Hert1882]. However, microgels follow only to some extend simple elasticity behavior. Contrary to other deformable matter such as rubber, microgels are usually anisotropic, e.g., the polymer density increases closer to the center. The anisotropic nature of some microgels can strongly affect the mechanical properties. When microgels are packed in

higher volume fractions, a simple Hertzian model insufficiently describes the mechanical properties of microgels [Berg2018; Rovi2019]. However, Bergman et al. [Berg2018] showed that a cascade of Hertzian interactions here referred to as the Multi-Hertz model resembles the microgel's pair interactions more accurately. In the following, the Multi-Hertz model is presented based on Bergman's work. It accounts for the anisotropy of the microgel by subdividing it into radial sections.

In this work, the pair interactions between microgels were determined by a Multi-Hertz model based on Bergman's model [Berg2018]. In contrast to a simple Hertz model, the Multi-Hertz model subdivides a spherical particle into shells with different mechanical properties. Thus, a microgel's anisotropic properties (e.g., the density distribution) can be described to a certain extent. Here, the microgel particle is subdivided into two parts: 1) a shell and 2) a core. A third shell, the corona, as proposed by Bergman, is neglected in terms of simplicity. As illustrated in Figure 8.2, three types of interaction result when subdividing the particle into two parts: 1) shell-shell interactions (U_{SS}), 2) shell-core interactions U_{SC}, and 3) core-core interactions U_{CC}.

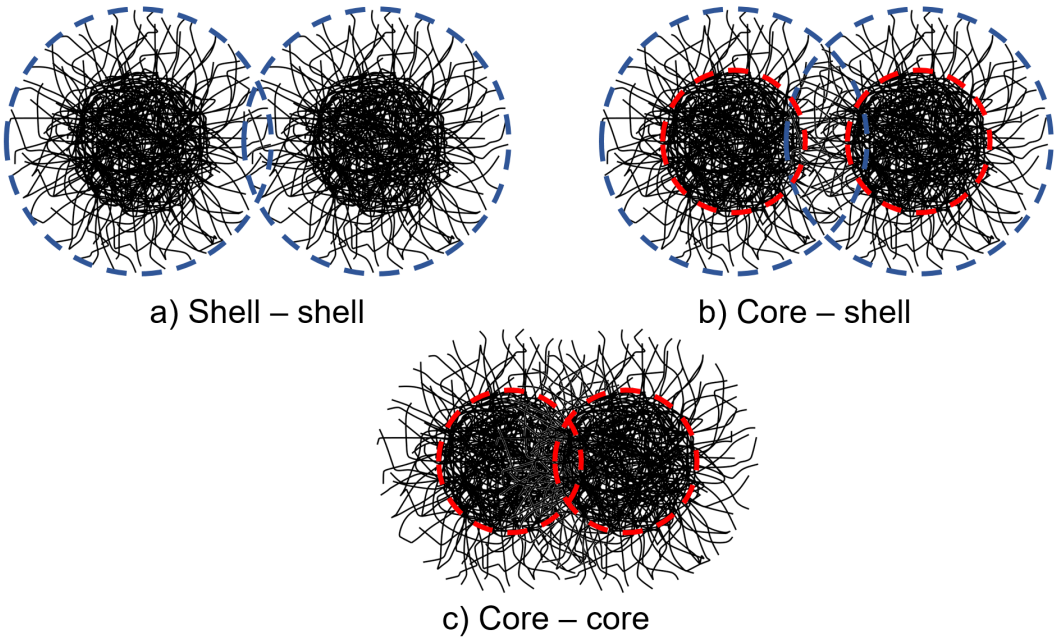

Figure 8.2: Illustration of the multi-Hertz model: 1) shell-shell interactions, 2) shell-core interactions and 3) core-core interactions

The corresponding interaction strengths can be calculated by U_{ss}, U_{cs} and U_{cc}. The effective interaction potential in the Multi-Hertz approach is described as follows:

$$\begin{aligned} V_{\mathrm{MH}}(r) =& U_{\mathrm{ss}}\left(1-\frac{r}{\sigma_{\mathrm{ss}}}\right)^{\frac{5}{2}}\Theta\left(\sigma_{\mathrm{ss}}-r\right) \\ &+ U_{\mathrm{sc}}\left(1-\frac{r}{\sigma_{\mathrm{sc}}}\right)^{\frac{5}{2}}\Theta\left(\sigma_{\mathrm{sc}}-r\right) \\ &+ U_{\mathrm{cc}}\left(1-\frac{r}{\sigma_{\mathrm{cc}}}\right)^{\frac{5}{2}}\Theta(\sigma_{\mathrm{cc}}-r), \end{aligned} \tag{8.1}$$

where V_{MH} is the Multi-Hertz potential, σ is the diameter of the specific parts, Θ is the Heaviside step function and r is the distance between two particle centers. The Hertzian strength U of the individual shells is approximated by the elastic mechanical deformation as follows:

$$U = \frac{2Y\sigma^3}{15(1-\nu^2)} \tag{8.2}$$

where Y is the effective Young's modulus and ν is the Poisson ratio. The Poisson ratio is assumed to be constant for all parts of the microgel. The effective core-shell Young's modulus Y_sc is approximated as follows:

$$Y_{sc}^{-1} = Y_s^{-1} + Y_c^{-1} \tag{8.3}$$

where Y_s and Y_c is the Young's modulus of the shell and the core, respectively.

Besides the spring-like forces, Hertzian damping forces and lubrication force are considered (see Equations 3.6, 3.12 and 2.25). Further, tangential forces and rolling friction between the microgels are calculated based on 3.6, 3.12 and 3.5.

The interaction between the particle and the wall is calculated in a similar fashion as the inter-particle interactions. The interactions are subdivided

into 1) shell - hard sphere and 2) core - hard sphere interactions.

$$\begin{aligned} V_{\text{mem}}(r) =& U_{\text{sm}} \left(1 - \frac{r}{0.5\sigma_{\text{s}}}\right)^{\frac{5}{2}} \Theta\left(0.5\sigma_{\text{s}} - r\right) \\ &+ U_{\text{cm}} \left(1 - \frac{r}{0.5\sigma_{\text{cm}}}\right)^{\frac{5}{2}} \Theta(0.5\sigma_{\text{cm}} - r), \end{aligned} \tag{8.4}$$

Equation 8.2 is used to calculate the Hertzian interaction's strength based on Young's moduli and Poisson ratio. When assuming the Poisson ratio of the microgel equal to the membrane, the corresponding Young's between microgel and membrane can be approximated by:

$$Y_{sm}^{-1} = Y_s^{-1} + Y_m^{-1} \tag{8.5}$$

and

$$Y_{cm}^{-1} = Y_c^{-1} + Y_m^{-1} \tag{8.6}$$

where Y_m is the Young's modulus of the membrane. Similar to the inter-particle interactions, Hertzian damping forces, lubrication force, tangential interactions and rolling friction for the particle membrane interactions are considered (see Equations 3.6, 3.12, 2.25) and 3.5.

8.3.2 Mechanical properties of microgels

The choice of suitable material values that characterize the microgels' mechanical properties is crucial for the simulations. In the multi-hertz model used here, the mechanical properties are mainly determined by Young's moduli of the microgel core and the microgel shell and the interpenetration depth at which core interactions are assumed.

The Young's modulus of microgels vary significantly with the microgel material (e.g., poly(N-isopropylacrylamide) PNIPAm)), with the microgel architecture (e.g., core-shell microgels), with the degree of cross-linking, with solvent characteristics (pH, temperature) and other properties. This work's results shall be compared with the experimental data

from Linkhorst et al. [Link2018]. The microgels used in Linkhorst's study are $5\,\mu m$ N-isopropylacrylamideco-acrylic acid (p(NIPAM-co-AAc)) microgels possessing a core of trifluoroethyl methacrylate (TFMA) with a diameter of $0.5\,\mu m$. However, the microgels were not characterized in terms of mechanical properties. Burmistrova et al. [Burm2011] characterizes P(NIPAM-co-AAc) microgels with different amount of the crosslinker N,N'-methylenebisacrylamide (BIS), which are similar to the microgels used by Linkhorst et al. [Link2018]. They found Young's moduli of $80\,kPa$ up to $500\,kPa$ depending on the BIS concentration. This work chooses Young's modulus of the shell to be $100\,kPa$. The Young's modulus of the microgel core is chosen to be the 10-fold of the microgel shell, which is approximated based on the ratio used in Bergman et al. [Berg2018]. Further, the interpenetration depth at which core-core interactions occur is assumed according to Bergman et al. [Berg2018] at $0.83\ \sigma_{SS}$. It has to be noted that the microgels used by Linkhorst et al. have a TFMA core [Link2018]. Since the core is only $0.5\,\mu m$ in size, the microgel's TFMA cores do not get into contact. In this work, core-interactions do not describe the interactions between the hard TFMA core. But, the core interactions refer to interactions with considerable overlap according to the terminology of Bergman et al. [Berg2018].

8.3.3 Permeability of microgels

Microgels are partly permeable in contrast to impermeable hard spheres. The microgel's permeability has to be accounted for to describe the fluid void fraction in the CFD mesh. Roa et al. [Roa2015] described the particles permeability by the non-dimensional parameter χ to account for the particle permeability:

$$\chi = \kappa a \tag{8.7}$$

where κ is the hydrodynamic penetration depth normalized to the radius of a hard-sphere a. χ can range from an impermeable sphere ($\chi -> \infty$), down to small values characterizing high permeable particles. Figure 8.4

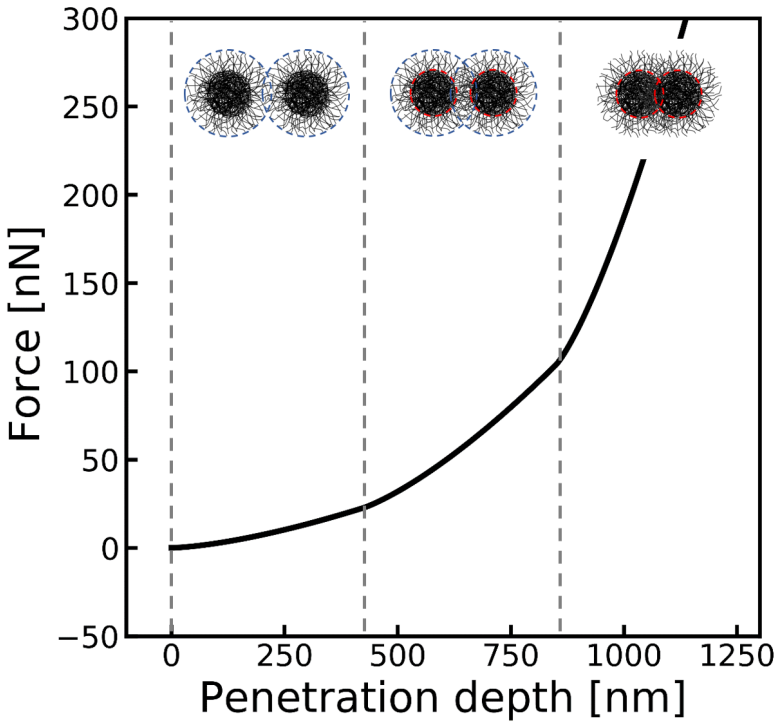

Figure 8.3: Multi-Hertz interaction force depending on the interpenetration depth for a microgel with the Young's modulus of the shell Y_s to be 100 kPa and of the core Y_c to be 1000 kPa

schematically illustrates the modeling approach of a partially permeable particle. The hydrodynamic radius a_h can be approximated by the following equation:

$$a_h = (1 - \frac{1}{\chi})a \tag{8.8}$$

Based on experimental studies, the hydrodynamic radius can be assumed to be between $95 - 100\%$ of the radius of a hard-sphere [Roa2015]. In this study, the hydrodynamic radius is assumed to be 97.5%. The minimal void fraction of a CFD cell is chosen to be 10%, which can physically be regarded as the limit of the microgel's intrinsic permeability.

This approach only estimates the real void fraction of the soft filter cake. Since the pressure drop caused by the filter cake scales with the void fraction, a more refined description of the void fraction is of high interest for future studies.

Additionally, the void fraction and the momentum exchange term is

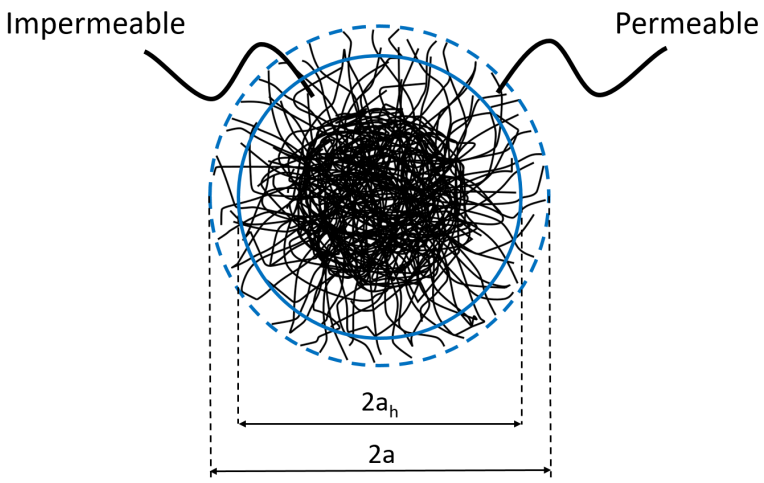

Figure 8.4: Regions of permeability inside the microgel. The outer region is assumed to be permeable, whereas it is assumed to be impermeable closer to the center.

smoothed according to Equation 3.27. By smoothing the void fraction and the momentum term, large differences in the hydrodynamic resistance between bordering mesh elements are avoided, which can lead to instabilities in the simulation of strongly compacted soft packing. However, the smoothing causes the pressure gradients to be not entirely resolved, whereby the pressure loss of the filter cake is underestimated. Deviations of pressure loss between simulations with and without smoothing of fixated sphere packings were measured to be $10 - 20\%$.

Furthermore, this study chose a drag correlation based on the work of Gidaspow et al. [Gida1991] for hard spherical particles. Due to particle deformation, soft particles' spherical nature can diminish, which is neglected in this modeling approach. The role of particle deformation on the fluid flow should be reviewed in a future study.

8.3.4 Simulation conditions

The simulations were performed in a cuboid, which is shown in Figure 8.5. As explained in detail in Chapter 3, the unresolved CFD - DEM approach was used. The divided volume fraction method is used and the mesh is chosen to be a structured mesh with mesh sizes of 5x5x5 µm. The particles

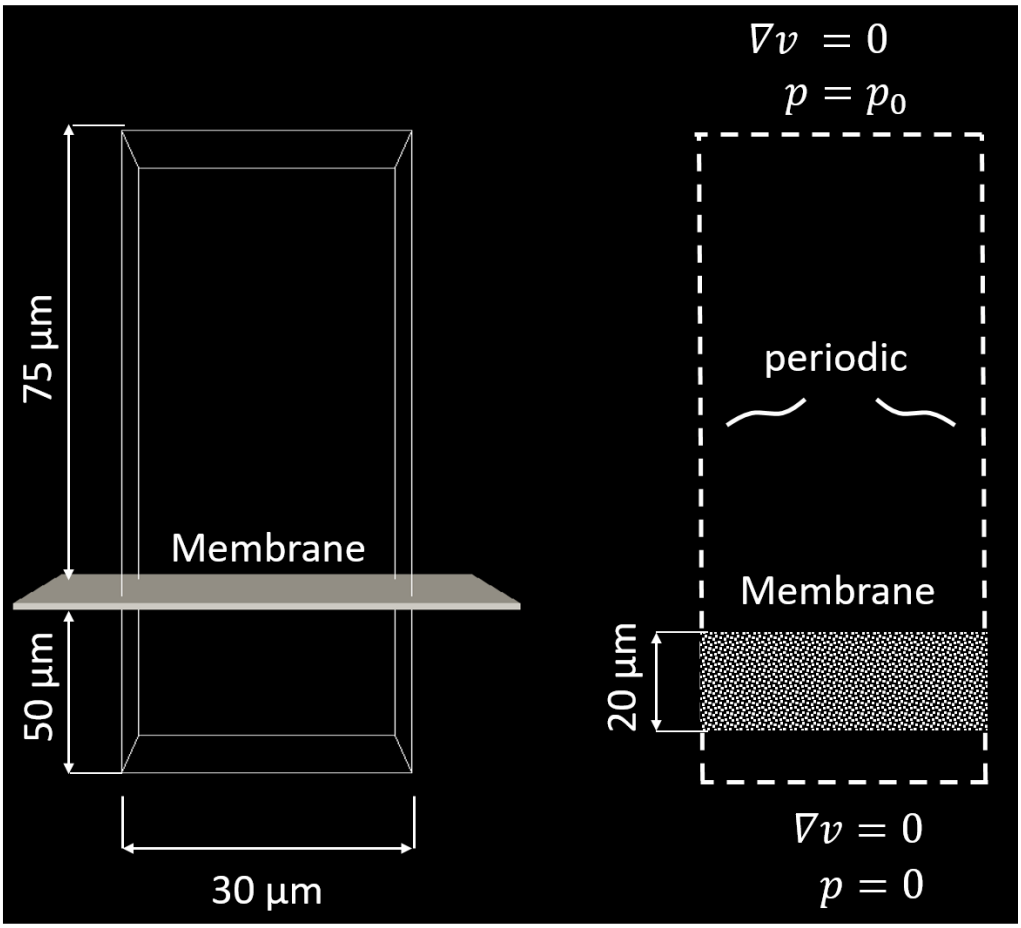

Figure 8.5: Simulation domain and boundary conditions

were filtered with a constant transmembrane pressure (TMP) until the filter cake reached a height of roughly 40 µm. A porous layer is integrated into the CFD part of the simulations, in order to achieve better comparability of the simulations to the experiments of Linkhorst [Link2018]. Without the porous layer, the flow velocity at the beginning of the simulation would be very high leading to unrealistic filtration conditions. The hydrodynamic resistance of the membrane is added to the Navier-Stokes equation as follows:

$$\frac{\partial \epsilon u_f}{\partial t} + \nabla \cdot (\epsilon u_f u_f) = -\epsilon \nabla \frac{p}{\rho_f} + \nabla \cdot \tau - R_{pf} + S_m \tag{8.9}$$

$$S_m = -\nu k_M u_f \tag{8.10}$$

The membrane resistance k_M is chosen to reflect the hydrodynamic resistance of the crystalline sphere template in the microfluidic experiments of Linkhorst [Link2018]. The Ergun equation is used to estimate the hydrodynamic resistance of the sphere templates applied in the filtration experiment:

$$\Delta p = \frac{150\eta H}{D_p^2}\frac{(1-\epsilon)^2}{\epsilon^3}u_s + \frac{1.75L\rho}{D_p}\frac{(1-\epsilon)}{\epsilon^3}u_s \mid u_s \mid \tag{8.11}$$

where Δp is the pressure drop over the sphere packing (transmembrane pressure TMP), H represents the height of the cake, D_p is particle's diameter,η is the viscosity, ϵ is the fluid's void fraction and u_s is the superficial velocity. The second part of the Ergun equation is neglectable in this system since the viscous part controls the pressure drop. The crystalline sphere packing has a void fraction of $\epsilon = 0.26$ and the particle's diameter is $D_p = 5\mu m$. The crystalline sphere template consists of three particle layers resulting in a cake height H of approximately $13.2\,\mu m$. A thickness-normalized membrane resistance $R_M = 2.4e9m^{-1}$ can be derived leading to the following relationship:

$$\Delta p = \eta\frac{1}{R_M + R_C}u_s \tag{8.12}$$

with the cake resistance $R_C = 0$ equal to zero. The membrane thickness is selected to be $15\,\mu m$ in the simulations. The membrane is displaced by a particle radius to the DEM wall to avoid particles penetrating into the porous media. Figure 8.6 a) displays the CFD simulation of a particle-free channel including the porous media. Figure 8.6 b) shows the resulting transmembrane pressure depending on the velocity reflecting the linear relationship between TMP and superficial velocity explained in Equation 8.12. Table 8.1 provides an overview of the simulation parameters used.

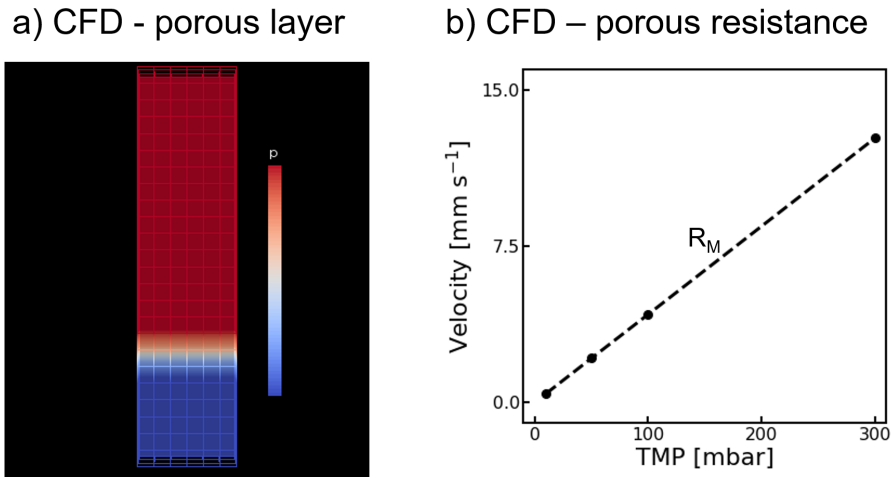

Figure 8.6: a) Pressure profile of a CFD simulation of a particle-free channel including a membrane. b) The flux depending on the transmembrane pressure (TMP)

8.3.5 Data analysis

The simulation results were analyzed with a python script to gain more information about the cake compression and the cake morphology.

The filter cake compaction was calculated equivalent to the work of Linkhorst illustrated in Figure 8.1e). The filter cake was subdivided into regions of 5 µm in the z-direction. The distance between contacting spheres was calculated under consideration of the periodic boundaries. The resulting contact distances were averaged for each segment, and the standard deviation was calculated. Hence, the degree of compaction can be measured depending on the distance to the membrane.

The coordination number of the particles was calculated to analyze the cake packing. The coordination number describes the number of contacts of a particle. Equal sized spheres in crystalline regions posses in close-packing a coordination number of 12. Again, the particle's location was subdivided into regions of 5 µm in the z-direction. Thereby, the degree of coordination is measured depending on the distance to the membrane.

Parameter	Symbol	Value
Particle shell diameter	σ_{ss}	5 µm
Particle core diameter	σ_{cc}	4.15 µm
Young modulus - core	E	$1e3$ kPa
Young modulus - shell	E	$1e2$ kPa
Young modulus - hard sphere	E	$1e6$ kPa
Particle concentration	c	30 $vol\%$
Poisson ratio	$\tilde{\nu}$	0.3
Coefficient of restitution	e	0.6
Lubrication separation distance	D_{lub}	10 nm
DEM-time step	Δt_{DEM}	2×10^{-10} s
CFD-time step	Δt_{CFD}	1×10^{-8} s

Table 8.1: Parameters applied in the simulations

8.4 Results & discussion

8.4.1 Cake formation of soft and hard spheres

Two simulations were performed to compare the cake formation of the hard and soft filter cake. Thereby, the particles were filtered with a transmembrane pressure (TMP) of 300 mbar.

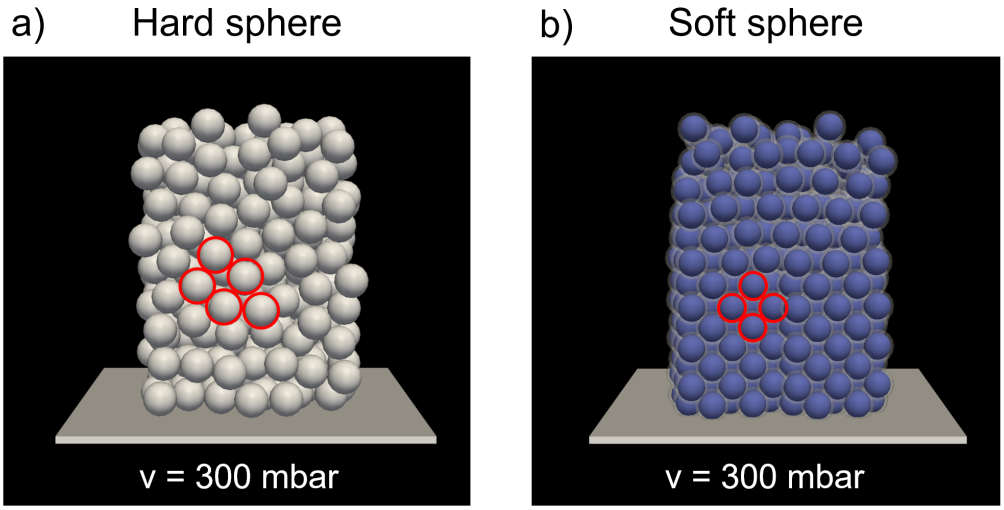

Figure 8.7: Cake structure of a) hard and b) soft sphere filter cake after filtration at a TMP of 300 mbar.

Figure 8.7 shows the filter cake of the hard (a) and soft spheres (b) at

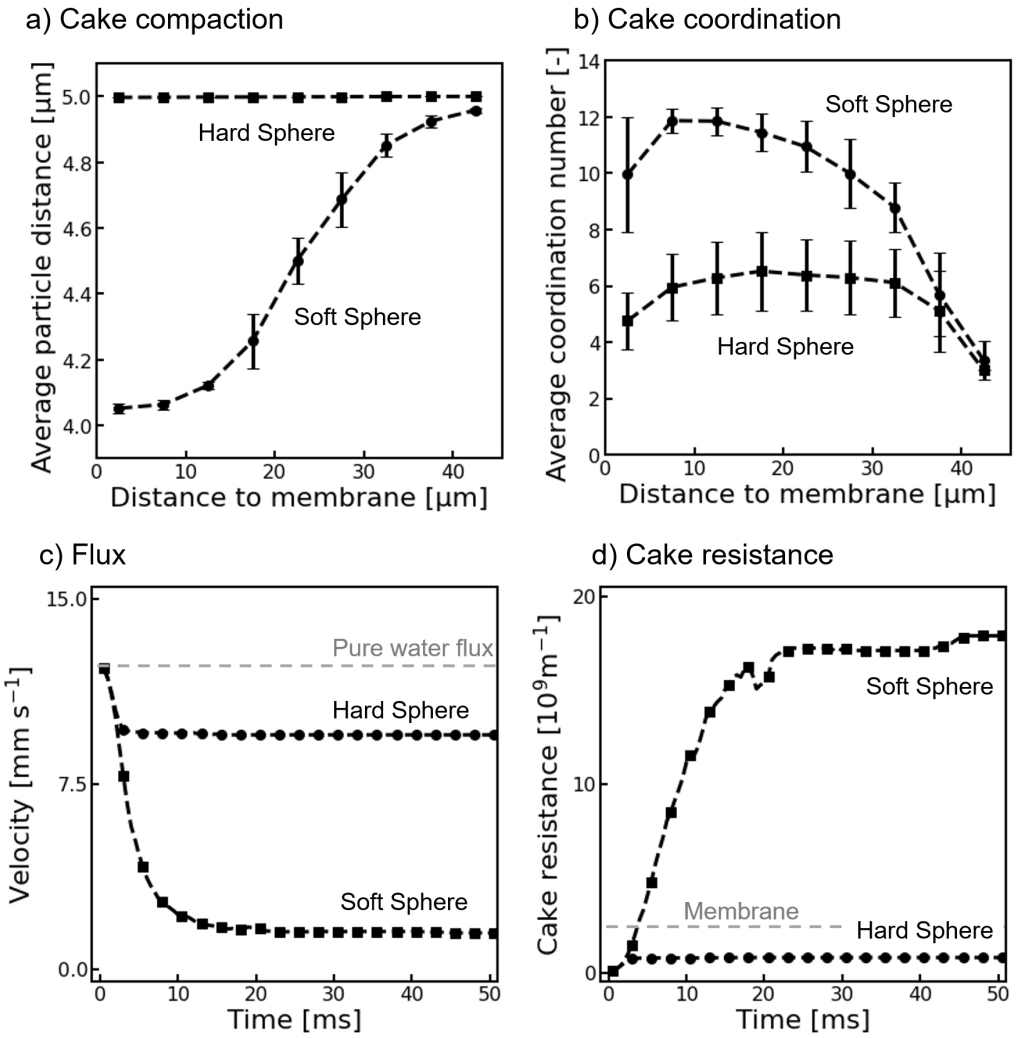

Figure 8.8: Simulation results of soft and hard particles at a TMP of 300 mbar. a) shows the average particle distance in contact depending on the distance to the membrane; b) plots the coordination number of the hard and soft sphere cake; c) displays the flux of the hard and the soft filter cake. d) shows the cake resistance.

the end of the simulation. From the visual representation, it can already be seen that the hard-sphere packing is more loosely and unstructured packed compared to the soft sphere packing. The hard-sphere filter cake had an average solid fraction of approximately $\phi = 0.6$, which is close to random close packing ($\phi_{rcp} = 0.64$) [Scot1969]. Contrary, the soft filter cake had an average solid fraction of more than 0.7.

The cake morphology is analyzed as explained in Section 8.3.5 to get quantitative information about the cake properties. Figure 8.8a) shows the average particle distance in contact depending on the distance to the

membrane. Contrary to hard spheres, the soft filter cake is significantly compressed, manifesting in a decrease in average particle distance. The degree of compaction sharply increases closer to the membrane, which is intuitive as the force on the particles increases closer to the membrane. Below particle distances of $4.15\,\mu m$, more rigid core-core interactions set in, which flattens the compaction closer to the membrane resulting in an S-shaped profile.

Besides the compaction of the filter cake, the degree of coordination of the filter cake was analyzed. The spheres' coordination number was calculated depending on the distance to the membrane, as explained in Section 8.3.5. The coordination of the soft sphere cake was significantly higher than the one of the hard-sphere cake, as illustrated in Figure 8.8 b). Further, the soft sphere cake's coordination is raised closer to the membrane reaching a value of 12, which is the characteristic value of a crystalline close-packing of equal spheres. Contrary, the hard spheres built up an amorphous, isotropic filter cake with an average coordination number of around $5-6$.

The difference in compaction and crystallinity between soft and hard spheres significantly affected the flux, as shown in Figure 8.8 c). The flux with the soft filter cake was around $1.5\,mm\,s^{-1}$ at controlled conditions, whereas the flux with the hard filter cake was $9.5\,mm\,s^{-1}$. The cake resistance can be determined with equation 8.12. Figure 8.8 d) displays the development of the cake resistance over time. The cake resistance of the hard filter cake is lower than the membrane resistance. In contrast, the soft filter cake's resistance surpasses the membrane resistance by approximately a magnitude. Noticeable is a small drop of the cake resistance at about 20 ms caused by re-arrangements of the particles inside the soft filter cake.

Since the compaction degree depends on the applied TMP and the individual particles' softness, the dependence between TMP, softness, and cake morphology is discussed in the following sections.

8.4.2 Cake compression depending on TMP

The filtration of soft and hard spheres was performed at TMPs of 100 and 10 mbar to analyze the cake compression depending on the applied pressure.

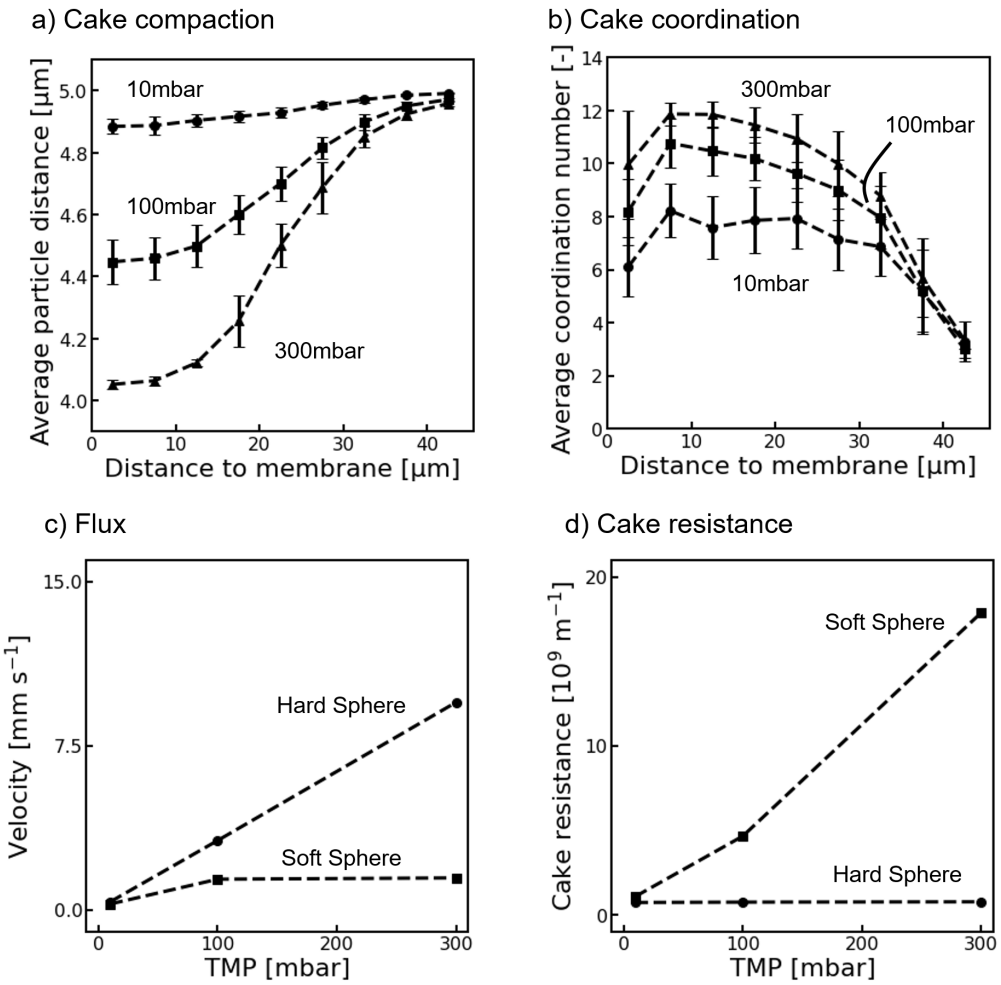

Figure 8.9: Filtration of soft particles at TMPs of 300, 100 and 10 mbar. a) shows the average particle distance in contact depending on the distance to the membrane; b) plots the coordination number of the soft sphere cake; c) displays the flux of the hard and the soft filter cake at different pressure levels. d) shows the cake resistance at varying pressure levels.

A reduction of the applied pressure resulted in a less compacted soft filter cake, as shown in Figure 8.9 a). The average distances closest to the membrane between the particle's center raised from 4.1 µm to 4.9 µm. Furthermore, the coordination of the soft filter cake was less structured at smaller TMPs, which manifested in lower coordination, as illustrated in Fig-

ure 8.9 b). For a clear design of the graph, the hard particles' results were not included in Figure 8.9 a) and b). The hard-sphere packing morphology was almost identical to the results presented in Figure 8.8.

The flux of hard spheres filter cakes linearly scales with the TMP. The proportional relationship between flow rate and the pressure was reflected in the simulation results of hard spheres, as shown in Figure 8.9. A decrease in TMP by one magnitude lead to a reduced flux by one magnitude, which is reflected in a constant cake resistance, as shown in Figure 8.9 d). Contrary, the flux of the soft filter cake non-linear correlated with the applied TMP. At a TMP of $10\,\mathrm{mbar}$, the flux of the soft cake was similar to the one of the hard-sphere cake. However, the more substantial cake compaction and the higher degree of coordination at higher TMPs resulted in a disproportionate increase in pressure drop for soft particles. The filter cake resistance increases with TMP.

8.4.3 Cake compression depending on the softness

Besides the applied pressure, the dependence between the compression of a soft filter cake and the particles' softness is investigated. Therefore, simulations with soft microgels were performed with varying Young's moduli of the shell 50, 100 and $200\ kPa$. The Young's modulus of the core is adjusted accordingly to be ten times the shell. The TMP was varied to be 10, 100 and $300\,\mathrm{mbar}$.

Figure 8.10 a) shows how the compression of the filter cake scales with the softness of the individual particles at a TMP of $300\,\mathrm{mbar}$. The cake compaction increases with the softness of the particles. Accordingly, the cake resistance increases with softness, which is demonstrated in Figure 8.10 b). The increase of cake resistance with the softness of the particles depends on the applied TMP. At $300\,\mathrm{mbar}$ the filter cake resistance nearly proportional increases with the softness, whereas the cake resistance is significantly disproportional at lower TMPs. At lower TMPs, the filter cake morphology gets more ordered with softness, resulting in a significant increase in cake resistance with softness.

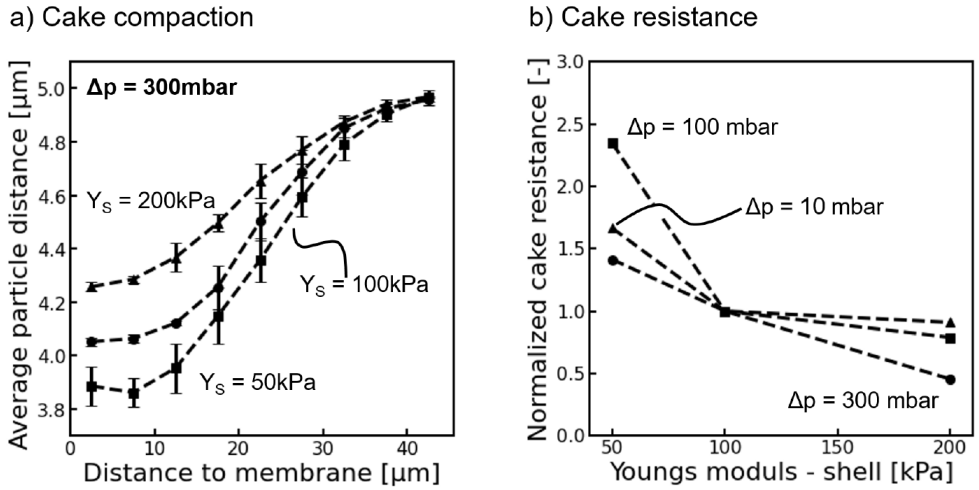

Figure 8.10: Filtration of soft particles with Young's moduli (50, 100 and $200kPa$) at a constant TMP of 100 and $300\,\mathrm{mbar}$. a) shows the average particle distance in contact depending on the distance to the membrane at $300\,\mathrm{mbar}$; b) displays the cake resistance normalized to the cake resistance at $100kPa$ at varying Young's modulus and TMPs.

8.4.4 Reversibility of cake compression

An important question is how the filter cake reacts to changes in process conditions and if short-term changes in filtration affect the filter cake properties. Two simulations were performed in a pressure-step mode to analyze the effect of short-term changes in filtration. Therefore, the developed soft filter cakes at filtration velocities of $10\,\mathrm{mbar}$ and $300\,\mathrm{mbar}$ served as an initial point for the respective flux step simulations. In one simulation, the compact filter cake at $300\,\mathrm{mm\,s^{-1}}$ were relaxed to $10\,\mathrm{mm\,s^{-1}}$ and subsequently exposed to the original filtration rate of $300\,\mathrm{mbar}$. In the second simulation, the less compacted filter cake at a filtration velocity of $10\,\mathrm{mbar}$ was exposed to a short-term higher filtration rate of $300\,\mathrm{mbar}$ and afterward relaxed to the original filtration rate of $10\,\mathrm{mbar}$.

The filtration conditions are summarized in Table 8.2. Particle insertion was turned off during the flux step simulations to concentrate exclusively on the filter cake condition changes. It shall be analyzed whether reversible or irreversible changes in the filter cake morphology occur.

Figure 8.11 a) shows the simulation results of the pressure-step of the

Packing	p(t= 0-30 ms)	p(35-50 ms)	p(50-80 ms)	p(85-100 ms)
Dense	300 - 10 mbar	10 mbar	10 - 300 mbar	300 mbar
Loose	10 - 300 mbar	300 mbar	300 - 10 mbar	10 mbar

Table 8.2: Pressure steps performed in the simulations depending on the initial cake morphology

densely packed filter cake. The filter cake relaxed caused by the decreased TMP, and the height of the filter cake grew. Afterward, the TMP was increased, and the filter cake was compacted again. The filter cake before and after the pressure-step were visually very similar. The similarities are confirmed when comparing the filter cake properties as plotted in Figure 8.11 a and b. The relaxation was purely reversible.

Figure 8.12 shows the simulation results of the short term compaction of the loosely packed filter cake. The cake was compacted due to an increased TMP. After the compaction, the TMP was reduced to the original value, and the filter cake relaxed. After the pressure step, the filter cake was visually more structured close to the membrane. The cake properties confirmed the higher degree of structuring close to the membrane. The filter cake's compaction was more substantial than before the pressure step 8.12 a). Further, the average coordination of the cake increased close to the membrane after the pressure step, as shown in Figure 8.12 b). Thus, the compaction step lead to irreversible changes in cake morphology.

A TMP decline lead to reversible changes in the morphology of a densely packed filter cake. On the contrary, a peak in TMP can lead to particle rearrangement and irreversible changes in loosely packed filter cakes' cake morphology.

8.4.5 Comparison with the literature

The simulations reveal important characteristics of soft filter cakes, which are compared to findings from the literature in this section.

Compaction of soft filter cakes

The simulations show that soft filter cakes compact close to the membrane. The compaction of soft filter cakes close to the membrane was

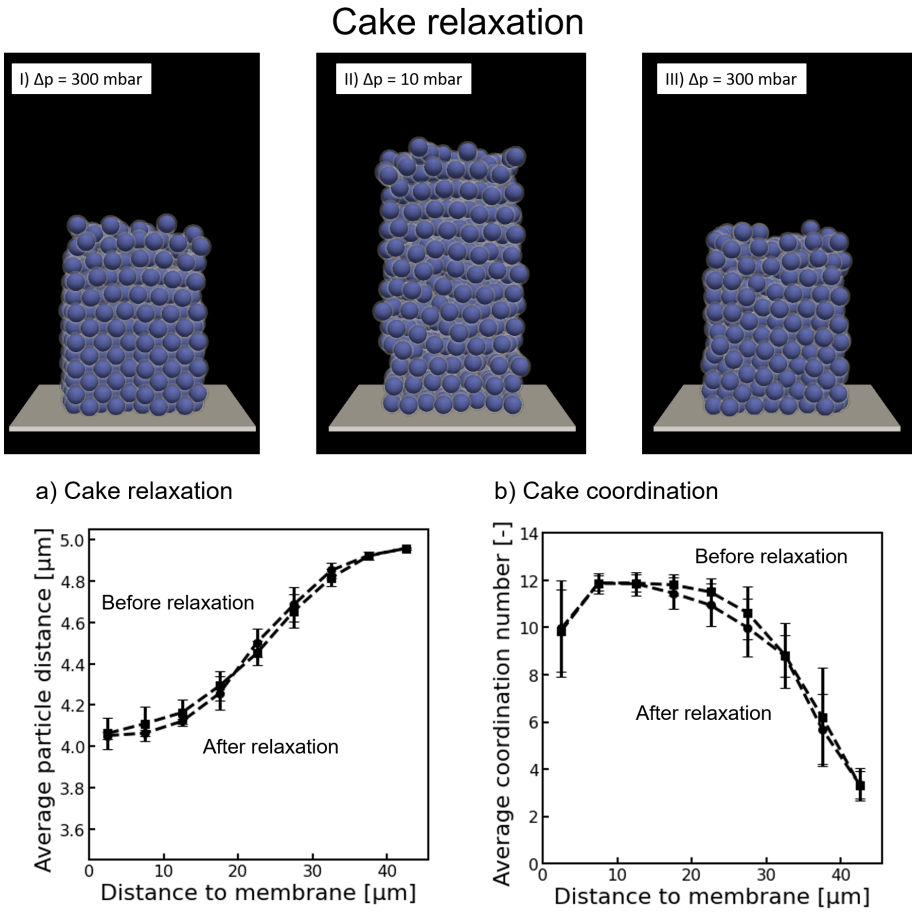

Figure 8.11: Cake relaxation simulations of a soft filter cake. a) The filter cake is shown during cake relaxation over time. At the beginning of the simulation, the filter cake is in a highly-ordered and strongly compacted state. Then, the filtration is reduced to 10 mbar and again increased to 300mbar. b) The change in cake properties before and after the cake relaxation.

also shown in combined experimental and mathematical studies by, e.g., [Lu2001; Hwan2003]. Lu et al. showed that filter cakes of rigid PMMA particles have significantly lower cake resistances than soft filter cakes of Ca-alginate [Lu2001]. The difference in cake resistance of hard and soft particles agrees with the simulations presented in this study. The origin of the higher cake resistances of soft particles relies on a smaller void fraction of soft filter cakes due to deformation. Lu et al., as well as Hwang et al., confirmed the existence of a compressed skin layer close to the membrane, which is mainly responsible for the overall cake resistance [Lu2001; Hwan2003]. The compact skin layer close to the membrane agrees with

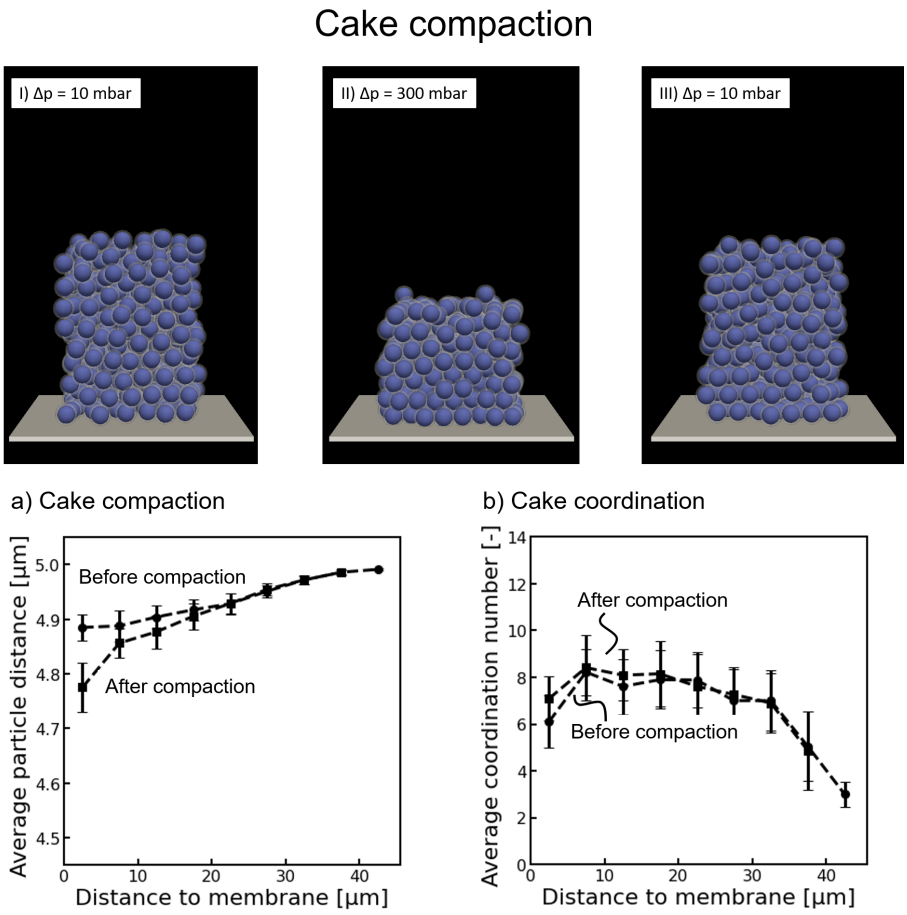

Figure 8.12: Cake compaction simulations of a soft filter cake. a) The filter cake is shown during cake compaction over time. At the beginning of the simulation, the filter cake is in a amorphous state. The filtration is increased to 300 mbar and again decreased to 10mbar. b) The change in cake properties at before and after the cake compaction.

the presented simulations. It has to be noted that the height of the filter cake in Lu's and Hwang's studies is in the millimeter range, whereas it is only 40 µm in this study. Hence, the simulation and experimental results are only qualitatively comparable.

The microfluidic experiments of Linkhorst et al. [Link2018] are more comparable to the simulation results. The microfluidic observations of Linkhorst optically visualize the filter cake compression of microgels. Similar to the presented simulations, the experiments by Linkhorst reveal compaction of particles towards the membrane. The measured compaction in the experiments is similar to the simulations. However, the simulations and the experimental results can only be compared qualitatively since some un-

certainties exist resulting from the process conditions, particle properties, impacts of module design, and filter cake height. First, the particle's softness was only approximated in the simulations and was not measured for the microgel's used in the study of Linkhorst et al. [Link2018]. The filtered particles' mechanical properties have to be measured for a more meaningful comparison between the experimental results. Second, wall effects are neglected in the simulations but can have a considerable influence due to the microfluidic device's dimensions. The microfluidic device has a small height of $20\,\mu m$ corresponding to 4 times the particle's radius. Third, the filter cake's height in the microfluidic experiment can not be extracted from the data. Figure 8.1 reveals that the microgel packing was larger than the image plane, and hence, the experimental cake was higher than in the simulations [Link2018]. For the reasons mentioned above, the experiments and simulations can only be compared qualitatively. Nonetheless, the simulation shows similar trends in cake compaction to the experiments.

Crystallization of microgel packing

Besides cake compaction, the simulations reveal crystallization of the microgels during filtration. The ability of microgels to form colloidal crystals is widely described in the literature. For example, Hellweg et al. [Hell2000], and Debord et al. [Debo2003] showed that pNIPAm and pNIPAm-AAc microgels arrange in crystal structures when concentrated. The crystallization of the microgel packings during filtration also confirms with experimental studies [Link2016; De A2017; Link2019]. Linkhorst et al. showed that microgels rearrange in crystalline structures to evade stress during filtration [Link2016] similarly to the simulations. Besides elastic behavior, the microgels can deswell in these concentrated packings [De A2017]. Deswelling of the particles is inadequately represented by the presented modeling approach since deswelling results from multi-particle interactions, which can hardly be described by pair interactions. Future studies can apply multi-sphere models to account for deswelling as proposed by Gnan et al. [Gnan2019]. The multi-sphere approach enables to describe faceting, deswelling, and deformation more precisely. However, multi-sphere approaches require high computational effort, which reduces them to small

particle numbers or 2D representations. Therefore, a simplified model based on pair interactions was chosen in this study, which already provides insights into soft filter cakes' behavior.

8.5 Conclusion

The present study investigates how the softness of particles impacts filter cake development. The softness is of decisive importance since it significantly controls the cake resistance. This study uses coupled CFD-DEM simulations incorporating a Multi-Hertz approach to describe the filter cake crystallinity and compaction of soft particles during filtration. These simulations allow three-dimensional insights into the filter cake and describe compaction phenomena during filtration of soft particles.

The simulation reveals that hard spheres arrange in loose, amorphous structures, which cause only low cake resistances. Contrary, particle softness enables the particles to arrange in partly crystalline and compacted structures causing cake resistances. Thereby, crystallinity and compaction of soft spheres depend on the applied TMP. High TMP causes strong compaction and a higher degree of crystallinity, whereas, at lower TMPs, a loosely packed, amorphous filter cake develops. These loosely packed, amorphous filter cakes can rearrange into more orderly packed cake structures by a short term increase in TMP. In contrast, ordered filter cake structures do not regress to looser, amorphous structures when exposed to a lower TMP. Thus, reversible and irreversible changes in the filter cake can occur depending on the filtration and the cake morphology.

Future research is of high interest to directly link experimental measured mechanical properties accomplished by microfluidic observations with the presented simulation approach. Thereby, quantitative comparisons can be made, which deepens our fundamental understanding of soft filter cakes and enables scientists to transform the microscopic findings into technical process systems.

The presented simulation approach is a powerful tool to investigate soft filter cake behavior. The approach enables future research to investigate

filter cakes with different degrees of particle softness and polydisperse filter cakes. Furthermore, an exciting field of application will be the permeation of small colloids through soft filter cakes. Depending on the cake's morphology and compaction, the permeation and retention behavior of the small colloids can change significantly.

9 Reflections and perspectives

This thesis examines the microscopic dynamics of colloidal fouling and resuspension. CFD-DEM simulations were developed, which enable a microscopic analysis of the interplay between colloidal interactions and hydrodynamics. The numerical simulations were supplemented by microfluidic experiments, which show that both methodologies have natural synergies in investigating fouling phenomena on the pore-scale level. By the powerful combination of microfluidic experiments and CFD-DEM simulations, clogging events on the microscopic level can be detected and interpreted.

Chapter 4 characterizes the microscopic events of colloidal clogging by CFD-DEM simulation. The simulations demonstrate that the inner pore structure decisively controls the clogging of a membrane miking pore constrictions, which is in agreement with microfluidic experiments performed by Bacchin et al. [Bacc2014b]. The simulation reveals that interparticle interactions can enhance particle deposition by pushing particles over energy barriers. Further, the downstream deposition was monitored, which results from particle gliding and particle resuspension. The presented methodology enables future research to systematically characterize the interplay between hydrodynamic conditions and surface energy contributions.

Chapter 5 characterizes the microscopic events during membrane backwash by combining microfluidic experiments with CFD-DEM simulations. Both the experimental and the numerical results consistently reveal that particle clusters instead of individual particles predominantly determine particle resuspension during backwash. The particle cluster behavior is categorized into two resuspension events: 1) fragmentation and resuspension of clusters, 2) cluster breakage, and unfolding of particle bridges. Whereas cluster resuspension is the desired mechanism to achieve high backwash efficiency; the unfolding of particle bridges need to be avoided. The unfolding of particle bridges results in particle clusters located in regions of lower drag, which prevents them from the removal. Additionally, the simulations reveal that the adhesive strength of particle-membrane decisively controls backwash efficiency. A decrease in adhesive strength substantially raises backwash efficiency. This study clarifies that 1) models based on single-particle considerations will not be able to predict the back-

wash process, and 2) membrane modification can substantially enhance backwash efficiency.

Chapter 6 describes the role of temperature on colloidal clogging by CFD-DEM simulation. The temperature significantly affects the hydrodynamics and the colloidal interactions, whose interplay majorly determines the clogging. On the hydrodynamic side, lubrication interactions and viscous drag decrease with temperature due to the decrease in viscosity. The temperature dependence of the colloidal interaction strongly varies with the material system. The clogging of two material combinations at 20 °C and 80 °C were investigated: 1) PDMS pore/anionic polystyrene particle; 2) Polyamide pore/ cationic polystyrene particle. In the case of PDMS and anionic polystyrene, the clogging probability reduces with higher temperatures due to a reduction of the acid-base interactions. Contrary, in the case of polyamide and cationic polystyrene, the clogging enhances due to diminished double layer interactions. Thus, both material combinations show opposite effects concerning temperature.

Within Chapter 7, the validity of the predictions of the temperature dependent clogging was experimentally investigated. Fouling and backwashing experiments with 4 µm polystyrene sulfate particles were conducted to examine the influence of temperature colloidal deposition and resuspension. A microfluidic setup was developed enabling tempered microfluidic filtration between 25 °C and 80 °C. The filtration experiments reveal that the clogging rate at higher temperatures exceeds that at ambient temperatures with the material combination polystyrene sulfate and PDMS. Backwashing was performed to gain more information about the developing filter cake at varying temperatures. Backwashing revealed that the fouling layers formed at 25 °C break immediately upon flow reversal. In contrast, at 80 °C, a large part of the filter cake remained stable at until exposure to 128 fold filtration flow velocity. Hence, the backwashing velocity at which pore unblocking occurs increases with the temperature. The increased backwash flow velocity required for pore unblocking at elevated temperatures can only partly be attributed to the decrease of the hydrodynamic drag force acting on the fouling layer. Thus, filtration and backwashing revealed increasing attractive

interactions between particles with increasing temperature. The increased clogging probability at increased temperatures are in stark contrast to the simulation results explained in Chapter 6. They cannot be explained with the chosen theoretical approach which is based on xDLVO theory and material property values found in literature. The discrepancy between simulations and experiments emphasizes the importance of further experimental and theoretical investigation of the temperature influence on colloidal fouling.

Chapter 8 discusses the filter cake compression of soft particles with the help of CFD-DEM simulations. In contrast to hard spheres, soft particles arrange in crystalline filter cake morphologies and compact due to hydrodynamic stress. The soft filter cakes cause a significantly higher cake resistance than hard filter cakes. Thereby, the TMP of soft filter cakes nonlinearly scales with filtration velocity, contrary to the proportional relationship of hard filter cakes. Furthermore, the simulations reveal that cake relaxation of soft filter cakes is fully reversible, whereas short-term cake compaction can lead to irreversible changes in cake morphology. The presented model allows a three-dimensional view inside a soft filter cake and connects cake morphology and hydrodynamic conditions. It enables future research to investigate polydisperse soft filter cakes and filtration of small colloids through soft filter cakes.

This thesis highlights dominant phenomena occurring during fouling and backwash on a pore-scale level. Based on these findings, the following conclusions are drawn:

- Inner pore structure and interparticle interactions can play a dominant role in pore-clogging (Chapter 4)
- Particle cluster phenomena control the backwash rather than single particle resuspension (Chapter 5)
- The temperature can strongly change colloidal deposition during filtration highlighting discrepancies between theory and experiments (Chapter 6 and 7)

- The softness of particles strongly increase the cake resistance due to cake compaction and cake crystallization (Chapter 8)

9.1 Future applications for the methodology

This thesis concentrates on the fouling of colloidal particles. However, the application of numerical and experimental methods can be valuable for a wide range of technical processes.

In collaborative work with Rall et al., we used CFD-DEM simulations to examine the role of particle percolation in slurry electrodes for the all vanadium redox flow battery [Loha2019]. Slurry electrodes (or flow suspension electrodes) were introduced as a potentially viable electrode system. Such electrode systems are so far only little understood. We developed a novel model of the particulate phase combining theories from fluid dynamics, colloidal physics, and electrochemistry with the CFD-DEM approach. The methodology enables us to visualize local phenomena occurring during the charging of the battery and to compute the net current of the slurry electrode system. An increase in particle volume fraction enables the formation of conducting networks in the flow electrode, which increases the net current until a threshold is reached illustrated in Figure 9.1. The study concludes that the assumption of all particles participating in the charge transfer, as assumed in pure CFD investigations, is not necessarily valid. This study is only a starting point to describe the complex physics of slurry electrodes. By increasing the number of physical phenomena such as mass transfer and particle contact resistances, this methodology may be used to identify a multitude of emergent phenomena of slurry electrodes [Shuk2019]. Of particular interest for the future would be to find a solution to non-invasive visualizes the charge percolation phenomena experimentally.

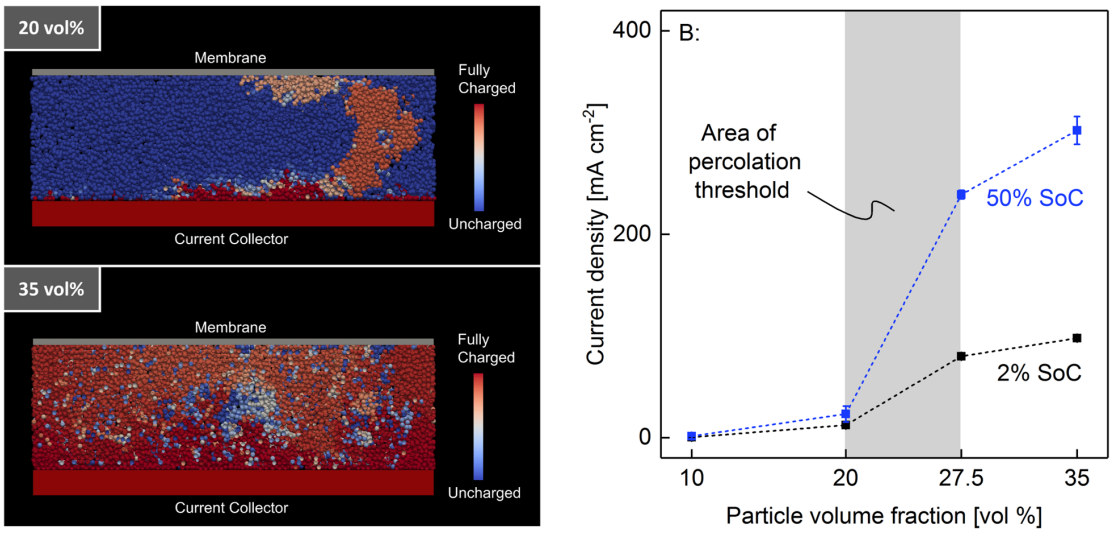

Figure 9.1: The left figures visualize the charge distribution on the slurry electrode particles at 20 and $35 vol\%$ particle volume fraction. The legend ranging from fully charged to uncharged corresponds to the charge of the individual slurry electrode particles. The images represent one characteristic time-step during cell operation. The right graph shows the non linear increase in charge transfer due to particle percolation at 2% and 50% state of charge (SoC).

9.2 Future model development

9.2.1 Hydrodynamic refinement

To improve the simulations accuracy, the hydrodynamic coupling between CFD and DEM simulation have to be refined. The unresolved coupling method limits the CFD cell to the particle size, which is only a rough estimate of the actual fluid flow profile. A more accurate description can be reached by the application of the resolved immersed boundary method [Klos2012]. The immersed boundary method resolves the surface of the particles individually and calculates the momentum exchange between fluid and particle by a surface force term. This enables a very accurate description of the fluid profile and the particle fluid interaction. However, it is computationally very demanding and is only suitable for small number of particles. Studies exist in literature, which use these types of simulations approaches to investigate pore clogging [Ando2012a; Ishi2013; Akam2016]. In order to reduce the simulation time, the fluid velocity is assumed to be

very high (up to $1 m/s$) and the geometries are nearly 2 magnitudes smaller than in this thesis. This results in clogging in a few microseconds and not in milliseconds as in this thesis, which allows the simulations to finish in a reasonable time frame. Recently, Mino et al. used a Lattice Boltzmann simulations instead of solving Navier-Stokes equation to simulate the fluid flow [Mino2018]. They were able to simulate clogging processes over a time period of some milliseconds. It will be of high interest to refine the results of our simulations with this modeling approach.

9.3 Future research on colloidal fouling

This thesis enables the view on microscopic events during membrane fouling. In a comparison between experimental and simulation results, the studies show experimental and numerical results show qualitative agreements. However, quantitative results sometimes show deviations between experiments and simulations. One prominent example is the lower backwash flow rate necessary for particle resuspension in the experiments compared to the theoretical simulations. The deviations between model and experiment may result from neglecting the influence of surface topology in charge and roughness on the colloidal interactions and lubrication.

Statistical distribution functions may be applied to account for the surface topology. A statistical distribution can consider heterogeneous surface charge distributions of particles. More complex is the role of surface roughness since it affects the colloidal interactions as well as viscous lubrication. To estimate the influence of surface roughness, the surface element integration presented by Elimelech and Hoek can be applied [Hoek2003; Hoek2006]. Thereby, the surface topology is approximated by protruding and intruding half-spheres. Elimelech and Hoek showed that surface roughness significantly reduces the magnitude of colloidal potentials. The reduction of the surface potentials can lead to more or non-zero deposition rates under repulsive conditions as demonstrated experimentally by Sjollema et al. [Sjol1990] and Darbha et al. [Darb2010].

Similarly, viscous lubrication should reduce in quantity for rough surfaces.

Contrary, the viscous drag force resulting from the fluid flow on micrometer-sized colloids is only minorly affected by the surface topology. Thus, the role of colloidal interactions and viscous lubrication is overestimated compared to viscous drag. Future work should investigate in which magnitude surface charge distribution and surface roughness influence the deposition and resuspension of colloids to achieve accurate quantitative results between simulation and experiments.

An essential question in colloidal clogging is the role of particle shape. Biological matter such as bacteria and viruses are often non-spherical. One prominent example is rod-shaped Escherichia coli (E. coli). Microfluidic experiments with E. coli bacteria were performed by the working groups of Bacchin and Lammertink [Mart2012; Send2016b]. They filtered E. coli bacteria through a microfluidic pore constriction. In the first publication, the working group of Bacchin showed that the bacteria build in the downstream part of the pore structure long streamers [Mart2012]. In the second publication, the working groups of Bacchin and Lammertink showed corporately the effects of mixed solutions of bacteria and latex on the clogging. The bacteria decelerated the clogging dynamics significantly, attributed to “slippery” interactions between the particles and the bacteria [Send2016b]. Future research can apply CFD-DEM simulations to decode the effects of shape.

The non-spherical shape can be approximated either by a multi-sphere approach or by superquadrics in numerical simulations. Superquadrics distinguish themselves by the computational effort since only one particle has to be simulated. However, the mapping of particle contact is complicated. First simulations with superquadric particles concerning clogging were developed in the bachelor thesis of Dunkel [Dunk2018]. The model is based on the work of Podlozhnyuk, which is implemented in the software package of LIGGGHTS 3.8 [Podl2017]. The model was extended to account for adhesive van der Waals forces and dampening lubrication forces. Pure particle simulations with force-directed orthogonal to the pore constriction were performed. Thereby, three-particle shapes were compared: 1) spheres, 2) ellipsoids, and 3) cylinders. The simulation results were illustrated in

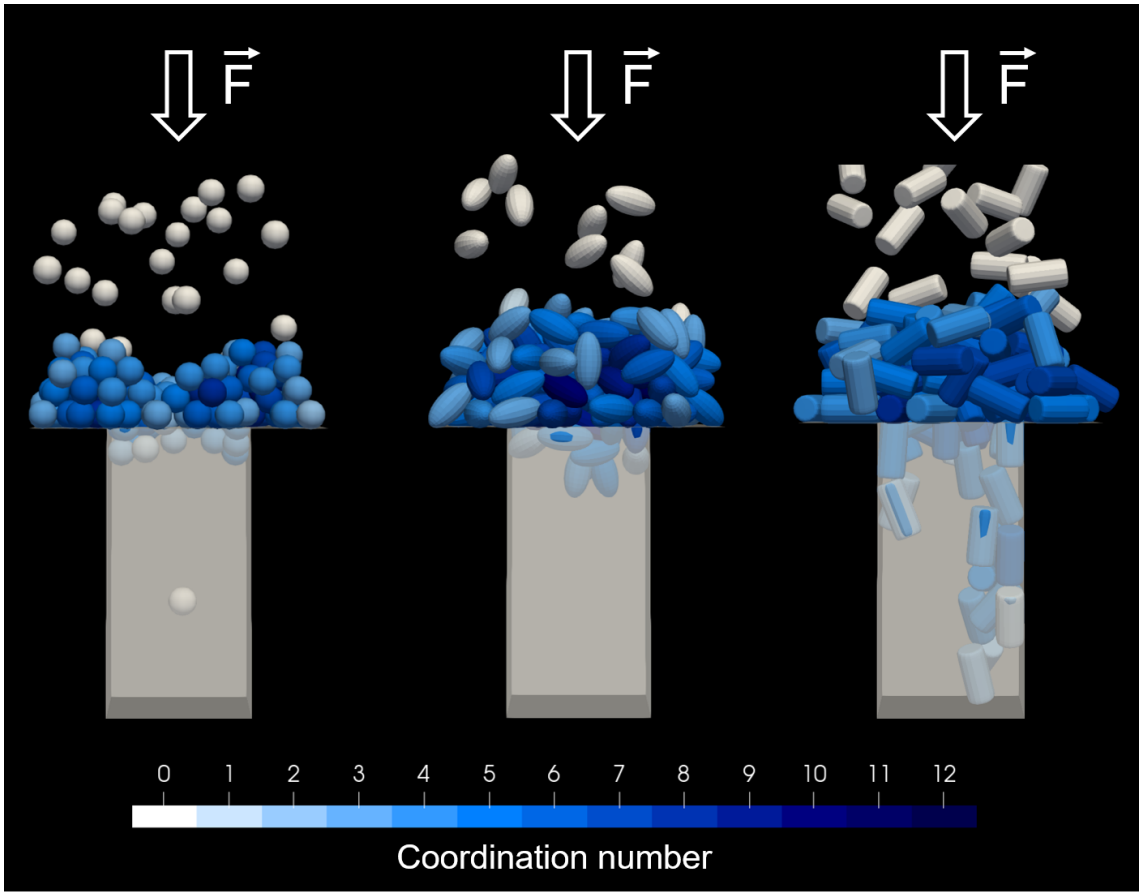

Figure 9.2: Simulation results on the clogging of spheres, ellipsoids, and cylinders of a pore structure. An orthogonal force acts on the particles to filter them to the pore structure. The simulations reveal that the average coordination of the particles decreases with a higher degree of sphericity.

Figure 9.2. The simulations reveal that the coordination number (the number of particle contacts) increases with the degree of nonsphericity. The increase in coordination may have essential implications e.g., on the backwash efficiency of non-spherical particles since high coordination can result in easier removal of particle clusters from the membrane surface. In future research, the coupling of superquadrics in DEM with CFD simulations will enable researchers to describe the impact of shape on the clogging and resuspension.

Another unanswered question in colloidal clogging is the role of particle deformation. CFD-DEM simulations can help to provide insights into the behavior of highly deformable, flexible particles. A fundamental limitation of usual DEM simulations is the assumption of particle preserving their shape. The preservation of shape does not hold when particles undergo substantial deformation. To account for deformation, Gnan et al. proposed a multi-sphere model to demonstrate the role of elasticity in a dense sphere packing [Gnan2019]. Thereby, the soft particles are composed of shell-particles surrounding a centered core-particle. The particles interact with a classical bead-spring model combined with an additional internal elasticity caused by the core particle.

The multi-sphere approach enables e.g. shrinkage of soft particles in filter cakes, to describe the permeability of deformable particles in filter media. Figure 9.3 demonstrates how a deformable multi-sphere particle permeates through a hard-sphere packing representing the filter media. The drag force pushes the multi-sphere particle through the filter media. Due to interactions with the filter media, the multi-sphere particle undergoes deformation represented by an elongated alignment of the shell-particles. The elongation allows the particle to permeate through the filter media. The model enables researchers to describe the interplay between particle deformation, hydrodynamic interactions, and inter-particle interactions. This combination will enable future research to resolve the role of deformation during filtration.

Summing up, this thesis demonstrates that combining Euler-Lagrangian simulations with microfluidics enables to decode of microscopic events of

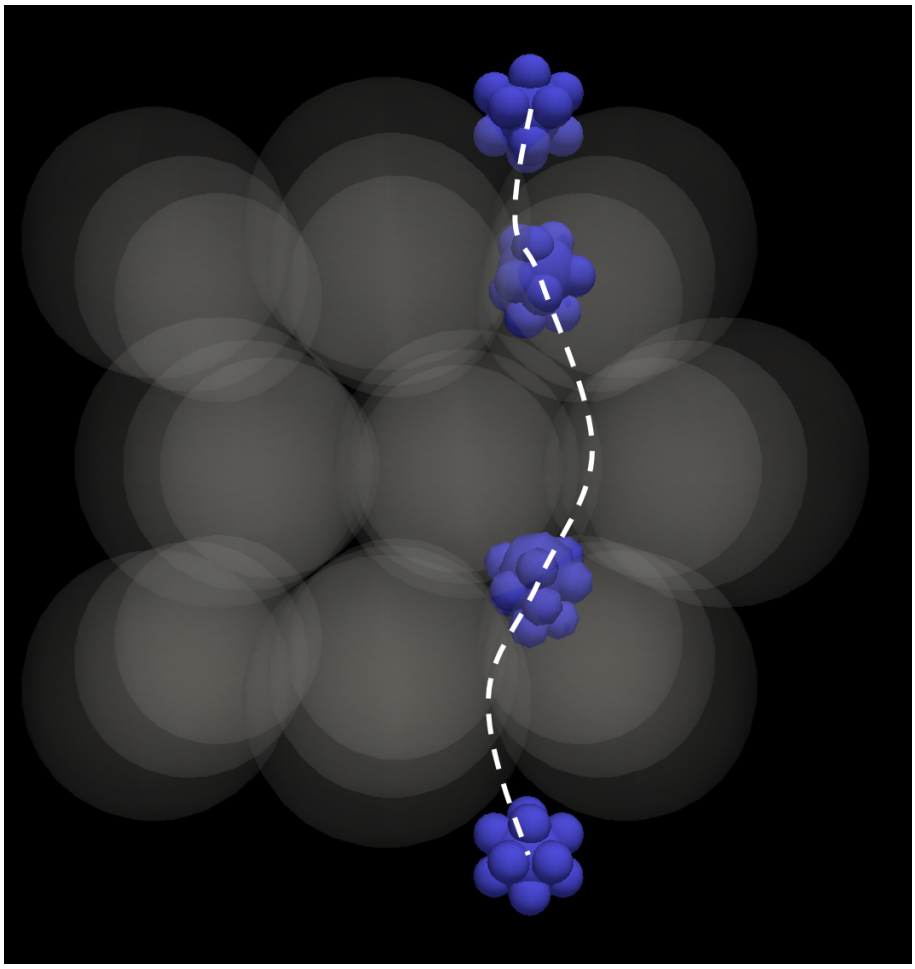

Figure 9.3: Simulation of the permeation of a soft, deformable particle through a sphere packing in hcp configuration. The soft particle is represented by a composite multi-sphere particle. The particle deforms during permeation through the sphere packing.

colloidal fouling and backwash. Combining these methodologies will allow a comprehensive picture of the fundamentals of colloidal fouling and will ultimately help to control colloidal fouling.

Bibliography

[Agba2012] G. Agbangla, É. Climent, and P. Bacchin. “Experimental investigation of pore clogging by microparticles: Evidence for a critical flux density of particle yielding arches and deposits”. *Separation and purification technology* 101 (2012). DOI: https://doi.org/10.1016/j.seppur.2012.09.011 (cit. on pp. 8, 10, 44, 58, 84, 87, 100).

[Agba2014a] G. Agbangla, P. Bacchin, and E. Climent. “Collective dynamics of flowing colloids during pore clogging”. *Soft Matter* 10.33 (2014). DOI: https://doi.org/10.1039/C4SM00869C (cit. on p. 59).

[Agba2014b] G. Agbangla, É. Climent, and P. Bacchin. “Numerical investigation of channel blockage by flowing microparticles”. *Computers & Fluids* 94 (2014). DOI: https://doi.org/10.1016/j.compfluid.2014.01.018 (cit. on pp. 12, 13, 51, 55, 59, 75, 80).

[Ai2011] J. Ai, J.-F. Chen, J. Rotter, and J. Ooi. “Assessment of Rolling Resistance Models in Discrete Element Simulations”. *Powder Technology* (2011). DOI: https://doi.org/10.1016/j.powtec.2010.09.030 (cit. on p. 34).

[Akam2016] K. Akamatsu, S. Kanasugi, T. Ando, O. Koike, M. Fujita, and S. Nakao. “Mesoscale simulations of particle rejection by microfiltration membranes with straight cylindrical pore during pressure-driven dead-end filtration”. *Journal of Chemical Engineering of Japan* 49.5 (2016). DOI: https://doi.org/10.1252/jcej.15we133 (cit. on pp. 80, 182).

[Ando2010] T. Ando, K. Akamatsu, M. Fujita, and S. Nakao. “Direct simulation model of concentrated particulate flow in pressure-driven dead-end microfiltration”. *Journal of chemical engineering of Japan* 43.10 (2010). DOI: https://doi.org/10.1252/jcej.10we103 (cit. on pp. 3, 12, 13).

[Ando2012a] T. Ando, K. Akamatsu, S. Nakao, and M. Fujita. “Simulation of fouling and backwash dynamics in dead-end microfiltration : Effect of pore size”. *Journal of Membrane Science* 392-393 (2012). DOI: https://doi.org/10.1016/j.memsci.2011.11.051 (cit. on pp. 3, 12–14, 75, 80, 182).

[Ando2012b] T. Ando, K. Akamatsu, S. Nakao, and M. Fujita. “Simulation of fouling and backwash dynamics in dead-end microfiltration: Effect of pore size”. *Journal of membrane science* 392 (2012). (Cit. on p. 29).

[Arma1999] D. Armani, C. Liu, and N. Aluru. “Re-configurable fluid circuits by PDMS elastomer micromachining”. In *Technical Digest. IEEE International MEMS 99 Conference. Twelfth IEEE International Conference on Micro Electro Mechanical Systems (Cat. No. 99CH36291)*. IEEE. 1999, pp. 222–227. DOI: https://doi.org/10.1109/MEMSYS.1999.746817 (cit. on pp. 51, 82, 103).

[Atta2003] P. Attard. “Nanobubbles and the hydrophobic attraction”. *Advances in Colloid and Interface Science* 104.1 (2003). DOI: https://doi.org/10.1016/S0001-8686(03)00037-X (cit. on p. 144).

[Aume2018] B. Aumeier, S. Yüce, and M. Wessling. “Temperature Enhanced Backwash”. *Water research* 142 (2018). DOI: https://doi.org/10.1016/j.watres.2018.05.007 (cit. on p. 74).

[Bacc1995] P. Bacchin, P. Aimar, and V. Sanchez. “Model for colloidal fouling of membranes”. *AIChE journal* 41.2 (1995). DOI: https://doi.org/10.1002/aic.690410218 (cit. on p. 101).

[Bacc2011] P. Bacchin, A. Marty, P. Duru, M. Meireles, and P. Aimar. “Colloidal surface interactions and membrane fouling: Investigations at pore scale”. *Advances in Colloid and Interface Science* 164.1-2 (2011). DOI: https://doi.org/10.1016/j.cis.2010.10.005 (cit. on pp. 2, 74).

[Bacc2014a] P. Bacchin, Q. Derekx, D. Veyret, K. Glucina, and P. Moulin. “Clogging of microporous channels networks: Role of connectivity and tortuosity”. *Microfluidics and Nanofluidics* 17.1 (2014). DOI: https://doi.org/10.1007/s10404-013-1288-4 (cit. on pp. 10, 46, 55, 68, 76, 138).

[Bacc2014b] P. Bacchin, Q. Derekx, D. Veyret, K. Glucina, and P. Moulin. “Clogging of microporous channels networks: role of connectivity and tortuosity”. *Microfluidics and nanofluidics* 17.1 (2014). DOI: https://doi.org/10.1007/s10404-013-1288-4 (cit. on pp. 2, 3, 11, 14, 45, 46, 49–52, 59, 70, 74–76, 84, 178).

[Berg1999a] J. Bergendahl and D. Grasso. “Prediction of colloid detachment in a model porous media: hydrodynamics”. *Chemical Engineering Science* 55 (1999). DOI: https://doi.org/10.1016/S0009-2509(99)00422-4 (cit. on p. 74).

[Berg1999b] J. Bergendahl and D. Grasso. “Prediction of Colloid Detachment in a Model Porous Media: Thermodynamics”. *AIChE Journal* 475-484.3 (1999). DOI: https://doi.org/10.1002/aic.690450305 (cit. on pp. 74, 94).

[Berg2003] J. A. Bergendahl and D. Grasso. “Mechanistic Basis for Particle Detachment from Granular Media”. *Environmental Science & Technology* 37.10 (2003). DOI: https://doi.org/10.1021/es0209316 (cit. on p. 74).

[Berg2018] M. Bergman, N. Gnan, M. Obiols-Rabasa, J.-M. Meijer, L. Rovigatti, E. Zaccarelli, and P. Schurtenberger. “A new look at effective interactions between microgel particles”. *Nature communications* 9.1 (2018). DOI: https://doi.org/10.1038/s41467-018-07332-5 (cit. on pp. 152, 156, 159).

[Bhus2008] B. Bhushan. *Nanotribology and nanomechanics: an introduction*. Springer Science & Business Media, 2008 (cit. on pp. 82, 103).

[Blai2016] B. Blais, M. Lassaigne, C. Goniva, L. Fradette, and F. Bertrand. “Development of an unresolved CFD-DEM model for the flow of viscous suspensions and its application to solid-liquid mixing”. *Journal of Computational Physics* 318 (2016). DOI: https://doi.org/10.1016/j.jcp.2016.05.008 (cit. on pp. 39, 80).

[Boua1998] B. Bouali, F. Ganachaud, J.-P. Chapel, C. Pichot, and P. Lanteri. “Acid-base approach to latex particles containing specific groups based on wettability measurements”. *Journal of colloid and interface science* 208.1 (1998). DOI: https://doi.org/10.1006/jcis.1998.5775 (cit. on pp. 115, 128).

[Burm2011] A. Burmistrova, M. Richter, C. Uzum, and R. v. Klitzing. “Effect of cross-linker density of P (NIPAM-co-AAc) microgels at solid surfaces on the swelling/shrinking behaviour and the Young’s modulus”. *Colloid and Polymer Science* 289.5-6 (2011). DOI: https://doi.org/10.1007/s00396-011-2383-2 (cit. on p. 159).

[Chap1913] D. Chapman. “A contribution to the theory of electrocapillarity”. *The London, Edinburgh, and Dublin philosophical magazine and journal of science* 25.148 (1913). DOI: https://doi.org/10.1080/14786440408634187 (cit. on p. 19).

[Cox1967] R. G. Cox and H. Brenner. “The slow motion of a sphere through a viscous fluid towards a plane surface—II Small gap widths, including inertial effects”. *Chemical Engineering Science* 22.12 (1967). DOI: https://doi.org/10.1016/0009-2509(61)80035-3 (cit. on p. 79).

[Cund1979] P. Cundall and O. Strack. “A discrete numerical model for granular assemblies”. *geotechnique* 29.1 (1979). DOI: https://doi.org/10.1680/geot.1979.29.1.47 (cit. on p. 32).

[Dahn1972] B. Dahneke. “The influence of flattening on the adhesion of particles”. *Journal of Colloid and Interface Science* 40.1 (1972). DOI: https://doi.org/10.1016/0021-9797(72)90168-3 (cit. on pp. 48, 51, 61).

[Darb2010] G. K. Darbha, T. Schäfer, F. Heberling, A. Lüttge, and C. Fischer. “Retention of latex colloids on calcite as a function of surface roughness and topography”. *Langmuir* 26.7 (2010). DOI: https://doi.org/10.1021/la9033595 (cit. on p. 183).

[De A2017] I. De Aguiar, T. Van de Laar, M. Meireles, A. Bouchoux, J. Sprakel, and K. Schroën. “Deswelling and deformation of microgels in concentrated packings”. *Scientific reports* 7.1 (2017). DOI: https://doi.org/10.1038/s41598-017-10788-y (cit. on p. 174).

[Debo2003] S. B. Debord and L. A. Lyon. “Influence of particle volume fraction on packing in responsive hydrogel colloidal crystals”. *The Journal of Physical Chemistry B* 107.13 (2003). (Cit. on p. 174).

[Derj1934] B. Derjaguin. “Untersuchungen über die Reibung und Adhäsion, IV”. *Colloid & polymer science* 69.2 (1934). DOI: https://doi.org/10.1007/BF01433225 (cit. on pp. 24, 117).

[Derj1941] B. Derjaguin and L. Landau. “Theory of the stability of strongly charged lyophobic sols and of the adhesion of strongly charged particles in solutions of electrolytes”. *Acta physicochim. URSS* 14.6 (1941). DOI: https://doi.org/10.1016/0079-6816(93)90013-L (cit. on p. 100).

[Ders2015] B. Dersoir, M. de Saint Vincent, M. Abkarian, and H. Tabuteau. “Clogging of a single pore by colloidal particles”. *Microfluidics and Nanofluidics* 19.4 (2015). DOI: https://doi.org/10.1007/s10404-015-1624-y (cit. on pp. 10, 57–61, 68, 74, 84).

[Ders2017] B. Dersoir, A. Schofield, and H. Tabuteau. “Clogging transition induced by self filtration in a slit pore”. *Soft Matter* 13.10 (2017). DOI: https://doi.org/10.1039/C6SM02605B (cit. on p. 10).

[Ders2019] B. Dersoir, A. Schofield, M. de Saint Vincent, and H. Tabuteau. “Dynamics of pore fouling by colloidal particles at the particle level”. *Journal of membrane science* 573 (2019). DOI: https://doi.org/10.1016/j.memsci.2018.12.025 (cit. on pp. 74, 93).

[Dhon1996] J. Dhont. *An introduction to dynamics of colloids*. Vol. 2. Elsevier, 1996 (cit. on p. 28).

[Di M2005] F. Di Maio and A. Di Renzo. “Modelling particle contacts in distinct element simulations: Linear and non-linear approach”. *Chemical Engineering Research and Design* 83.11 (2005). DOI: https://doi.org/10.1205/cherd.05089 (cit. on p. 33).

[Di R2004] A. Di Renzo and F. Di Maio. “Comparison of contact-force models for the simulation of collisions in DEM-based granular flow codes”. *Chemical Engineering Science* 59.3 (2004). DOI: https://doi.org/10.1016/j.ces.2003.09.037 (cit. on pp. 34, 36).

[Dres2017] E. Dressaire and A. Sauret. “Clogging of microfluidic systems”. *Soft matter* 13.1 (2017). DOI: https://doi.org/10.1039/C6SM01879C (cit. on pp. 6–8).

[Drum1997] C. Drummond and D. Chan. “van der Waals Interaction, Surface Free Energies, and Contact Angles: Dispersive Polymers and Liquids”. *Langmuir* (1997). DOI: https://doi.org/10.1021/la962131c (cit. on p. 107).

[Dunk2018] P. Dunkel. “CFD-DEM modeling of membrane fouling with non-spherical colloids [Bachelor thesis]”. *RWTH university* (2018). (Cit. on p. 184).

[Duru2015] P. Duru and Y. Hallez. “A three-step scenario involved in particle capture on a pore edge”. *Langmuir* 31.30 (2015). DOI: https://doi.org/10.1021/acs.langmuir.5b01298 (cit. on p. 60).

[Elim1995] M. Elimelech, J. Gregory, X. Jia, and R. A. Williams. *Particle Deposition and Aggregation: Measurement, Modelling and Simulation*. 1st ed. Woburn: Butterworth-Heinemann, 1995 (cit. on p. 142).

[Elim2013] M. Elimelech, J. Gregory, and X. Jia. *Particle deposition and aggregation: measurement, modelling and simulation*. Butterworth-Heinemann, 2013 (cit. on pp. 14, 19, 22, 78).

[Fern2001] A. Fernandez-Nieves, A. Fernandez-Barbero, B. Vincent, and F. De las Nieves. “Reversible aggregation of soft particles”. *Langmuir* 17.6 (2001). DOI: https://doi.org/10.1021/la001351u (cit. on p. 25).

[Fern2011] A. Fernandez-Nieves, H. Wyss, J. Mattsson, and D. Weitz. *Microgel suspensions: fundamentals and applications*. John Wiley & Sons, 2011 (cit. on p. 153).

[Fiel1995] R. Field, D. Wu, J. Howell, and B. Gupta. “Critical flux concept for microfiltration fouling”. *Journal of Membrane Science* 100 (1995). DOI: https://doi.org/10.1016/0376-7388(94)00265-Z (cit. on pp. 10, 13).

[Garc2006] S. Garcia-Garcia, M. Jonsson, and S. Wold. “Temperature Effect on the Stability of Bentonite Colloids in Water”. *Journal of Colloid and Interface Science* (2006). DOI: https://doi.org/10.1016/j.jcis.2006.01.018 (cit. on pp. 112, 113, 115, 123).

[Gavi2016] N. Gavish and K. Promislow. “Dependence of the Dielectric Constant of Electrolyte Solutions on Ionic Concentration - a Microfield Approach”. *Physical Review E* (2016). DOI: https://doi.org/10.1103/PhysRevE.94.012611 (cit. on p. 108).

[Gida1991] D. Gidaspow, R. Bezburuah, and J. Ding. *Hydrodynamics of circulating fluidized beds: kinetic theory approach*. Tech. rep. Illinois Inst. of Tech., Chicago, IL (United States). Dept. of Chemical . . ., 1991 (cit. on pp. 38, 161).

[Gnan2019] N. Gnan and E. Zaccarelli. “The microscopic role of deformation in the dynamics of soft colloids”. *Nature Physics* (2019). DOI: https://doi.org/10.1038/s41567-019-0480-1 (cit. on pp. 174, 186).

[Goni2010] C. Goniva, C. Kloss, A. Hager, and S. Pirker. “An open source CFD-DEM perspective”. In *Proceedings of OpenFOAM Workshop, Göteborg*. 2010, pp. 22–24 (cit. on pp. 32, 36).

[Goni2012] C. Goniva, C. Kloss, N. Deen, J. Kuipers, and S. Pirker. “Influence of Rolling Friction Modelling on Single Spout Fluidized Bed Simulations”. *Particuology* (2012). DOI: https://doi.org/10.1016/j.partic.2012.05.002 (cit. on p. 101).

[Good1979] J. Goodwin, R. Ottewill, and R. Pelton. “Studies on the preparation and characterization of monodisperse polystyrene latices V.: The preparation of cationic latices”. *Colloid and Polymer Science* 257.1 (1979). DOI: https://doi.org/10.1007/BF01539018 (cit. on p. 113).

[Gouy1910] M. Gouy. “Sur la constitution de la charge électrique à la surface d’un électrolyte”. *J. Phys. Theor. Appl.* 9.1 (1910). (Cit. on p. 19).

[Gras2002] D. Grasso, K. Subramaniam, M. Butkus, K. Strevett, and J. Bergendahl. “A Review of non-DLVO Interactions in Environmental Colloidal Systems”. *Reviews in Environmental Science and Bio/Technology* (2002). DOI: https://doi.org/10.1023/A:1015146710500 (cit. on p. 100).

[Greg1975] J. Gregory. “Interaction of unequal double layers at constant charge”. *Journal of Colloid and Interface Science* 51.1 (1975). DOI: https://doi.org/10.1016/0021-9797(75)90081-8 (cit. on pp. 20, 21, 111).

[Gu2016] Y. Gu, A. Ozel, and S. Sundaresan. “A modified cohesion model for CFD–DEM simulations of fluidization”. *Powder Technology* 296 (2016). DOI: https://doi.org/10.1016/j.powtec.2015.09.037 (cit. on pp. 50, 81).

[Guo2012] W. Guo, H.-H. Ngo, and J. Li. “A mini-review on membrane fouling”. *Bioresource technology* 122 (2012). DOI: https://doi.org/10.1016/j.biortech.2012.04.089 (cit. on p. 152).

[Hærv2017] J. Hærvig. “On the Adhesive Behaviour of Micron-sized Particles in Turbulent Flow: A Numerical Study Coupling the Discrete Element Method and Large Eddy Simulations”. PhD thesis. Aalborg Universitetsforlag, Oct. 2017 (cit. on p. 33).

[Hage2012] A. Hager, C. Kloss, S. Pirker, and C. Goniva. “Parallel open source CFD-DEM for resolved particle-fluid interaction”. In*Ninth International Conference on CFD in the Minerals and Process Industries CSIRO, Melbourne, Australia, Dec*. 2012, pp. 10–12 (cit. on p. 36).

[Hama1937] H. Hamaker. “The London-Van der Waals Attraction between Spherical Particles”. *Physica* (1937). DOI: https://doi.org/10.1016/S0031-8914(37)80203-7 (cit. on pp. 16, 106).

[Hell2000] T. Hellweg, C. Dewhurst, E. Brückner, K. Kratz, and W. Eimer. “Colloidal crystals made of poly (N-isopropylacrylamide) microgel particles”. *Colloid and Polymer Science* 278.10 (2000). DOI: https://doi.org/10.1007/s003960000350 (cit. on p. 174).

[Helm1853] H. v. Helmholtz. “Ueber einige Gesetze der Vertheilung elektrischer Ströme in körperlichen Leitern, mit Anwendung auf die thierisch-elektrischen Versuche”. *Annalen der Physik* 165.7 (1853). (Cit. on p. 18).

[Hend2010] G. Hendrickson and L. Lyon. “Microgel translocation through pores under confinement”. *Angewandte Chemie International Edition* 49.12 (2010). DOI: https://doi.org/10.1002/anie.200906606 (cit. on p. 11).

[Henr2012] C. Henry, J. Minier, and G. Lefèvre. “Towards a description of particulate fouling : From single particle deposition to clogging”. *Advances in Colloid and Interface Science* 185-186 (2012). DOI:

https://doi.org/10.1016/j.cis.2012.10.001 (cit. on pp. 12, 100).

[Hert1882] H. Hertz. “Ueber die Berührung fester elastischer Körper.” *Journal für die reine und angewandte Mathematik* 1882.92 (1882). (Cit. on p. 155).

[Heye2009] D. Heyes and A. Brańka. “Interactions between microgel particles”. *Soft Matter* 5.14 (2009). DOI: https://doi.org/10.1039/B901894H (cit. on pp. 25, 152, 153).

[Hing2017] M. Hinge and M. Christensen. “Non-ionic soft materials influence on filtration resistance and cake dry matter content”. *AIChE Journal* 63.6 (2017). DOI: https://doi.org/10.1002/aic.15632 (cit. on p. 153).

[Ho2000] C.-C. Ho and A. Zydney. “A combined pore blockage and cake filtration model for protein fouling during microfiltration”. *Journal of colloid and interface science* 232.2 (2000). DOI: https://doi.org/10.1006/jcis.2000.7231 (cit. on p. 12).

[Hoek2003] E. Hoek, S. Bhattacharjee, and M. Elimelech. “Effect of membrane surface roughness on colloid-membrane DLVO interactions”. *Langmuir* 19.11 (2003). DOI: https://doi.org/10.1021/la027083c (cit. on pp. 66, 86, 183).

[Hoek2006] E. Hoek and G. Agarwal. “Extended DLVO interactions between spherical particles and rough surfaces”. *Journal of Colloid and Interface science* 298.1 (2006). DOI: https://doi.org/10.1016/j.jcis.2005.12.031 (cit. on pp. 54, 66, 86, 94, 183).

[Hogg1966] R. Hogg, T. Healy, and D. Fuerstenau. “Mutual Coagulation of Colloidal Dispersions”. *Transactions of the Faraday Society* (1966). DOI: https://doi.org/10.1039/TF9666201638 (cit. on pp. 20, 111).

[Hunt2013] R. Hunter. *Zeta potential in colloid science: principles and applications*. Vol. 2. Academic press, 2013 (cit. on p. 19).

[Hwan2003] K.-J. Hwang and C. Hsueh. “Dynamic analysis of cake properties in microfiltration of soft colloids”. *Journal of Membrane Science* 214.2 (2003). DOI: https://doi.org/10.1016/S0376-7388(02)00556-2 (cit. on pp. 12, 152, 172).

[Inte1997] International Association for the Properties of Water and Steam. “Release on the Refractive Index of Ordinary Water Substance as a Function of Wavelength, Temperature and Pressure”. *Erlangen, Germany* (1997). DOI: https://doi.org/10.1063/1.556029@jpr.2019.IWPS2019.issue-1 (cit. on p. 109).

[Ishi2013] T. Ishigami, H. Fuse, S. Asao, D. Saeki, Y. Ohmukai, E. Kamio, and H. Matsuyama. “Permeation of Dispersed Particles through a Pore and Transmembrane Pressure Behavior in Dead-End Constant-Flux Microfiltration by Two-Dimensional Direct Numerical Simulation”. *Industrial & Engineering Chemistry Research* 52.12 (2013). DOI: https://doi.org/10.1021/ie302448x (cit. on pp. 80, 182).

[Isra1982] J. Israelachvili and R. Pashley. “The hydrophobic interaction is long range, decaying exponentially with distance”. *Nature* 300.5890 (1982). DOI: https://doi.org/10.1038/300341a0 (cit. on p. 24).

[Isra1984] J. Israelachvili and R. Pashley. “Measurement of the hydrophobic interaction between two hydrophobic surfaces in aqueous electrolyte solutions”. *Journal of colloid and interface science* 98.2 (1984). DOI: https://doi.org/10.1016/0021-9797(84)90177-2 (cit. on pp. 119, 120, 127).

[Isra2011] J. Israelachvili, ed. *Intermolecular and Surface Forces*. Elsevier, 2011 (cit. on pp. 14, 16–18, 20–22, 26, 47, 48, 51, 52, 61, 63, 77, 78, 82, 100, 103, 107, 108, 111).

[Jasp1972] J. J. Jasper. “The Surface Tension of Pure Liquid Compounds”. *Journal of physical and chemical reference data* 1.4 (1972). DOI: https://doi.org/10.1063/1.3253106 (cit. on p. 119).

[Jin2009] X. Jin, A. Jawor, S. Kim, and E. Hoek. “Effect of Feed Water Temperature on Separation Performance and Organic Fouling of Brackish Water RO Membranes”. *Desalination* (2009). DOI: https://doi.org/10.1016/j.desal.2008.03.026 (cit. on p. 100).

[Karg2019] M. Karg et al. “Nanogels and microgels: From model colloids to applications, recent developments, and future trends”. *Langmuir* 35.19 (2019). DOI: https://doi.org/10.1021/acs.langmuir.8b04304 (cit. on p. 153).

[Kell1975] G. Kell. “Density, Thermal Expansivity, and Compressibility of Liquid Water from 0° to 150°C: Correlations and Tables for Atmospheric Pressure and Saturation Reviewed and Expressed on 1968 Temperature Scale”. *Journal of Chemical and Engineering Data* (1975). DOI: https://doi.org/10.1021/je60064a005 (cit. on p. 109).

[Kim2017] Y. Kim, K. Ahn, and S. Lee. “Clogging mechanism of poly (styrene) particles in the flow through a single micro-pore”. *Journal of Membrane Science* 534 (2017). DOI: https://doi.org/10.1016/j.memsci.2017.04.010 (cit. on pp. 58, 68).

[Kirb2004a] B. Kirby and E. H. Jr. “Zeta Potential of Microfluidic Substrates: 1. Theory, Experimental Techniques, and Effects on Separations”. *Electrophoresis* (2004). DOI: https://doi.org/10.1002/elps.200305754 (cit. on p. 112).

[Kirb2004b] B. Kirby and E. H. Jr. “Zeta potential of Microfluidic Substrates: 2. Data for Polymers”. *Electrophoresis* (2004). DOI: https://doi.org/10.1002/elps.200305755 (cit. on pp. 112, 113).

[Klos2012] C. Kloss, C. Goniva, A. Hager, S. Amberger, and S. Pirker. “Models, algorithms and validation for opensource DEM and CFD–DEM”. *Progress in Computational Fluid Dynamics, an International Journal* 12.2-3 (2012). DOI: https://doi.org/10.1504/PCFD.2012.047457 (cit. on pp. 32, 34, 36, 37, 51, 52, 80, 182).

[Kuzn2007] Z. Kuznar and M. Elimelech. “Direct microscopic observation of particle deposition in porous media: Role of the secondary energy minimum”. *Colloids and Surfaces A: Physicochemical and Engineering Aspects* 294.1–3 (2007). DOI: https://doi.org/10.1016/j.colsurfa.2006.08.007 (cit. on p. 49).

[Ladd2001] A. Ladd and R. Verberg. “Lattice-Boltzmann simulations of particle-fluid suspensions”. *Journal of statistical physics* 104.5-6 (2001). DOI: https://doi.org/10.1023/A:1010414013942 (cit. on p. 79).

[Leck2001] D. Leckband and J. Israelachvili. “Intermolecular forces in biology”. *Quarterly reviews of biophysics* 34.2 (2001). DOI: https://doi.org/10.1017/S0033583501003687 (cit. on pp. 24, 25).

[Li2013] Y. Li, E. Kumacheva, and A. Ramachandran. “The motion of a microgel in an axisymmetric constriction with a tapered entrance”. *Soft Matter* 9.43 (2013). DOI: https://doi.org/10.1039/C3SM51594J (cit. on p. 11).

[Lifs1956] E. Lifshitz. “The Theory of Molecular Attractive Forces between Solids”. *Soviet Physics* (1956). DOI: https://doi.org/10.1016/B978-0-08-036364-6.50031-4 (cit. on p. 107).

[Lifs1992] E. Lifshitz, M. Hamermesh, et al. “The theory of molecular attractive forces between solids”. *Perspectives in Theoretical Physics* (1992). DOI: https://doi.org/10.1016/B978-0-08-036364-6.50031-4 (cit. on p. 17).

[Link2016] J. Linkhorst, T. Beckmann, D. Go, A. Kuehne, and M. Wessling. “Microfluidic colloid filtration”. *Scientific Reports* 6.1 (2016). DOI: https://doi.org/10.1038/srep22376 (cit. on pp. 2, 11, 12, 44, 74, 93, 100, 153, 154, 174).

[Link2018] J. Linkhorst. *Mechanistic analysis of soft colloid filtration*. Verlagshaus Mainz GmbH, 2018 (cit. on pp. 153–155, 159, 162, 163, 173, 174).

[Link2019] J. Linkhorst, J. Rabe, L. Hirschwald, A. Kuehne, and M. Wessling. “Direct observation of Deformation in Microgel filtration”. *Scientific Reports* 9.1 (2019). DOI: https://doi.org/10.1038/s41598-019-55516-w (cit. on pp. 2, 11, 93, 153, 154, 174).

[Lisi2016] M. Lisicki and G. Nägele. “Colloidal Hydrodynamics and Interfacial Effects”. In*Soft Matter at Aqueous Interfaces*. Springer, 2016. Pp. 313–386. (Cit. on pp. 27–29, 63, 105).

[Loha2018a] J. Lohaus, Y. Perez, and M. Wessling. “What are the microscopic events of colloidal membrane fouling?” *Journal of membrane science* 553 (2018). DOI: https://doi.org/10.1016/j.memsci.2018.02.023 (cit. on p. 101).

[Loha2018b] T. Lohaus, N. Herkenhoff, R. Shankar, and M. Wessling. “Feed flow patterns of Combined Rayleigh-Bénard Convection and Membrane Permeation”. *Journal of Membrane Science* 549 (2018). DOI: https://doi.org/10.1016/j.memsci.2017.11.061 (cit. on p. 100).

[Loha2019] J. Lohaus, D. Rall, M. Kruse, V. Steinberger, and M. Wessling. “On charge percolation in slurry electrodes used in vanadium redox flow batteries”. *Electrochemistry Communications* 101 (2019). DOI: https://doi.org/10.1016/j.elecom.2019.02.013 (cit. on p. 181).

[Loha2020] T. Lohaus, J. Beck, T. Harhues, P. de Wit, N. E. Benes, and M. Wessling. “Direct membrane heating for temperature induced fouling prevention”. *Journal of Membrane Science* (2020). DOI: https://doi.org/10.1016/j.memsci.2020.118431 (cit. on p. 100).

[Löls2018] J. Lölsberg, J. Linkhorst, A. Cinar, A. Jans, A. J. C. Kuehne, and M. Wessling. “3D nanofabrication inside rapid prototyped microfluidic channels showcased by wet-spinning of single micrometre fibres”. *Lab on a chip* 18.9 (2018). DOI: https://doi.org/10.1039/c7lc01366c (cit. on p. 75).

[Löls2019] J. Lölsberg, A. Cinar, D. Felder, G. Linz, S. Djeljadini, and M. Wessling. “Two-Photon Vertical-Flow Lithography for Microtube Synthesis”. *Small* (2019). DOI: https://doi.org/10.1002/smll.201901356 (cit. on p. 75).

[Lu2001] W.-M. Lu, K.-L. Tung, S.-M. Hung, J.-S. Shiau, and K.-J. Hwang. “Constant pressure filtration of mono-dispersed deformable particle slurry”. *Separation Science and Technology* 36.11 (2001). DOI: https://doi.org/10.1081/SS-100106098 (cit. on pp. 152, 172).

[Lüke2020] A. Lüken, J. Linkhorst, R. Fröhlingsdorf, L. Lippert, D. Rommel, L. De Laporte, and M. Wessling. “Unravelling colloid filter cake motions in membrane cleaning procedures”. *Scientific reports* 10.1 (2020). DOI: https://doi.org/10.1038/s41598-020-76970-x (cit. on p. 153).

[Ma2000] H. Ma, C. Bowman, and R. Davis. “Membrane fouling reduction by backpulsing and surface modification”. *Journal of Membrane Science* 173.2 (2000). DOI: https://doi.org/10.1016/S0376-7388(00)00360-4 (cit. on p. 74).

[Malm1956] C. Malmberg and A. Maryott. “Dielectric Constant of Water from 0° to 100° C”. *Journal of Research of the National Bureau of Standards* (1956). (Cit. on p. 108).

[Mark1999] J. Mark, ed. *Polymer Data Handbook*. Oxford University Press, Inc, 1999 (cit. on pp. 107, 108).

[Mark2010] C. Markos, K. Vlachos, and G. Kakarantzas. “Bending Loss and Thermo-optic Effect of a Hybrid PDMS/Silica Photonic Crystal Fiber”. *OPTICS EXPRESS* (2010). DOI: https://doi.org/10.1364/OE.18.024344 (cit. on p. 108).

[Mars2015] J. Marshall and S. Renjitham. “Simulation of particulate fouling at a microchannel entrance region”. *Microfluidics and Nanofluidics* 18.2 (2015). DOI: https://doi.org/10.1007/s10404-014-1428-5 (cit. on pp. 12, 75).

[Mart2012] A. Marty, C. Roques, C. Causserand, and P. Bacchin. “Formation of bacterial streamers during filtration in microfluidic systems”. *Biofouling* 28.6 (2012). DOI: https://doi.org/10.1080/08927014.2012.695351 (cit. on pp. 59, 184).

[Mart2018] M. Martí-Calatayud, S. Schneider, S. Yüce, and M. Wessling. “Interplay between physical cleaning, membrane pore size and fluid rheology during the evolution of fouling in membrane bioreactors”. *Water Research* 147 (2018). DOI: https://doi.org/10.1016/j.watres.2018.10.017 (cit. on p. 74).

[Maru1997] S. Maruo, O. Nakamura, and S. Kawata. “Three-dimensional microfabrication with two-photon-absorbed photopolymerization”. *Optics Letters* 22.2 (1997). DOI: https://doi.org/10.1364/OL.22.000132 (cit. on p. 75).

[Mass2016] S. Massenburg, E. Amstad, and D. Weitz. “Clogging in parallelized tapered microfluidic channels”. *Microfluidics and Nanofluidics* 20.6 (2016). DOI: https://doi.org/10.1007/s10404-016-1758-6 (cit. on p. 44).

[Mino2018] Y. Mino, S. Sakai, and H. Matsuyama. “Simulations of particulate flow passing through membrane pore under dead-end and constant-pressure filtration condition”. *Chemical Engineering Science* 190 (2018). DOI: https://doi.org/10.1016/j.ces.2018.05.061 (cit. on pp. 3, 12, 13, 59, 75, 80, 183).

[Mo2008] H. Mo, K. Tay, and H. Ng. “Fouling of Reverse Osmosis Membrane by Protein (BSA): Effects of pH, Calcium, Magnesium, Ionic Strength and Temperature”. *Journal of Membrane Science* (2008). DOI: https://doi.org/10.1016/j.memsci.2008.02.002 (cit. on p. 100).

[Mond2016] S. Mondal, C. Wu, and M. Sharma. “Coupled CFD-DEM simulation of hydrodynamic bridging at constrictions”. *International Journal of Multiphase Flow* 84 (2016). DOI: https://doi.org/10.1016/j.ijmultiphaseflow.2016.05.001 (cit. on p. 75).

[Must2010] B. Mustin and B. Stoeber. “Deposition of particles from polydisperse suspensions in microfluidic systems”. *Microfluidics and nanofluidics* 9.4-5 (2010). DOI: https://doi.org/10.1007/s10404-010-0613-4 (cit. on pp. 9, 58, 68).

[Must2016] B. Mustin and B. Stoeber. “Single Layer Deposition of Polystyrene Particles onto Planar Polydimethylsiloxane Substrates”. *Langmuir : the ACS journal of surfaces and colloids* 32.1 (2016). DOI: https://doi.org/10.1021/acs.langmuir.5b02914 (cit. on pp. 48, 51, 68, 75, 82, 86, 112, 115, 127, 128).

[Naka1987] K. Nakanishi, T. Tadokoro, and R. Matsuno. “On the specific resistance of cakes of microorganisms”. *Chemical Engineering Communications* 62.1-6 (1987). DOI: https://doi.org/10.1080/00986448708912059 (cit. on p. 152).

[Napp1977] D. Napper. “Steric stabilization”. *Journal of colloid and interface science* 58.2 (1977). DOI: https://doi.org/10.1016/0021-9797(77)90150-3 (cit. on pp. 24, 25).

[Napp1983] D. Napper. *Polymeric stabilization of colloidal dispersions*. Vol. 3. Academic Press, 1983 (cit. on p. 24).

[Ngen2010] I. Ngene, R. Lammertink, M. Wessling, and W. van der Meer. “A microfluidic membrane chip for in situ fouling characterization”. *Journal of Membrane Science* 346.1 (2010). DOI: https://doi.org/10.1016/j.memsci.2009.09.035 (cit. on pp. 2, 44, 74, 100).

[Ngen2011] I. Ngene, R. Lammertink, M. Wessling, and W. Van der Meer. “Visual characterization of fouling with bidisperse solution”. *Journal of Membrane Science* 368.1-2 (2011). DOI: https://doi.org/10.1016/j.memsci.2010.11.026 (cit. on pp. 2, 44, 100).

[Ninh1999] B. Ninham. “On Progress in Forces since the DLVO Theory”. *Advances in Colloid and Interface Science* (1999). DOI: https://doi.org/10.1016/S0001-8686(99)00008-1 (cit. on p. 100).

[Nir2016] O. Nir, T. Trieu, S. Bannwarth, and M. Wessling. “Microfiltration of deformable microgels”. *Soft Matter* 12.31 (2016). DOI: https://doi.org/10.1039/C6SM01345G (cit. on pp. 44, 153).

[Nish2019] J. Nishitani, Y. Mino, and H. Matsuyama. “Numerical simulation of particulate cake formation in cross-flow microfiltration: Effects of attractive forces”. *Advanced Powder Technology* 30.8 (2019). DOI: https://doi.org/10.1016/j.apt.2019.05.006 (cit. on p. 12).

[Nobl1995] R. D. Noble and S. A. Stern. *Membrane separations technology: principles and applications*. Elsevier, 1995 (cit. on p. 2).

[Noro2016] H. Norouzi, R. Zarghami, R. Sotudeh-Gharebagh, and N. Mostoufi. *Coupled CFD-DEM Modeling: Formulation, Implementation and Application to Multiphase Flows*. John Wiley & Sons, 2016 (cit. on pp. 34, 36, 37).

[Ohsh1982] H. Ohshima, T. Healy, and L. White. “Accurate Analytic Expressions for the Surface Charge Density/ Surface Potential Relationship and Double-Layer Potential Distribution for a Spherical Colloidal Particle”. *Journal of Colloid and Interface Science* (1982). DOI: https://doi.org/10.1016/0021-9797(82)90393-9 (cit. on pp. 21, 112).

[Ohsh2006] H. Ohshima. *Theory of colloid and interfacial electric phenomena*. Vol. 12. Elsevier, 2006 (cit. on pp. 18, 25).

[Oss1988] C. van Oss, R. Good, and M. Chaudhurys. “Additive and Nonadditive Surface Tension Components and the Interpretation of Contact Angles”. *Langmuir* (1988). DOI: https://doi.org/10.1021/la00082a018 (cit. on p. 116).

[Oss1993] C. van Oss. “Acid-base Interfacial Interactions in Aqueous Media”. *Colloids and Surfaces A: Physicochemical and Engineering Aspects* (1993). DOI: https://doi.org/10.1016/0927-7757(93)80308-2 (cit. on pp. 115–117).

[Oss2006] C. van Oss, ed. *Interfacial Forces in Aqueous Media*. CRC Press, 2006 (cit. on pp. 77–79, 82, 106, 115–117, 119).

[Oss2008] C. van Oss, ed. *The Properties of Water and their Role in Colloidal and Biological Systems*. Academic Press, 2008 (cit. on p. 119).

[Parq2013] B. Parquette and D. O’Brien. *Refractive Index Measurement of Fibers Through Fizeau Interferometry*. Tech. rep. ARMY RESEARCH LAB ABERDEEN PROVING GROUND MD, 2013 (cit. on p. 108).

[Pars1970] V. Parsegian and B. Ninham. “Temperature-Dependent van der Waals Forces”. *Biophysical Journal* 10.7 (1970). DOI: https://doi.org/10.1016/S0006-3495(70)86327-5 (cit. on p. 110).

[Podl2017] A. Podlozhnyuk, S. Pirker, and C. Kloss. “Efficient implementation of superquadric particles in Discrete Element Method within an open-source framework”. *Computational Particle Mechanics* 4.1 (2017). DOI: https://doi.org/10.1007/s40571-016-0131-6 (cit. on p. 184).

[Repp2003] P. Reppert and F. Morgan. “Temperature-dependent Streaming Potentials: 1. Theory”. *Journal of Geophysical Research* (2003). DOI: https://doi.org/10.1029/2002JB001754 (cit. on p. 112).

[Roa2015] R. Roa, E. Zholkovskiy, and G. Nägele. “Ultrafiltration modeling of non-ionic microgels”. *Soft matter* 11.20 (2015). DOI: https://doi.org/10.1039/c5sm00678c (cit. on pp. 159, 160).

[Rovi2019] L. Rovigatti, N. Gnan, L. Tavagnacco, A. J. Moreno, and E. Zaccarelli. “Numerical modelling of non-ionic microgels: an overview”. *Soft matter* 15.6 (2019). (Cit. on pp. 25, 156).

[Sado2014] M. Sadowska, Z. Adamczyk, and M. Nattich-Rak. “Mechanism of Nanoparticle Deposition on Polystyrene Latex Particles”. *Langmuir* (2014). DOI: https://doi.org/10.1021/la404046c (cit. on p. 112).

[Sain2016] M. de Saint Vincent, M. Abkarian, and H. Tabuteau. “Dynamics of colloid accumulation under flow over porous obstacles”. *Soft matter* 12.4 (2016). DOI: https://doi.org/10.1039/C5SM01952D (cit. on pp. 8, 60, 100).

[Scot1969] G. Scott and D. Kilgour. “The density of random close packing of spheres”. *Journal of Physics D: Applied Physics* 2.6 (1969). (Cit. on p. 166).

[Seeb1995] J. Seebergh and J. Berg. “Evidence of a hairy layer at the surface of polystyrene latex particles”. *Colloids and Surfaces A: Physicochemical and Engineering Aspects* 100 (1995). (Cit. on p. 142).

[Send2016a] Z. Sendekie and P. Bacchin. “Colloidal Jamming Dynamics in Microchannel Bottlenecks”. *Langmuir* 32.6 (2016). DOI: https://doi.org/10.1021/acs.langmuir.5b04218 (cit. on pp. 9, 58–60, 68, 76).

[Send2016b] Z. Sendekie, A. Gaveau, R. Lammertink, and P. Bacchin. “Bacteria delay the jamming of particles at microchannel bottlenecks”. *Scientific reports* 6 (2016). DOI: https://doi.org/10.1038/srep31471 (cit. on p. 184).

[Senf1999] H. Senff and W. Richtering. “Temperature sensitive microgel suspensions: Colloidal phase behavior and rheology of soft spheres”. *The Journal of chemical physics* 111.4 (1999). DOI: https://doi.org/10.1063/1.479430 (cit. on p. 25).

[Seth2010] M. Sethi and M. Satake. *Chemical Bonding*. Discovery Publishing House, 2010 (cit. on p. 110).

[Shar1992] M. M. Sharma, H. Chamoun, D. R. Sarma, and R. S. Schechter. “Factors controlling the hydrodynamic detachment of particles from surfaces”. *Journal of Colloid and Interface Science* 149.1 (1992). DOI: https://doi.org/10.1016/0021-9797(92)90398-6 (cit. on p. 74).

[She2012] S. She, C. Xu, X. Yin, W. Tong, and C. Gao. “Shape deformation and recovery of multilayer microcapsules after being squeezed through a microchannel”. *Langmuir* 28.11 (2012). DOI: https://doi.org/10.1021/la3003299 (cit. on p. 11).

[Shuk2019] G. Shukla and A. Franco. “Interphases in Electroactive Suspension Systems: Where Chemistry Meets Mesoscale Physics”. *Batteries & Supercaps* 2.7 (2019). DOI: https://doi.org/10.1002/batt.201800152 (cit. on p. 181).

[Sjol1990] J. Sjollema and H. Busscher. “Deposition of polystyrene particles in a parallel plate flow cell. 1. The influence of collector surface properties on the experimental deposition rate”. *Colloids and surfaces* 47 (1990). DOI: https://doi.org/10.1016/0166-6622(90)80081-E (cit. on p. 183).

[Song1994] L. Song, P. Johnson, and M. Elimelech. “Kinetics of colloid deposition onto heterogeneously charged surfaces in porous media”. *Environmental science & technology* 28.6 (1994). DOI: https://doi.org/10.1021/es00055a030 (cit. on p. 54).

[Ster1924] O. Stern. “The theory of the electrolytic double-layer”. *Z. Elektrochem* 30.508 (1924). (Cit. on p. 19).

[Stoc2015] P. Stock, T. Utzig, and M. Valtiner. “Direct and quantitative AFM measurements of the concentration and temperature dependence of the hydrophobic force law at nanoscopic contacts”. *Journal of colloid and interface science* 446 (2015). DOI: https://doi.org/10.1016/j.jcis.2015.01.032 (cit. on p. 119).

[Sun2004] G. Sun, M. Kappl, T. Pakula, K. Kremer, and H.-J. Butt. “Equilibrium interaction of solid surfaces across a polymer melt”. *Langmuir* 20.19 (2004). (Cit. on p. 107).

[Tan2005] S. Tan, R. Sherman, D. Qin, and W. Ford. “Surface heterogeneity of polystyrene latex particles determined by dynamic force microscopy”. *Langmuir* 21.1 (2005). DOI: https://doi.org/10.1021/la047821s (cit. on pp. 54, 86).

[Tana1994] T. Tanaka, R. Kamimura, R. Fujiwara, and K. Nakanishi. “Crossflow filtration of yeast broth cultivated in molasses”. *Biotechnology and bioengineering* 43.11 (1994). DOI: https://doi.org/10.1002/bit.260431113 (cit. on p. 152).

[Tang2011] C. Tang, T. Chong, and A. Fane. “Colloidal interactions and fouling of NF and RO membranes: A review”. *Advances in Colloid and Interface Science* 164.1–2 (2011). DOI: https://doi.org/10.1016/j.cis.2010.10.007 (cit. on p. 1).

[Trza2016] K. Trzaskus, A. Zdeb, W. de Vos, A. Kemperman, and K. Nijmeijer. “Fouling behavior during microfiltration of silica nanoparticles and polymeric stabilizers”. *Journal of Membrane Science* 505 (2016). DOI: https://doi.org/10.1016/j.memsci.2016.01.032 (cit. on p. 44).

[Tsai1991] C. Tsai, D. Pui, and B. Liu. “Particle detachment from disk surfaces of computer disk drives”. *Journal of aerosol science* 22.6 (1991). DOI: https://doi.org/10.1016/0021-8502(91)90066-Q (cit. on p. 74).

[Tufe2004] N. Tufenkji and M. Elimelech. “Deviation from the Classical Colloid Filtration Theory in the Presence of Repulsive DLVO Interactions”. *Langmuir* 20.25 (2004). DOI: https://doi.org/10.1021/la0486638 (cit. on p. 101).

[Tufe2005] N. Tufenkji and M. Elimelech. “Breakdown of colloid filtration theory: Role of the secondary energy minimum and surface charge heterogeneities”. *Langmuir* 21.3 (2005). DOI: https://doi.org/10.1021/la048102g (cit. on p. 101).

[Van 1873] J. Van der Waals. *Over de Continuiteit van den Gas-en Vloeistoftoestand*. Vol. 1. Sijthoff, 1873 (cit. on p. 16).

[Van 1987] T. J. Van den Hoven and B. Bijsterbosch. “Streaming currents, streaming potentials and conductances of concentrated dispersions of negatively-charged, monodisperse polystyrene particles. Effect”. *Colloids and surfaces* 22.2 (1987). (Cit. on p. 142).

[Van 1988] C. J. Van Oss, M. K. Chaudhury, and R. J. Good. “Interfacial Lifshitz-van der Waals and polar interactions in macroscopic systems”. *Chemical reviews* 88.6 (1988). (Cit. on p. 22).

[Van 2006] C. Van Oss. *Interfacial forces in aqueous media*. CRC press, 2006 (cit. on pp. 14, 15, 22–24, 54, 61, 63, 82, 118, 120, 128).

[Van 2008] C. Van Oss. *The properties of water and their role in colloidal and biological systems*. Vol. 16. Academic Press, 2008 (cit. on pp. 23, 119, 127, 128).

[Ven2008] W. van de Ven, K. Sant, I. Pünt, A. Zwijnenburg, A. Kemperman, W. van der Meer, and M. Wessling. “Hollow fiber dead-end ultrafiltration: Influence of ionic environment on filtration of alginates”. *Journal of Membrane Science* 308.1-2 (2008). (Cit. on p. 74).

[Vend2006] R. Venditti, X. Xuan, and D.-D. Li. “Experimental Characterization of the Temperature Dependence of Zeta Potential and its Effect on Electroö-osmotic Flow Velocity in Microchannels”. *Microfluidics and Nanofluidics* (2006). DOI: https://doi.org/10.1007/s10404-006-0100-0 (cit. on p. 112).

[Verw1948] E. Verwey and J. Overbeek. “Theory of the Stability of Lyphobic Colloids”. *Elsevier* (1948). DOI: https://doi.org/10.1021/j150453a001 (cit. on p. 100).

[Vinc1986] B. Vincent, J. Edwards, S. Emmett, and A. Jones. “Depletion flocculation in dispersions of sterically-stabilised particles”. *Colloids and Surfaces* 18.2-4 (1986). DOI: https://doi.org/10.1016/0166-6622(86)80317-1 (cit. on p. 25).

[Viss1995] J. Visser. “Particle adhesion and removal: A review”. *Particulate science and technology* 13.3-4 (1995). DOI: https://doi.org/10.1080/02726359508906677 (cit. on pp. 48, 51, 61).

[Visw2007] D. Viswanath, T. Ghosh, D. Prasad, N. Dutt, and K. Rani. *Viscosity of liquids: theory, estimation, experiment, and data*. Springer Science & Business Media, 2007 (cit. on p. 104).

[Wang2014] H. Wang and B.-m. Newby. “Applicability of the Extended Derjaguin-Landau-Verwey-Overbeek Theory on the Adsorption of Bovine Serum Albumin on Solid Surfaces”. *Biointerphases* (2014). DOI: https://doi.org/10.1116/1.4904074 (cit. on p. 115).

[Wars1997] P. Warszynski and Z. Adamczyk. “Calculations of Double-Layer Electrostatic Interactions for the Sphere/Plane Geometry”. *Journal of Colloid and Interface Science* (1997). DOI: https://doi.org/10.1006/jcis.1996.4671 (cit. on pp. 20, 21, 111).

[Wess2001] M. Wessling. “Two-dimensional stochastic modeling of membrane fouling”. *Separation and purification technology* 24.3 (2001). DOI: https://doi.org/10.1016/S1383-5866(01)00138-1 (cit. on pp. 2, 12, 47, 75, 101).

[Whit2006] G. Whitesides. “The origins and the future of microfluidics”. *Nature* 442.7101 (2006). DOI: https://doi.org/10.1038/nature05058 (cit. on p. 41).

[Wick2010] S. Wickramasinghe, E. Stump, D. Grzenia, S. Husson, and J. Pellegrino. “Understanding virus filtration membrane performance”. *Journal of Membrane Science* 365.1-2 (2010). DOI: https://doi.org/10.1016/j.memsci.2010.09.002 (cit. on p. 44).

[Wied2011] S. Wiederseiner, N. Andreini, G. Epely-Chauvin, and C. Ancey. “Refractive-index and Density Matching in Concentrated Particle Suspensions: a Review”. *Experiments in Fluids* (2011). DOI: https://doi.org/10.1007/s00348-010-0996-8 (cit. on p. 108).

[Wies1970] G. Wiese and T. Healy. “Effect of Particle Size on Colloid Stability”. *Transactions of the Faraday Society* (1970). DOI: https://doi.org/10.1039/TF9706600490 (cit. on pp. 20, 111).

[Will1998] R. Williams, ed. *Particle Deposition and Aggregation: Measurement, Modelling and Simulation*. Butterworth-Heinemann, 1998 (cit. on pp. 20, 22, 111, 112).

[Wyss2006] H. Wyss, D. Blair, J. Morris, H. Stone, and D. Weitz. “Mechanism for clogging of microchannels”. *Physical review E* 74.6 (2006). DOI: 10.1016/j.memsci.2009.09.035 (cit. on pp. 1, 2, 6–10, 44, 74, 86, 100).

[Xu1995] Y. Xu, J. Dodds, and D. Leclerc. “Optimization of a discontinuous microfiltration-backwash process”. *The Chemical Engineering Journal and the Biochemical Engineering Journal* 57.3 (1995). DOI: https://doi.org/10.1016/0923-0467(94)02874-A (cit. on p. 74).

[Yan2015] Z. Yan, X. Huang, and C. Yang. “Deposition of Colloidal Particles in a Microchannel at Elevated Temperatures”. *Microfluid Nanofluid* (2015). DOI: https://doi.org/10.1007/s10404-014-1448-1 (cit. on pp. 100, 103, 109, 112).

[Zama2016] F. Zamani, A. Ullah, E. Akhondi, H. Tanudjaja, E. Cornelissen, A. Honciuc, A. Fane, and J. Chew. “Impact of the surface energy of particulate foulants on membrane fouling”. *Journal of Membrane Science* 510 (2016). DOI: https://doi.org/10.1016/j.memsci.2016.02.064 (cit. on p. 57).

[Zhu2007] H. Zhu, Z. Zhou, R. Yang, and A. Yu. “Discrete particle simulation of particulate systems: theoretical developments”. *Chemical Engineering Science* 62.13 (2007). DOI: https://doi.org/10.1016/j.ces.2006.12.089 (cit. on pp. 32, 34, 37, 38, 41).

[Zisk2006] G. Ziskind. “Particle resuspension from surfaces: Revisited and re-evaluated”. Review Paper. Beer-Sheva, Israel: Ben-Gurion University of the Negev, 2006. DOI: https://doi.org/10.1515/REVCE.2006.22.1-2.1 (cit. on p. 74).